Università
di Genova

Polytechnic School

DITEN - Electrical, Electronics and Telecommunication
Engineering and Naval Architecture Department

Ph.D. in Sciences and Technologies for Electrical Engineering
and Complex Systems for Mobility

Stability Analysis and advanced control strategies for Matrix Converter

Supervisors:

Prof. Mario Marchesoni

Prof. Luis Vaccaro

Prof. Andrea Formentini

Author:

Lorenzo Carbone

2023/2024

To my beloved family

Acknowledgement

I would like to express my sincere gratitude to my supervisors, Prof. Mario Marchesoni and Prof. Luis Vaccaro, for their guidance, support, and trust during my Ph.D. activity. A special thanks also goes to Prof. Andrea Formentini for the invaluable teachings provided throughout this period. I extend my gratitude to Prof. Patrick Wheeler, Prof. Michele Degano, Dr. Andrew Trentin, and Dr. Jacopo Riccio for their warm welcome during the six months I spent at the University of Nottingham.

I want to thank my colleagues at PETRA Lab, Alessandro Benevieri, Simone Cosso, Krishneel Kumar, Massimiliano Passalacqua, Dmytro Rodkin with whom I have shared this journey. I have collected moments (and cirulla matches) that I will carry in my heart.

I would like to extend my gratitude to my fellow Nottingham adventurers Antonio, Gaia, Liam and Riccardo, your presence made my time in Nottingham one of the most fun and carefree periods of my life. I certainly have to thank my closest friends Alessandro, Alessio, Andrea, Federico, Irene, Milena who, unknowingly, have provided me with irreplaceable help. A heartfelt thank you goes out to my cousin Alessandro, you have been and continue to be one of my biggest supporters. I truly lack the words to express my gratitude.

Lastly, I express my deepest appreciation to my mother, father, and sister for their unwavering support throughout these years. Mum and Dad, thank you for allowing me to follow my dreams and for always encouraging me to do my best. I dedicate this achievement to you. Mimi thank you for being an amazing sister but also my best friend. Without your presence in my life I would not be who I am today.

Abstract

Matrix Converter allows for m-phase to n-phase direct AC-AC conversion through an m×n array of bidirectional switches. It is a four-quadrant converter with controllable input power factor. Its main advantage lies on the absence of an intermediate DC stage, thereby obviating the necessity for heavy and bulky electrolytic capacitors. In fact, these components are prone to aging, compromising the overall system reliability. The focus of this dissertation is on three-phase to three-phase Matrix Converters, specifically on investigating the stability of three-phase applications employing this converter. The input side of the Matrix Converter can be considered as a controlled current source, requiring the connection of an LC filter to reduce the harmonic content of the input current and meet the EMC requirements. It is well know that this component connected to the input side of a power converter introduce instabilities, which depends on system topology and control strategy. This becomes more evident in presence of high bandwidth closed-loops. In the case of the Matrix Converter, this phenomenon is worsen by the absence of a DC stage, which, in traditional AC-AC converters, enhances stability. In particular, when analysing open-loop conditions, it is possible to demonstrate that instabilities depend primarily on the power exchanged between input and output. In the case of closed-loops the effect is worsen depending on control bandwidth. Stability studies on this converter are complicated by the fact that its average model equations are nonlinear making calculations more complex. Over the past few decades, the research on this field focus on solutions to enhance Matrix Converter applications stability. For example, the input filter can be properly designed to maximise the power transmission and the control bandwidth. However, this method is still intrinsically limited. Another approach adopted is to filter the input voltage signal necessary for the converter modulation. While this method allows to increase the transmittable power, it proves limited in case of high control bandwidth. In the literature there are also solutions that allow the transmitted power to be increased by modifying the voltage reference supplied to the modulator, however even in this case limitations are encountered in terms of control bandwidth. Model Predictive Control (MPC) strategies have been studied for this converter. Unfortunately, due to the high number of switches combinations, this approach requires a significant com-

putational burden. In the preliminary phase of this dissertation, an analysis of existing stabilization methods is presented, focusing on their limits in terms of power and control bandwidth. Subsequently, a novel stabilization method employing full-state feedback is proposed. An H_2-LMI inequality (LMI) algorithm is utilized to compute feedback gains that guarantee robust performance across a predefined bidirectional power operational range with high control bandwidth. The proposed system was found to be more stable than the methods present in the literature, thus increasing both transmissible power and control bandwidth while reducing the harmonic content of the input and output quantities, with a low computation burden. The effectiveness of the proposed algorithm has been tested firstly through simulations, using MATLAB Simulink, followed by subsequent experimental validation.

Abbreviations

MC	Matrix Converter
AC	Alternating Current
DC	Direct Current
DMC	Direct Matrix Converter
IMC	Indirect Matrix Converter
LC	Inductor-Capacitor
MDCM	Modulation Duty-Cycle Matrix
SVM	Space Vector Modulation
EMC	Electromagnetic Compatibility
MPC	Model Predictive Control
EMI	Electromagnetic Interferance
IGBT	Insulated-Gate Bipolar Transistor
Si	Silicon
SiC	Silicon Carbide
MOSFET	Metal-Oxide-Semiconductor Field-Effect Transistor
SVM	Space Vector Modulation
VSI	Voltage Source Inverter
RL	Resistor-Inductor
SM-PMSM	Surface Mounted Permanent Magnet Synchronous Motor
DSP	Digital Signal Processor
RMS	Root-Mean-Square
LPF	Low-Pass Filter
HPF	High-Pass Filter
MIMO	Multiple-Input and Multiple-Output

Contents

List of Figures

List of Tables

Chapter 1:

Introduction to Matrix Converter

1.1 Literature Review and Thesis Objectives

A Matrix Converter (MC) is a direct four-quadrant AC-AC converter that allows the conversion of the m-phase input to n-phase. Thanks to its structure, this process does not necessitate any intermediate DC stage. This is made possible by an m×n array of ideal switches, which ideally can connect each input phase with each output phase. Over the years, two topologies have been proposed for this converter: First in order of time, the Direct Matrix Converter (DMC) presented in [1], followed by the Indirect Matrix Converter (IMC) [2]. There are numerous technical reviews of this technologies in literature [3, 4]. A comparison between DMC and IMC in terms of efficiency is presented in [5]. Both topologies enable AC-AC conversion without the need for a DC intermediate stage. The absence of a DC link eliminates the need for heavy and bulky electrolytic capacitors. The resulting AC-AC converter is therefore lighter and less bulky than a conventional back-to-back converter, maximising its power density [6, 7]. In addition, electrolytic capacitors are a critical component as they significantly reduce the overall converter reliability. The above characteristics mean that the matrix converter is preferred over the back-to-back converter in applications where small size and low weight, together with high reliability, are required. These applications include avionics and aerospace applications [8, 9, 10], renewable energy, particularly wind power [11, 12, 13], variable speed drives [14, 15, 16, 17, 18, 19] and distributed energy applications [20, 21]. In Fig. 1.1 the simplified schematic of a three-phase to three-phase Direct Matrix Converter is shown. As evident from Fig. 1.1 this MC is composed of nine ideal switches. These components must be capable of conducting the current in both direction. This requirement necessitates the use of bidirectional switches. The MC input side can be seen as a controlled current source, while the output side as a controlled voltage source. This means that an inductor-capacitor LC filter

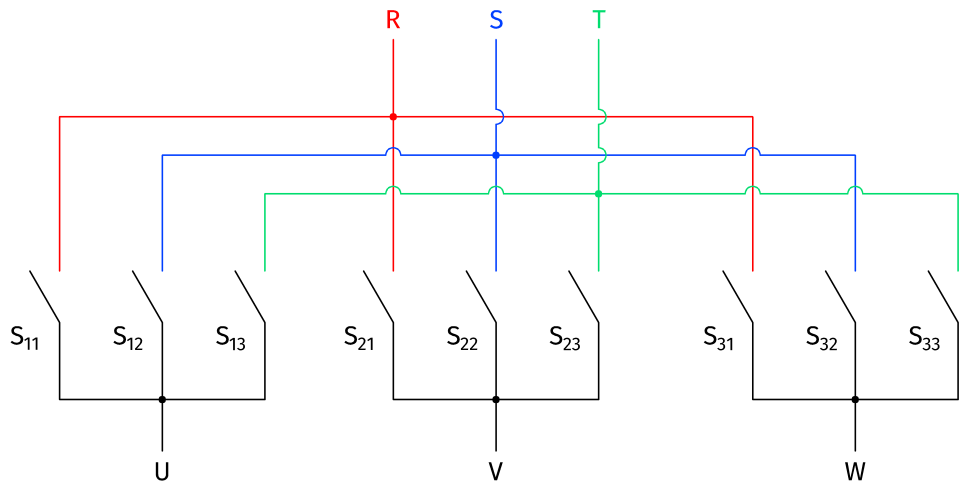

Figure 1.1: Three-phase to three-phase Matrix Converter simplified schematic

must be used on the input-side to reduce the harmonic content of the input currents, according to the regulations imposed by the supplying grid. It is precisely the presence of the LC input filter combined with the absence of a DC link that leads to the biggest limitation of this converter. In fact, the matrix converter has stability problems due to the resonant nature of the filter and the lack of intermediate energy storage such as the DC link. In particular the instabilities increase as the amount of power transmitted increases [22, 23, 24, 25]. Furthermore, the instabilities become more problematic when the converter is controlled by a closed-loop with high control bandwidth. A first approach to the problem could be to design the LC filter to reduce its effect on stability [26]. However, this approach has significant limitations. Research therefore turned to solving the problem by implementing stabilization algorithms, and there are various examples in literature. In [27], the effect of a digital low-pass filter applied to the input voltage measurement necessary for the modulation was studied. Transmissible power increases, but unfortunately, the difference between the filtered input voltages used for modulation and the actual input voltages leads to a worsening in the harmonic content of the output current. Another approach is presented in [28], where a corrective term was added to the reference signals of the modulator to increase the input admittance. Again, this method increases the range of power that can be transmitted, but it degrades the quality of the input currents. Specifically, the more the range is increased, the worse the distortion will be. A Predictive Power Control strategy with Active Damping was presented in [29]. Model Predictive Control (MPC) algorithms have also been studied to solve

the instability problem [30, 31]. But despite their development in recent years and their capability to increase the transmissible power range even with high control bandwidth, they have some criticalities. In fact, systems employing MPC algorithms usually present variable switching frequency and high ripple currents, which may necessitate the use of output filters [29]. It is however possible to realize MPC algorithms that have fixed switching frequency, as presented in [32]. This study solved the switching frequency problem, but highlighted another critical issue with the MPC algorithms, which cannot be easily solved, namely the high computational burden. In the matrix converter this problem is worsen by the high number of switching components. The limitations of the solutions illustrated so far have therefore been: combining high power with high control bandwidth and keeping computing power low. In the following dissertation the development of a stabilization method based on full state feedback is presented. To achieve high performance in terms of power and control bandwidth, a H_2-LMI algorithm has been used. This technique allows to obtain robust performance in a defined power range maintaining a high control speed. In addition, because it based on PWM modulation, it guarantee fixed switching frequency. Moreover, what makes it advantageous over the MPC method is that it requires a relatively low computation burden, and can therefore be implemented on common microcontrollers. The H_2-LMI full state feedback approach has already been investigated for the control of other grid-connected converters, such as is [33, 34], to design Automatic Voltage Regulators (AVR) [35] and to develop AC-microgrid control strategies [36]. Being a full state feedback requires the measurement of all system state variables. In order not to add further measurements to the system, and to be able to compare the proposed control strategy with stabilisation methods in the literature, an observer was developed using a Kalman filter. Chapter 1 of this study provides an introduction to the matrix converter in terms of design and function, while Chapter 2 introduces the mathematical models that will be used in Chapter 3 for the stability study and analysis of the methods proposed in the literature. Chapter 4 presents the development of the new control strategy based on H_2-LMI full state feedback and the development of the Kalman filter. Chapter 5 presents the experimental setup and the results obtained by comparing the proposed new method with those already existing in the literature. The Conclusion chapter summarises the results obtained and the real benefits of the proposed method.

1.2 Operating Principle

The operating principle of the matrix converter can be summarised as follows: the output voltage is generated by applying the input voltages to each output phase for a specific period of time. The duration of the application of the input voltages is determined by the modulation algorithm. The latter is provided with reference output voltages, reference input phase shift between input voltage and current, and actual input voltages. From this data, the application periods for each phase are calculated. Fig. 1.2 shows a simplified example of how the input voltages are applied to obtain an output phase voltage. The figure shows a significantly lower switching frequency than the one actually used. This choice was made in order to make the operating principle more understandable, simplifying the representation without compromising the accuracy of the actual operating context. When analysing a single switching period T_s and a single

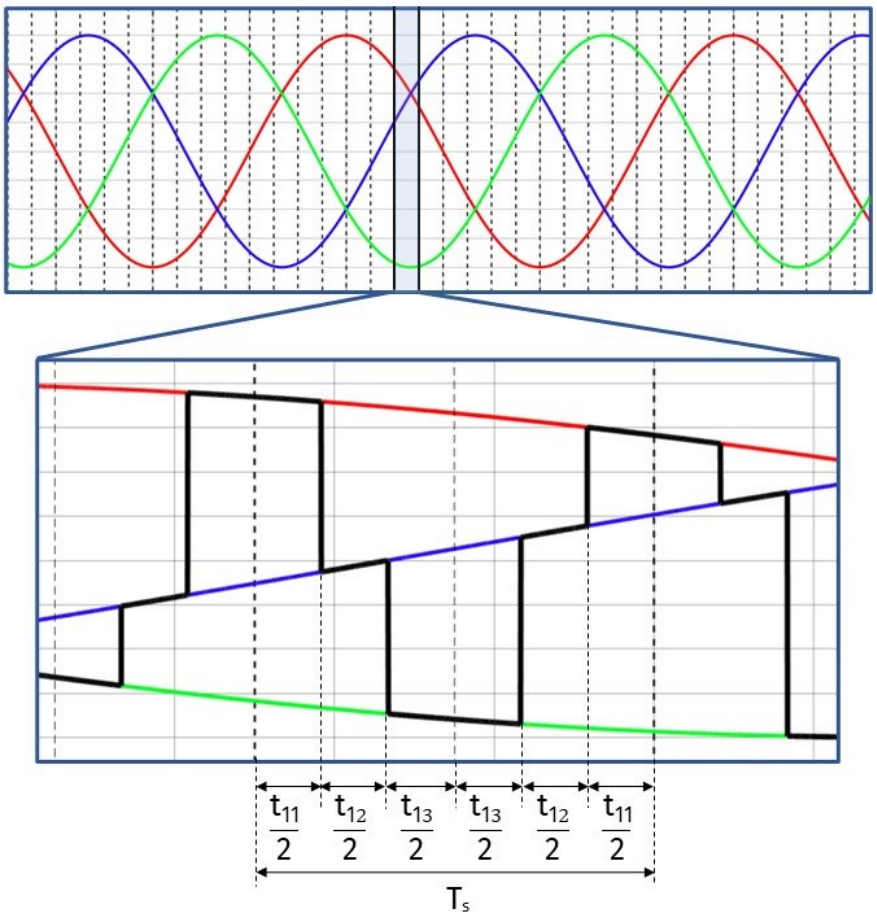

Figure 1.2: Three-phase to three-phase Matrix Converter operating principle. Output phase voltage (black) obtained by combining three-phase input voltages

output phase, it can be seen that the application times, respectively t_{11}, t_{12} and t_{13} are divided into two parts. The input voltages V_{ir}, V_{is} and V_{it} are applied at the output starting with the higher one and proceeding towards the lower one, and then back towards the higher one. This is one of the methods that can be used to apply the input voltage to the output. In particular, the method shown in Fig. 1.2 is implemented to reduce the harmonic content of the input and output quantities. From a mathematical point of view, the average voltage applied to the output phase can be calculated as follows:

$$V_{ou} = \frac{t_{11}\, V_{ir} + t_{12}\, V_{is} + t_{13}\, V_{it}}{T_s} \tag{1.1}$$

Practically, t_{11}, t_{12} and t_{13} represent the switch-on time of switches S_{11}, S_{12} and S_{13}. Application times can be recalculated at each half switching period if higher performance is required. When one switch is switched on, the others must necessarily be switched off to avoid short circuits between the input phases. The output voltages thus obtained have discontinuous waveform, whereas the input voltages are continuous due to the presence of the LC filter capacitors. The output currents, since the load applied to the output is inductive, are continuous. Taking a power balance between input and output, it is clear that the input currents will have a discontinuous waveform. The method by which application times are calculated depends on the type of modulation adopted. Modulation strategies are one of the hardest task related to the matrix converter. Two main approaches to solving this problem have been studied in the literature, the Modulation Duty-Cycle Matrix (MDCM) approach and the Space Vector Modulation (SVM) approach respectively. The following is a brief introduction to the modulation methods presented in the literature.

1.3 Modulation Methods

Considering what is stated in the (1.1) it is possible to define the duty cycle as:

$$m_{11} = \frac{t_{11}}{T_s}; \qquad m_{12} = \frac{t_{12}}{T_s}; \qquad m_{13} = \frac{t_{13}}{T_s} \tag{1.2}$$

So (1.1) can be rewritten as follows:

$$V_{ou} = m_{11}\, V_{ir} + m_{12}\, V_{is} + m_{13}\, V_{it} \tag{1.3}$$

The same assumptions can be made for the other output phases. It is therefore possible to summarise the relationship between output voltages and input voltages as follows:

$$\begin{bmatrix} V_{ou} \\ V_{ov} \\ V_{ow} \end{bmatrix} = \begin{bmatrix} m_{11} & m_{12} & m_{13} \\ m_{21} & m_{22} & m_{23} \\ m_{31} & m_{32} & m_{33} \end{bmatrix} \begin{bmatrix} V_{ir} \\ V_{is} \\ V_{it} \end{bmatrix} \tag{1.4}$$

Where $0 \leq m_{ij} < 1, \quad i = 1, 2, 3, \quad j = 1, 2, 3.$

The same duty cycle matrix also links input currents to output currents:

$$\begin{bmatrix} I_{ir} \\ I_{is} \\ I_{it} \end{bmatrix} = \begin{bmatrix} m_{11} & m_{12} & m_{13} \\ m_{21} & m_{22} & m_{23} \\ m_{31} & m_{32} & m_{33} \end{bmatrix} \begin{bmatrix} I_{ou} \\ I_{ov} \\ I_{ow} \end{bmatrix} \tag{1.5}$$

To prevent short-circuits between input phases and to ensure continuous load current the duty-cycles has to satisfy the following condition:

$$\begin{aligned} m_{11} + m_{12} + m_{13} &= 1 \\ m_{21} + m_{22} + m_{23} &= 1 \\ m_{31} + m_{32} + m_{33} &= 1 \end{aligned} \tag{1.6}$$

(1.4) and (1.5) can be rewritten in compact form as follows:

$$\begin{aligned} \boldsymbol{V}_o &= \boldsymbol{M}\, \boldsymbol{V}_i \\ \boldsymbol{I}_i &= \boldsymbol{M}\, \boldsymbol{I}_o \end{aligned} \tag{1.7}$$

The MDCM approaches are based on the duty-cycle matrix $\boldsymbol{M}$ calculation. In each switching period the duty-cycle matrix in calculated as a function of desired output voltage and input power factor.

1.3.1 Alesina-Venturini method

In 1981, in [1] a first solution for $\boldsymbol{M}$ matrix calculation was presented. Assuming a set of input voltages and output currents:

$$\boldsymbol{V}_i = |\boldsymbol{V}_i| \begin{bmatrix} cos\left(\omega_i\, t\right) \\ cos\left(\omega_i\, t + \frac{2\pi}{3}\right) \\ cos\left(\omega_i\, t + \frac{4\pi}{3}\right) \end{bmatrix}; \quad \boldsymbol{I}_o = |\boldsymbol{I}_o| \begin{bmatrix} cos\left(\omega_o\, t + \gamma\right) \\ cos\left(\omega_o\, t + \gamma + \frac{2\pi}{3}\right) \\ cos\left(\omega_o\, t + \gamma + \frac{4\pi}{3}\right) \end{bmatrix} \tag{1.8}$$

Where ω_i and ω_o are the input and output angular frequency respectively, and γ is the phase shift between output voltage and current. A matrix $\boldsymbol{M}$ has to be calculated in order to obtain the output voltage and input currents that satisfy the following definitions together with (1.6).

$$\boldsymbol{V}_o = q\ |\boldsymbol{V}_i| \begin{bmatrix} cos\left(\omega_o\, t\right) \\ cos\left(\omega_o\, t + \frac{2\pi}{3}\right) \\ cos\left(\omega_o\, t + \frac{4\pi}{3}\right) \end{bmatrix} \tag{1.9}$$

$$\boldsymbol{I}_i = q\, \frac{cos\left(\gamma\right)}{cos\left(\phi\right)}\ |\boldsymbol{I}_o| \begin{bmatrix} cos\left(\omega_i\, t + \phi\right) \\ cos\left(\omega_i\, t + \phi + \frac{2\pi}{3}\right) \\ cos\left(\omega_i\, t + \phi + \frac{4\pi}{3}\right) \end{bmatrix} \tag{1.10}$$

With ϕ that represents the phase shift between input voltage and currents, while q expresses the ratio between the modules of the output voltage and the input voltage. The proposed relation for the input current (1.10) can be obtained by balancing the input and output power.

$$P_i = \frac{3}{2}\ |V_i|\ |I_i|\ cos\left(\phi\right) = \frac{3}{2}\, q\ |V_i|\ |I_o|\ cos\left(\gamma\right) = P_o \tag{1.11}$$

In [1] A. Alesina and M. Venturini present a solution to the modulation problem based on two duty-cycle matrix, shown in the following.

$$\boldsymbol{M}_1 = \frac{1}{3}\begin{bmatrix} 1+2\,q\,cos\left(\omega_m\,t\right) & 1+2\,q\,cos\left(\omega_m\,t-\frac{2\pi}{3}\right) & 1+2\,q\,cos\left(\omega_m\,t-\frac{4\pi}{3}\right) \\ 1+2\,q\,cos\left(\omega_m\,t-\frac{4\pi}{3}\right) & 1+2\,q\,cos\left(\omega_m\,t\right) & 1+2\,q\,cos\left(\omega_m\,t-\frac{2\pi}{3}\right) \\ 1+2\,q\,cos\left(\omega_m\,t-\frac{2\pi}{3}\right) & 1+2\,q\,cos\left(\omega_m\,t-\frac{4\pi}{3}\right) & 1+2\,q\,cos\left(\omega_m\,t\right) \end{bmatrix} \tag{1.12}$$

Where $\omega_m = \omega_o - \omega_i$

$$\boldsymbol{M}_2 = \frac{1}{3}\begin{bmatrix} 1+2\,q\,cos\left(\omega_n\,t\right) & 1+2\,q\,cos\left(\omega_n\,t-\frac{2\pi}{3}\right) & 1+2\,q\,cos\left(\omega_n\,t-\frac{4\pi}{3}\right) \\ 1+2\,q\,cos\left(\omega_n\,t-\frac{2\pi}{3}\right) & 1+2\,q\,cos\left(\omega_n\,t-\frac{4\pi}{3}\right) & 1+2\,q\,cos\left(\omega_n\,t\right) \\ 1+2\,q\,cos\left(\omega_n\,t-\frac{4\pi}{3}\right) & 1+2\,q\,cos\left(\omega_n\,t\right) & 1+2\,q\,cos\left(\omega_n\,t-\frac{2\pi}{3}\right) \end{bmatrix} \tag{1.13}$$

Where $\omega_n = -\left(\omega_o + \omega_i\right)$

The first duty-cycle matrix $\boldsymbol{M}_1$ represent the solution in the case of equal input and output phase shift ($\phi = \gamma$), while $\boldsymbol{M}_2$ in case of equal and opposite phase shift ($\phi = -\gamma$). By combining these two matrices, as shown in (1.14), it is possible to obtain the duty cycle matrix that guarantees the desired output voltage and input phase shift.

$$\boldsymbol{M} = \lambda_1\,\boldsymbol{M}_1 + \lambda_2\,\boldsymbol{M}_2 \tag{1.14}$$

Where:

$$\begin{gathered} \lambda_1 = \frac{1}{2}\left(1 + tg\left(\phi\right)\,ctg\left(\gamma\right)\right) \\ \lambda_1 + \lambda_2 = 1 \end{gathered} \tag{1.15}$$

When λ_1 is set equal to λ_2, then ϕ is equal to zero, ensuring unity input power factor. The input power factor can be then varied with the proper λ_1 and λ_2 combination, varying in turn the output phase shift. Assuming unity power factor ($\lambda_1 = \lambda_2$) the $\boldsymbol{M}$ matrix

components can be calculated as follows:

$$m_{ij} = \frac{1}{3}\left\{1 + 2\,q\,cos\left[\alpha_o - (i-1)\,\frac{2\pi}{3}\right] cos\left[\beta_i - (j-1)\,\frac{2\pi}{3}\right]\right\} \tag{1.16}$$

With $i = 1, 2, 3$ and $j = 1, 2, 3$.

In (1.16) the parameters α_o and β_i are the angle of the output voltage vector and the angle of the input current vector respectively represented in the abc reference frame. The biggest limitation of this modulation strategy is that the voltage transfer ratio q is limited to 0.5, a problem later solved by Alesina and Venturini themselves.

1.3.2 Optimum Alesina-Venturini method

In 1989, A. Alesina and M. Venturini presented a new paper [37], in which they solve the voltage transfer ratio issue. In particular they added the third harmonic components of the input and output frequencies to the desired output voltage $\boldsymbol{V}_o$. This strategy is known as common-mode addition [38]. The $\boldsymbol{M}$ matrix components can be calculated as follows for unity input power factor.

$$\begin{aligned} m_{ij} = \frac{1}{3}\Bigg\{1 + 2\,q\,cos\left[\beta_i - \frac{2\pi\,(j-1)}{3}\right] \cdot \\ \cdot \left[cos\left(\alpha_o - \frac{2\pi\,(i-1)}{3}\right) - \frac{cos\,(3\alpha_o)}{6} + \frac{cos\,(3\beta_i)}{2\sqrt{3}}\right] - \\ -\frac{2}{3\sqrt{3}}\,q\left[cos\left(4\,\beta_i - (j-1)\,\frac{2\pi}{3}\right) - cos\left(2\,\beta_i + (j-1)\,\frac{2\pi}{3}\right)\right]\Bigg\} \end{aligned} \tag{1.17}$$

With $i = 1, 2, 3$ and $j = 1, 2, 3$.

The results is an increase in the voltage transfer ratio, which is now 0.866. The method presented in [37] retains the possibility of imposing the input power factor, but requires knowledge of the output power factor. This is the modulation algorithm that has been used in the simulations and experimental result presented in the following dissertation.

1.3.3 Space Vector Modulation

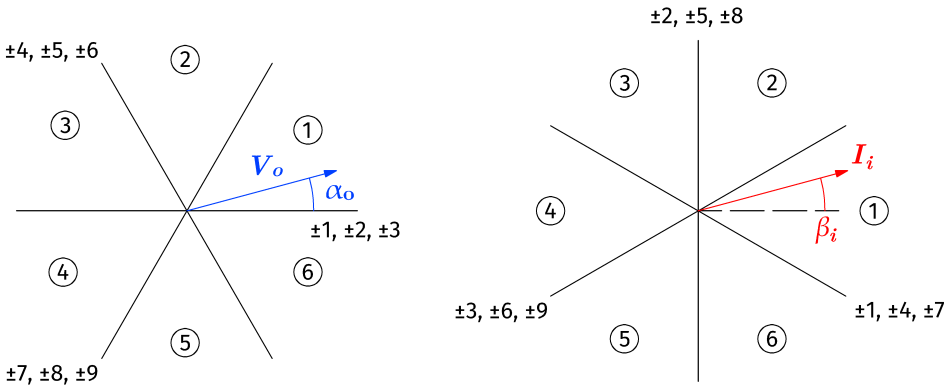

Figure 1.3: Synthesis of output voltage and input current vector

The switching combination in a matrix converter are 2^9, but excluding combinations that would lead to a short circuit leaves 27. Of these 27, only 21 can be used actively in the SVM. The first 18 switching combination produce output voltage and input current vectors with fixed direction, whose amplitude depends on input voltage and output current amplitude. The remaining three combination lead to zero output voltage and input current. For each switching period, it is possible to represent the fixed vectors resulting from the combination on two abc reference frame, one for the output voltages, and one for the input currents. This results in two reference frames divided into 6 areas Fig. 1.3. Now, by plotting the rotating vectors representing the output voltage and input current in the corresponding abc reference frame, it is possible to determine which combination will apply and the application time as a function of the position of the rotation vectors in relation to the combination fixed vectors. This approach inherently has the ability to achieve complete control over both the output voltage vector and the instantaneous angle of the input current vector [39, 40, 41].

1.4 Bidirectional Switches

As discussed earlier, a bidirectional switch is able to conduct current in both directions and block voltage. It is possible to obtain a bidirectional switch by starting from more common unidirectional device, although there are integrated solutions on the mar-

ket that are essentially combinations of the latter. Firstly, it is necessary to choose the starting component. Si IGBTs are particularly well-suited for this application, as they exhibit high withstand voltage and have relatively low on-state voltage even at high current and high temperature. Moreover, they present low switching losses and low conduction losses. Recent studies have compared the use of Si IGBTs and SiC MOSFETs as components for matrix converter in terms of efficiency and EMI requirements [42]. SiC MOSFETs have features that make them suitable for this applications, including high breakdown voltage, low on-resistance, fast switching speed and enhanced thermal conductivity. The study presented in [42] conclude that Sic MOSFETs allows to reach higher switching frequency than Si IGBT while maintaining constant efficiency. However, it was found that efficiency is strongly affected by gate resistors, whose design directly depends on the EMI requirements of the application. In the present study, MC employing Si IGBT will be considered. In fact, the chosen switching frequency of 10 kHz does not justify the use of SiC components. In studies such as [43], [44] and [45] bidirectional switches obtained combining IGBTs and diodes have been studied. Mainly two configuration are employed in matrix converters, common-emitter anti-parallel IGBTs and the common-collector anti-parallel IGBTs.

1.4.1 Common-Emitter Anti-Parallel IGBTs

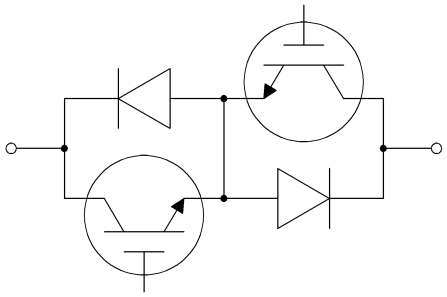

Figure 1.4: Bidirectional Switch, Common-Emitter Anti-Parallel IGBTs

In Fig. 1.4 a bidirectional switch is realized connecting two IGBTs and two diodes in anti-parallel. The diodes are essential for blocking voltage during commutations, as will be discussed later. In this configuration, as implied by the name, the IGBTs emitters are connected together. This allows for driving, two IGBTs by referring to the common emitters. Notwithstanding, this makes it necessary to use an isolated voltage source for

each pair of IGBTs. In fact, when the bidirectional switch is turned on, the connection point of the common emitters is subjected to the input phase voltage. The schematic in Fig. 1.5 illustrates a matrix converter employing this bidirectional switch configuration along with an example of gate drive connection.

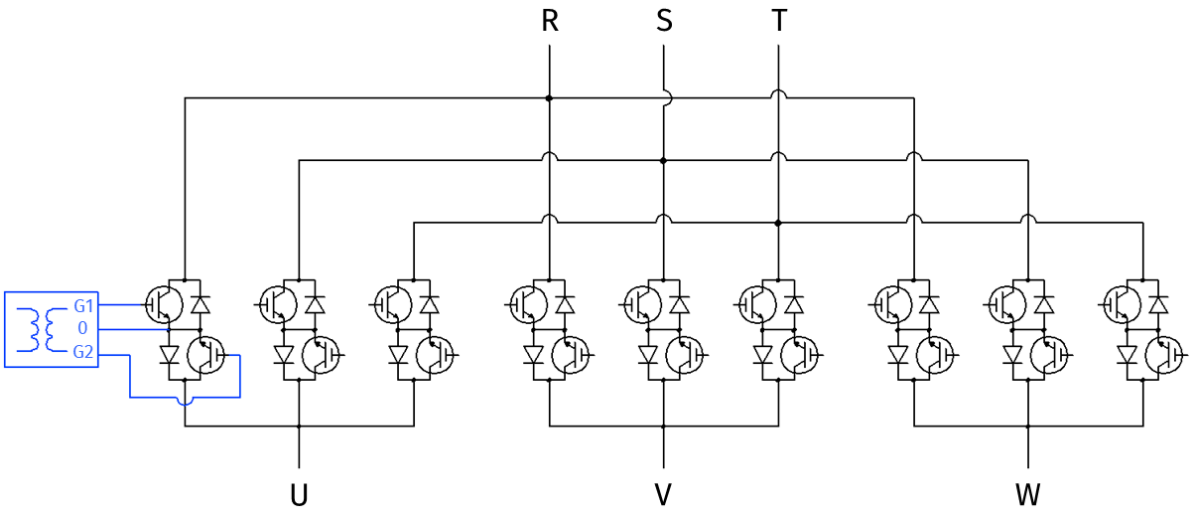

Figure 1.5: Matrix Converter with Common-Emitter Anti-Parallel IGBTs

The common-emitter configuration then, in the case of a Three-Phase to Three-Phase Matrix Converter, requires the utilization of nine isolated voltage sources.

1.4.2 Common-Collector Anti-Parallel IGBTs

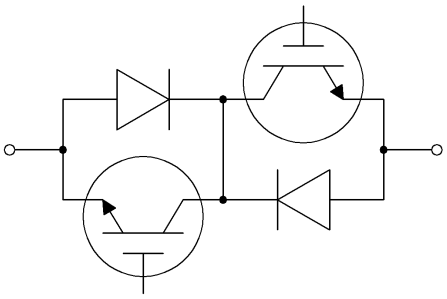

Figure 1.6: Bidirectional Switch, Common-Collector Anti-Parallel IGBTs

Fig. 1.6 illustrate the Common-Collector Anti-Parallel IGBTs configuration. In this case, the collectors are connected together and opposing diodes are once again present. In this configuration, analysing the schematic in Fig. 1.7 it is possible to note that the emitters of the input side IGBTs and the output side IGBT are connected together. Each output and input phase can therefore be used as a reference point for controlling the IGBTs. This

means that is possible to use one insulated power supply for every three IGBTs to drive them. Consequently, six isolated voltage sources are sufficient to control all bidirectional switches, In Fig. 1.7 an example of gate drive connection is reported.

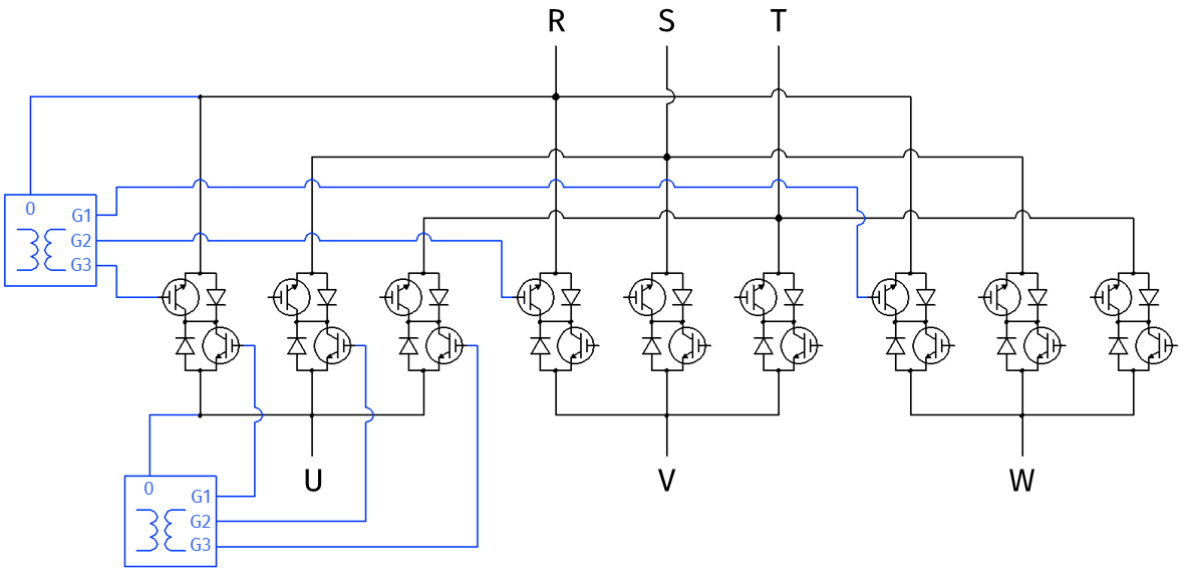

Figure 1.7: Matrix Converter with Common-Collector Anti-Parallel IGBTs

1.4.3 Comparison

The common-collector configuration clearly has the advantage of requiring fewer isolated voltage sources to supply the gate drives of the IGBTs. However, connecting the gate circuits of IGBTs to different bi-directional switches can generate current loops, potentially impacting switching. This problem can be overcome through appropriate precautions. On the other hand, the common-emitter configuration is recommended when bidirectional switches are made from individual components, as this reduces the length of the gate circuits, minimising parasitic inductance. The common-collector configuration is preferred when using specific Matrix Converter modules, which may contain all bidirectional switches or only one output leg. These modules allow for shorter gate circuits, eliminating parasitic inductance issues. In the following dissertation a Matrix Converter realized using the Common-Emitter configuration is employed to carry out simulations and experimental verification.

1.5 Commutations Strategy

The switching of bidirectional switches is one of the most challenging aspects for the matrix converter. In fact, it is more intricate than in common Voltage Source Inverters (VSI). The reason lies in the fact that there are no natural free-wheeling paths for the output currents. Two rules should primarily be observed. Referring to Fig 1.8 , firstly, two bidirectional switches belonging to the same output phase should never be closed simultaneously, as this would cause a two-phase short with fatal effects (a). Secondly, the output currents should never be interrupted abruptly, as this could generate a lethal overvoltage for the IGBTs (b). To address the first rule numerous methods for switching

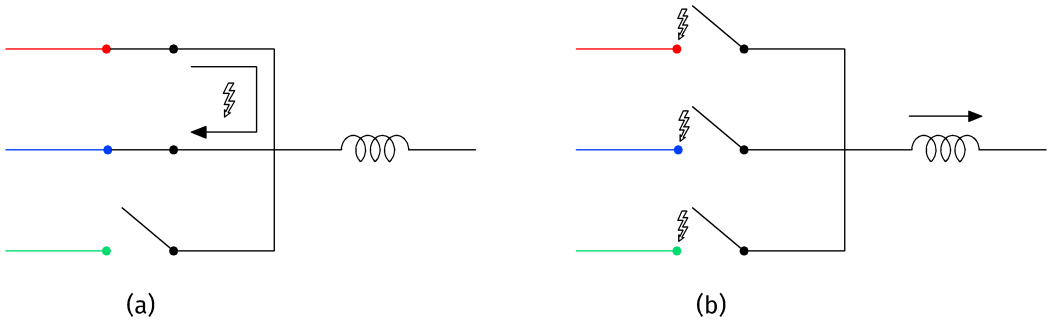

Figure 1.8: Matrix Converter with Common-Collector Anti-Parallel IGBTs

have been studied, as shown in [46, 47, 48]. Good results can be obtained using what is called the 'semi-soft commutation' or 'four-step commutation' method. This method, presented in [49] meet the matrix converter commutation rules, and is based on current detection. With regard to the second rule, the opening of switches may be necessary in the event of a fault, which is why protection strategies and circuits are introduced.

1.5.1 Four-Step Commutation

To make the four-step commutation easier to understand, consider the Fig. 1.9 which illustrates the procedure steps in relation to the direction of the output current. Initially the output u-phase is connected to the input r-phase through the bidirectional switch composed of S_1 and S_2, both of which are switched on, but only S_1 conducts the output current. Components that are not conducting the output current are coloured grey in

Fig. 1.9. This can be easily deduced from the current direction, which is constantly measured. When a commutation is need, the four-step algorithm detects which of the two IGBTs composing the bidirectional switch is conducting the output current, depending on the current direction. At this point the first step begins, in which the IGBT that is not conducting is switched off, in the proposed example S_2. After the first step, there are no changes in the input and output quantities. The second step involves the bidirectional switch of the s-phase, or in general of the phase on which it is necessary to switch. The IGBT that will conduct the output current is switched on, in figure S_3. The diodes avoid any short circuit between the input phases, and both S_1 and S_3 can conduct the output current. The conducting diode D_1 is now subject to the phase to phase voltage V_{rs}, This produces two possible scenarios for the third step. If $V_{rs} < 0$ then the diode stop conducting the output current because it is reversed-bias, leading to a natural commutation. Consequently, when the third step occur, which consists of switching off the conducting IGBT in the start phase (S_1), the IGBT is already not conducting the current. If $V_{rs} \geq 0$ the diode continues to conduct the output current, and when the third step occur a hard commutation take place. Finally, in the fourth step, the non-conducting IGBT of the target phase is switched-on (S_1). This commutation strategy is named semisoft-switching because in any switching period half of the commutation are natural.

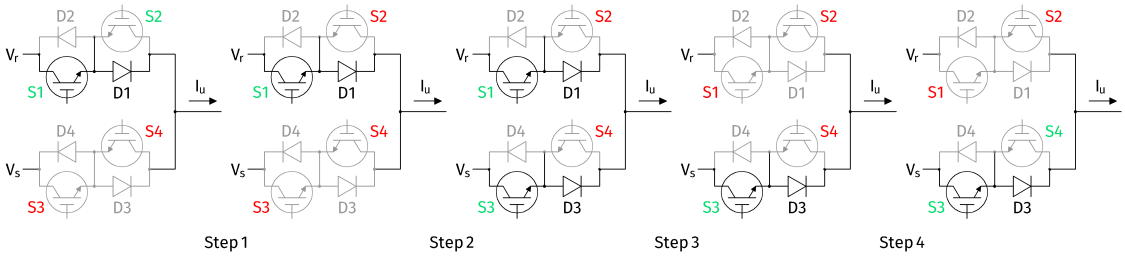

Figure 1.9: Example of four-step commutation

1.5.2 Protection Strategies and Circuit

Unlike most common back-to-back converters, the matrix converter has no free-wheeling paths. This makes a number of precautions necessary to protect the devices. Over-load, short-circuit and over-voltage protection are usually implemented. Overload protection is based on the measurement of the output current. If the control system

detects a current exceeding the rated current, the device are switched off. However, this is not sufficient in the case of an output short circuit, as the dynamics of the currents are too fast for the control system to timely switch off the devices. Short-circuit protection is therefore based on the measurement of the collector-emitter voltages of each device. In both cases, however, the rule against turning off all switches at the same time is not observed. To allow the switches to be opened safely, a double diode bridge clamp is introduced across input and output. The circuit is shown in Fig. 1.10. This circuit allows

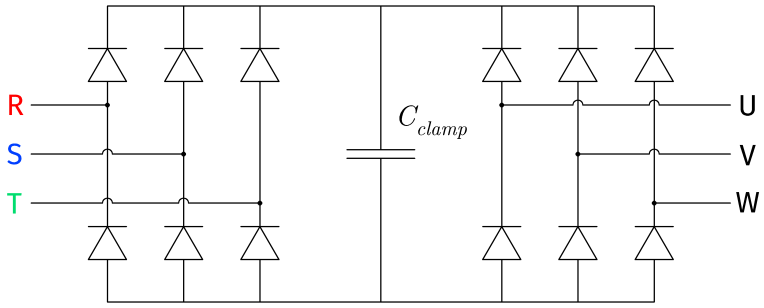

Figure 1.10: Clamp circuit

currents to have a free-wheeling path avoiding overvoltages on the switching device. The C_{clamp} capacitor absorb the current resulting in an increase of its voltage. The instabilities to which the matrix converter is prone, however, generate fluctuations in the input voltage, which affect the value of the C_{clamp} voltage. For this reason, the latter voltage must also be monitored and the converter must be switched off if it exceeds a given safety level.

1.6 Input Filter Design

As mentioned earlier, the input currents of a matrix converter are discontinuous waveform, thus presenting a high harmonic content. The harmonic distortion is injected to the supplying grid and could potentially compromise the operation of electronic equipment connected to it. The standards that every power converter must satisfy to be connected to the supply grid are in IEEE 519 [50]. To satisfy the Electromagnetic Interference (EMI) requirements a three-phase LC filter is introduced at the input side of the matrix converter. The filter is designed to satisfy the following requirements:

- The filter cut-off frequency should be significantly lower than the switching frequency. The cut-off frequency can be approximated to the resonance frequency of the filter, that can be defined as follows:

$$f_{res} = \frac{1}{2\,\pi\,\sqrt{L_f\,C_f}} \tag{1.18}$$

  Where L_f and C_f are the inductor and capacitor values respectively.

- The reactive current flowing in the capacitors reduce the overall power factor, especially when the converter is providing low power to the load. The capacitors should therefore be selected to ensure a power factor of 0.8 when the converter is supplying 10% of the rated power.

- The inductor should minimize the voltage drop in order to maximize the voltage transfer ratio.

- Finally, the volume and the weight of the filter should be minimised in order to maximise the overall power density of the system.

1.7 Chapter Summary

This introductory chapter examined the characteristics and possible applications of the matrix converter. First, the operating principle of the converter was explained, accompanied by an exposition of the most common modulation algorithms. The technical specifications of bidirectional switches were then examined in detail, together with construction details. The switching strategy of such switches was presented, together with the protection criteria and circuit. Finally, an approach to the design of input filters was proposed.

References 1

[1] M. Venturini, “A new sine wave in sine wave out, conversion technique which eliminates reactive elements,” 1980.

[2] T. B. Soeiro and M. L. Heldwein, “High efficiency indirect matrix converter topologies,” in IECON 2013 - 39th Annual Conference of the IEEE Industrial Electronics Society, pp. 4856–4861, 2013.

[3] P. Wheeler, J. Rodriguez, J. Clare, L. Empringham, and A. Weinstein, “Matrix converters: a technology review,” IEEE Transactions on Industrial Electronics, vol. 49, no. 2, pp. 276–288, 2002.

[4] A. Ammar, H. Y. Kanaan, N. Moubayed, M. Hamouda, and K. Al-Haddad, “A technology survey of matrix converters in power generation systems,” in IECON 2017 - 43rd Annual Conference of the IEEE Industrial Electronics Society, pp. 6145–6152, 2017.

[5] A. Trentin, L. Empringham, L. de Lillo, P. Zanchetta, P. Wheeler, and J. Clare, “Experimental efficiency comparison between a direct matrix converter and an indirect matrix converter using both si igbts and sic mosfets,” IEEE Transactions on Industry Applications, vol. 52, no. 5, pp. 4135–4145, 2016.

[6] L. Empringham, P. Wheeler, and J. Clare, “Power density improvement and robust commutation for a 100 kw si-sic matrix converter,” in 2009 13th European Conference on Power Electronics and Applications, pp. 1–8, 2009.

[7] K. Koiwa and J.-I. Itoh, “A maximum power density design method for nine switches matrix converter using sic-mosfet,” IEEE Transactions on Power Electronics, vol. 31, no. 2, pp. 1189–1202, 2016.

[8] S. L. Arevalo, P. Zanchetta, P. W. Wheeler, A. Trentin, and L. Empringham, “Control and implementation of a matrix-converter-based ac ground power-supply unit for aircraft servicing,” IEEE Transactions on Industrial Electronics, vol. 57, no. 6, pp. 2076–2084, 2010.

[9] L. Empringham, L. de Lillo, S. Khwan-On, C. Brunson, P. W. Wheeler, and J. C. Clare, “Enabling technologies for matrix converters in aerospace applications,” in 2011

7th International Conference-Workshop Compatibility and Power Electronics (CPE), pp. 451–456, 2011.

[10] X. Huang, A. Goodman, C. Gerada, Y. Fang, and Q. Lu, "A single sided matrix converter drive for a brushless dc motor in aerospace applications," IEEE Transactions on Industrial Electronics, vol. 59, no. 9, pp. 3542–3552, 2012.

[11] C. N. El-Khoury, H. Y. Kanaan, I. Mougharbel, and K. Al-Haddad, "A review of matrix converters applied to pmsg based wind energy conversion systems," in IECON 2013 - 39th Annual Conference of the IEEE Industrial Electronics Society, pp. 7784–7789, 2013.

[12] E. Karaman, M. Farasat, and A. M. Trzynadlowski, "Indirect matrix converters as generator–grid interfaces for wind energy systems," IEEE Journal of Emerging and Selected Topics in Power Electronics, vol. 2, no. 4, pp. 776–783, 2014.

[13] Y. Xu, Z. Wang, P. Liu, Q. Wei, F. Deng, and Z. Zou, "The modular current-fed high-frequency isolated matrix converters for wind energy conversion," IEEE Transactions on Power Electronics, vol. 37, no. 4, pp. 4779–4791, 2022.

[14] L. Empringham, J. W. Kolar, J. Rodriguez, P. W. Wheeler, and J. C. Clare, "Technological issues and industrial application of matrix converters: A review," IEEE Transactions on Industrial Electronics, vol. 60, no. 10, pp. 4260–4271, 2013.

[15] S. Khwan-on, L. de Lillo, L. Empringham, and P. Wheeler, "Fault-tolerant matrix converter motor drives with fault detection of open switch faults," IEEE Transactions on Industrial Electronics, vol. 59, no. 1, pp. 257–268, 2012.

[16] E. Reyes, R. Pena, R. Cardenas, J. Clare, P. Wheeler, and R. Blasco-Gimenez, "A topology for multiple generation system with doubly fed induction machines and indirect matrix converter.," in 2008 IEEE International Symposium on Industrial Electronics, pp. 2463–2468, 2008.

[17] E. Levi, N. Bodo, O. Dordevic, and M. Jones, "Recent advances in power electronic converter control for multiphase drive systems," in 2013 IEEE Workshop on Electrical Machines Design, Control and Diagnosis (WEMDCD), pp. 158–167, 2013.

[18] W. Deng and S. Li, "Direct torque control of matrix converter-fed pmsm drives using multidimensional switching table for common-mode voltage minimization," IEEE Transactions on Power Electronics, vol. 36, no. 1, pp. 683–690, 2021.

[19] W. Deng, H. Li, and J. Rong, "A novel direct torque control of matrix converter-fed pmsm drives using dynamic sector boundary for common-mode voltage minimization," IEEE Transactions on Industrial Electronics, vol. 68, no. 1, pp. 70–80, 2021.

[20] E. H. Miliani, I. Zein, L. Kefsi, and A. Battiston, "Matrix converter topology for distributed energy applications," in 2016 18th European Conference on Power Electronics and Applications (EPE'16 ECCE Europe), pp. 1–13, 2016.

[21] S. Paweł, "Matrix converter interfaces two three-phase ac systems as a component of smart-grid," in 2014 International Symposium on Power Electronics, Electrical Drives, Automation and Motion, pp. 683–688, 2014.

[22] D. Casadei, G. Serra, A. Tani, A. Trentin, and L. Zarri, "Theoretical and experimental investigation on the stability of matrix converters," IEEE Transactions on Industrial Electronics, vol. 52, no. 5, pp. 1409–1419, 2005.

[23] K. B. Tawfiq, M. N. Ibrahim, and P. Sergeant, "An enhanced fault-tolerant control of a five-phase synchronous reluctance motor fed from a three-to-five-phase matrix converter," IEEE Journal of Emerging and Selected Topics in Power Electronics, vol. 10, no. 4, pp. 4182–4194, 2022.

[24] D. Casadei, G. Serra, A. Tani, A. Trentin, and L. Zarri, "Theoretical and experimental investigation on the stability of matrix converters," IEEE Transactions on Industrial Electronics, vol. 52, pp. 1409–1419, Oct 2005.

[25] D. Casadei, J. Clare, L. Empringham, G. Serra, A. Tani, A. Trentin, P. Wheeler, and L. Zarri, "Large-signal model for the stability analysis of matrix converters," IEEE Transactions on Industrial Electronics, vol. 54, no. 2, pp. 939–950, 2007.

[26] A. Trentin, P. Zanchetta, J. Clare, and P. Wheeler, "Automated optimal design of input filters for direct ac/ac matrix converters," IEEE Transactions on Industrial Electronics, vol. 59, no. 7, pp. 2811–2823, 2012.

[27] D. Casadei, G. Serra, A. Tani, and L. Zarri, "Effects of input voltage measurement on stability of matrix converter drive system," IEE Proceedings - Electric Power Applications, vol. 151, pp. 487–497, July 2004.

[28] Y. Sun, M. Su, X. Li, H. Wang, and W. Gui, "A general constructive approach to matrix converter stabilization," IEEE Transactions on Power Electronics, vol. 28, no. 1, pp. 418–431, 2013.

[29] J. Lei, B. Zhou, J. Wei, J. Bian, Y. Zhu, J. Yu, and Y. Yang, "Predictive power control of matrix converter with active damping function," IEEE Transactions on Industrial Electronics, vol. 63, no. 7, pp. 4550–4559, 2016.

[30] A. Formentini, L. De Lillo, M. Marchesoni, A. Trentin, P. Wheeler, and P. Zanchetta, "A new mains voltage observer for PMSM drives fed by matrix converters," in 16th European Conference on Power Electronics and Applications, pp. 1–10, 2014.

[31] A. Formentini, A. Trentin, M. Marchesoni, P. Zanchetta, and P. Wheeler, "Speed finite control set model predictive control of a pmsm fed by matrix converter," IEEE Trans. Ind. Electron., vol. 62, no. 11, pp. 6786–6796, 2015.

[32] L. Tarisciotti, J. Lei, A. Formentini, A. Trentin, P. Zanchetta, P. Wheeler, and M. Rivera, "Modulated predictive control for indirect matrix converter," IEEE Transactions on Industry Applications, vol. 53, no. 5, pp. 4644–4654, 2017.

[33] Z. Li, C. Zang, P. Zeng, H. Yu, S. Li, and J. Bian, "Control of a grid-forming inverter based on sliding-mode and mixed H_2/H_∞ control," IEEE Transactions on Industrial Electronics, vol. 64, no. 5, pp. 3862–3872, 2017.

[34] L. A. Maccari, J. R. Massing, L. Schuch, C. Rech, H. Pinheiro, R. C. L. F. Oliveira, and V. F. Montagner, "Lmi-based control for grid-connected converters with lcl filters under uncertain parameters," IEEE Transactions on Power Electronics, vol. 29, no. 7, pp. 3776–3785, 2014.

[35] S. Das and I. Pan, "On the mixed H_2/H_∞ loop-shaping tradeoffs in fractional-order control of the avr system," IEEE Transactions on Industrial Informatics, vol. 10, no. 4, pp. 1982–1991, 2014.

[36] M. Dehghani, M. Ghiasi, T. Niknam, K. Rouzbehi, Z. Wang, P. Siano, and H. H. Alhelou, "Control of lpv modeled ac-microgrid based on mixed H_2/H_∞ time-varying linear state feedback and robust predictive algorithm," IEEE Access, vol. 10, pp. 3738–3755, 2022.

[37] A. Alesina and M. G. Venturini, "Analysis and design of optimum-amplitude nine-switch direct ac-ac converters," IEEE Transactions on Power Electronics, vol. 4, no. 1, pp. 101–112, 1989.

[38] J. Oyama, T. Higuchi, E. Yamada, T. Koga, and T. Lipo, "New control strategy for matrix converter," in 20th Annual IEEE Power Electronics Specialists Conference, pp. 360–367 vol.1, 1989.

[39] D. Casadei, G. Grandi, G. Serra, and A. Tani, "Space vector control of matrix converters with unity input power factor and sinusoidal input/output waveforms," in 1993 Fifth European Conference on Power Electronics and Applications, pp. 170–175 vol.7, 1993.

[40] J. Haruna, J. Tsuchiya, H. Ueda, and H. Funato, "An optimized switching pattern for reducing input current distortion of matrix converter using space vector modulation," in 2017 IEEE 3rd International Future Energy Electronics Conference and ECCE Asia (IFEEC 2017 - ECCE Asia), pp. 68–74, 2017.

[41] A. M. Bozorgi, M. Monfared, and H. R. Mashhadi, "Optimum switching pattern of matrix converter space vector modulation," in 2012 2nd International eConference on Computer and Knowledge Engineering (ICCKE), pp. 89–93, 2012.

[42] A. Trentin, L. de Lillo, L. Empringham, P. Wheeler, and J. Clare, "Experimental comparison of a direct matrix converter using si igbt and sic mosfets," IEEE Journal of Emerging and Selected Topics in Power Electronics, vol. 3, no. 2, pp. 542–554, 2015.

[43] M. Bland, P. Wheeler, J. Clare, and L. Empringham, "Comparison of bi-directional switch components for direct ac-ac converters," in 2004 IEEE 35th Annual Power Electronics Specialists Conference (IEEE Cat. No.04CH37551), vol. 4, pp. 2905–2909 Vol.4, 2004.

[44] C. Klumpner and F. Blaabjerg, "Using reverse-blocking igbts in power converters for adjustable-speed drives," IEEE Transactions on Industry Applications, vol. 42, no. 3, pp. 807–816, 2006.

[45] P. Szczesniak, "Challenges and design requirements for industrial applications of ac/ac power converters without dc-link," Energies, vol. 12, no. 8, 2019.

[46] L. Empringham, P. Wheeler, and J. Clare, "Intelligent commutation of matrix converter bi-directional switch cells using novel gate drive techniques," in PESC 98 Record. 29th Annual IEEE Power Electronics Specialists Conference (Cat. No.98CH36196), vol. 1, pp. 707–713 vol.1, 1998.

[47] L. Empringham, P. Wheeler, and J. Clare, "Matrix converter bi-directional switch commutation using intelligent gate drives," in 1998 Seventh International Conference on Power Electronics and Variable Speed Drives (IEE Conf. Publ. No. 456), pp. 626–631, 1998.

[48] A. Ecklebe, A. Lindemann, and S. Schulz, "Bidirectional switch commutation for a matrix converter supplying a series resonant load," IEEE Transactions on Power Electronics, vol. 24, no. 5, pp. 1173–1181, 2009.

[49] N. Burany, "Safe control of four-quadrant switches," in Conference Record of the IEEE Industry Applications Society Annual Meeting,, pp. 1190–1194 vol.1, 1989.

[50] "Ieee standard for harmonic control in electric power systems," IEEE Std 519-2022 (Revision of IEEE Std 519-2014), pp. 1–31, 2022.

Chapter 2:

System Models

The following chapter examines the mathematical models used in stability studies. Firstly, the reference frame transformation is introduced. This technique allows to simplify the analysis of three-phase AC circuits by projecting three-phase quantities onto two stationary axes or onto axes rotating synchronously with the reference angular frequency. The methodology used to derive the Matrix Converter Average Model is then presented and the input filter modelling process is discussed. The first load on the output side of the converter, the Resistor-Inductor (RL) load, and its model are then presented. The input filter model, the average model and the RL load model are then used to obtain a first complete open-loop system model, the accuracy of which is demonstrated by simulation. A current control based on a Proportional-Integral (PI) controller is then introduced and the gain tuning procedure is presented. Finally, the model of the second load, a Surface-Mounted Permanent Magnet Synchronous Motor (SM-PMSM), and its control strategy are presented, and the accuracy of the complete system is again verified by simulation.

2.1 Reference Frame Transformations

Reference Frame Transformations are widely used in the analysis and control of machines and power converter. They in fact entail considerable simplifications in terms of calculation and modelling of these components [1]. In the following, the transform in the stationary reference frame ,also known as the Clarke Transformation, and the transformation in the rotating reference frame, also called the Park transformation, will be introduced.

2.1.1 Clarke Transformation

It is necessary to begin by recalling that a three-phase quantity, whether current or voltage, can be represented as a trio of vectors in the complex plane, known as phasors, which by convention, if the angular frequency ω is positive, rotate anti-clockwise. If the sum of these vectors is zero, the phasors, and consequently the three-phase quantity, are termed balanced; otherwise, they are referred to as unbalanced. In 1918 Charles Legeyt Fortescue demonstrated in a paper that a set of N unbalanced phasors could be represented as the combination of N symmetrical sets of balanced phasors, specifically for prime values of N. The phasors represent only a singular frequency component. This approach is also known as Symmetrical Components Method. In 1943 Edith Clarke published her book "Circuit Analysis of A-C Power Systems" [2] in which she made a series of modification to this method in order to simplify the calculation. The Clarke Transformation was one of this modification. Consider the generic three-phase quantity $\boldsymbol{x}$. This can be represented in the abc reference frame as a rotating vector $\boldsymbol{x}$ at angular frequency w as shown in Fig. 2.1. Its projection on the abc-axes returns the three quantities that make up the three-phase set. The Clarke transform assumes that it is possible to retain the information on the three-phase starting set while only using the projections on the $\alpha\beta$-axes. In addition, component 0 is defined. This contains the information of the projection error if the three-phase vector is unbalanced.

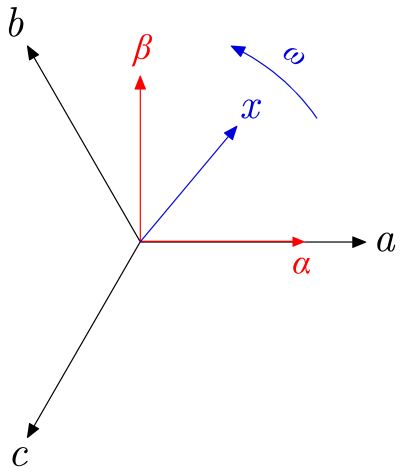

Figure 2.1: $\alpha\beta$ reference frame and its relation with three-phase quantity

The relationship between the projections of the rotating $\boldsymbol{x}$ vector on the abc reference

frame, and those on the $\alpha\beta$ reference frame is as follows

$$\boldsymbol{x}^{\alpha\beta 0} = \begin{bmatrix} x_\alpha \\ x_\beta \\ x_0 \end{bmatrix} = \boldsymbol{K}_c\, \boldsymbol{x} = \frac{2}{3} \begin{bmatrix} 1 & -\frac{1}{2} & -\frac{1}{2} \\ 0 & \frac{\sqrt{3}}{2} & -\frac{\sqrt{3}}{2} \\ \frac{1}{2} & \frac{1}{2} & \frac{1}{2} \end{bmatrix} \begin{bmatrix} x_a \\ x_b \\ x_c \end{bmatrix} \tag{2.1}$$

The transform is designed in such a way that the modulus of the resulting vectors remains unchanged. Given that the determinant of matrix K_c is non-zero, it implies invertibility. Clarke inverse transform is then defined.

$$\boldsymbol{x} = \begin{bmatrix} x_a \\ x_b \\ x_c \end{bmatrix} = \boldsymbol{K}_c^{-1}\, \boldsymbol{x}^{\alpha\beta 0} = \begin{bmatrix} 1 & 0 & 1 \\ -\frac{1}{2} & \frac{\sqrt{3}}{2} & 1 \\ -\frac{1}{2} & -\frac{\sqrt{3}}{2} & 1 \end{bmatrix} \begin{bmatrix} x_\alpha \\ x_\beta \\ x_0 \end{bmatrix} \tag{2.2}$$

As already mentioned, component 0 is useful if the three-phase quantity to be transformed is unbalanced. Considering that all the quantities that will be studied in the following dissertation are balanced, the 0 term can be neglected without losing any information relative to the starting three-phase vector. In fact, all the system components and even the converter are symmetrical. It is then possible to rewrite the Clarke transform and the Inverse Clarke transform in the following manner.

$$\boldsymbol{x}^{\alpha\beta} = \begin{bmatrix} x_\alpha \\ x_\beta \end{bmatrix} = \boldsymbol{K}_c\, \boldsymbol{x} = \frac{2}{3} \begin{bmatrix} 1 & -\frac{1}{2} & -\frac{1}{2} \\ 0 & \frac{\sqrt{3}}{2} & -\frac{\sqrt{3}}{2} \end{bmatrix} \begin{bmatrix} x_a \\ x_b \\ x_c \end{bmatrix} \tag{2.3}$$

$$\boldsymbol{x} = \begin{bmatrix} x_a \\ x_b \\ x_c \end{bmatrix} = \boldsymbol{K}_c^{-1}\, \boldsymbol{x}^{\alpha\beta 0} = \begin{bmatrix} 1 & 0 \\ -\frac{1}{2} & \frac{\sqrt{3}}{2} \\ -\frac{1}{2} & -\frac{\sqrt{3}}{2} \end{bmatrix} \begin{bmatrix} x_\alpha \\ x_\beta \end{bmatrix} \tag{2.4}$$

Application of the transform to a three-phase set composed of a vector of three state variables leads to a vector with two state variables. The resultant system is thereby reduced from a third-order to a second-order system. This reduction by one order leads to a significant simplification in terms of calculations.

2.1.2 Clarke to Park Transformation

Despite the considerable simplifications achieved through the Clarke transform, the problem of time-varying parameters still remains. In 1913 André-Eugène Blondel published his book "Synchronous motors and converters" in which he faced the AC poly-phase machines modelization problem and where he lays the foundations of rotating reference frame transform. In 1929 Robert H. Park in his paper "Two-reaction theory of synchronous machines generalized method of analysis-part I" [3] took some assumptions to simplify the Blondel's equations, in particular he neglected saturation and harmonics effect, making them easier to interpret and use. His assumption led to what is now called the Park transformation. This transformation was applied to poly-phase synchronous machines, but can be extended to three-phase systems. To simplify understanding, consider what has already been mentioned for the Clarke transform. It is possible to introduce a new reference frame, composed of dq-axes, rotating synchronously with the three-phase vector $\boldsymbol{x}$ and with the d-axis aligned to $\boldsymbol{x}$ as shown in Fig. 2.2. The dq-axes rotate with respect to the $\alpha\beta$-axes by θ angle defined as in (2.5)

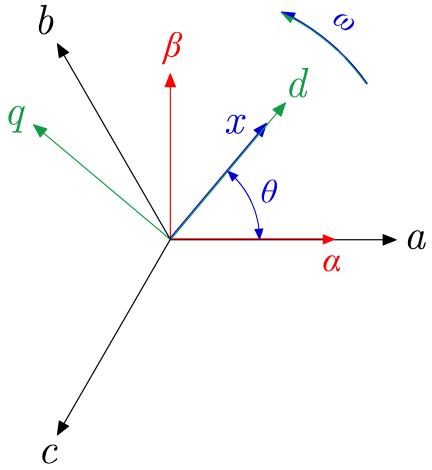

Figure 2.2: dq, $\alpha\beta$ and abc reference frame relationship

$$\theta = \omega t \tag{2.5}$$

It can therefore be interpreted as the rotation of one reference frame with respect to another. This can be expressed mathematically through a rotation matrix. The component 0 does not change between $\alpha\beta$ and dq, always expressing the projection error in the case of an unbalanced three-phase quantity. The relation between $\alpha\beta 0$ and $dq0$ quantities, also known as Clarke to Park transform, is shown below.

$$\boldsymbol{x}^{dq0} = \begin{bmatrix} x_d \\ x_q \\ x_0 \end{bmatrix} = \boldsymbol{K}_{cp}(\theta)\ \boldsymbol{x}^{\alpha\beta 0} = \begin{bmatrix} cos(\theta) & sin(\theta) & 0 \\ -sin(\theta) & cos(\theta) & 0 \\ 0 & 0 & 1 \end{bmatrix} \begin{bmatrix} x_\alpha \\ x_\beta \\ x_0 \end{bmatrix} \tag{2.6}$$

Since the matrix K_{cp} is orthogonal, it is invertible and in particular its inverse coincides with its transpose, the Park to Clarke transform can be written as follows:

$$\boldsymbol{x}^{\alpha\beta 0} = \begin{bmatrix} x_\alpha \\ x_\beta \\ x_0 \end{bmatrix} = \boldsymbol{K}_{cp}^{\mathsf{T}}(\theta)\ \boldsymbol{x}^{dq0} = \begin{bmatrix} cos(\theta) & -sin(\theta) & 0 \\ sin(\theta) & cos(\theta) & 0 \\ 0 & 0 & 1 \end{bmatrix} \begin{bmatrix} x_d \\ x_q \\ x_0 \end{bmatrix} \tag{2.7}$$

Neglecting the 0 component, the relationships can be rewritten as:

$$\boldsymbol{x}^{dq} = \begin{bmatrix} x_d \\ x_q \end{bmatrix} = \boldsymbol{K}_{cp}(\theta)\ \boldsymbol{x}^{\alpha\beta} = \begin{bmatrix} cos(\theta) & sin(\theta) \\ -sin(\theta) & cos(\theta) \end{bmatrix} \begin{bmatrix} x_\alpha \\ x_\beta \end{bmatrix} \tag{2.8}$$

$$\boldsymbol{x}^{\alpha\beta} = \begin{bmatrix} x_\alpha \\ x_\beta \end{bmatrix} = \boldsymbol{K}_{cp}^{\mathsf{T}}(\theta)\ \boldsymbol{x}^{dq} = \begin{bmatrix} cos(\theta) & -sin(\theta) \\ sin(\theta) & cos(\theta) \end{bmatrix} \begin{bmatrix} x_d \\ x_q \end{bmatrix} \tag{2.9}$$

Thanks to the rotating reference frame, the dq components remain constant at steady-state. This results in several simplifications in terms of control and data analysis. For instance, it allows the use of proportional-integral controllers, which do not operate effectively with sinusoidal variables. In the case of the stability analysis presented in

the next chapter, the dq reference frame will allow to solve the system at steady-state, a fundamental step in the linearization of the system.

2.1.3 Park Transform

It is possible to write a relationship that directly links the abc reference frame to the $dq0$ rotating reference frame, and it is this that is called the Park transform.

$$\boldsymbol{x}^{dq0} = \boldsymbol{K}_p(\theta)\,\boldsymbol{x} = \frac{2}{3}\begin{bmatrix} cos(\theta) & cos\left(\theta - \frac{2\pi}{3}\right) & cos\left(\theta + \frac{2\pi}{3}\right) \\ -sin(\theta) & -sin\left(\theta - \frac{2\pi}{3}\right) & -sin\left(\theta + \frac{2\pi}{3}\right) \\ \frac{1}{2} & \frac{1}{2} & \frac{1}{2} \end{bmatrix}\boldsymbol{x} \tag{2.10}$$

This is also defined in such a way as to keep the module of the vector unchanged. It is mathematically demonstrable that the determinant of the matrix $\boldsymbol{K}_p$ is always non-zero, and thus the matrix is invertible. This lead to the Inverse Park transform presented in the following:

$$\boldsymbol{x} = \boldsymbol{K}_p^{-1}(\theta)\,\boldsymbol{x}^{dq0} = \begin{bmatrix} cos(\theta) & -sin(\theta) & 1 \\ cos\left(\theta - \frac{2\pi}{3}\right) & -sin\left(\theta - \frac{2\pi}{3}\right) & 1 \\ cos\left(\theta + \frac{2\pi}{3}\right) & -sin\left(\theta + \frac{2\pi}{3}\right) & 1 \end{bmatrix}\boldsymbol{x}^{dq0} \tag{2.11}$$

As in the previous cases, the contribution of component 0 can be neglected. It is therefore possible to rewrite the transform.

$$\boldsymbol{x}^{dq} = \boldsymbol{K}_p(\theta)\,\boldsymbol{x} = \frac{2}{3}\begin{bmatrix} cos(\theta) & cos\left(\theta - \frac{2\pi}{3}\right) & cos\left(\theta + \frac{2\pi}{3}\right) \\ -sin(\theta) & -sin\left(\theta - \frac{2\pi}{3}\right) & -sin\left(\theta + \frac{2\pi}{3}\right) \end{bmatrix} \tag{2.12}$$

$$\boldsymbol{xx} = \boldsymbol{K}_p^{-1}(\theta)\,\boldsymbol{x}^{dq} = \begin{bmatrix} cos(\theta) & -sin(\theta) \\ cos\left(\theta - \frac{2\pi}{3}\right) & -sin\left(\theta - \frac{2\pi}{3}\right) \\ cos\left(\theta + \frac{2\pi}{3}\right) & -sin\left(\theta + \frac{2\pi}{3}\right) \end{bmatrix}\boldsymbol{x}^{dq} \tag{2.13}$$

Throughout the following dissertation, the Clarke and Park transforms will be considered, neglecting the zero component.

2.1.4 Park Transform and Derivatives

In the following thesis, as differential equations will be used to model the system, the effect of the Park transform on the derived three-phase quantities has to be analysed. Considering what was introduced with the Park transform, it is possible to rewrite the derivative of a generic three-phase quantity $\boldsymbol{x}$ as follows:

$$\frac{d}{dt}\,\boldsymbol{x} = \frac{d}{dt}\,\left(\boldsymbol{K}_p^{-1}\left(\theta\right)\,\boldsymbol{x}^{\,dq}\right) \tag{2.14}$$

It is then possible to decompose the derivative of the product in (2.14) as shown below:

$$\frac{d}{dt}\,\left(\boldsymbol{K}_p^{-1}\left(\theta\right)\,\boldsymbol{x}^{\,dq}\right) = \frac{d}{dt}\,\left(\boldsymbol{K}_p^{-1}\left(\theta\right)\right)\,\boldsymbol{x}^{\,dq} + \boldsymbol{K}_p^{-1}\left(\theta\right)\,\frac{d}{dt}\,\boldsymbol{x}^{\,dq} \tag{2.15}$$

Consider the first element of the resulting sum in (2.15), more specifically the derivative of the inverse Park transform, remembering the definition of θ (2.5) this can be expressed as follows:

$$\frac{d}{dt}\,\left(\boldsymbol{K}_p^{-1}\left(\theta\right)\right) = \omega \begin{bmatrix} -sin(\theta) & -cos(\theta) \\ -sin\left(\theta - \dfrac{2\pi}{3}\right) & -cos\left(\theta - \dfrac{2\pi}{3}\right) \\ -sin\left(\theta + \dfrac{2\pi}{3}\right) & -cos\left(\theta + \dfrac{2\pi}{3}\right) \end{bmatrix} \tag{2.16}$$

Which can then be rewritten as shown below:

$$\frac{d}{dt}\,\left(\boldsymbol{K}_p^{-1}\left(\theta\right)\right) = \omega\,\boldsymbol{K}_p^{-1}\left(\theta\right)\,\boldsymbol{S} = \omega\,\boldsymbol{K}_p^{-1}\left(\theta\right)\begin{bmatrix} 0 & -1 \\ 1 & 0 \end{bmatrix} \tag{2.17}$$

Then substituting (2.17) in (2.15), the derivative of a three-phase quantity expressed through the Park transform can be written as follows:

$$\frac{d}{dt}\,\boldsymbol{x} = \boldsymbol{K}_p^{-1}\left(\theta\right)\,\left(\omega\,\boldsymbol{S}\,\boldsymbol{x}^{\,dq} + \frac{d}{dt}\,\boldsymbol{x}^{\,dq}\right) \tag{2.18}$$

2.2 Matrix Converter Average Model

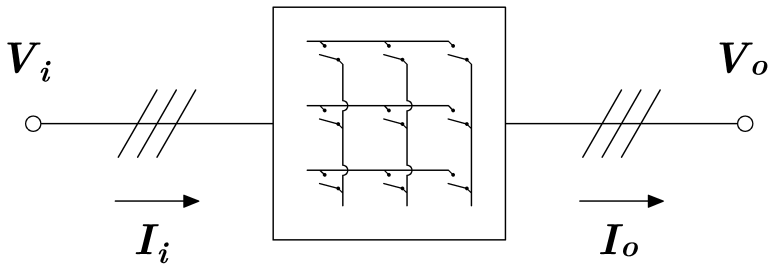

Figure 2.3: Matrix Converter, Input Output Schematic

To derive the relationships expressing the average model of the matrix converter, consider the following quantities at the input and output of the converter, as shown in the Fig. 2.3.

$$\boldsymbol{V}_i = \begin{bmatrix} V_{ir} \\ V_{is} \\ V_{it} \end{bmatrix}; \quad \boldsymbol{I}_i = \begin{bmatrix} I_{ir} \\ I_{is} \\ I_{it} \end{bmatrix}; \quad \boldsymbol{V}_o = \begin{bmatrix} V_{ou} \\ V_{ov} \\ V_{ow} \end{bmatrix}; \quad \boldsymbol{I}_o = \begin{bmatrix} I_{ou} \\ I_{ov} \\ I_{ow} \end{bmatrix} \tag{2.19}$$

Where, V_i and I_i represent input voltage and current, while V_o and I_o denote the output voltage and currents. The aim is to calculate relations that link input and output quantities. Firstly, it is necessary to define the quantities that represent the average model input. V_i is an input variable and it is constantly measured, as it is needed for the modulation algorithm. Another quantity required for modulation is the reference output voltage, defined as follows:

$$\boldsymbol{V}_{o\_r} = \begin{bmatrix} V_{ou\_r} \\ V_{ov\_r} \\ V_{ow\_r} \end{bmatrix} \tag{2.20}$$

When supplied with the correct input voltages, the modulator, disregarding switching effects and dead-times, ensures that the converter produces the desired output voltages.

Therefore, the following assumption can be made.

$$\boldsymbol{V}_o = \boldsymbol{V}_{o\_r} \tag{2.21}$$

The reference phase-shift between input voltage and current ϕ_r is an input of the modulator but also of the average model, and as in the case of output voltages, the modulator if given the correct input voltages, maintains the desired phase shift at the input, so:

$$\phi = \phi_r \tag{2.22}$$

Output current I_o depends on the output voltage and applied load. So, it is a quantity that depends on another model. For now, concerning the converter average model, it will be treated as an input variable. Only one variable remains that needs to be calculated from these inputs, and that is the input current $\boldsymbol{I}_i$. From the input voltage vector expressed in the $\alpha\beta$ stationary reference frame it is possible to calculate the input voltage angle θ_v as:

$$\theta_v = arctan\left(\frac{V_{i\beta}}{V_{i\alpha}}\right) \tag{2.23}$$

The input current angle θ_i is phase-shifted with respect to the input voltage angle θ_v by the angle ϕ_r. This can be expressed as reported below:

$$\theta_i = \theta_v + \phi_r \tag{2.24}$$

And so, substituting (2.23) in (2.24):

$$\theta_i = arctan\left(\frac{V_{i\beta}}{V_{i\alpha}}\right) + \phi_r \tag{2.25}$$

Now, focusing on the input current angle, it is possible to define the components of the input current vector in the α-β stationary reference as follows:

$$\begin{aligned} I_{i\alpha} &= \left|\boldsymbol{I}_i^{\alpha\beta}\right| cos\left(\theta_i\right); \\ I_{i\beta} &= \left|\boldsymbol{I}_i^{\alpha\beta}\right| sin\left(\theta_i\right) \end{aligned} \tag{2.26}$$

Where:

$$\left|\boldsymbol{I}_i^{\alpha\beta}\right| = \sqrt{I_{i\alpha}^2 + I_{i\beta}^2} \tag{2.27}$$

It is then possible to replace (2.25) into (2.26):

$$\begin{aligned} I_{i\alpha} &= \left|\boldsymbol{I}_i^{\alpha\beta}\right| cos\left(arctan\left(\frac{V_{i\beta}}{V_{i\alpha}}\right) + \phi_r\right); \\ I_{i\alpha} &= \left|\boldsymbol{I}_i^{\alpha\beta}\right| sin\left(arctan\left(\frac{V_{i\beta}}{V_{i\alpha}}\right) + \phi_r\right) \end{aligned} \tag{2.28}$$

Now, attention will be focused on the trigonometric relations in (2.28). Remembering that it is possible to decompose the goniometric functions applied to the sum of two angles as shown below:

$$\begin{aligned} cos\,(x+y) &= cos\,(x)\,cos\,(y) - sin\,(x)\,sin\,(y); \\ sin\,(x+y) &= sin\,(x)\,cos\,(y) + cos\,(x)\,sin\,(y) \end{aligned} \tag{2.29}$$

The above decompositions can be applied to the trigonometric function in (2.28):

$$\begin{aligned} &cos\left(arctan\left(\frac{V_{i\beta}}{V_{i\alpha}}\right) + \phi_r\right) = ... \\ &... = cos\left(arctan\left(\frac{V_{i\beta}}{V_{i\alpha}}\right)\right) cos\,(\phi_r) - sin\left(arctan\left(\frac{V_{i\beta}}{V_{i\alpha}}\right)\right) sin\,(\phi_r); \\ &sin\left(arctan\left(\frac{V_{i\beta}}{V_{i\alpha}}\right) + \phi_r\right) = ... \\ &... = sin\left(arctan\left(\frac{V_{i\beta}}{V_{i\alpha}}\right)\right) cos\,(\phi_r) - cos\left(arctan\left(\frac{V_{i\beta}}{V_{i\alpha}}\right)\right) sin\,(\phi_r) \end{aligned} \tag{2.30}$$

It is possible to mathematically prove the following substitutions:

$$\begin{aligned} cos\left(arctan\left(\frac{V_{i\beta}}{V_{i\alpha}}\right)\right) &= \frac{V_{i\alpha}}{\left|\boldsymbol{V}_i^{\alpha\beta}\right|} \\ sin\left(arctan\left(\frac{V_{i\beta}}{V_{i\alpha}}\right)\right) &= \frac{V_{i\beta}}{\left|\boldsymbol{V}_i^{\alpha\beta}\right|} \end{aligned} \tag{2.31}$$

Where:

$$\left|\boldsymbol{V}_i^{\alpha\beta}\right| = \sqrt{V_{i\alpha}^2 + V_{i\beta}^2} \tag{2.32}$$

Substituting (2.31) in (2.30):

$$\begin{aligned} cos\left(arctan\left(\frac{V_{i\beta}}{V_{i\alpha}}\right)+\phi_r\right) &= \frac{V_{i\alpha}\,cos\left(\phi_r\right)-V_{i\beta}\,sin\left(\phi_r\right)}{\left|\boldsymbol{V}_i^{\alpha\beta}\right|}; \\ sin\left(arctan\left(\frac{V_{i\beta}}{V_{i\alpha}}\right)+\phi_r\right) &= \frac{V_{i\beta}\,cos\left(\phi_r\right)+V_{i\alpha}\,sin\left(\phi_r\right)}{\left|\boldsymbol{V}_i^{\alpha\beta}\right|} \end{aligned} \tag{2.33}$$

And finally substituting in (2.28) the input current angle is defined:

$$\begin{aligned} I_{i\alpha} &= \left|\boldsymbol{I}_i^{\alpha\beta}\right| \frac{V_{i\alpha}\,cos\left(\phi_r\right)-V_{i\beta}\,sin\left(\phi_r\right)}{\left|\boldsymbol{V}_i^{\alpha\beta}\right|}; \\ I_{i\alpha} &= \left|\boldsymbol{I}_i^{\alpha\beta}\right| \frac{V_{i\beta}\,cos\left(\phi_r\right)+V_{i\alpha}\,sin\left(\phi_r\right)}{\left|\boldsymbol{V}_i^{\alpha\beta}\right|} \end{aligned} \tag{2.34}$$

These relationships can be rewritten as follows:

$$\boldsymbol{I}_i^{\alpha\beta} = \frac{\left|\boldsymbol{I}_i^{\alpha\beta}\right|}{\left|\boldsymbol{V}_i^{\alpha\beta}\right|}\,\boldsymbol{N}\left(\phi_r\right)\,\boldsymbol{V}_i^{\alpha\beta} \tag{2.35}$$

Where:

$$\boldsymbol{N}\left(\phi_r\right) = \begin{bmatrix} cos\left(\phi_r\right) & -sin\left(\phi_r\right) \\ sin\left(\phi_r\right) & cos\left(\phi_r\right) \end{bmatrix} \tag{2.36}$$

$\boldsymbol{N}$ represents a rotation matrix. In particular, this matrix rotates the vector by which it is multiplied, in this case $\boldsymbol{V}_i^{\alpha\beta}$, counterclockwise by the angle ϕ_r. It is orthogonal matrix, this means that its inverse it is equal to its transpose. At this point, it is necessary to switch from the $\alpha\beta$ stationary reference frame to the dq synchronous reference frame. In fact, it will be necessary to solve a system of nonlinear equations to study the stability of the system, which is not possible with sinusoidal quantities. Clarke to Park transform is used for this purpose (2.9). For now, the three-phase reference vector to be used to realise the transform is not chosen. In fact, the reference vector do not involve changes to the equations, but only to the dq components of the transformed vectors. A generic angle θ_i will be considered, indicating an angle that varies at the input side angular frequency ω_i. It is important to remember that in the case of the matrix converter, two

synchronous reference frame will be defined, one for the input side and one for the output side, which usually have different angular frequencies. Applying (2.9), $\boldsymbol{V}_i^{\alpha\beta}$ and $\boldsymbol{I}_i^{\alpha\beta}$ can be defined as follows:

$$\begin{aligned} \boldsymbol{V}_i^{\alpha\beta} &= \boldsymbol{K}_{cp}^{\mathsf{T}}(\theta_i)\ \boldsymbol{V}_i^{dq} \\ \boldsymbol{I}_i^{\alpha\beta} &= \boldsymbol{K}_{cp}^{\mathsf{T}}(\theta_i)\ \boldsymbol{I}_i^{dq} \end{aligned} \tag{2.37}$$

This transformation maintains the vector modules unchanged, so:

$$\begin{aligned} \left|\boldsymbol{V}_i^{\alpha\beta}\right| &= \left|\boldsymbol{V}_i^{dq}\right| \\ \left|\boldsymbol{I}_i^{\alpha\beta}\right| &= \left|\boldsymbol{I}_i^{dq}\right| \end{aligned} \tag{2.38}$$

Substituting (2.37) and (2.38), (2.35) can be rewritten as follows:

$$\boldsymbol{K}_{cp}^{\mathsf{T}}(\theta_i)\,\boldsymbol{I}_i^{dq} = \frac{\left|\boldsymbol{I}_i^{dq}\right|}{\left|\boldsymbol{V}_i^{dq}\right|}\,\boldsymbol{N}(\phi_r)\ \boldsymbol{K}_{cp}^{\mathsf{T}}(\theta_i)\ \boldsymbol{V}_i^{dq} \tag{2.39}$$

Multiplying both sides of the equation by $\boldsymbol{K}_{cp}$, and remembering that:

$$\boldsymbol{K}_{cp}(\theta_i)\ \boldsymbol{K}_{cp}^{\mathsf{T}}(\theta_i) = I \tag{2.40}$$

where $I \in \mathbb{R}^{2\times 2}$ represent identity matrix, (2.39) results in:

$$\boldsymbol{I}_i^{dq} = \frac{\left|\boldsymbol{I}_i^{dq}\right|}{\left|\boldsymbol{V}_i^{dq}\right|}\,\boldsymbol{K}_{cp}(\theta_i)\ \boldsymbol{N}(\phi_r)\ \boldsymbol{K}_{cp}^{\mathsf{T}}(\theta_i)\ \boldsymbol{V}_i^{dq} \tag{2.41}$$

At this point, recalling that the matrices $\boldsymbol{N}$ and $\boldsymbol{K}_{cp}$ denote rotation matrices, the product $\boldsymbol{K}_{cp}\,\boldsymbol{N}\,\boldsymbol{K}_{cp}^{\mathsf{T}}$ can be interpreted as a sequence of rotations: initially clockwise by the angle θ_i, followed by a counterclockwise rotation by the angle ϕ_r, and ultimately a counterclockwise rotation by the angle θ_i. This implies that the overall transformation is reducible to a singular counterclockwise rotation by the angle ϕ_r, as the rotations by the angle θ_i cancel each other out. Then (2.41) can be simplified as follows:

$$\boldsymbol{I}_i^{dq} = \frac{\left|\boldsymbol{I}_i^{dq}\right|}{\left|\boldsymbol{V}_i^{dq}\right|} \boldsymbol{N}\left(\phi_r\right) \boldsymbol{V}_i^{dq} \tag{2.42}$$

And thus decomposing:

$$\begin{aligned} I_{id} &= \left|\boldsymbol{I}_i^{dq}\right| \frac{V_{id}\, cos\left(\phi_r\right) - V_{iq}\, sin\left(\phi_r\right)}{\left|\boldsymbol{V}_i^{dq}\right|}; \\ I_{id} &= \left|\boldsymbol{I}_i^{dq}\right| \frac{V_{iq}\, cos\left(\phi_r\right) + V_{id}\, sin\left(\phi_r\right)}{\left|\boldsymbol{V}_i^{dq}\right|} \end{aligned} \tag{2.43}$$

Therefore, when passing from the $\alpha\beta$ stationary reference frame to the dq synchronous reference, the relationships remain almost unchanged. It remains to calculate the module of the input current. This can be obtained from a power balance between input and output. In general, as anticipated, modulation algorithms are designed to provide the desired output voltage and to ensure the requested input power factor. So, input power can be evaluated as shown below:

$$P_i = \frac{3}{2} \left|\boldsymbol{V}_i^{dq}\right| \left|\boldsymbol{I}_i^{dq}\right| cos(\phi_r) \tag{2.44}$$

While the output power, calculated in the output dq synchronous reference frame is defined as follows:

$$P_o = \frac{3}{2} \left(V_{od} I_{od} + V_{oq} I_{oq}\right) \tag{2.45}$$

Since as stated in (2.21) the output voltage coincides with the reference voltage, (2.45) can be rewritten as:

$$P_o = \frac{3}{2} \left(V_{od\_r} I_{od} + V_{oq\_r} I_{oq}\right) \tag{2.46}$$

Neglecting switching and conduction losses, it is possible to equalise the input power P_i with the output power P_o:

$$P_i = P_o \tag{2.47}$$

And then determine the module of the input current.

$$\left|\boldsymbol{I}_i^{dq}\right| = \frac{(V_{od\_r}I_{od} + V_{oq\_r}I_{oq})}{\left|\boldsymbol{V}_i^{dq}\right| \, cos(\phi_r)} \tag{2.48}$$

Finally, the input currents components in d-q synchronous reference frame can be expressed as follows:

$$\begin{aligned} I_{id} &= (V_{od\_r}I_{od} + V_{oq\_r}I_{oq}) \, \frac{V_{id}\, cos\,(\phi_r) - V_{iq}\, sin\,(\phi_r)}{\left|\boldsymbol{V}_i^{dq}\right|^2 \, cos\,(\phi_r)}; \\ I_{iq} &= (V_{od\_r}I_{od} + V_{oq\_r}I_{oq}) \, \frac{V_{iq}\, cos\,(\phi_r) + V_{id}\, sin\,(\phi_r)}{\left|\boldsymbol{V}_i^{dq}\right|^2 \, cos\,(\phi_r)} \end{aligned} \tag{2.49}$$

The relations that link the converter input variables with the output variables have been formulated. As already mentioned, in order to examine the stability of the system, it is necessary to define the model of the applied load. This model, depending on the output voltage, determines the output current profile, which, as shown in the equations, has an impact on the input current. In addition, the model of the input filter must also be defined; it is this component that will present the most critical issues in terms of stability.

2.3 Input Filter Model

The input LC filter has been modelled as shown in Fig. 2.4. The inductance has been modelled by considering its series resistance R_{sf}, which is easily measured, and including a parallel resistance R_{pf}. The parallel resistance cannot be measured directly, but can be estimated. It has been demonstrated that its value has a significant impact on the stability of the system, and by means of the open-loop instability analysis, it is possible to adjust this parameter so that the point at which instabilities are experimentally observed coincides with that calculated analytically. The capacitor has been modelled as an ideal capacitor neglecting its parasitic quantities that has been observed do not affect the stability study. The reason why R_{pf} has such an impact on the stability of the system is that it influences the gain at the resonance frequency of the transfer function that describes the behaviour of the filter as shown in Fig. 2.5.

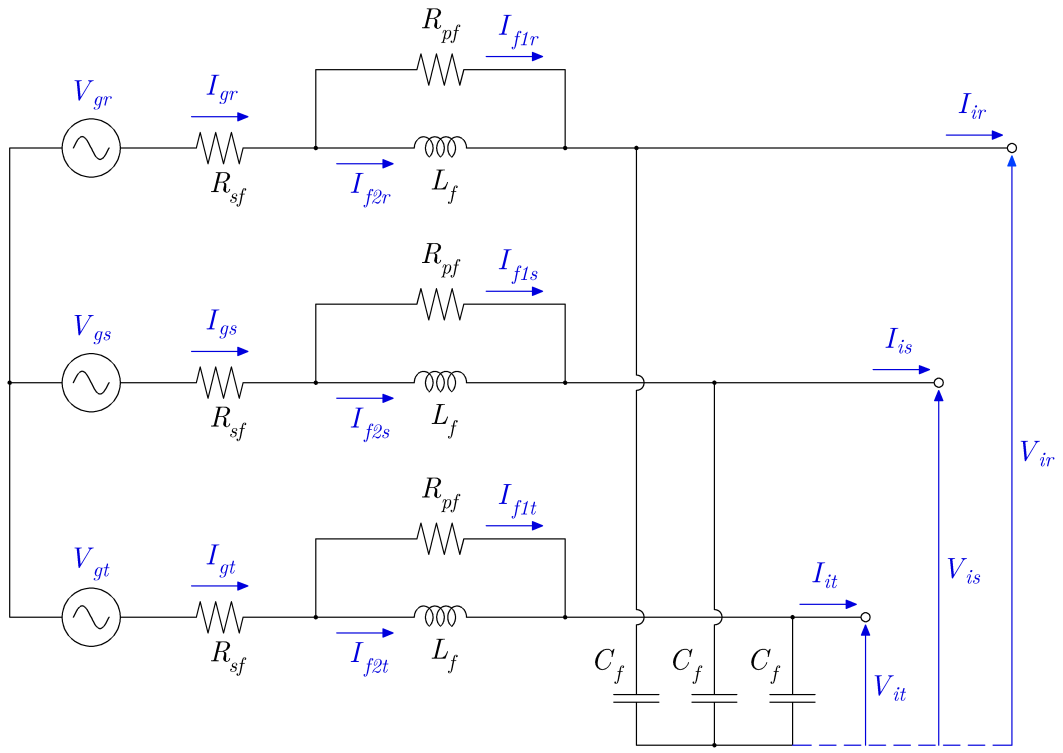

Figure 2.4: Input Filter Model

The Input Filter Bode Diagram in Fig. 2.5 has been obtained considering the parameters reported in Tab. 2.1:

Table 2.1: Input Filter Model Parameters

Parameters		Value
Inductance	L_f	$2.4\ mH$
Capacitance	C_f	$12\ uF$
Series Resistance	R_{sf}	$1.5\ \Omega$

It is evident that the change in resistance R_{pf} affects the gain at the resonance frequency, defined in (2.50). In particular, as the resistance value increases, there is a corresponding increase in the maximum gain at the resonance frequency.

$$f_{res} = \frac{1}{2\,\pi\,\sqrt{L_f\,C_f}} = 937.82\ Hz \tag{2.50}$$

This modelling approach makes it possible to obtain a mathematical model of the filter

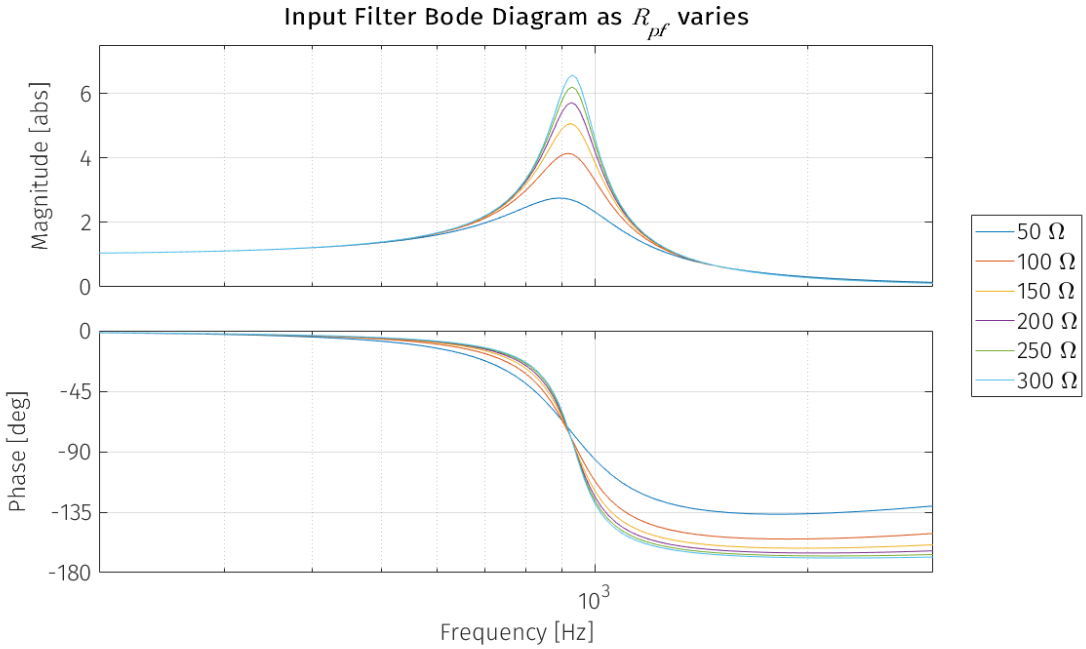

Figure 2.5: Input Filter Transfer Function Bode Diagram varying R_{pf}

as close as possible to the real one with as few components as possible. Comparing the instabilities found on the experimental setup with the results obtained through the analytical study, it has been found that the R_{pf} value that best approximated the behaviour of the setup was $200\ \Omega$. At this point, once the model used is known, the equations describing its behaviour has to be calculated from it. The following vectors are defined:

$$\boldsymbol{V}_g = \begin{bmatrix} V_{gr} \\ V_{gs} \\ V_{gt} \end{bmatrix}; \quad \boldsymbol{I}_g = \begin{bmatrix} I_{gr} \\ I_{gs} \\ I_{gt} \end{bmatrix}; \quad \boldsymbol{I}_{f1} = \begin{bmatrix} I_{f1r} \\ I_{f1s} \\ I_{f1t} \end{bmatrix}; \quad \boldsymbol{I}_{f2} = \begin{bmatrix} I_{f2r} \\ I_{f2s} \\ I_{f2t} \end{bmatrix} \tag{2.51}$$

Where $\boldsymbol{V}_g$ represent the grid voltage, $\boldsymbol{I}_g$ the grid current, $\boldsymbol{I}_{f1}$ the current through R_{pf} and $\boldsymbol{I}_{f2}$ the current trough L_f. By means of some circuit calculations, the following set of equations defined in state-space can be obtained:

$$\frac{d}{dt}\boldsymbol{I}_{f2} = \frac{1}{L_f}\left(\boldsymbol{V}_g - R_{sf}\frac{\boldsymbol{V}_g - \boldsymbol{V}_i + R_{sf}\boldsymbol{I}_{f2}}{R_{sf}+R_{pf}} - \boldsymbol{V}_i\right); \tag{2.52}$$

$$\frac{d}{dt}\boldsymbol{V}_i = \frac{1}{C_f}\left(\frac{\boldsymbol{V}_g - \boldsymbol{V}_i + R_{sf}\boldsymbol{I}_{f2}}{R_{sf}+R_{pf}} - \boldsymbol{I}_i\right) \tag{2.53}$$

The other system variables can be calculated through the following relationships:

$$\begin{aligned} \boldsymbol{I}_g &= \frac{\boldsymbol{V}_g - \boldsymbol{V}_i + R_{sf}\,\boldsymbol{I}_{f2}}{R_{sf} + R_{pf}}; \\ \boldsymbol{I}_{f1} &= \boldsymbol{I}_g - \boldsymbol{I}_{f2} \end{aligned} \tag{2.54}$$

The equations that will be used to realize the complete model of the system are given in (2.53). The system composed of these two equations describes the behaviour of a sixth-order system. The system variables are sinusoidal, and as anticipated, for the stability study of the system it is necessary to transform these abc quantities into a synchronous reference frame. For this purpose, the Park transform is used (2.12). Once more, consider the generic angle θ_i to realize the transformation. Referring to (2.13) and (2.18), the appropriate substitutions in equations (2.53) have been performed.

$$\begin{aligned} &\boldsymbol{K}_p^{-1}(\theta_i)\left(\omega_i\,\boldsymbol{S}\,\boldsymbol{I}_{f2}^{dq} + \frac{d}{dt}\boldsymbol{I}_{f2}^{dq}\right) = \ldots \\ &\ldots = \frac{1}{L_f}\,\boldsymbol{K}_p^{-1}(\theta_i)\left(\boldsymbol{V}_g^{dq} - R_{sf}\,\frac{\boldsymbol{V}_g^{dq} - \boldsymbol{V}_i^{dq} + R_{sf}\,\boldsymbol{I}_{f2}^{dq}}{R_{sf} + R_{pf}} - \boldsymbol{V}_i^{dq}\right) \end{aligned} \tag{2.55}$$

$$\begin{aligned} &\boldsymbol{K}_p^{-1}(\theta_i)\left(\omega_i\,\boldsymbol{S}\,\boldsymbol{V}_i^{dq} + \frac{d}{dt}\boldsymbol{V}_i^{dq}\right) = \ldots \\ &\ldots = \frac{1}{C_f}\,\boldsymbol{K}_p^{-1}(\theta_i)\left(\frac{\boldsymbol{V}_g^{dq} - \boldsymbol{V}_i^{dq} + R_{sf}\,\boldsymbol{I}_{f2}^{dq}}{R_{sf} + R_{pf}} - \boldsymbol{I}_i^{dq}\right) \end{aligned} \tag{2.56}$$

Now it is sufficient to multiply both sides of (2.55) and (2.56) by the $\boldsymbol{K}_p(\theta_i)$ matrix to obtain the following differential equations.

$$\frac{d}{dt}\boldsymbol{I}_{f2}^{dq} = \frac{1}{L_f}\left(\boldsymbol{V}_g^{dq} - R_{sf}\,\frac{\boldsymbol{V}_g^{dq} - \boldsymbol{V}_i^{dq} + R_{sf}\,\boldsymbol{I}_{f2}^{dq}}{R_{sf} + R_{pf}} - \boldsymbol{V}_i^{dq}\right) - \omega_i\,\boldsymbol{S}\,\boldsymbol{I}_{f2}^{dq} \tag{2.57}$$

$$\frac{d}{dt}\boldsymbol{V}_i^{dq} = \frac{1}{C_f}\left(\frac{\boldsymbol{V}_g^{dq} - \boldsymbol{V}_i^{dq} + R_{sf}\,\boldsymbol{I}_{f2}^{dq}}{R_{sf} + R_{pf}} - \boldsymbol{I}_i^{dq}\right) - \omega_i\,\boldsymbol{S}\,\boldsymbol{V}_i^{dq} \tag{2.58}$$

The equations thus obtained can be decomposed into their respective dq components.

$$\begin{aligned}
\frac{d}{dt} I_{f2d} &= \frac{1}{L_f}\left(V_{gd} - R_{sf}\,\frac{V_{gd} - V_{id} + R_{sf}\,I_{f2d}}{R_{sf} + R_{pf}} - V_{id}\right) + \omega_i\, I_{f2q} \\
\frac{d}{dt} I_{f2q} &= \frac{1}{L_f}\left(V_{gq} - R_{sf}\,\frac{V_{gq} - V_{iq} + R_{sf}\,I_{f2q}}{R_{sf} + R_{pf}} - V_{iq}\right) - \omega_i\, I_{f2d}
\end{aligned} \tag{2.59}$$

$$\begin{aligned}
\frac{d}{dt} V_{id} &= \frac{1}{C_f}\left(\frac{V_{gd} - V_{id} + R_{sf}\,I_{f2d}}{R_{sf} + R_{pf}} - I_{id}\right) + \omega_i\, V_{iq} \\
\frac{d}{dt} V_{iq} &= \frac{1}{C_f}\left(\frac{V_{gq} - V_{iq} + R_{sf}\,I_{f2q}}{R_{sf} + R_{pf}} - I_{iq}\right) - \omega_i\, V_{id}
\end{aligned} \tag{2.60}$$

The system composed of (2.59) and (2.60) describes the behavior of a fourth-order system. Thanks to the Park transform, not only have non-sinusoidal variables been obtained, but the complexity of the system has also been reduced by two orders. This simplification does not entail any loss of information of the resulting three-phase system.

2.4 Three-Phase RL load

At the output side of the matrix converter, loads can be connected as long as they are inductive, since the converter behaves like a voltage-controlled generator at the output. Consequently, the first load that is applied to the converter output-side is the simplest three-phase inductive load, the three-phase RL load, shown in Fig. 2.6.

Analysing the schematic, through some circuit calculations it is possible to obtain the following equations describing the dynamic behaviour of the inductive load.

$$\frac{d}{dt}\,\boldsymbol{I}_o = \frac{\boldsymbol{V}_o - R_o\,\boldsymbol{I}_o}{L_o} \tag{2.61}$$

The equation describes the behaviour of a third-order dynamic system. The Park transform will also be applied in this case. In this case, however, it will be applied as a function of the generic output angle θ_o, whose angular frequency is ω_o. In practical applications, for the RL load, this angle is calculated and imposed by the microcontroller, depending on the desired angular frequency. It is then used to generate the three-phase voltage reference from a dq vector via Park inverse transform. Returning to the load model, pro-

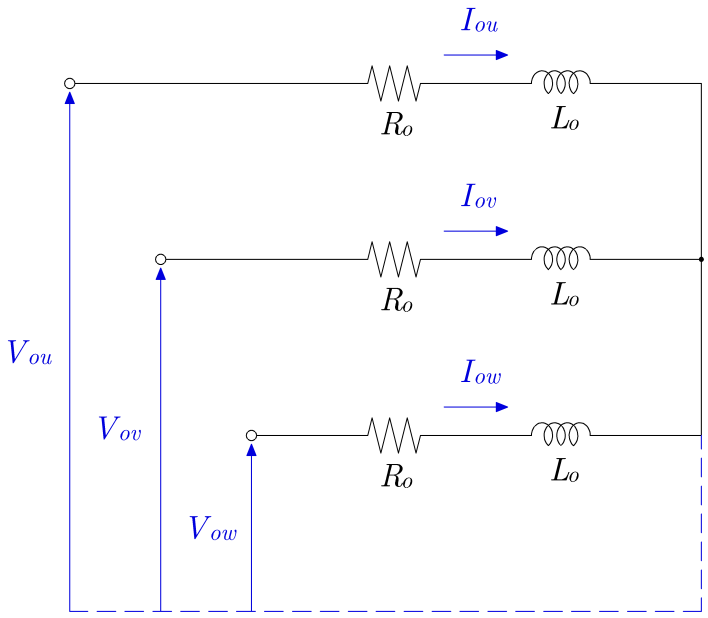

Figure 2.6: Three-phase RL load schematic

ceeding similarly to the filter equations, the following dq relation is obtained:

$$\frac{d}{dt}\,\boldsymbol{I}_o^{dq} = \frac{\boldsymbol{V}_o^{dq} - R_o\,\boldsymbol{I}_o^{dq}}{L_o} - \omega_o\,\boldsymbol{S}\,I_o^{dq} \tag{2.62}$$

And decomposing:

$$\begin{aligned} \frac{d}{dt}\,I_{od} &= \frac{V_{od} - R_o\,I_{od}}{L_o} + \omega_o\,I_{oq} \\ \frac{d}{dt}\,I_{oq} &= \frac{V_{oq} - R_o\,I_{oq}}{L_o} - \omega_o\,I_{od} \end{aligned} \tag{2.63}$$

The three-phase RL load is then modelled as a second-order dynamic system. It is certainly the simplest load that can be applied to the matrix converter, but allows the dependence of matrix converter instabilities on output power to be clearly explained.

2.5 Complete system model with RL load

Once all the equations describing the components of the system have been defined, it is finally possible to use them to compose the model of the complete system. In Fig. 2.7 a simplified schematic of the complete system is presented.

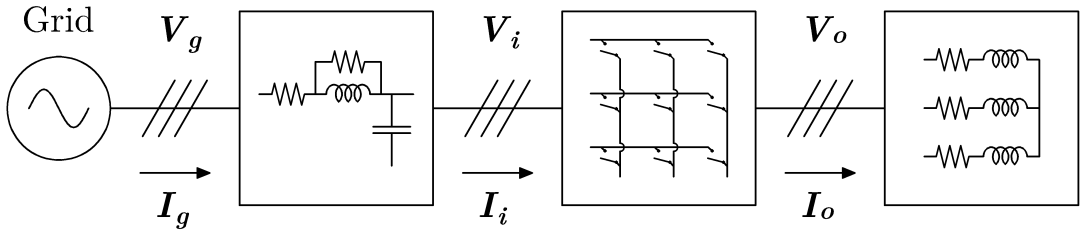

Figure 2.7: Complete System Model

The system consists of the supply grid, which through the LC filter feeds the matrix converter, which in turn supplies the RL load. To describe the converter input side behaviour (2.59) and (2.60) are re-proposed

$$\begin{aligned}
\frac{d}{dt} I_{f2d} &= \frac{1}{L_f}\left(V_{gd} - R_{sf}\,\frac{V_{gd} - V_{id} + R_{sf}\,I_{f2d}}{R_{sf} + R_{pf}} - V_{id}\right) + \omega_i\, I_{f2q} \\
\frac{d}{dt} I_{f2q} &= \frac{1}{L_f}\left(V_{gq} - R_{sf}\,\frac{V_{gq} - V_{iq} + R_{sf}\,I_{f2q}}{R_{sf} + R_{pf}} - V_{iq}\right) - \omega_i\, I_{f2d}
\end{aligned} \tag{2.64}$$

$$\begin{aligned}
\frac{d}{dt} V_{id} &= \frac{1}{C_f}\left(\frac{V_{gd} - V_{id} + R_{sf}\,I_{f2d}}{R_{sf} + R_{pf}} - I_{id}\right) + \omega_i\, V_{iq} \\
\frac{d}{dt} V_{iq} &= \frac{1}{C_f}\left(\frac{V_{gq} - V_{iq} + R_{sf}\,I_{f2q}}{R_{sf} + R_{pf}} - I_{iq}\right) - \omega_i\, V_{id}
\end{aligned} \tag{2.65}$$

These are equations have to be related to the output equations.

$$\begin{aligned}
\frac{d}{dt}\, I_{od} &= \frac{V_{od} - R_o\, I_{od}}{L_o} + \omega_o\, I_{oq} \\
\frac{d}{dt}\, I_{oq} &= \frac{V_{oq} - R_o\, I_{oq}}{L_o} - \omega_o\, I_{od}
\end{aligned} \tag{2.66}$$

The relationships that are used to link these two systems are those expressed by the

Average Model of the converter, and they are reported in the following:

$$\begin{aligned} I_{id} &= (V_{od\_r} I_{od} + V_{oq\_r} I_{oq}) \ \frac{V_{id}\, cos\,(\phi_r) - V_{iq}\, sin\,(\phi_r)}{\left| \boldsymbol{V}_i^{dq} \right|^2 \ cos\,(\phi_r)}; \\ I_{iq} &= (V_{od\_r} I_{od} + V_{oq\_r} I_{oq}) \ \frac{V_{iq}\, cos\,(\phi_r) + V_{id}\, sin\,(\phi_r)}{\left| \boldsymbol{V}_i^{dq} \right|^2 \ cos\,(\phi_r)} \end{aligned} \tag{2.67}$$

$$\begin{aligned} V_{od} &= V_{od\_r} \\ V_{oq} &= V_{oq\_r} \end{aligned} \tag{2.68}$$

The converter input current, reported in (2.67) have to be substituted in (2.65), while the relation between output voltage reference and actual output voltage in (2.68) have to be replaced in (2.66). With this procedure, it is possible to obtain the model that completely describes the behaviour of the system as a function of the input variables, which are respectively V_{gd}, V_{gq}, V_{od_r}, V_{oq_r} and ϕ_r. The latter will not be varied for the time being, in particular it will be set to 0, it can be considered as a system, parameter. The complete sixth-order dynamic model is presented in (2.69).

$$
\begin{cases}
\dfrac{d}{dt} I_{f2d} &= \dfrac{1}{L_f}\left(V_{gd} - R_{sf}\,\dfrac{V_{gd} - V_{id} + R_{pf}\,I_{f2d}}{R_{sf} + R_{pf}} - V_{id}\right) + \omega_i\, I_{f2q} \\[2ex]
\dfrac{d}{dt} I_{f2q} &= \dfrac{1}{L_f}\left(V_{gq} - R_{sf}\,\dfrac{V_{gq} - V_{iq} + R_{pf}\,I_{f2q}}{R_{sf} + R_{pf}} - V_{iq}\right) - \omega_i\, I_{f2d} \\[2ex]
\dfrac{d}{dt} V_{id} &= \dfrac{1}{C_f}\left(\dfrac{V_{gd} - V_{id} + R_{pf}\,I_{f2d}}{R_{sf} + R_{pf}} - (V_{od\_r} I_{od} + V_{oq\_r} I_{oq})\,\dfrac{V_{id}\,cos\,(\phi_r) - V_{iq}\,sin\,(\phi_r)}{\left|\boldsymbol{V}_i^{dq}\right|^2\,cos\,(\phi_r)}\right) + \omega_i\, V_{iq} \\[2ex]
\dfrac{d}{dt} V_{iq} &= \dfrac{1}{C_f}\left(\dfrac{V_{gq} - V_{iq} + R_{pf}\,I_{f2q}}{R_{sf} + R_{pf}} - (V_{od\_r} I_{od} + V_{oq\_r} I_{oq})\,\dfrac{V_{iq}\,cos\,(\phi_r) + V_{id}\,sin\,(\phi_r)}{\left|\boldsymbol{V}_i^{dq}\right|^2\,cos\,(\phi_r)}\right) - \omega_i\, V_{id} \\[2ex]
\dfrac{d}{dt}\, I_{od} &= \dfrac{V_{od\_r} - R_o\, I_{od}}{L_o} + \omega_o\, I_{oq} \\[2ex]
\dfrac{d}{dt}\, I_{oq} &= \dfrac{V_{oq\_r} - R_o\, I_{oq}}{L_o} - \omega_o\, I_{od}
\end{cases}
\tag{2.69}
$$

The dynamic model of the open-loop system is then defined by the system of equations presented in (2.69). This is referred to as an open-loop system since the voltage output reference is directly imposed, without any feedback. (2.69) represents a non-linear dynamic system. It can therefore be expressed as in the following:

$$\dot{\boldsymbol{x}} = \boldsymbol{f}\left(\boldsymbol{x},\, \boldsymbol{u},\, \boldsymbol{d}_{op}\right) \tag{2.70}$$

Where:

$$\boldsymbol{x} = \begin{bmatrix} I_{f2d} \\ I_{f2q} \\ V_{id} \\ V_{iq} \\ I_{od} \\ I_{oq} \end{bmatrix}; \quad \boldsymbol{u} = \begin{bmatrix} V_{od\_r} \\ V_{od\_r} \end{bmatrix}; \quad \boldsymbol{d} = \begin{bmatrix} V_{gd} \\ V_{gq} \end{bmatrix} \tag{2.71}$$

The vector $\boldsymbol{x} \in \mathbb{R}^{6\times 1}$ represent the state variables vector, while $\boldsymbol{u} \in \mathbb{R}^{2\times 1}$ is the reference input vector. $\boldsymbol{d} \in \mathbb{R}^{2\times 1}$ represent the grid voltage vector that, despite being an input to the system, is considered separately from the reference input vector, as if it was a system disturbance. This because, as will be shown later, it simplifies the substitutions that will be applied in the closed loop case.

2.5.1 System Model Simulative Validation

A simulator can be used to validate the mathematical model that has just been described. Using MATLAB/Simulink, and in particular the Simscape library "Specialised Power System", it is possible to create a complete simulator of the system, including discrete components, switches, and modulation algorithms. This provides a first method of validating the calculations carried out so far and, in particular, checking the correctness of the relationships between the input and output of the converter. The behaviour of the mathematical model has been simulated in parallel with the system simulator using the same inputs, as follows. A Simulink block that calculate the derivative state variables, as a function of input variables and state variables of the previous simula-

tion step, has been defined. The result is then integrated to obtain the state variables that are displayed and used to calculate the next simulation step state variable. It is clearly necessary to provide the integrator with the appropriate initial conditions. There is no need to introduce the concept of discretization, since the simulator, as defined, uses computational steps and algorithms to solve the integral that make the difference between continuous and discrete systems negligible in this case. Before comparing the results, it is important to remember that the mathematical model is defined on two distinct dq reference systems, one for the input-side and one for the output-side. In order to compare the results correctly, it is necessary to define the reference quantities for these two rotating frame. The input-side dq frame is considered oriented with the grid voltage angle θ_g, in particular the transform d-axis is considered aligned to the r-phase of the $\boldsymbol{V}_g$ vector. This implies that the d components of $\boldsymbol{V}_g^{dq}$ is equal to the module of the grid voltage vector $\boldsymbol{V}_g$, while the q components is zero. The output-side reference frame, is obtained starting from the θ_o angle, that in simulation and in the experimental setup is simply calculated as a sawtooth function of time, where the slope corresponds to the angular frequency ω_o. All transform of the output variables are calculated by referring to this angle. In Fig. 2.8 a schematic of the simulation comparison realized is presented. The parameters used to realise the simulations are shown in Tab. 2.2.

Table 2.2: Simulation Parameters

Parameters		Value
Filter Inductance	L_f	$2.4\ mH$
Filter Capacitance	C_f	$12\ uF$
Series Resistance	R_{sf}	$1.5\ \Omega$
Parallel Resistance	R_{pf}	$200\ \Omega$
Output Resistance	R_o	$10\ \Omega$
Output Inductance	L_o	$2\ mH$
Grid Voltage phase-to-phase	V_{g_pp}	$120\ V_{rms}$
Grid Frequency	f_i	$50\ Hz$
Input Phase Shift	ϕ_r	$0\ rad$
Output Frequency	f_o	$60\ Hz$
Switching Frequency	f_{sw}	$10\ kHz$

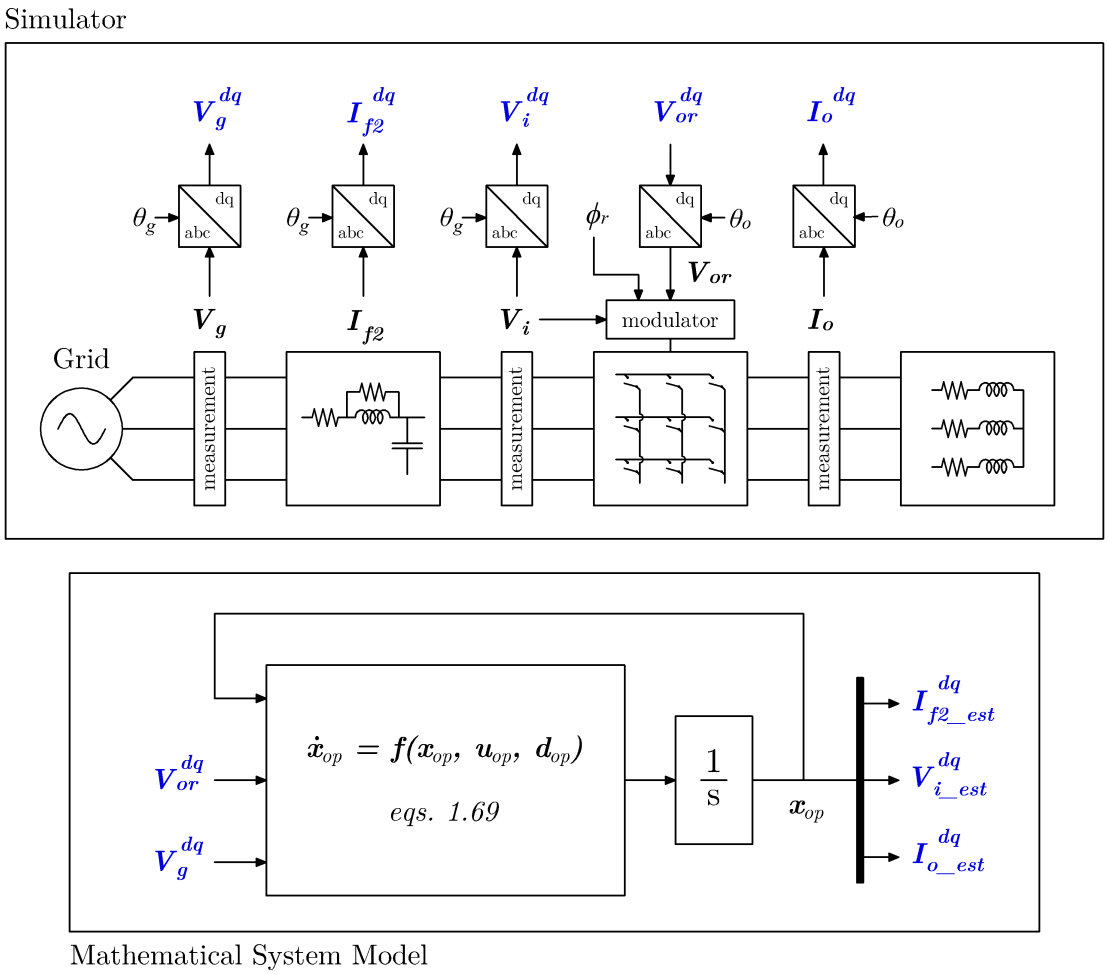

Figure 2.8: Comparison simulation between simulated system and mathematical model

The output voltage reference vector $V_{o\_r}^{dq}$ applied is reported in Fig. 2.9

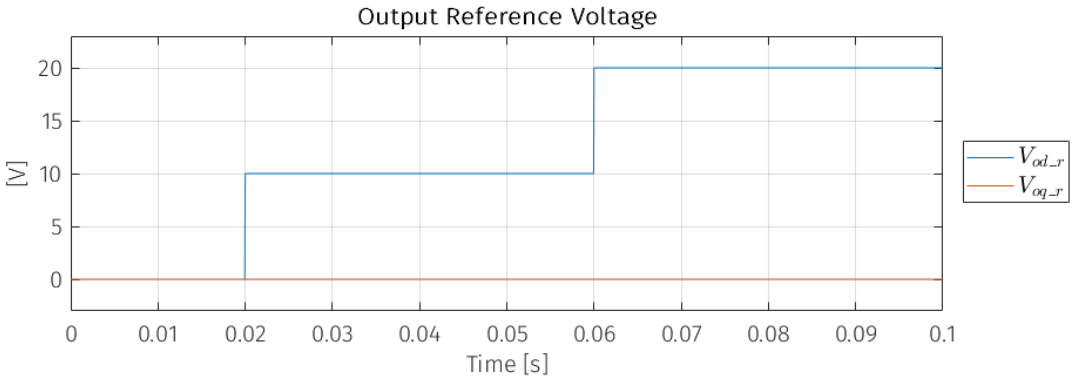

Figure 2.9: Output voltage reference

In Fig. 2.10 the comparison results are shown in dq reference frame sampling the measurement at the switching frequency T_s to eliminate the ripple and increase the graph readability.

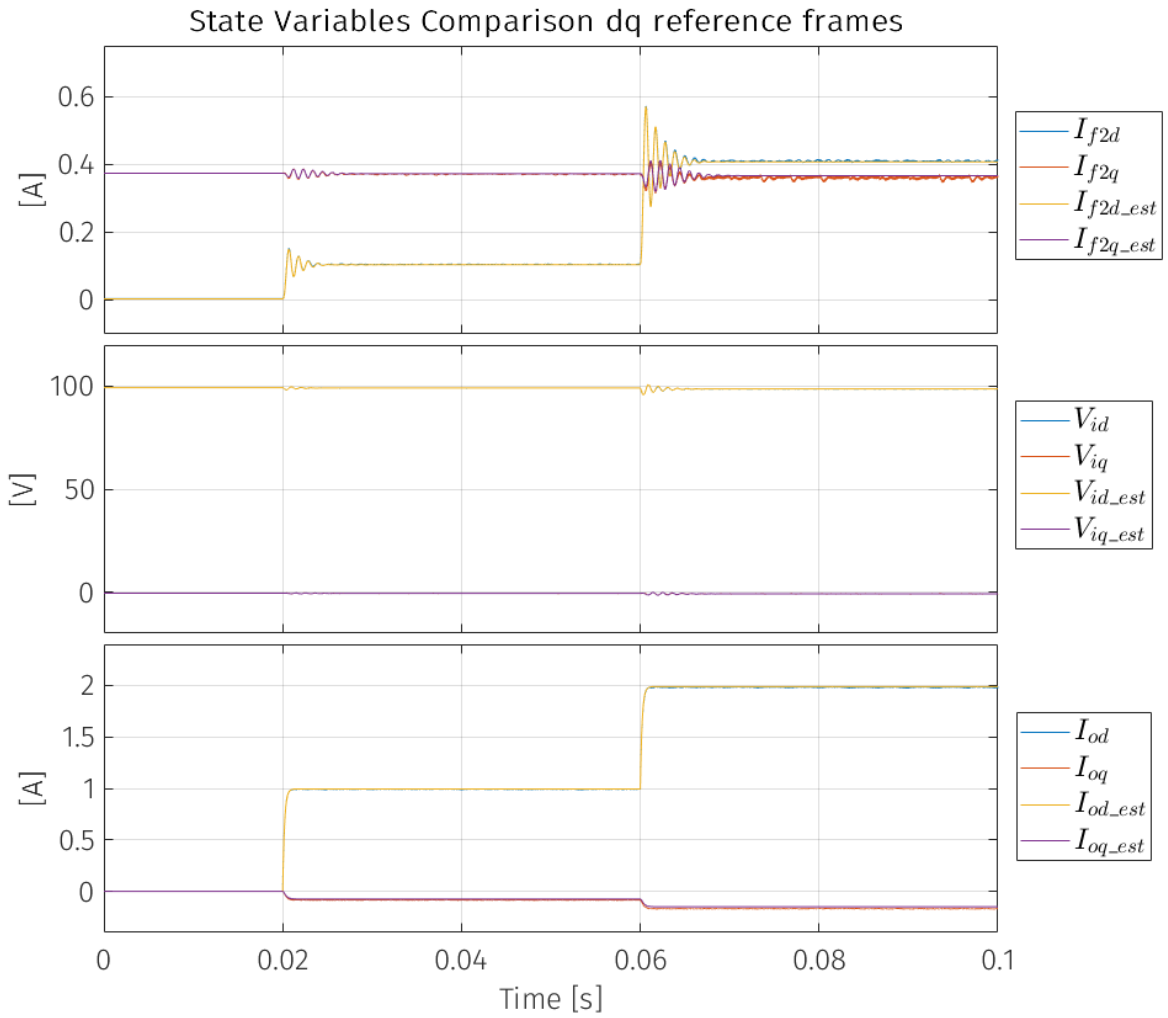

Figure 2.10: Simulator and Mathematical Model state variables behaviour comparison, sample time T_s

It is clear from this comparison that the mathematical model of the system reproduces the behaviour of the simulated system almost perfectly. In fact, except for the ripple on the output currents and some input oscillations due to switching, when the reference output voltage is varied in steps, the mathematical model and the simulated model show the same dynamic behaviour, with the same oscillation frequency and the same damping. This comparative simulation was useful to validate the mathematical model of the system, in particular the average model of the converter. From these results, it is then possible to use the mathematical model thus obtained to study the stability of the system. This will be analysed in the dedicated chapter. Fig. 2.11 shows the trends of the three-phase state variables of the simulated system with a sampling time of $T_s/10$. In this graph, the ripple on the output currents is visible and the ripple on

the input voltages begins to be visible. It is already evident that as the reference voltage increases, and thus the output power transmitted, the oscillations during the transient are higher.

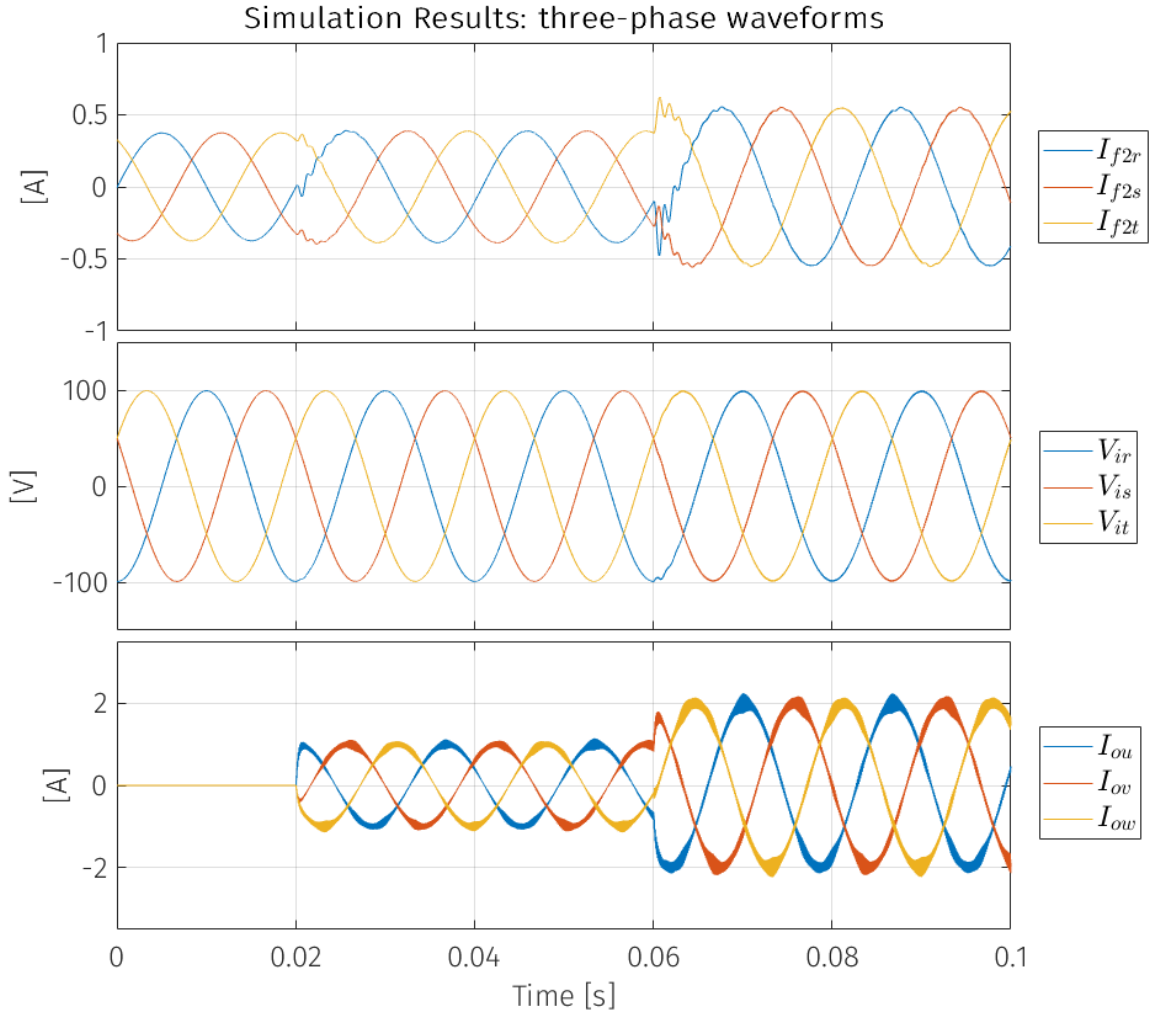

Figure 2.11: Simulator three-phase state variables behaviour, sample time $T_s/10$

2.6 PI regulators

Once the open-loop system has been defined, it is time to introduce a control algorithm. In fact, it will be necessary to dynamically control the output currents. In applications where the matrix converter is used, whether to drive electrical machines or an Active Front End (AFE) between two networks at different frequencies, it is necessary to control the output current in order to control the power flow. PI controllers are introduced for this purpose. A Proportional-Integral (PI) controller is a closed-loop con-

trol system that relies on feedback. This controller involves the calculation of an error value, which is determined by the difference between a reference value and the measured variable. The PI controller then uses a correction mechanism that combine both proportional and integral terms. The proportional term addresses the current error and provides a response proportional to the current deviation from the desired reference. At the same time, the integral term takes into account the accumulated historical error over time, providing a comprehensive approach to minimising long-term deviations between the reference and actual output. This combination of proportional and integral action enhances the controller's ability to provide accurate and stable control in dynamic systems. Moreover, this type of controller is able to cancel the steady state error between reference and measurement. In Fig. 2.12 a schematic of a PI controller is reported. As pre-

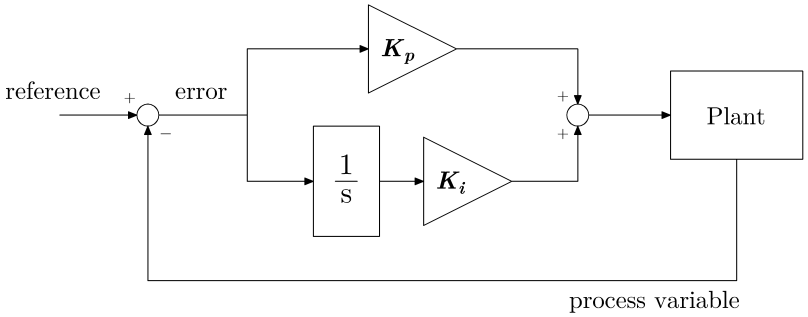

Figure 2.12: Proportional-Integral (PI) Controller schematic

viously mentioned, the PI controller is used to control the output current, this is possible by providing the correct V_{o_r} to the modulator such that the desired I_{o_r} is obtained at steady state. Unfortunately, the PI controller cannot function properly in the case of sinusoidal variables, but this is also why the dq transforms were introduced. In fact, two PI controller are used, one for each axes, in the output-side synchronous reference frame, and they provide the voltage reference vector $V_{o\_r}^{dq}$ as a function of the error between the current reference vector $I_{o\_r}^{dq}$ and the measured current vector I_o^{dq}.

2.6.1 Gains Tuning

In order for the PI controller to work properly, the gains has to be tuned correctly. The proportional gain K_p and the integral gain K_i depend strictly on the output model. In case of RL load the gains can be tuned starting from the transfer functions, in the dq reference frame, that describe the behaviour of the output current as a function of the

output reference voltage. To obtain the transfer function consider (2.63) in the Laplace domain:

$$\begin{aligned} sL_oI_{od} + R_o\,I_{od} &= V_{od\_r} + \omega_o\,L_o\,I_{oq} \\ sL_oI_{oq} + R_o\,I_{oq} &= V_{oq\_r} - \omega_o\,L_o\,I_{od} \end{aligned} \tag{2.72}$$

It is assumed that the converter is providing to the load exactly the reference voltage $V_{o\_r}^{dq}$. Transfer functions has to be calculated as the ratio of output variables to input variables on the same axis. For this purpose, decoupling terms are introduced.

$$\begin{aligned} U_{od\_r} &= V_{od\_r} + \omega_o\,L_o\,I_{oq} \\ U_{oq\_r} &= V_{oq\_r} - \omega_o\,L_o\,I_{od} \end{aligned} \tag{2.73}$$

This allows two separate transfer functions to be defined, one for the d-axis and one for the q-axis. The quantities U_{od_r} and U_{oq_r} are now considered as the output of the PI controller, but the link between the two axes is not lost. In fact, to obtain the desired dynamics of the system, it will be necessary to do the opposite operation to that presented in (2.73) and derive V_{od_r} and V_{oq_r} from U_{od_r} and U_{oq_r}. Then substituting (2.73) into (2.72) yields the following relations:

$$\begin{aligned} I_{od} &= H_{op}(s)\,U_{od\_r} \\ I_{od} &= H_{op}(s)\,U_{od\_r} \end{aligned} \tag{2.74}$$

Where:

$$H_{op}(s) = \frac{1}{sL_o + R_o} \tag{2.75}$$

The PI controller output can be defined as shown below:

$$\begin{aligned} U_{od\_r} &= K_p\,(I_{od\_r} - I_{od}) + \frac{K_i}{s}\,(I_{od\_r} - I_{od}) \\ U_{od\_r} &= K_p\,(I_{od\_r} - I_{od}) + \frac{K_i}{s}\,(I_{od\_r} - I_{od}) \end{aligned} \tag{2.76}$$

By substituting this relationship into (2.75), it is possible to obtain the transfer functions that describes the closed-loops dynamic.

$$I_{od} = H_{cl}(s)\, I_{od\_r}$$
$$I_{od} = H_{cl}(s)\, I_{od\_r} \tag{2.77}$$

Where:

$$H_{cl}(s) = \frac{\frac{s\,K_p + K_i}{L_o}}{s^2 + \frac{K_p + R_o}{L_o}\, s + \frac{K_i}{L_o}} \tag{2.78}$$

This transfer function is similar to the transfer function of the generic second-order system shown below.

$$G(s) = \frac{\omega_c^2}{s^2 + 2\,\xi\,\omega_c + \omega_c^2} \tag{2.79}$$

Where ξ represent the damping factor and ω_c the control bandwidth. The damping factor ξ describe the damping level in a dynamic system. If the damping factor is equal to zero, when a disturbance occur, the system oscillation continue indefinitely. If the damping factor is equal to one the system is critically damped, resulting in the quickest settling time achievable without any oscillations. All the values between zero and one results in oscillations that are gradually attenuated, while if the damping factor is bigger then one it result in slow dynamic. The control bandwidth ω_c is the range of frequencies within which a control system can operate efficiently and adapt to changes in the input signal. The only difference between the closed-loop transfer function is the zero at the transfer function numerator. It is possible to eliminate this zero by making a small modification to the PI controller. The modification is shown in the Fig. 2.13.

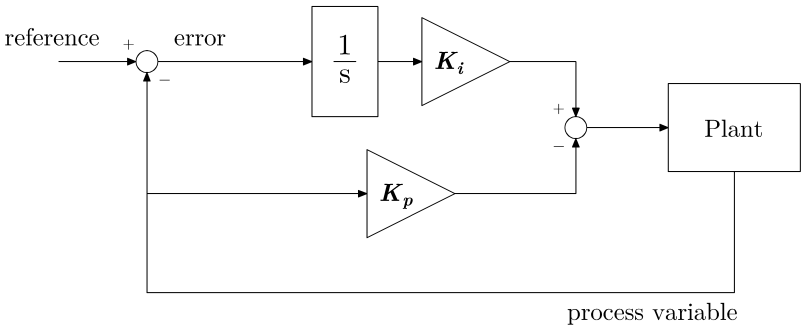

Figure 2.13: Modified PI Controller schematic

The modification consists in eliminating the contribution of the reference to the proportional term, this changes the relationships describing the outputs of the controller, and thus also vary the transfer function describing the closed-loop behaviour. The PI output are now:

$$\begin{aligned} U_{od\_r} &= -K_p\, I_{od} + \frac{K_i}{s}\,(I_{od\_r} - I_{od}) \\ U_{oq\_r} &= -K_p\, I_{oq} + \frac{K_i}{s}\,(I_{oq\_r} - I_{oq}) \end{aligned} \tag{2.80}$$

Which lead, together with (2.75), to the following transfer functions:

$$H_{cl}(s) = \frac{\dfrac{K_i}{L_o}}{s^2 + \dfrac{K_p + R_o}{L_o}\, s + \dfrac{K_i}{L_o}} \tag{2.81}$$

At this point, looking at the second-order dynamic system, it is possible to proceed by comparison and obtain gain values as a function of system parameters, damping factor and control bandwidth. The square of the control bandwidth in (2.79) is defined in (2.81) by:

$$\omega_c^2 = \frac{K_i}{L_o} \tag{2.82}$$

From which the integral gain K_i can be derived.

$$K_i = \omega_c^2\, L_o \tag{2.83}$$

Finally, comparing the values that multiply s in the denominators of both expressions, it is possible to calculate the proportional gain K_p.

$$K_p = 2\,\xi\,\omega_c\, L_o - R_o \tag{2.84}$$

Through this procedure, the gains of the PI controller can then be calculated such that the closed-loop transfer function actually presents the desired damping factor ξ and control bandwidth ω_c. Looking at the poles of the transfer function in Fig. 2.14, it is possible to see that the complex conjugate pole position is imposed as a function of ξ and ω_c.

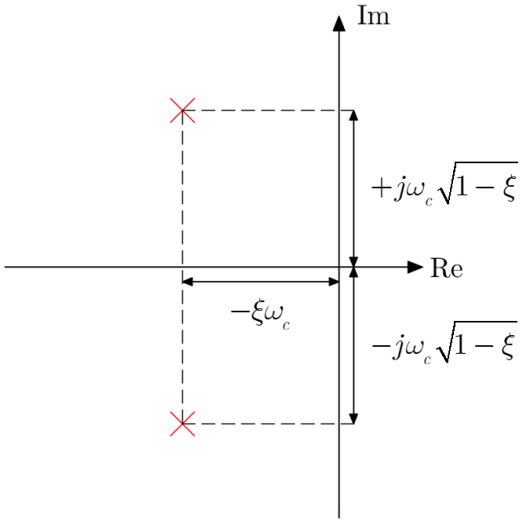

Figure 2.14: Closed-loop transfer function poles

However, there may be cases where, due to the selected damping factor, control bandwidth and system parameters, the gain calculation results in a negative K_p value. This is particularly the case when:

$$2\,\xi\,\omega_c\,L_o - R_o < 0 \tag{2.85}$$

Choosing the damping factor ξ equal to one, the inequality (2.85) gives:

$$\omega_c < \frac{R_o}{2\,L_o} \tag{2.86}$$

In this case, it is preferable to set the K_p value to zero and tune differently. Analysing the denominator of (2.81), if K_p is equal to zero, then the poles of the control system depend only on the value of K_i and, of course, on the parameters of the system.

$$s^2 + \frac{R_o}{L_o}\,s + \frac{K_i}{L_o} \tag{2.87}$$

Apparently, the possibility of imposing the damping factor has been lost, but it is still possible to impose the control bandwidth. From the (2.87), the poles of the system can be calculated as:

$$s_{1,2} = \frac{-\dfrac{R_o}{L_o} \pm \sqrt{\dfrac{R_o^2}{L_o^2} - \dfrac{4\,K_i}{L_o}}}{2} \tag{2.88}$$

Starting from this relationship, it is possible to impose the position at the dominant pole of the closed-loop system, as a function of K_i. In a transfer function, the dominant pole is the one closest to the imaginary axis, and its dynamics characterize the system. The dominant pole is therefore required to be real, negative and equal to the control bandwidth. Is demonstrable that the other pole will be real and negative as well, but further away from the imaginary axis and will not affect the dynamics of the transfer function. To impose the position to the dominant pole it is possible to start from the following equation:

$$-\omega_c = \frac{-\frac{R_o}{L_o} + \sqrt{\frac{R_o^2}{L_o^2} - \frac{4\,K_i}{L_o}}}{2} \tag{2.89}$$

The solution for K_i is:

$$K_i = \omega_c\,R_o - \omega_c^2\,L_o \tag{2.90}$$

In Fig. 2.15 the poles positioning with this procedure is shown.

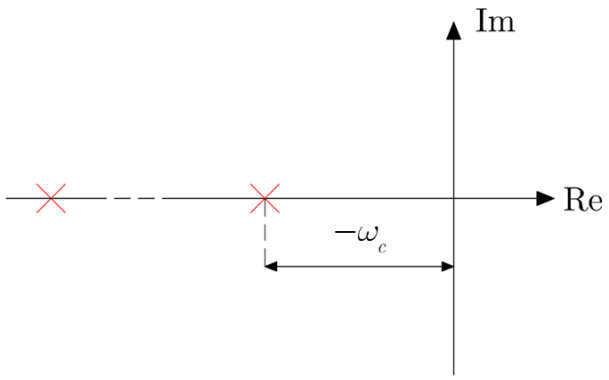

Figure 2.15: Closed-loop transfer function poles

In conclusion, the procedure for tuning the gains of PI controllers, assuming the damping factor ξ is one, can be summarised as follows:

$$\begin{cases} if \quad \omega_c < \dfrac{R_o}{L_o} \quad \rightarrow & \begin{matrix} K_p = 0 \\ K_i = \omega_c\,R_o - \omega_c^2\,L_o \end{matrix} \\ if \quad \omega_c \geq \dfrac{R_o}{L_o} \quad \rightarrow & \begin{matrix} K_p = 2\,\xi\,\omega_c\,L_o - R_o \\ K_i = \omega_c^2\,L_o \end{matrix} \end{cases} \tag{2.91}$$

Finally, a schematic of the output current control algorithm is shown in Fig. 2.16.

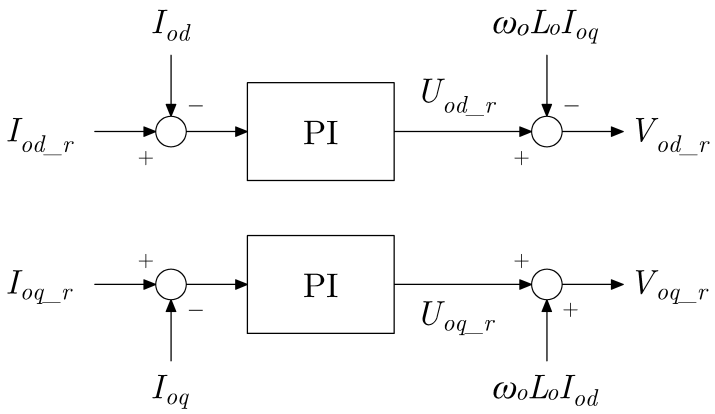

Figure 2.16: Current controller for RL load

In synthesis the output currents are transformed into the output synchronous reference frame and then fed back to the controller. The PI controller processes the error between the measure and the reference and generates the output U_{od_r} and U_{oq_r}, from which, through feedback, it is possible to obtain the output reference voltage $V_{o\_r}^{dq}$. Subsequently, this dq vector has to be anti-transformed to obtain the three-phase reference, which is then supplied to the modulator.

2.7 SM-PMSM

The matrix converter is a four-quadrant converter, this means that is able to move the power from the input-side to the output-side and vice versa. Unfortunately, the RL load only allows power to flow in one direction. To obtain a bidirectional power flow setup a SM-PMSM motor is applied to the output-side. SM-PMSM motor is a type of electric motor in which the permanent magnets are mounted on the surface of the rotor, facing outwards. This motor has been chosen because it is very easy to model and control. Using this motor slightly complicates the setup. In fact, knowing the angular position of the rotor is essential for correct modelling and control. The Park transform is used to define the interaction between the rotor and the stator, this is precisely why it was invented. To understand the modelization procedure consider Fig. 2.17.

The figure shows the cross-section of a three-phase SM-PMSM with a single poles pair.

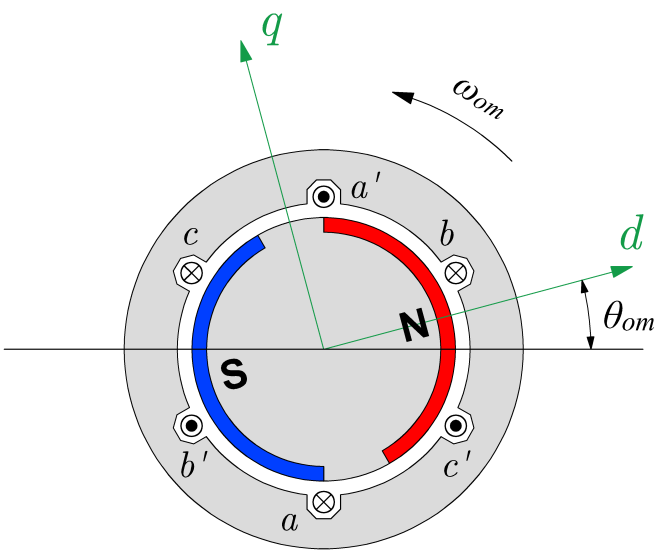

Figure 2.17: SM-PMSM relationship with the dq reference frame

A dq reference frame is introduced, its d-axis is oriented with the magnetic flux generated by the permanent magnets. To obtain torque on the rotor, it is necessary for the currents flowing in the three-phase windings of the stator to generate a magnetic flux vector with a component along the q-axis. When this magnetic flux is entirely along the q-axis, the torque is maximised in relation to the power supplied to the motor. This flux orientation, is made possible by the Park transformation, which allows the three-phase stator current that produce the magnetic flux, to be oriented as a function of θ_{om}, so that the desired magnetic flux can be obtained in the dq reference frame. θ_{om} is defined as the angle between the d-axis and the line representing the magnetic flux generated by the current flowing in the phase-a windings. As the rotor rotates, it generates an induced voltage at the ends of the stator terminals, which is defined in the reference dq on the q-axis of the stator voltage. This voltage, also known as back Electromotive Force (back EMF), is directly proportional to the rotor speed ω_{om} and to the magnetic flux generated by the permanent magnets, and opposes the voltage applied to the stator. Therefore, knowing the angle θ_{om} it is possible to control the torque supplied to the motor and to model the effects of the induced voltages on the stator. In the case of a single polar pair motor, the angle describing the mechanical rotation of the rotor and the angle describing the variation of the electrical quantities coincide. For machines with multiple polar pairs, it is sufficient to define the relationship between the mechanical angle and the electrical

angle.

$$\theta_{om} = \frac{\theta_o}{p} \tag{2.92}$$

Where p represent the number of pole pairs. The same relation can be applied to the mechanical and electrical angular frequency

$$\omega_{om} = \frac{\omega_o}{p} \tag{2.93}$$

Therefore, using the θ_o angle to orient the stator currents, it is possible obtain what has been stated before for the motor with a single polar pair. In the following study, the rotor angle is directly measured. Finally, the SM-PMSM model is reported in the following, the dq reference frame identified by θ_o.

$$\begin{aligned} \frac{d}{dt} I_{od} &= \frac{V_{od} - R_o I_{od}}{L_o} + \omega_o I_{oq} \\ \frac{d}{dt} I_{oq} &= \frac{V_{oq} - R_o I_{oq} - \omega_o \Phi_{PM}}{L_o} - \omega_o I_{od} \end{aligned} \tag{2.94}$$

Where Φ_{PM} represent the permanent magnets flux. The SM-PMSM model is simplified compared to that of the other electrical machines, since given the shape of the rotor, the reluctance of the magnetic circuits coupling stator and rotor do not vary as a function of the rotor position, which translates into the fact that a single inductance L_o can be defined for both axes d and q.

2.7.1 Bidirectional Power Flow

The SM-PMSM has been introduced to realize a bidirectional power flow load. In fact, an electric motor is by nature a reversible machine and can therefore make power flow in both directions. In other words, it can convert electrical power into mechanical power and vice versa. Assume that there is a system that can keep the speed of the SM-PMSM constant. A system that can therefore brake the SM-PMSM when it applies torque to the shaft and accelerate it when it applies negative torque. From the matrix converter point of view, this means that it can supply power to the motor or draw it freely. In simulation this can easily achieved just imposing the speed to the motor, while in the experimental setup it is necessary to design this system. Another SM-PMSM directly

connected to the first, whose control algorithm is designed to maintain a constant speed is used for this purpose. The motor connected to the matrix converter is referred to as SM-PMSM1, while the constant speed motor is referred to as SM-PMSM2. Both motor control strategies are explained below. It will be considered that for both, the angle at which to orientate the flow is known. It is important to note that SM-PMSM2 will not be considered when the complete mathematical model of the system will be presented. In fact, the mathematical model will only include the input filter, the matrix converter and the SM-PMSM1. It will simply be considered that the speed of the SM-PMSM1 motor is imposed. This simplification is legitimate if the torque control band of the SM-PMSM2, which will be presented later, is higher than the torque control band of the SM-PMSM1 motor.

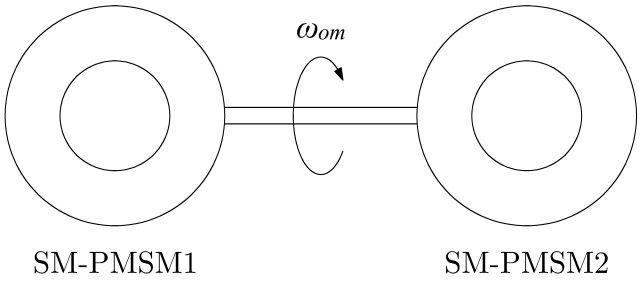

Figure 2.18: SM-PMSMs directly coupled

2.7.2 SM-PMSM1 Control Strategy

As anticipated, the SM-PMSM torque can be controlled by properly orienting the stator currents. This can be achieved if, starting from a current vector I_o^{dq}, the Park anti-transform is applied as a function of the angle θ_o, and the resulting currents are imposed to the stator windings. This control strategy is named Field Oriented Control (FOC). The relation between the stator current vector and torque is presented in the following:

$$T_e = \frac{3}{2} p \, \Phi_{PM} \, I_{oq} \tag{2.95}$$

Where T_e represent the torque generated by the motor. It is evident from the relationship that the torque produced depends solely on the q-axis component of the stator current. Providing a negative d-axis current can be useful if it is necessary to increase the mo-

tor speed without increase the module of the stator voltage applied. This technique is named flux weakening, and consists of reducing the magnetic flux on the d-axis, so as to reduce the back EMF. However, in the following dissertation this technique has not been used so I_{od} has been set to zero. The I_{oq} on the other hand, is allowed to vary freely to impose the desired torque, which will be negative in the case of a negative I_{oq} and positive in the case of a positive I_{oq}. I_{oq}, and consequently the torque, are imposed thanks to PI controllers, that provides the correct $V_{o\_r}^{dq}$ in order to obtain the desired $I_{o\_r}^{dq}$ vector. In the case of the SM-PMSM1, these are named current loops, since for the stability study it will be important to impose the currents supplied or absorbed by the motor in order to assess the power in transit. But for an SM-PMSM, the current control loop corresponds to the torque control loop, given the direct proportionality between these quantities. The gains tuning is similar to the one proposed for the RL load. Considering the SM-PMSM equation (2.94) in the Laplace domain:

$$\begin{aligned} sL_oI_{od} + R_o\,I_{od} &= V_{od\_r} + \omega_o\,L_o\,I_{oq} \\ sL_oI_{oq} + R_o\,I_{oq} &= V_{oq\_r} - \omega_o\,\Phi_{PM} - \omega_o\,L_o\,I_{od} \end{aligned} \tag{2.96}$$

In SM-PMSM case, the decoupling terms can be calculated by including the back EMF.

$$\begin{aligned} U_{od\_r} &= V_{od\_r} + \omega_o\,L_o\,I_{oq} \\ U_{oq\_r} &= V_{oq\_r} - \omega_o\,\Phi_{PM} - \omega_o\,L_o\,I_{od} \end{aligned} \tag{2.97}$$

In this way the resulting transfer function is the same obtained in the RL load case. So the gain tuning equations (2.91) shown for the RL load are also valid in the SM-PMSM case. As in the previous case, it will then be sufficient to add the decoupling terms and the back EMF compensation term to the PI output to obtain the desired dynamics, as shown in Fig. 2.19. The resulting control algorithm allows to flow the power in both direction just imposing the I_{oq_r} positive or negative. I_{od_r} is simply imposed to zero as stated before.

2.7.3 SM-PMSM2 Control Strategy

In addition to the current control, which this time imposes the reference torque, a speed control loop has also to be designed. The speed controller compare the speed reference ω_{o_r} with the actual ω_o and generate the torque reference T_{e_r}. The torque ref-

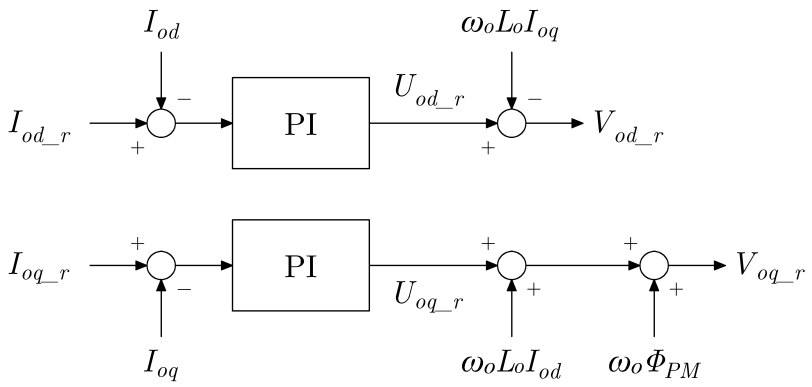

Figure 2.19: Current controller for SM-PMSM

erence is then applied to the q-axis current control loop by calculating the corresponding I_{oq_r} as follows:

$$I_{oq\_r} = \frac{2}{3} \frac{T_{e\_r}}{p\,\Phi_{PM}} \tag{2.98}$$

The speed control loop has to have significantly lower control bandwidth compared to the current loop. The speed loop gain tuning can be achieved starting from the differential equation of motion that describe the variation of the speed ω_o over time on no-load condition.

$$T_{e\_r} = B\,\omega_o + J\,\frac{d}{dt}\,\omega_o \tag{2.99}$$

Expressing this equation in the Laplace domain it is possible to obtain the following transfer function, which describes the behaviour of ω_o as a function of T_{e_r}.

$$\frac{\omega_o}{T_{e\_r}} = \frac{1}{sJ + B} \tag{2.100}$$

Where J represents the rotational inertia of the motor and B the viscous friction coefficient. In the bidirectional power flow setup the inertia and the viscous friction coefficient have to contain those of both the SM-PMSM, since they are directly coupled. Using a similar approach to that used for the RL load, with the modified PI controller shown in Fig. (??), the following relationships are obtained for tuning the speed PI controller as a

function of desired control bandwidth and ω_c and damping factor ξ:

$$\begin{cases} if \quad \omega_c < \dfrac{B}{J} \quad \rightarrow & \begin{matrix} K_p = 0 \\ K_i = \omega_c B - \omega_c^2 J \end{matrix} \\ if \quad \omega_c \geq \dfrac{B}{J} \quad \rightarrow & \begin{matrix} K_p = 2\,\xi\,\omega_c J - B \\ K_i = \omega_c^2 J \end{matrix} \end{cases} \tag{2.101}$$

2.8 Complete System Model with SM-PMSM

At this point, knowing the SM-PMSM model, the complete system model can be composed. Although, as seen, the SM-PMSM motor necessarily requires the introduction of a control algorithm for its operation, and the orientation of the quantities with respect to the rotor angle, it is still possible to define an open-loop model of the system, assuming the motor equations (2.94) defined in case of correct orientation. The control contribution to the system dynamics will be introduced in the next chapter when the closed-loop model is discussed. The input filter and the SM-PMSM equation are linked by the average model equation of the matrix converter. As stated before, the motor that keep the speed constant is not included in the model. In Fig. 2.20 a schematic of the complete system is reported and the system of equation that makes up the mathematical model of the setup is presented in the next page.

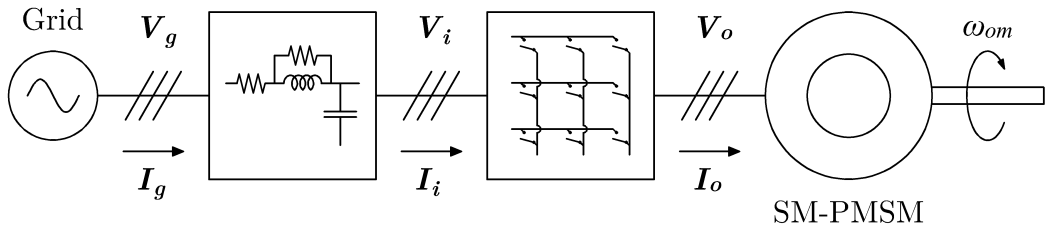

Figure 2.20: Complete system model with SM-PMSM

$$
\begin{cases}
\dfrac{d}{dt} I_{f2d} &= \dfrac{1}{L_f}\left(V_{gd} - R_{sf}\,\dfrac{V_{gd} - V_{id} + R_{pf}\,I_{f2d}}{R_{sf} + R_{pf}} - V_{id}\right) + \omega_i\, I_{f2q} \\[2ex]
\dfrac{d}{dt} I_{f2q} &= \dfrac{1}{L_f}\left(V_{gq} - R_{sf}\,\dfrac{V_{gq} - V_{iq} + R_{pf}\,I_{f2q}}{R_{sf} + R_{pf}} - V_{iq}\right) - \omega_i\, I_{f2d} \\[2ex]
\dfrac{d}{dt} V_{id} &= \dfrac{1}{C_f}\left(\dfrac{V_{gd} - V_{id} + R_{pf}\,I_{f2d}}{R_{sf} + R_{pf}} - \left(V_{od\_r} I_{od} + V_{oq\_r} I_{oq}\right)\,\dfrac{V_{id}\,cos\left(\phi_r\right) - V_{iq}\,sin\left(\phi_r\right)}{\left|\boldsymbol{V}_i^{\,dq}\right|^2\,cos\left(\phi_r\right)}\right) + \omega_i\, V_{iq} \\[2ex]
\dfrac{d}{dt} V_{iq} &= \dfrac{1}{C_f}\left(\dfrac{V_{gq} - V_{iq} + R_{pf}\,I_{f2q}}{R_{sf} + R_{pf}} - \left(V_{od\_r} I_{od} + V_{oq\_r} I_{oq}\right)\,\dfrac{V_{iq}\,cos\left(\phi_r\right) + V_{id}\,sin\left(\phi_r\right)}{\left|\boldsymbol{V}_i^{\,dq}\right|^2\,cos\left(\phi_r\right)}\right) - \omega_i\, V_{id} \\[2ex]
\dfrac{d}{dt}\, I_{od} &= \dfrac{V_{od\_r} - R_o\, I_{od}}{L_o} + \omega_o\, I_{oq} \\[2ex]
\dfrac{d}{dt}\, I_{oq} &= \dfrac{V_{oq\_r} - R_o\, I_{oq} - \omega_o\, \Phi_{PM}}{L_o} - \omega_o\, I_{od}
\end{cases}
\tag{2.102}
$$

2.9 Chapter Summary

In this chapter, all aspects of system modelling were examined. Initially, the transformations in the stationary and synchronous reference frame were illustrated. Subsequently, the procedure used to obtain the average model of the matrix converter was outlined. The modelling of the input filter and the RL load were then addressed. A complete model of the system was created by combining the filter model and the load model, joining them through the relationships of the converter average model. A simulation was then conducted to confirm the effectiveness of the modelling, focusing in particular on the average model. The proportional-integrative (PI) controllers were introduced, which will be used later, along with the gain tuning procedure. Next, the bidirectional load consisting of two SM-PMSM motors and their control strategies were presented. Finally, the system model including both the filter model and the bidirectional load model was presented.

References 2

[1] C. J. O'Rourke, M. M. Qasim, M. R. Overlin, and J. L. Kirtley, "A geometric interpretation of reference frames and transformations: dq0, clarke, and park," IEEE Transactions on Energy Conversion, vol. 34, no. 4, pp. 2070–2083, 2019.

[2] E. Clarke, Circuit Analysis of A-C Power Systems: Symmetrical and Related Components. No. v. 1 in Circuit Analysis of A-C Power Systems, Wiley, 1943.

[3] R. H. Park, "Two-reaction theory of synchronous machines generalized method of analysis-part i," Transactions of the American Institute of Electrical Engineers, vol. 48, no. 3, pp. 716–727, 1929.

Chapter 3:

Stability Issues and Stabilization Methods

As introduced in the previous chapter, the combination of the input filter model with the loads, through the relationships of the matrix converter average model, results in nonlinear systems. Various methodologies exist to study the stability of nonlinear systems, in general numerical simulation of nonlinear models are performed to evaluate the system behaviour. However, it is possible to approximate the system behaviour using the Small Signal Stability Analysis approach [1] that will be argued in the following chapter. Using the system model with the RL load as an example, it will be shown how to apply the small signal approach to obtain the state-space model of the open-loop system at a given steady-state operating point. Since the state-space system thus obtained only provides information of the open-loop system, and in application reality there is almost always an output current or power control loop, the state-space model of the closed-loop system will be realised by following the steps below. The open-loop state-space model will be discretized in order to integrate its equation with those of the discrete current controllers obtaining desired the closed-loop state-space system model. The stability of the closed-loop model will finally be studied through poles analysis and simulations to evaluate the system limits in term of power. A physical explanation of matrix converter instabilities will then be provided. Next, a stabilization method based on filtering the input voltages supplied to the modulator will be introduced. Through a procedure similar to the one above stabilizing effect in the closed-loop system will be evaluated as a function of transmitted power and control bandwidth. The results will be validated through simulations. Finally, the focus will move on to the analysis of the system with the bidirectional power flow load. A stabilization method to increase the transmittable power in both directions by varying the voltage output reference will be analysed. Also in this case its performance in terms of control bandwidth will be evaluated.

3.1 Small Signal Stability Analysis

Consider the generic non linear system model reported below:

$$\begin{aligned}
\dot{x}_1 &= f_1\left(x_1, x_2, ..., x_m, u_1, u_2, ..., u_n, d_1, d_2, ..., d_p\right); \\
\dot{x}_2 &= f_2\left(x_1, x_2, ..., x_m, u_1, u_2, ..., u_n, d_1, d_2, ..., d_p\right); \\
&\vdots \\
\dot{x}_3 &= f_3\left(x_1, x_2, ..., x_m, u_1, u_2, ..., u_n, d_1, d_2, ..., d_p\right)
\end{aligned} \tag{3.1}$$

The system of equations reported in (3.1) is composed of m equations and state variables, n reference input and p disturbance input. It can be rewritten in a more compact way, as follows:

$$\dot{\boldsymbol{x}} = \boldsymbol{f}\left(\boldsymbol{x},\, \boldsymbol{u},\, \boldsymbol{d}\right) \tag{3.2}$$

When the system described in (3.2) is in equilibrium, and thus the derivatives are zero, the system is said to be at steady-state, and can be expressed as follows:

$$0 = \boldsymbol{f}\left(\overline{\boldsymbol{x}},\, \overline{\boldsymbol{u}},\, \overline{\boldsymbol{d}}\right) \tag{3.3}$$

Where the overline indicate the steady-state values. If $\boldsymbol{x}$, $\boldsymbol{u}$ and $\boldsymbol{v}$ are close enough to $\overline{\boldsymbol{x}}$, $\overline{\boldsymbol{u}}$ and $\overline{\boldsymbol{d}}$ they can be defined as follows:

$$\boldsymbol{x} = \overline{\boldsymbol{x}} + \delta\boldsymbol{x}; \quad \boldsymbol{u} = \overline{\boldsymbol{u}} + \delta\boldsymbol{u}; \quad \boldsymbol{d} = \overline{\boldsymbol{d}} + \delta\boldsymbol{d} \tag{3.4}$$

And can thus be substituted into the (3.2):

$$\frac{d}{dt}\left(\overline{\boldsymbol{x}} + \delta\boldsymbol{x}\right) = \boldsymbol{f}\left(\overline{\boldsymbol{x}} + \delta\boldsymbol{x},\, \overline{\boldsymbol{u}} + \delta\boldsymbol{u},\, \overline{\boldsymbol{d}} + \delta\boldsymbol{d}\right) \tag{3.5}$$

Recalling what has been stated in (3.3) for the system at steady-state and using Taylor's expansion for multi-variable functions, (3.5) can be rewritten as follows:

$$\dot{\delta\boldsymbol{x}} = \overline{\boldsymbol{A}}\,\delta\boldsymbol{x} + \overline{\boldsymbol{B}}\,\delta\boldsymbol{u} + \overline{\boldsymbol{G}}\,\delta\boldsymbol{d} \tag{3.6}$$

Where $\overline{\boldsymbol{A}}$, $\overline{\boldsymbol{B}}$ and $\overline{\boldsymbol{G}}$ are the Jacobian matrices evaluated at steady state, reported in the following:

$$\overline{\boldsymbol{A}} = \left[\begin{array}{ccc} \dfrac{\partial f_1}{\partial x_1} & \cdots & \dfrac{\partial f_1}{\partial x_m} \\ \vdots & \ddots & \vdots \\ \dfrac{\partial f_m}{\partial x_1} & \cdots & \dfrac{\partial f_m}{\partial x_m} \end{array}\right]\Bigg|_{\overline{\boldsymbol{x}},\, \overline{\boldsymbol{u}},\, \overline{\boldsymbol{d}}} \tag{3.7}$$

$$\overline{\boldsymbol{B}} = \left[\begin{array}{ccc} \dfrac{\partial f_1}{\partial u_1} & \cdots & \dfrac{\partial f_1}{\partial u_n} \\ \vdots & \ddots & \vdots \\ \dfrac{\partial f_m}{\partial u_1} & \cdots & \dfrac{\partial f_m}{\partial u_n} \end{array}\right]\Bigg|_{\overline{\boldsymbol{x}},\, \overline{\boldsymbol{u}},\, \overline{\boldsymbol{d}}} \tag{3.8}$$

$$\overline{\boldsymbol{G}} = \left[\begin{array}{ccc} \dfrac{\partial f_1}{\partial d_1} & \cdots & \dfrac{\partial f_1}{\partial d_p} \\ \vdots & \ddots & \vdots \\ \dfrac{\partial f_m}{\partial d_1} & \cdots & \dfrac{\partial f_m}{\partial d_p} \end{array}\right]\Bigg|_{\overline{\boldsymbol{x}},\, \overline{\boldsymbol{u}},\, \overline{\boldsymbol{d}}} \tag{3.9}$$

The system is now linearized around the steady state point, and the stability of the system can be now evaluated by studying the eigenvalues of the matrix $\overline{\boldsymbol{A}}$. Caution is advised, however, as the stability analysis is only valid around the operating point identified by (3.3). If the steady-state point changes then it is necessary to recalculate the matrix $\overline{\boldsymbol{A}}$.

3.2 Stability Analysis Procedure: System with RL Load

3.2.1 Small Signal Approach Application

Consider the equations describing the system with load RL given in (2.69). The first step, necessary to apply the approach presented previously, is to evaluate all the system variables at steady state. This can be done solving the system of equations (2.70) in the following:

$$0 = \boldsymbol{f}\left(\boldsymbol{x}_{op},\, \boldsymbol{u}_{op},\, \boldsymbol{d}_{op}\right) \tag{3.10}$$

The system is composed of six equations, six state variables, two reference input and two system disturbance all represented in two different dq reference frame. The input-side dq frame will be considered oriented with the grid voltage, in particular the transform d-axis is considered aligned to the r-phase of the $\boldsymbol{V}_g$ vector. This implies that the d components of $\boldsymbol{V}_g^{dq}$ will be equal to module of the three-phase voltage $\boldsymbol{V}_g$, while the q components will be zero. The output-side reference frame, is obtained starting from the θ_o angle, that in simulation and in the experimental setup is simply calculated as a sawtooth function of time, where the slope corresponds to the angular frequency ω_o. All transform of the output variables are calculated by referring to this angle. The system of equation is solved imposing the grid voltage $\boldsymbol{V}_g^{dq}$ and the output current $\boldsymbol{I}_o^{dq}$, all the other quantities are considered unknowns of the system. The reason why the output current $\boldsymbol{I}_o^{dq}$ is imposed instead of the $\boldsymbol{V}_{od_r}^{dq}$ is that in the following a closed loop current control will be introduced, so it will be easier to adapt the algorithm that calculate the steady state variables. Actually, in terms of stability, there are no difference. In Tab. 3.4 the known and unknown variables are reported together with the system parameters.

Table 3.1: Known and Unknown System Variables

Known Variables	Unknown Varables	System Parameters
V_{gd}	I_{f2d}	L_f
V_{gq}	I_{f2q}	C_f
I_{od}	V_{id}	R_{pf}
I_{oq}	V_{iq}	R_{sf}
	V_{od_r}	R_po
	V_{oq_r}	L_o
		ω_i
		ω_o
		ϕ_r

Finally there are six equations and six unknowns, so it is possible to solve the system of equations. These calculations have been carried out using MATLAB, in particular the fsolve function. It is a nonlinear system solver that allows to find the solution of the steady state problem defined as in (3.11):

$$0 = \boldsymbol{g}(\boldsymbol{v}) \tag{3.11}$$

Where $\boldsymbol{g}$ reports the system of equations $\boldsymbol{f}$ written as a function of the vector of unknown variables $\boldsymbol{v}$, and where all known variables and system parameters have been substituted. Note that the ϕ_r is considered a parameter of the system, this is because it is not varied and remains constant. The fsolve algorithm is designed to minimise the value of the function $\boldsymbol{f}(\boldsymbol{v})$, starting from a vector of initial values $\boldsymbol{v}_0$ and converge to the solution of the system, assuming it exists. Once the steady-state problem has been solved, the values obtained can be applied, together with the known values, to the linearized matrices of the system $\overline{\boldsymbol{A}}_{op}$, $\overline{\boldsymbol{B}}_{op}$ and $\overline{\boldsymbol{G}}_{op}$ calculated with respect to the vectors x, u, and d are reported in the following page, while in the following the state variables vector x, the input vector u, and the disturbance vector d are reported:

$$\begin{aligned} \boldsymbol{x} &= \begin{bmatrix} I_{f2d} & I_{f2q} & V_{id} & V_{iq} & I_{od} & I_{oq} \end{bmatrix}^T \\ \boldsymbol{u} &= \begin{bmatrix} V_{od\_r} & V_{oq\_r} \end{bmatrix}^T \\ \boldsymbol{d} &= \begin{bmatrix} V_{gd} & V_{gq} \end{bmatrix}^T \end{aligned} \tag{3.12}$$

At this point it is sufficient to calculate the eigenvalues of the matrix $\overline{\boldsymbol{A}}_{op}$ to obtain information on the stability of the open-loop system in that specific steady-state point. This procedure is repeated iteratively, progressively increasing the I_{od} value of the output current, which allows the stability range of the system to be assessed as a function of the output current, and then as a function of the power value. I_{oq} will be set to zero, in order to simplify the iterative loop and to have in practice only one for loop. The phase of the voltages, and consequently that of the currents, does not influence the stability of the system, but only the power transmitted.

$$\overline{\boldsymbol{A}}_{op} = \begin{bmatrix} -\frac{R_{pf}\,Rsf}{L_f f\,(R_{pf}+R_{sf})} & \omega_i & \frac{R_{sf}}{L_f\,(R_{pf}+R_{sf})} - \frac{1}{L_f} & 0 & 0 & 0 \\ -\omega_i & -\frac{R_{pf}\,R_{sf}}{L_f\,(R_{pf}+R_{sf})} & 0 & \frac{R_{sf}}{L_f\,(R_{pf}+R_{sf})} - \frac{1}{L_f} & 0 & 0 \\ \frac{R_{pf}}{C_f\,(R_{pf}+R_{sf})} & 0 & -\frac{\sigma_1 + \frac{1}{R_{pf}+R_{sf}} - \frac{2\,\overline{V}_{id}\,\sigma_1\,\sigma_2}{cos\,(\phi_r)}}{C_f} & \omega_i + \frac{\sigma_1\,sin\,(\phi_r) + 2\,\overline{V}_{iq}\,\sigma_1\,\sigma_2}{C_f\,cos\,(\phi_r)} & -\frac{\overline{V}_{od\_r}\,\sigma_2}{C_f\,cos\,(\phi_r)} & -\frac{\overline{V}_{od\_r}\,\sigma_2}{C_f\,cos\,(\phi_r)} \\ 0 & \frac{R_{pf}}{C_f\,(R_{pf}+R_{sf})} & -\omega_i - \frac{\sigma_1\,sin\,(\phi_r) - 2\,\overline{V}_{id}\,\sigma_1\,\sigma_3}{C_f\,cos\,(\phi_r)} & -\frac{\sigma_1 + \frac{1}{R_{pf}+R_{sf}} - \frac{2\,\overline{V}_{iq}\,\sigma_1\,\sigma_3}{cos\,(\phi_r)}}{C_f} & -\frac{\overline{V}_{od\_r}\,\sigma_3}{C_f\,cos\,(\phi_r)} & -\frac{\overline{V}_{od\_r}\,\sigma_3}{C_f\,cos\,(\phi_r)} \\ 0 & 0 & 0 & 0 & -\frac{R_o}{L_o} & \omega_o \\ 0 & 0 & 0 & 0 & -\omega_o & -\frac{R_o}{L_o} \end{bmatrix} \tag{3.13}$$

$$\overline{\boldsymbol{B}}_{op} = \begin{bmatrix} 0 & 0 \\ 0 & 0 \\ -\dfrac{\overline{I}_{od}\,\sigma_2}{C_f\,cos\,(\phi_r)} & -\dfrac{\overline{I}_{oq}\,\sigma_2}{C_f\,cos\,(\phi_r)} \\ -\dfrac{\overline{I}_{od}\,\sigma_3}{C_f\,cos\,(\phi_r)} & -\dfrac{\overline{I}_{oq}\,\sigma_3}{C_f\,cos\,(\phi_r)} \\ \dfrac{1}{L_o} & 0 \\ 0 & \dfrac{1}{L_o} \end{bmatrix} \tag{3.14}$$

$$\overline{\boldsymbol{G}}_{op} = \begin{bmatrix} -\dfrac{R_{sf}}{L_f\,(R_{pf}+R_{sf})} - \dfrac{1}{L_f} & 0 \\ 0 & -\dfrac{R_{sf}}{L_f\,(R_{pf}+R_{sf})} - \dfrac{1}{L_f} \\ \dfrac{1}{C_f\,(R_{pf}+R_{sf})} & 0 \\ 0 & \dfrac{1}{C_f\,(R_{pf}+R_{sf})} \\ 0 & 0 \\ 0 & 0 \end{bmatrix} \tag{3.15}$$

Where:

$$\begin{aligned} \sigma_1 &= \frac{\overline{V}_{od\_r}\,\overline{I}_{od} + \overline{V}_{oq\_r}\,\overline{I}_{oq}}{\overline{V}_{id}^2 + \overline{V}_{iq}^2} \\ \sigma_2 &= \frac{\overline{V}_{id}\,cos\,(\phi_r) - \overline{V}_{iq}\,sin\,(\phi_r)}{\overline{V}_{id}^2 + \overline{V}_{iq}^2} \\ \sigma_3 &= \frac{\overline{V}_{iq}\,cos\,(\phi_r) + \overline{V}_{id}\,sin\,(\phi_r)}{\overline{V}_{id}^2 + \overline{V}_{iq}^2} \end{aligned} \tag{3.16}$$

The linearized system can then be written as follows. Note that δ are no longer reported in the equation, as in (3.6), because it is subtended that the system is valid around the steady-state point.

$$\dot{\boldsymbol{x}} = \overline{\boldsymbol{A}}_{op}\,\boldsymbol{x} + \overline{\boldsymbol{B}}_{op}\,\boldsymbol{u} + \overline{\boldsymbol{G}}_{op}\,\boldsymbol{x} \tag{3.17}$$

At this point, the next step is to calculate the closed-loop system model, since in the real applications there is almost always a control of the output quantities. For example, in the case of a converter interfacing two networks, it will be necessary to control the power exchange, or in the case of controlling a motor, it will be necessary to control the currents to deliver the torque required to impose the reference speed. PI controllers are then introduced and the stability of the system composed of the open-loop model of the system and the control has to be studied. Two PI controllers are introduced to control the output currents, one for d-axis currents and one for q-axis currents. These controllers are implemented on the Digital Signal Processor (DSP). This component fundamental to converter operation, each switching period receives the system measurements as input, through the PI calculates the reference voltages to be applied at the output and from these, through the modulation algorithm, calculates the duty-cycle matrix. The input data are then processed every switching period, which makes it necessary to redesign the PI controllers to operate in discrete time within the DSP. Since the PI are defined in discrete time, the previously calculated open-loop model, being defined in continuous time, cannot be integrated with discrete PI for the stability analysis. Discretization of the open-loop model is therefore necessary.

3.2.2 Linearized Model Discretization

Starting from the system defined in (3.18), it is possible to obtain a discrete-time state-space system equivalent while maintaining the dynamic in time domain. This is possible thanks to the discretization method known as Zero-Order Hold [1]. This method can be applied through the MATLAB command "c2d" by providing as input the continuous-time state-space system to discretize and the sampling time, which in this study corresponds to the switching period. Therefore,the discrete state-space model reported in the following is obtained:

$$\boldsymbol{x}\left(k+1\right)=\overline{\boldsymbol{\Phi}}_{op}\,\boldsymbol{x}\left(k\right)+\overline{\boldsymbol{\Gamma}}_{op}\,\boldsymbol{u}\left(k\right)+\overline{\boldsymbol{\Psi}}_{op}\,\boldsymbol{d}\left(k\right) \tag{3.18}$$

This model can be integrated with the equations describing the operation of discrete PI controllers in order to obtain the closed-loop state-space model.

3.2.3 Introduction of Discrete PI regulators

In the previous chapter, PI controllers and their tuning procedure were presented. For the following study, the tuning procedure presented is maintained, but the decoupling contributions are neglected as their contribution to the dynamics is minimal. The equations describing the output of PI controllers are:

$$\begin{aligned} V_{od\_r} &= -K_p\, I_{od} + \frac{K_i}{s}\,(I_{od\_r} - I_{od}) \\ V_{oq\_r} &= -K_p\, I_{oq} + \frac{K_i}{s}\,(I_{oq\_r} - I_{oq}) \end{aligned} \tag{3.19}$$

It is necessary to discretize the relationships so that they can be implemented in the DSP. Primarily, the relationship can be rewritten defining two state variables X_{id} and X_{iq} as follows:

$$\begin{aligned} sX_{id} &= (I_{od\_r} - I_{od}) \\ sX_{iq} &= (I_{oq\_r} - I_{oq}) \\ V_{od\_r} &= -K_p\, I_{od} + K_i\, X_{id} \\ V_{oq\_r} &= -K_p\, I_{oq} + K_i\, X_{iq} \end{aligned} \tag{3.20}$$

At this point, it is possible to proceed to the discretization using the Forward Euler method. Note that the Zero-Order Hold method was used to discretize the open-loop state-space model in order to maintain the system dynamic in the time domain. In this case Forward Euler is used to implement the controller integrators in the DSP, it is exactly these controllers that will interact with the system and whose closed-loop behavior one aims to understand. In the following the discretized PI relations:

$$\begin{aligned} X_{id}\,(k+1) &= X_{id}\,(k) + T_s\,(I_{od\_r} - I_{od}) \\ X_{iq}\,(k+1) &= X_{iq}\,(k) + T_s\,(I_{oq\_r} - I_{oq}) \\ V_{od\_r}\,(k) &= -K_p\, I_{od}\,(k) + K_i\, X_{id}\,(k) \\ V_{oq\_r}\,(k) &= -K_p\, I_{oq}\,(k) + K_i\, X_{iq}\,(k) \end{aligned} \tag{3.21}$$

At this point, an important application detail must be introduced, namely the delay in the application of references. In fact, the DSP every switching period performs the following functions:

- Application of the duty-cycle calculated in the previous step;
- Measurements acquire;
- Calculation of the voltage references to be applied at the next step;
- Calculation of the duty-cycle to be applied at the next step

Thus, as can be deduced, the reference voltage that is calculated is applied at the next instant through duty-cycles. The voltage that is applied at each instant is thus affected by a delay of one switching period. So the output of the controllers, which will be the input of the system, can be written as:

$$\begin{aligned} V_{od\_r}^{d}\left(k+1\right) &= V_{od\_r}\left(k\right) \\ V_{oq\_r}^{d}\left(k+1\right) &= V_{od\_r}\left(k\right) \end{aligned} \tag{3.22}$$

It is then possible to rewrite the equations of the PI controller through 4 difference equations, thus defining 4 state variables.

$$\begin{aligned} X_{id}\left(k+1\right) &= X_{id}\left(k\right) + T_s\left(I_{od\_r} - I_{od}\right) \\ X_{iq}\left(k+1\right) &= X_{iq}\left(k\right) + T_s\left(I_{oq\_r} - I_{oq}\right) \\ V_{od\_r}^{d}\left(k+1\right) &= -K_p\, I_{od}\left(k\right) + K_i\, X_{id}\left(k\right) \\ V_{oq\_r}^{d}\left(k+1\right) &= -K_p\, I_{oq}\left(k\right) + K_i\, X_{iq}\left(k\right) \end{aligned} \tag{3.23}$$

3.2.4 Closed-loop State Space Model

To realise the state-space model of the closed-loop system, it is necessary to integrate the relations of the linearized open-loop model with those of the control. To do this, the vector of state variables, inputs and disturbances must be redefined. Please note that the grid voltage vector has been considered as disturbance, only to consider it separately from the active inputs, so those on which the control acts. The vector are defined as

follows:

$$\boldsymbol{x}_{cl}(k) = \begin{bmatrix} I_{f2d}(k) \\ I_{f2q}(k) \\ V_{id}(k) \\ V_{iq}(k) \\ I_{od}(k) \\ I_{oq}(k) \\ X_{id}(k) \\ X_{iq}(k) \\ V^{d}_{od\_r}(k) \\ V^{d}_{od\_r}(k) \end{bmatrix}; \quad \boldsymbol{u}_{cl}(k) = \begin{bmatrix} I_{od\_r}(k) \\ I_{od\_r}(k) \end{bmatrix}; \quad \boldsymbol{d}_{cl}(k) = \begin{bmatrix} V_{gd}(k) \\ V_{gq}(k) \end{bmatrix} \tag{3.24}$$

The PI controller relations in (3.23) can be rewritten as a function of these vectors as follows:

$$\begin{bmatrix} X_{id}(k+1) \\ X_{iq}(k+1) \\ V^{d}_{od\_r}(k+1) \\ V^{d}_{od\_r}(k+1) \end{bmatrix} = \boldsymbol{A}_c\, \boldsymbol{x}_{cl}(k) + \boldsymbol{B}_c\, \boldsymbol{u}_{cl}(k) \tag{3.25}$$

Where:

$$\boldsymbol{A}_c = \begin{bmatrix} 0 & 0 & 0 & 0 & -T_s & 0 & 1 & 0 & 0 & 0 \\ 0 & 0 & 0 & 0 & 0 & -T_s & 0 & 1 & 0 & 0 \\ 0 & 0 & 0 & 0 & -K_p & 0 & K_i & 0 & 0 & 0 \\ 0 & 0 & 0 & 0 & 0 & -K_p & 0 & K_i & 0 & 0 \end{bmatrix}; \qquad \boldsymbol{B}_c = \begin{bmatrix} T_s & 0 \\ 0 & T_s \end{bmatrix} \tag{3.26}$$

At this point, the closed-loop state-space model can be composed by merging the linearized open-loop state-space model matrices with those of the control just obtained. Remember that now the input vector of the open-loop system is part of the state vari-

ables.

$$\boldsymbol{x}_{cl}\left(k+1\right)=\overline{\boldsymbol{A}}_{cl}\,\boldsymbol{x}_{cl}\left(k\right)+\overline{\boldsymbol{B}}_{cl}\,\boldsymbol{u}_{cl}\left(k\right)+\overline{\boldsymbol{G}}_{cl}\,\boldsymbol{d}_{cl}\left(k\right) \tag{3.27}$$

With:

$$\overline{\boldsymbol{A}}_{cl}=\begin{bmatrix}\begin{bmatrix}\overline{\boldsymbol{\Phi}}_{op}\end{bmatrix}_{6\times 6} & \begin{bmatrix}\boldsymbol{0}\end{bmatrix}_{6\times 2} & \begin{bmatrix}\overline{\boldsymbol{\Gamma}}_{op}\end{bmatrix}_{6\times 2}\\ \begin{bmatrix} & \boldsymbol{A}_c & \end{bmatrix}_{4\times 10}\end{bmatrix};\qquad \begin{aligned}\overline{\boldsymbol{B}}_{cl}&=\boldsymbol{B}_c;\\ \overline{\boldsymbol{G}}_{cl}&=\overline{\boldsymbol{\Psi}}_{op}\end{aligned} \tag{3.28}$$

It is now possible to study the eigenvalues of $\overline{\boldsymbol{A}}_{cl}\in\mathbb{R}^{10\times 10}$ to obtain information on the stability of the system.

3.2.5 Continuous time and Discrete time Stability Analysis

Consider the following state-space model defined in continuous time.

$$\dot{\boldsymbol{x}}=\boldsymbol{A}\boldsymbol{x}+\boldsymbol{B}\boldsymbol{u} \tag{3.29}$$

From the matrix $\boldsymbol{A}\in\mathbb{R}^{n\times n}$, by calculating the eigenvalues, n poles can be calculated. These poles can then be represented in the s-plane, and the stability of the system can be calculated as a function of their position. In particular, if one of the pole is to the right of the imaginary axis, the system is unstable. This is because the coordinates of the poles of the system correspond to the parameters of the solution of the differential equations that make up the state space system. In particular, the real part is linked to the exponential component of the solution, from which it is possible to calculate the convergence or divergence of the solution and thus the stability or instability of the system. If the exponent of the solution is greater than zero, the resulting function will increase and tend to infinity, and so it will diverge, whereas if it is less than zero, it will tend to zero and thus converge. Finally, the poles imaginary components define whether the system will diverge or converge with a certain oscillation. Now consider instead the following discrete state-space system:

$$\boldsymbol{x}\left(k+1\right)=\boldsymbol{\Phi}\,\boldsymbol{x}\left(k\right)+\boldsymbol{\Gamma}\,\boldsymbol{u}\left(k\right) \tag{3.30}$$

This system is made up of difference equations. While the Laplace Transform is used to transform differential equations into algebraic equations, the Z-Transform is used for difference equations. The combination of the difference equation coefficients in this case is represented by the eigenvalues of the matrix $\mathbf{\Phi} \in \mathbb{R}^{n \times n}$. These poles can be represented in the z plane, and as for continuous-time systems in the s-plane, through their position it is possible to evaluate the stability of the system. In the case of the z-plane, the poles of the system must lie within the circle of unit radius with centre in the origin of the axes to ensure stability. This can be intuitively understood by considering a single differential equation.

$$x\left(k+1\right) = \alpha\, x\left(k\right) + \beta\, u\left(k\right) \tag{3.31}$$

If $|\alpha| > 1$ the difference equations tends to infinity, so it diverges, while if $|\alpha| < 1$ converges. The poles obtained by calculating the eigenvalues allow to obtain the combined behaviour of the difference equations that make up the system. In Fig. 3.1 a comparison of the stability region in s-plane and z-plane is shown.

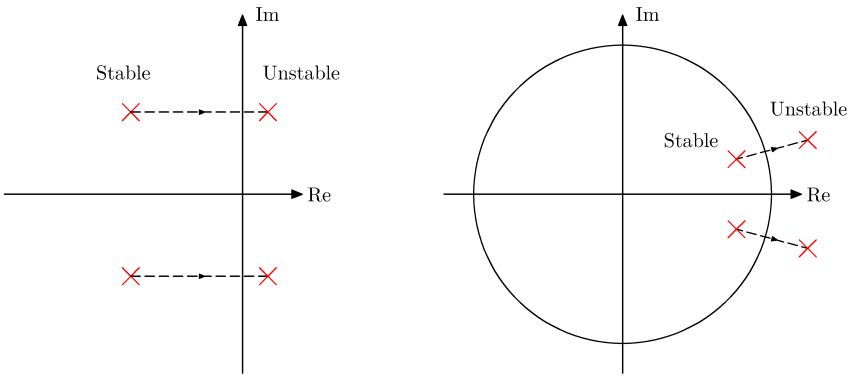

Figure 3.1: s-plane and z-plane stability region

3.2.6 Stability Analysis of Closed-Loop System with RL load

It was shown how to obtain the linearized state-space system of the open-loop system for a defined value of current I_{od}, and thus power, and its discretization. Subsequently, the controllers were introduced in discretized form and their relationships were used to compose the linearized state-space system in closed loop. At this point, the stability region analysis can be carried out. The steps to be followed to obtain the estimate

of the stability region are the following:

1. Solve the system steady-state problem imposing the desired I_{od};
2. Substitute the steady-value thus obtained in the linearized matrix $\overline{\boldsymbol{A}}_{op}$, $\overline{\boldsymbol{B}}_{op}$ and $\overline{\boldsymbol{G}}_{op}$;
3. Discretize the system through the Zero-Order Hold method;
4. Compose the closed-loop state-space system integrating PI controllers;
5. Calculate the $\overline{\boldsymbol{A}}_{cl}$ eigenvalues;
6. Study the stability checking the eigenvalues position.

Below is an example of the study of the eigenvalues of the matrix $\overline{\boldsymbol{A}}_{cl}$ as the I_{od} current varies. The system variables and parameters used are given in the Tab. 3.2, while the controller parameters are reported in Tab. 3.3.

Table 3.2: System Variables and Parameters

System Variables			System Parameters		
V_{gd}	100	V	L_f	2.4	mH
V_{gq}	0	V	C_f	12	μF
I_{oq_r}	0	A	R_{pf}	200	Ω
			R_{sf}	1.5	Ω
			R_o	10	Ω
			L_o	2	mH
			ω_i	$2\,\pi\,50$	$\frac{rad}{s}$
			ω_o	$2\,\pi\,60$	$\frac{rad}{s}$
			ϕ_r	0	rad

Table 3.3: Control Parameters

Control Parameters		
ω_c	$2\,\pi\,1000$	$\frac{rad}{s}$
ξ	1	
K_p	15.3	
K_i	78957	

In the following page, Fig. 3.3 shows the poles in the z-plane in the case of $I_{od} = 2A$. As can be easily understood the system is stable in this condition. In the same figure, an enlargement of the plot around the poles is shown, allowing for their enumeration. This is useful for keeping track of them as the current I_{od} and, consequently, the power vary. In Fig. 3.4 the variation of the pole coordinates with respect to the current I_{od} is shown. It can be seen that of the 10 poles of the system, only 4 vary as the current changes. The other 6 remain in the same position, which is why only the pole corresponding to $4A$ is visible, because they overlap. The dashed black line indicates the trajectory followed by the poles as the current changes, while the poles corresponding to certain current values are shown for ease of understanding. Looking at Poles 1 and 2, it can be seen that for $I_{od} = 3.7A$, they are crossing the unit circle, that is the limit of stability, beyond which the system is unstable. Pole 3 and 4 moves inside the unit circle without affecting the system stability. Poles 5 to 10 doesn't change as stated before. The system schematic is reported in Fig. 3.2.

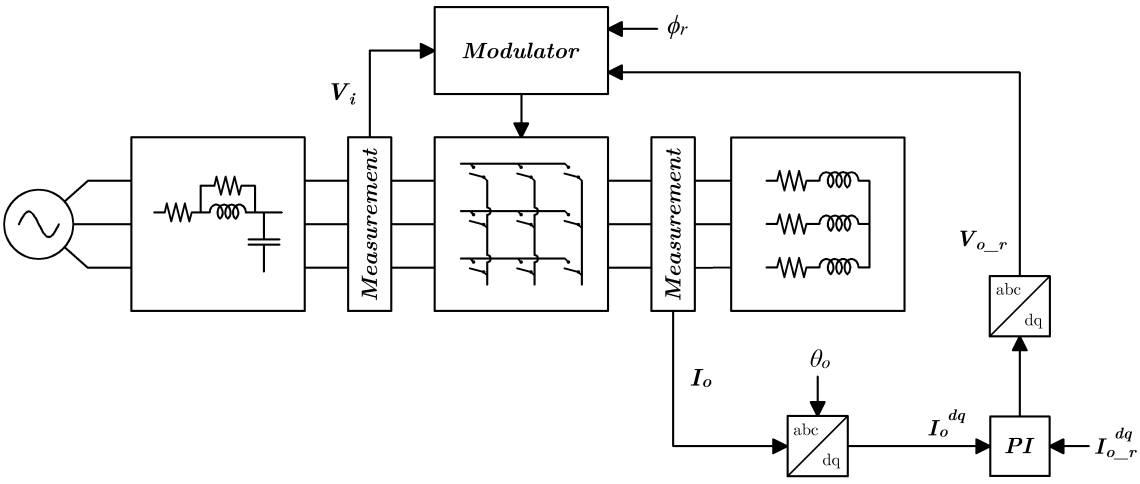

Figure 3.2: Closed-loop system with RL load

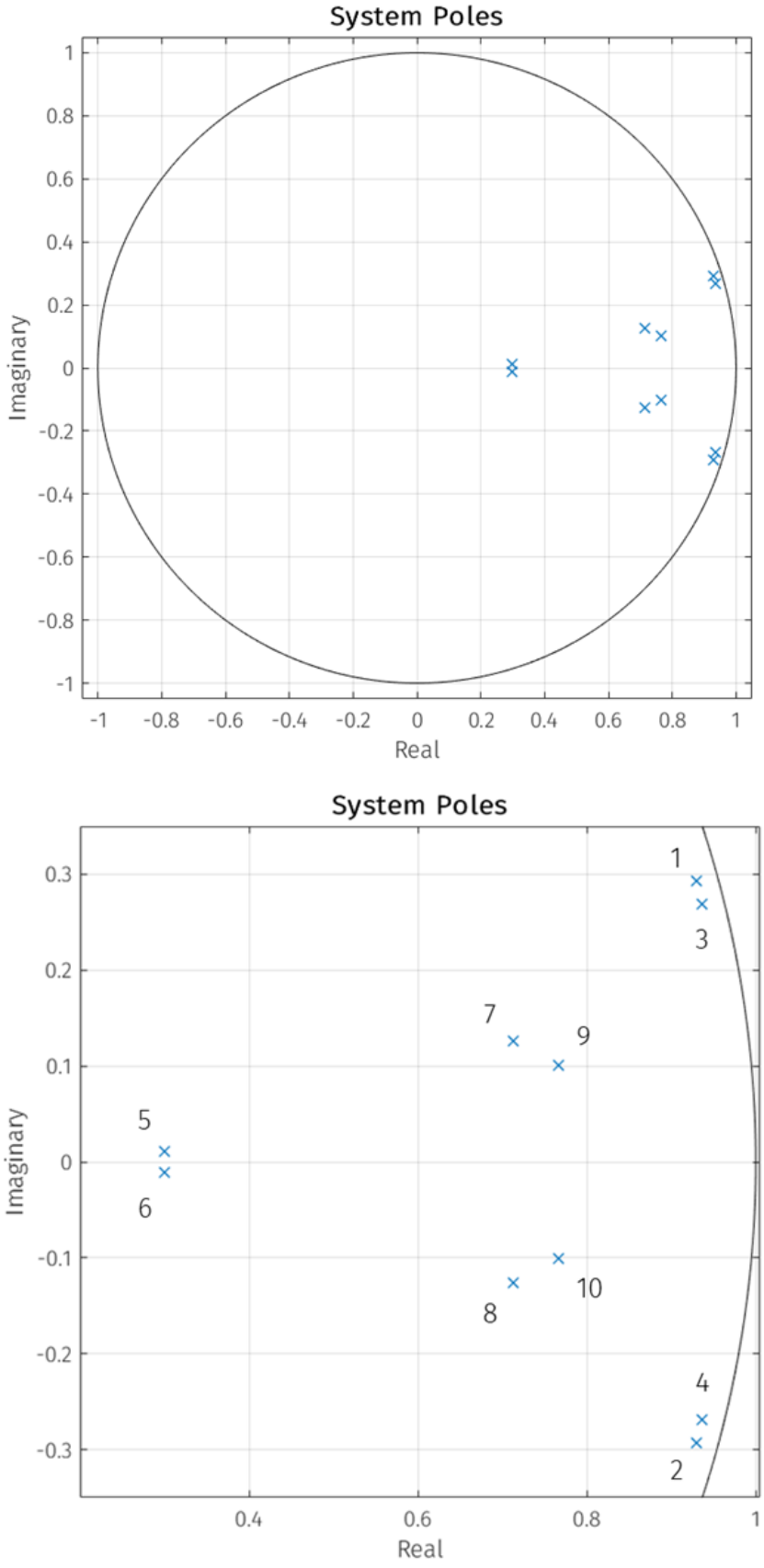

Figure 3.3: Closed loop pole with $I_{od_r} = 2A$

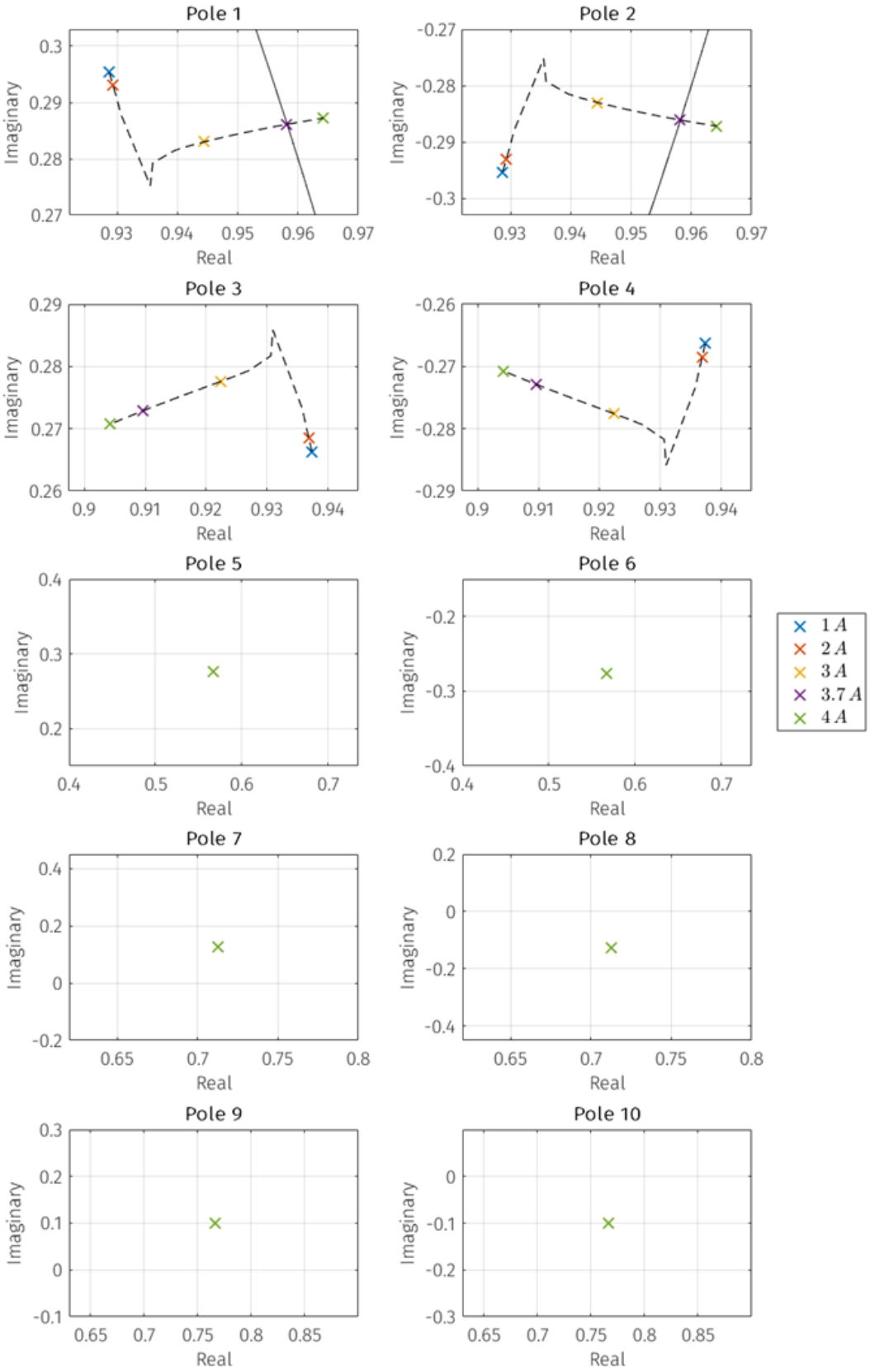

Figure 3.4: Closed loop pole as the output current increase

3.2.7 Simulations Results with RL load

Using MATLAB Simulink, simulations of the closed-loop system described above were carried out. The simulator consists of a power supply network, the input filter, schematized as shown in Chapter 1, the matrix converter, composed by the 9 bidirectional switches, and the RL load. The modulation algorithm and the discrete PI controllers are implemented as well. The simulation is carried out using the parameters shown in the Tab. 3.2 and 3.3. Below in Fig. 3.5 are presented the results in the input and output dq reference frame obtained by increasing in steps the current reference I_{od_r} until instability is reached.

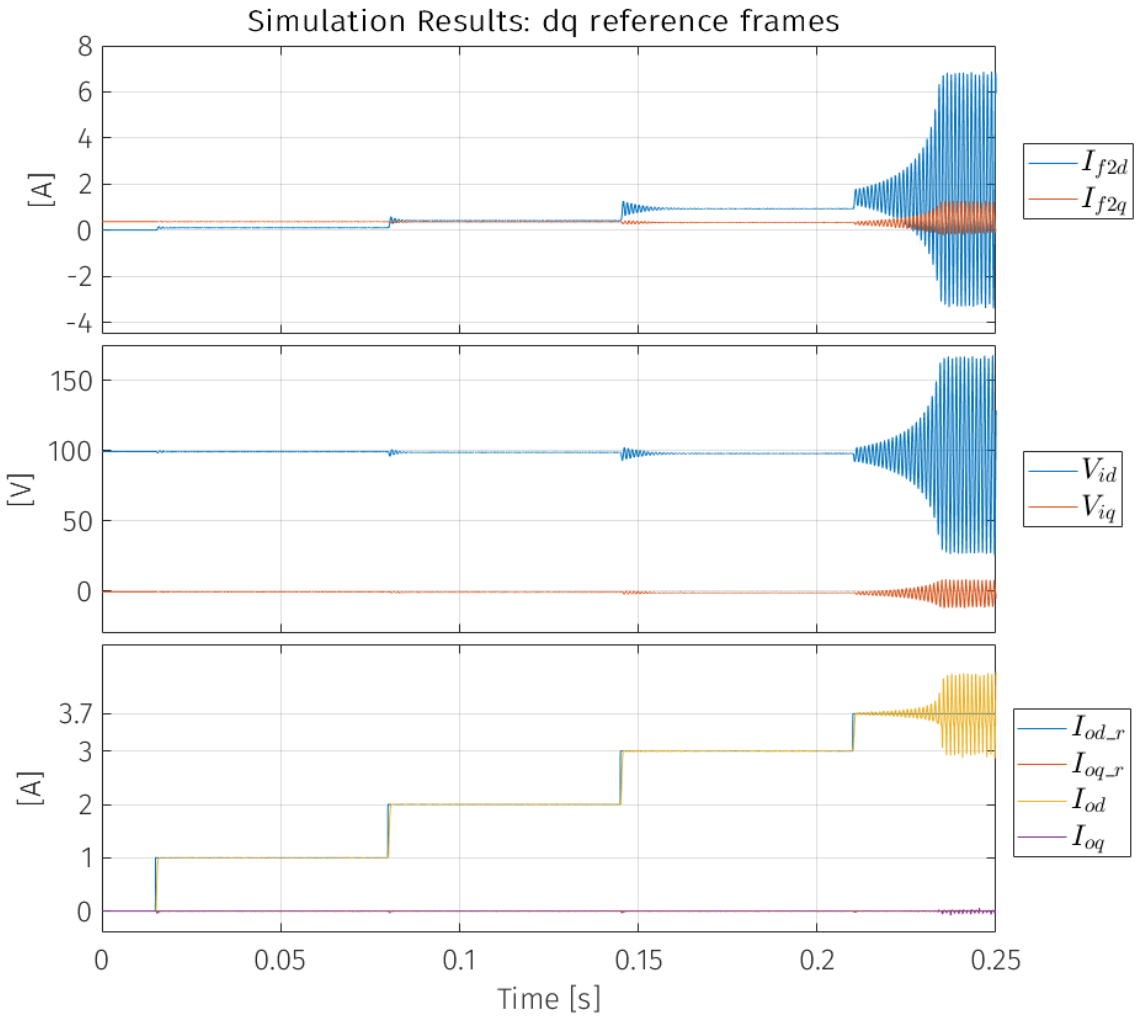

Figure 3.5: Simulations result in the input and output dq reference frame as I_{od_r} increases, sample time T_s

Note that the value given for the system variables refer to values on the dq axes. This

means that their modulus refers to the peak value. The Root-Mean-Square (RMS) value of the system quantity can be calculated just dividing the module of each dq vector by $\sqrt{3}$. Observe how with each step increase in the reference current, the settling time on the reference increases, until the system becomes unstable at $I_{od_r} = 3.7\,A$. The increase in settling time is due to the progressive approach to the unit circle. The system is therefore unstable at the point predicted by the pole study. The three-phase variables are reported in Fig. 3.6. Before instability, when the output current reaches its reference, the input waveform are sinusoidal.

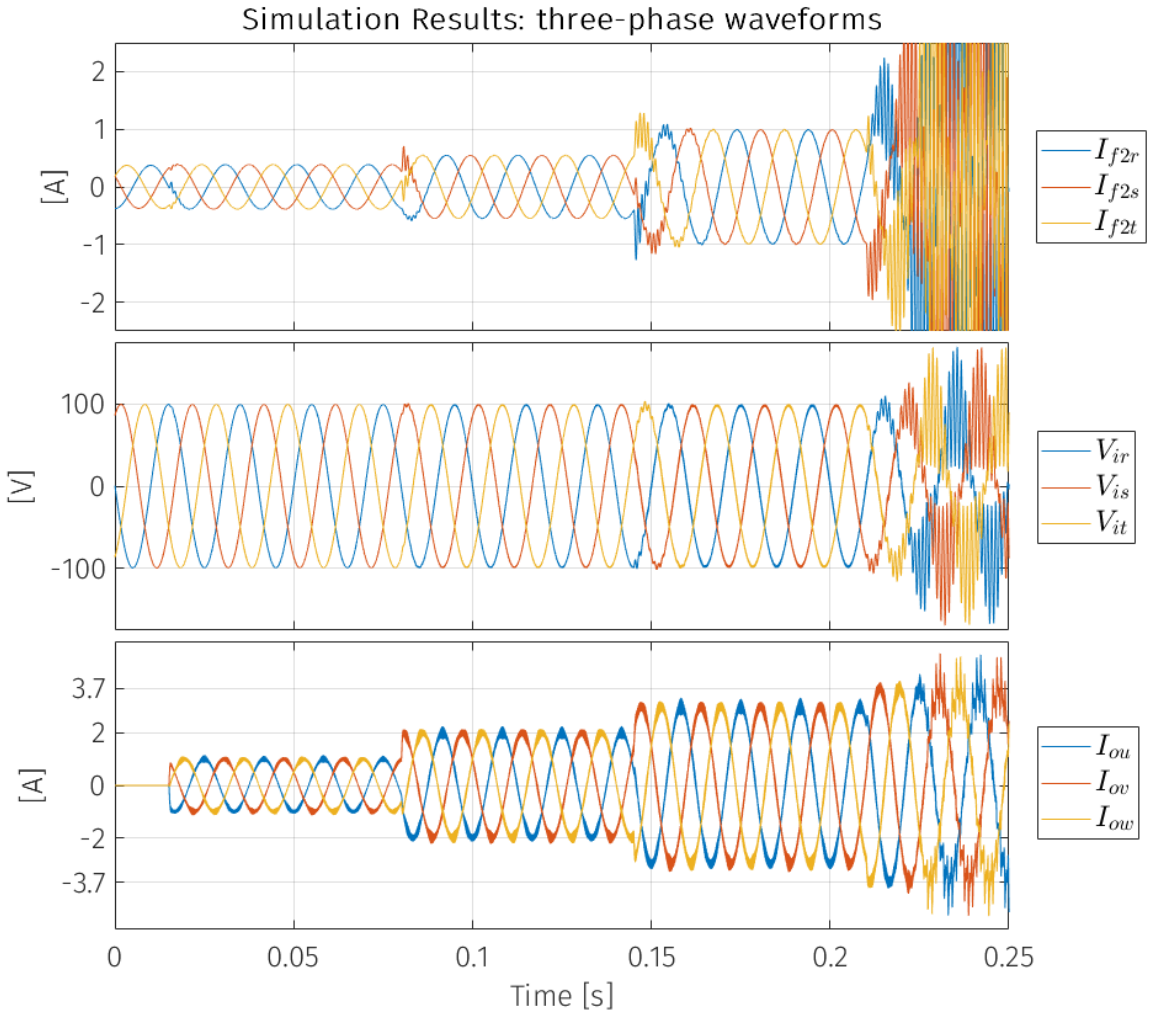

Figure 3.6: Three-Phase waveforms as I_{od_r} increases, sample time $T_s/10$

This is due to the action of the filter whose design minimises harmonic content. The same applies to the output currents, which, as a result of the presence of a high output resistance and inductance, are perfectly sinusoidal The power supplied to the load that triggers the instabilities is therefore $205.35\,W$.

3.2.8 Instability Phenomena, a physical explanation

The source of instability is the resonant nature of the filter. When the input current to one phase of the converter is positive, the voltage across the corresponding filter capacitor drops, while when the current is negative, the voltage rises. Below the stability threshold, the voltage oscillation is not significant and is compensated by the grid voltage, which, due to the resulting voltage difference, supplies not only the load current but also the current required to damp the fluctuations. Unfortunately, the dynamic of this current, which can be called 'stabilizing', is limited by the value of the filter inductance. Above the stability threshold, the dynamics of the 'stabilising' current is no longer able to compensate for the magnitude of the disturbance caused by the input current, and instability occurs. Therefore, the values that most influence the stability of the converter are the inductance value and the grid voltage. By doubling the mains voltage, for example, and repeating the process described above, the maximum deliverable output current is around $7.4\,A$ so the double that the previous case. The purpose of this study, however, is to investigate stabilization methods, so it is necessary to keep the converter in its worst condition. For this reason, an unusual value of grid voltage of approximately $70\,V_{rms}$ ($100\,V$ peak) was chosen.

3.3 Stabilization Method: Filter on Input Voltage Measurement

A first stabilization method was proposed in [2] and [3] and consist of applying a low-pass filter (LPF) to the input voltage measurement supplied to the modulation algorithm. This filter can be implemented in the input dq reference frame as follows:

$$\begin{aligned} V_{ifd} &= \frac{1}{s\,\tau + 1}\,V_{id} \\ V_{ifq} &= \frac{1}{s\,\tau + 1}\,V_{iq} \end{aligned} \tag{3.32}$$

With

$$\tau = \frac{1}{2\,\pi\,f_{cut\_LPF}} \tag{3.33}$$

The variables V_{ifd} and V_{ifq} are thus obtained, which together make up the vector $\boldsymbol{V}_{if}^{dq}$. This vector needs to be anti-transformed in the abc domain to derive the three-phase vector $\boldsymbol{V}_{if}$ which is then provide to the modulator. This means that the duty-cycle matrix $\boldsymbol{M}$ is now evaluated from these voltage vector. The following relationships are therefore valid:

$$\begin{aligned} \boldsymbol{V}_{o\_r} &= \boldsymbol{M}\,\boldsymbol{V}_{if} \\ \boldsymbol{I}_{i} &= \boldsymbol{M}\,\boldsymbol{I}_{o} \end{aligned} \tag{3.34}$$

At the input of the converter, however, there are voltages defined by the vector V_i. This means that due to the presence of the LPF there will be a difference between the output voltage reference $\boldsymbol{V}_{o\_r}$ and the actual output voltage $\boldsymbol{V}_{o}$. The actual output voltage is defined by:

$$\boldsymbol{V}_{o} = \boldsymbol{M}\,\boldsymbol{V}_{i} \tag{3.35}$$

To evaluate the difference between $\boldsymbol{V}_{o\_r}$ and $\boldsymbol{V}_{o}$, consider the following power balance:

$$\frac{3}{2}\,|\boldsymbol{V}_{if}|\,|\boldsymbol{I}_{i}|\,cos\,(\phi_r) = \frac{3}{2}\,(V_{od\_r}\,I_{od} + V_{oq\_r}\,I_{oq}) \tag{3.36}$$

This power balance is ensured by the modulator that calculate the duty-cycle to guarantee the desired output voltage reference and the desired input phase-shift reference based on $\boldsymbol{V}_{if}$. As mentioned above, however, at the input side of the converter actually there is the voltage vector V_i. It is therefore possible to write another power balance, which this time will be the actual one across the converter terminals.

$$\frac{3}{2}\,|\boldsymbol{V}_{i}|\,|\boldsymbol{I}_{i}|\,cos\,(\phi) = \frac{3}{2}\,(V_{od}\,I_{od} + V_{oq}\,I_{oq}) \tag{3.37}$$

With: $\phi = \phi_r + \eta$

The input current $\boldsymbol{I}_i$ and the output current $\boldsymbol{I}_o$ remain the same as the duty cycle matrix $\boldsymbol{M}$ is not changed. But this means that the phase shift between $\boldsymbol{I}_i$ and the input voltage $\boldsymbol{V}_i$ is now determined by the angle ϕ, which is the sum of the reference angle ϕ_r with the difference between the angle of $\boldsymbol{V}_{if}$ and the angle of $\boldsymbol{V}_i$, named η. This angle can

be defined as follows in the dq synchronous reference frame:

$$\eta = arctan\left(\frac{V_{ifq}}{V_{ifd}}\right) - arctan\left(\frac{V_{iq}}{V_{id}}\right) \tag{3.38}$$

Then with reference to (3.37), it is possible to rewrite $cos\,(\phi)$ as:

$$cos\,(\phi) = cos\left(\phi_r + arctan\left(\frac{V_{ifq}}{V_{ifd}}\right) - arctan\left(\frac{V_{iq}}{V_{id}}\right)\right) \tag{3.39}$$

Through the substitutions and simplifications presented in Chapter 2 for the calculation of the average model of the converter, specifically (2.29) and (2.31), the following relationship is obtained for $cos\,(\phi)$.

$$cos\,(\phi) = \frac{V_{id}\left(V_{ifd}\,cos\,(\phi_r) - V_{ifq}\,sin\,(\phi_r)\right) + V_{iq}\left(V_{ifq}\,cos\,(\phi_r) + V_{ifd}\,sin\,(\phi_r)\right)}{\left|\boldsymbol{V}_i^{dq}\right|\,\left|\boldsymbol{V}_{if}^{dq}\right|} \tag{3.40}$$

In Chapter 2, these simplifications were made in the $\alpha\beta$ domain, but as demonstrated in the same chapter, they can also be applied in the dq domain. Substituting (3.40) and $|\boldsymbol{I}_i|$ derived from (3.36) into (3.37), it is possible to define the actual output voltage $\boldsymbol{V}_o^{dq}$ as a function of the output reference voltage $\boldsymbol{V}_{o\_r}^{dq}$.

$$\begin{aligned} V_{od} &= V_{od\_r}\left(\frac{V_{id}\left(V_{ifd}\,cos\,(\phi_r) - V_{ifq}\,sin\,(\phi_r)\right) + V_{iq}\left(V_{ifq}\,cos\,(\phi_r) + V_{ifd}\,sin\,(\phi_r)\right)}{\left|\boldsymbol{V}_{if}^{dq}\right|^2\,cos\,(\phi_r)}\right) \\ V_{oq} &= V_{oq\_r}\left(\frac{V_{id}\left(V_{ifd}\,cos\,(\phi_r) - V_{ifq}\,sin\,(\phi_r)\right) + V_{iq}\left(V_{ifq}\,cos\,(\phi_r) + V_{ifd}\,sin\,(\phi_r)\right)}{\left|\boldsymbol{V}_{if}^{dq}\right|^2\,cos\,(\phi_r)}\right) \end{aligned} \tag{3.41}$$

As far as input currents are concerned, the module can be calculated from the relation (3.36), while for the dq components calculation, the same relation carried out in Chapter 2 (2.49) can be used, but applying instead of the voltage $\boldsymbol{V}_i^{dq}$ the filtered voltage $\boldsymbol{V}_{if}^{dq}$.

$$\begin{aligned} I_{id} &= \left(V_{od\_r}I_{od} + V_{oq\_r}I_{oq}\right)\,\frac{V_{ifd}\,cos\,(\phi_r) - V_{ifq}\,sin\,(\phi_r)}{\left|\boldsymbol{V}_{if}^{dq}\right|^2\,cos\,(\phi_r)}; \\ I_{iq} &= \left(V_{od\_r}I_{od} + V_{oq\_r}I_{oq}\right)\,\frac{V_{ifq}\,cos\,(\phi_r) + V_{ifd}\,sin\,(\phi_r)}{\left|\boldsymbol{V}_{if}^{dq}\right|^2\,cos\,(\phi_r)} \end{aligned} \tag{3.42}$$

All these changes make it necessary to redefine the system model. The filter model remains unchanged:

$$\begin{aligned}
\frac{d}{dt} I_{f2d} &= \frac{1}{L_f}\left(V_{gd} - R_{sf}\,\frac{V_{gd} - V_{id} + R_{sf}\,I_{f2d}}{R_{sf} + R_{pf}} - V_{id}\right) + \omega_i\,I_{f2q} \\
\frac{d}{dt} I_{f2q} &= \frac{1}{L_f}\left(V_{gq} - R_{sf}\,\frac{V_{gq} - V_{iq} + R_{sf}\,I_{f2q}}{R_{sf} + R_{pf}} - V_{iq}\right) - \omega_i\,I_{f2d}
\end{aligned} \tag{3.43}$$

$$\begin{aligned}
\frac{d}{dt} V_{id} &= \frac{1}{C_f}\left(\frac{V_{gd} - V_{id} + R_{sf}\,I_{f2d}}{R_{sf} + R_{pf}} - I_{id}\right) + \omega_i\,V_{iq} \\
\frac{d}{dt} V_{iq} &= \frac{1}{C_f}\left(\frac{V_{gq} - V_{iq} + R_{sf}\,I_{f2q}}{R_{sf} + R_{pf}} - I_{iq}\right) - \omega_i\,V_{id}
\end{aligned} \tag{3.44}$$

So are the load equations:

$$\begin{aligned}
\frac{d}{dt}\,I_{od} &= \frac{V_{od} - R_o\,I_{od}}{L_o} + \omega_o\,I_{oq} \\
\frac{d}{dt}\,I_{oq} &= \frac{V_{oq} - R_o\,I_{oq}}{L_o} - \omega_o\,I_{od}
\end{aligned} \tag{3.45}$$

What has changed, therefore, are the equations linking the input and output side of the converter, the average model, whose relationships are defined in (3.41) and (3.42). In addition, the equations describing the filter behaviour are integrated in the system. Although the filter in reality is implemented within the DSP, it is modelled in continuous time together with the system state variables. This is because its cutoff frequency as will be shown in the following is much lower than the switching frequency, and therefore the effect of the difference between modelling it in continuous or discrete time is negligible. The LPF filter differential equation are reported reported below:

$$\begin{aligned}
\frac{d}{dt}\,V_{ifd} &= \frac{V_{id} - V_{ifd}}{\tau} \\
\frac{d}{dt}\,V_{ifq} &= \frac{V_{iq} - V_{ifq}}{\tau}
\end{aligned} \tag{3.46}$$

(3.47) shows the complete system model with LPF on the input voltage measurement and RL load.

$$
\begin{cases}
\frac{d}{dt} I_{f2d} &= \frac{1}{L_f}\left(V_{gd} - R_{sf}\,\frac{V_{gd} - V_{id} + R_{pf}\,I_{f2d}}{R_{sf}+R_{pf}} - V_{id}\right) + \omega_i\, I_{f2q} \\
\frac{d}{dt} I_{f2q} &= \frac{1}{L_f}\left(V_{gq} - R_{sf}\,\frac{V_{gq} - V_{iq} + R_{pf}\,I_{f2q}}{R_{sf}+R_{pf}} - V_{iq}\right) - \omega_i\, I_{f2d} \\
\frac{d}{dt} V_{id} &= \frac{1}{C_f}\left(\frac{V_{gd} - V_{id} + R_{pf}\,I_{f2d}}{R_{sf}+R_{pf}} - (V_{od\_r} I_{od} + V_{oq\_r} I_{oq})\,\frac{V_{ifd}\,cos\,(\phi_r) - V_{ifq}\,sin\,(\phi_r)}{\left|\boldsymbol{V}_{if}^{dq}\right|^2\,cos\,(\phi_r)}\right) + \omega_i\, V_{iq} \\
\frac{d}{dt} V_{iq} &= \frac{1}{C_f}\left(\frac{V_{gq} - V_{iq} + R_{pf}\,I_{f2q}}{R_{sf}+R_{pf}} - (V_{od\_r} I_{od} + V_{oq\_r} I_{oq})\,\frac{V_{ifq}\,cos\,(\phi_r) + V_{ifd}\,sin\,(\phi_r)}{\left|\boldsymbol{V}_{if}^{dq}\right|^2\,cos\,(\phi_r)}\right) - \omega_i\, V_{id} \\
\frac{d}{dt}\, I_{od} &= \frac{1}{L_o}\left[V_{od\_r}\left(\frac{V_{id}\,(V_{ifd}\,cos\,(\phi_r) - V_{ifq}\,sin\,(\phi_r)) + V_{iq}\,(V_{ifq}\,cos\,(\phi_r) + V_{ifd}\,sin\,(\phi_r))}{\left|\boldsymbol{V}_{if}^{dq}\right|^2\,cos\,(\phi_r)}\right) - R_o\, I_{od}\right] + \omega_o\, I_{oq} \\
\frac{d}{dt}\, I_{oq} &= \frac{1}{L_o}\left[V_{oq\_r}\left(\frac{V_{id}\,(V_{ifd}\,cos\,(\phi_r) - V_{ifq}\,sin\,(\phi_r)) + V_{iq}\,(V_{ifq}\,cos\,(\phi_r) + V_{ifd}\,sin\,(\phi_r))}{\left|\boldsymbol{V}_{if}^{dq}\right|^2\,cos\,(\phi_r)}\right) - R_o\, I_{oq}\right] - \omega_o\, I_{od} \\
\frac{d}{dt}\, V_{ifd} &= \frac{V_{id} - V_{ifd}}{\tau} \\
\frac{d}{dt}\, V_{ifq} &= \frac{V_{iq} - V_{ifq}}{\tau}
\end{cases}
\tag{3.47}
$$

3.3.1 Stability Analysis

The system presented in (3.47) is as in the previous case a nonlinear system. It is necessary to use the small signal analysis to evaluate the system stability. As in the previous case, the steady state system will be solved by setting a certain value of I_{od}. Then the values obtained will be applied to the linearized matrices. This time the system to be solved has two more unknowns but also two more equations, which makes it solvable. In Tab. 3.4 are reported the known and unknown parameters: A linearized

Table 3.4: Known and Unknown System Variables

Known Variables	Unknown Varables	System Parameters
V_{gd}	I_{f2d}	L_f
V_{gq}	I_{f2q}	C_f
I_{od}	V_{id}	R_{pf}
I_{oq}	V_{iq}	R_{sf}
	V_{ifd}	R_po
	V_{ifq}	L_o
	V_{od_r}	ω_i
	V_{oq_r}	ω_o
		ϕ_r

state-space model whose stability properties are valid around the steady-state point is thus obtained. Its equations is shown below:

$$\dot{\boldsymbol{x}}_f = \overline{\boldsymbol{A}}_{op\_f}\, \boldsymbol{x}_f + \overline{\boldsymbol{B}}_{op\_f}\, \boldsymbol{u}_f + \overline{\boldsymbol{G}}_{op\_f}\, \boldsymbol{d}_f \tag{3.48}$$

Where:

$$\begin{aligned} \boldsymbol{x}_f &= \begin{bmatrix} I_{f2d} & I_{f2q} & V_{id} & V_{iq} & I_{od} & I_{oq} & V_{ifd} & V_{ifq} \end{bmatrix}^T \\ \boldsymbol{u}_f &= \begin{bmatrix} V_{od\_r} & V_{oq\_r} \end{bmatrix}^T \\ \boldsymbol{d}_f &= \begin{bmatrix} V_{gd} & V_{gq} \end{bmatrix}^T \end{aligned} \tag{3.49}$$

And where $\overline{\boldsymbol{A}}_{op\_f}$, $\overline{\boldsymbol{B}}_{op\_f}$ and $\overline{\boldsymbol{G}}_{op\_f}$ are the linearized system matrices with respect to $\boldsymbol{x}_f$, $\boldsymbol{u}_f$ and $\boldsymbol{d}_f$ as shown in (3.7), (3.8) and (3.9). Again as in the previous case, the closed-loop stability of the system is to be evaluated. In order to integrate discrete controllers, it is therefore necessary to discretize the state-space model in order to obtain the discrete state-space model:

$$\boldsymbol{x}_f\left(k+1\right)=\overline{\boldsymbol{\Phi}}_{op\_f}\,\boldsymbol{x}_f\left(k\right)+\overline{\boldsymbol{\Gamma}}_{op\_f}\,\boldsymbol{u}_f\left(k\right)+\overline{\boldsymbol{\Psi}}_{op\_f}\,\boldsymbol{d}_f\left(k\right) \tag{3.50}$$

To integrate the PI controllers, the state space vector, the input vector and the disturbance vector have to be redefined as follows:

$$\boldsymbol{x}_{cl\_f}\left(k\right)=\begin{bmatrix}\begin{bmatrix}\boldsymbol{x}_f\left(k\right)\end{bmatrix}_{8\times 2}\\ X_{id}\left(k\right)\\ X_{iq}\left(k\right)\\ V^{d}_{od\_r}\left(k\right)\\ V^{d}_{od\_r}\left(k\right)\end{bmatrix};\quad \boldsymbol{u}_{cl\_f}\left(k\right)=\begin{bmatrix}I_{od\_r}\left(k\right)\\ I_{od\_r}\left(k\right)\end{bmatrix};\quad \boldsymbol{d}_{cl\_f}\left(k\right)=\begin{bmatrix}V_{gd}\left(k\right)\\ V_{gq}\left(k\right)\end{bmatrix} \tag{3.51}$$

The PI controller relations in (3.23) can be summarized in the following matrix, with respect to $\boldsymbol{x}_{cl\_f}\left(k\right)$.

$$\begin{bmatrix}X_{id}\left(k+1\right)\\ X_{iq}\left(k+1\right)\\ V^{d}_{od\_r}\left(k+1\right)\\ V^{d}_{od\_r}\left(k+1\right)\end{bmatrix}=\boldsymbol{A}_{c\_f}\,\boldsymbol{x}_{cl\_f}\left(k\right)+\boldsymbol{B}_{c\_f}\,\boldsymbol{u}_{cl\_f}\left(k\right) \tag{3.52}$$

Where:

$$\boldsymbol{A}_c=\begin{bmatrix}0&0&0&0&-T_s&0&0&0&1&0&0&0\\ 0&0&0&0&0&-T_s&0&0&0&1&0&0\\ 0&0&0&0&-K_p&0&0&0&K_i&0&0&0\\ 0&0&0&0&0&-K_p&0&0&0&K_i&0&0\end{bmatrix};\quad \boldsymbol{B}_c=\begin{bmatrix}T_s&0\\ 0&T_s\end{bmatrix} \tag{3.53}$$

And finally, the closed-loop state-space model can be composed by merging the new linearized open-loop state-space model matrices with the new control matrix, remembering that now the input vector of the open-loop system is part of the state variables. Please again, note that the stability information obtained analysing the closed-loop matrix will only be valid around the steady-state point where the system has been linearized. Each time the output current value requires repeating the procedure all over again. In the following the closed-loop state-space model:

$$\boldsymbol{x}_{cl\_f}\left(k+1\right)=\overline{\boldsymbol{A}}_{cl\_f}\,\boldsymbol{x}_{cl\_f}\left(k\right)+\overline{\boldsymbol{B}}_{cl\_f}\,\boldsymbol{u}_{cl\_f}\left(k\right)+\overline{\boldsymbol{G}}_{cl\_f}\,\boldsymbol{d}_{cl\_f}\left(k\right) \tag{3.54}$$

With:

$$\overline{\boldsymbol{A}}_{cl\_f}=\begin{bmatrix}\left[\overline{\boldsymbol{\Phi}}_{op\_f}\right]_{8\times8} & \left[\boldsymbol{0}\right]_{8\times2} & \left[\overline{\boldsymbol{\Gamma}}_{op\_f}\right]_{8\times2}\\ \left[\qquad\qquad\boldsymbol{A}_{c\_f}\qquad\qquad\right]_{4\times12}\end{bmatrix};\qquad\begin{aligned}\overline{\boldsymbol{B}}_{cl\_f}&=\boldsymbol{B}_{c\_f};\\ \overline{\boldsymbol{G}}_{cl\_f}&=\overline{\boldsymbol{\Psi}}_{op\_f}\end{aligned} \tag{3.55}$$

The stability study and simulations that follow have been carried out using the same system parameters as in the previous case, shown in Tab. 3.2 and 3.3. The simulator schematic is reported in Fig. 3.7. The filter on the input voltages was chosen with a cut-off frequency of $100Hz$. It is not advisable to go below this value, as there is a risk of introducing too much phase shift between $\boldsymbol{V}_i$ and $\boldsymbol{V_{if}}$, compromising the proper functioning of the converter. The study of eigenvalues shows that instability should occurs for $I_{od}\cong5.5\,A$. The following pages shows the results of the simulations. Those in the synchronous reference dq are sampled at the switching frequency T_s, while to evaluate the three-phase waveforms the variables have been sampled at $T_s/10$. It can immediately be seen, in Fig. 3.8 that the system is much more stable than in the case without a filter. In fact, it is possible to achieve an I_{od} current of $5\,A$ and thus a power of $375\,W$. Again, at each step increase in current, the settling time to the reference increase since it reach the instability when $I_{od\_r}=5.5\,A$. This stabilization method has a limitation in terms of control bandwidth. In fact, as the control bandwidth increases, the stabilizing effect of the filter tends to be negligible. Fig. 3.10 shows a graph relating the maximum current that can be delivered to the filter cut-off frequency of the input voltage. Each

curve on the graph shows a different control band. The lower is the cut-off frequency the higher is the current that can be delivered, but as stated before choose a cut-off frequency too low can compromise the converter operating. Moreover, note how as the control bandwidth increases, the curves tend to converge to the limit value of the case without filter. Furthermore, the proposed method is not effective in the case of inverse power flow, which stabilization algorithm will be addressed a little later.

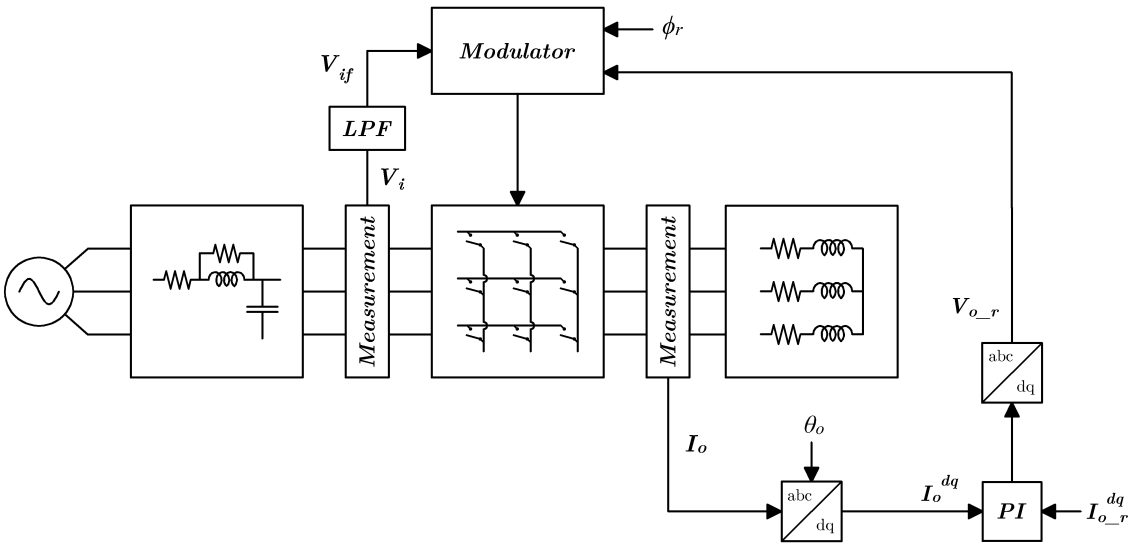

Figure 3.7: Closed-loop schematic with LPF on input voltage measurements

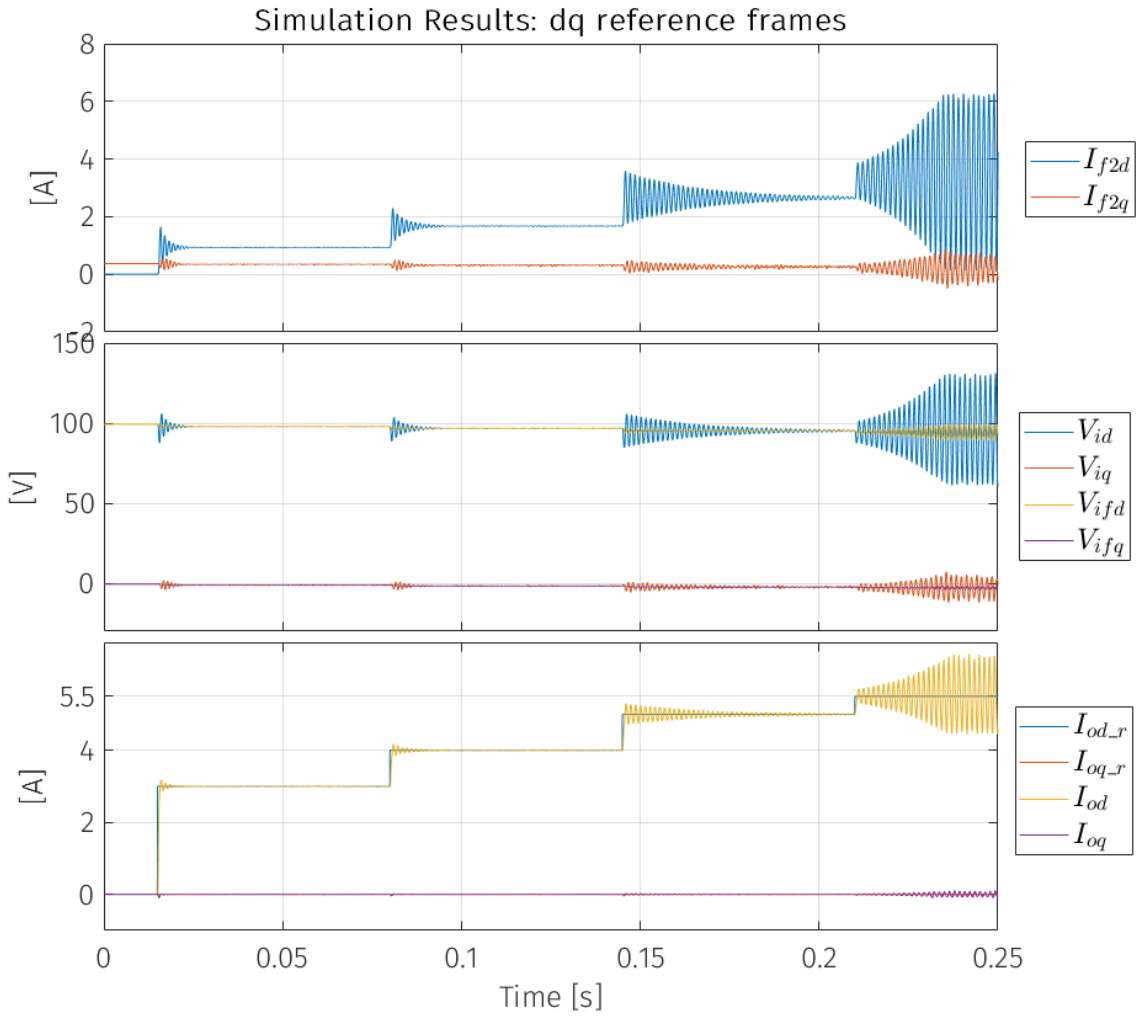

Figure 3.8: Simulations result in the input and output dq reference frame as I_{od_r} increases, sample time T_s

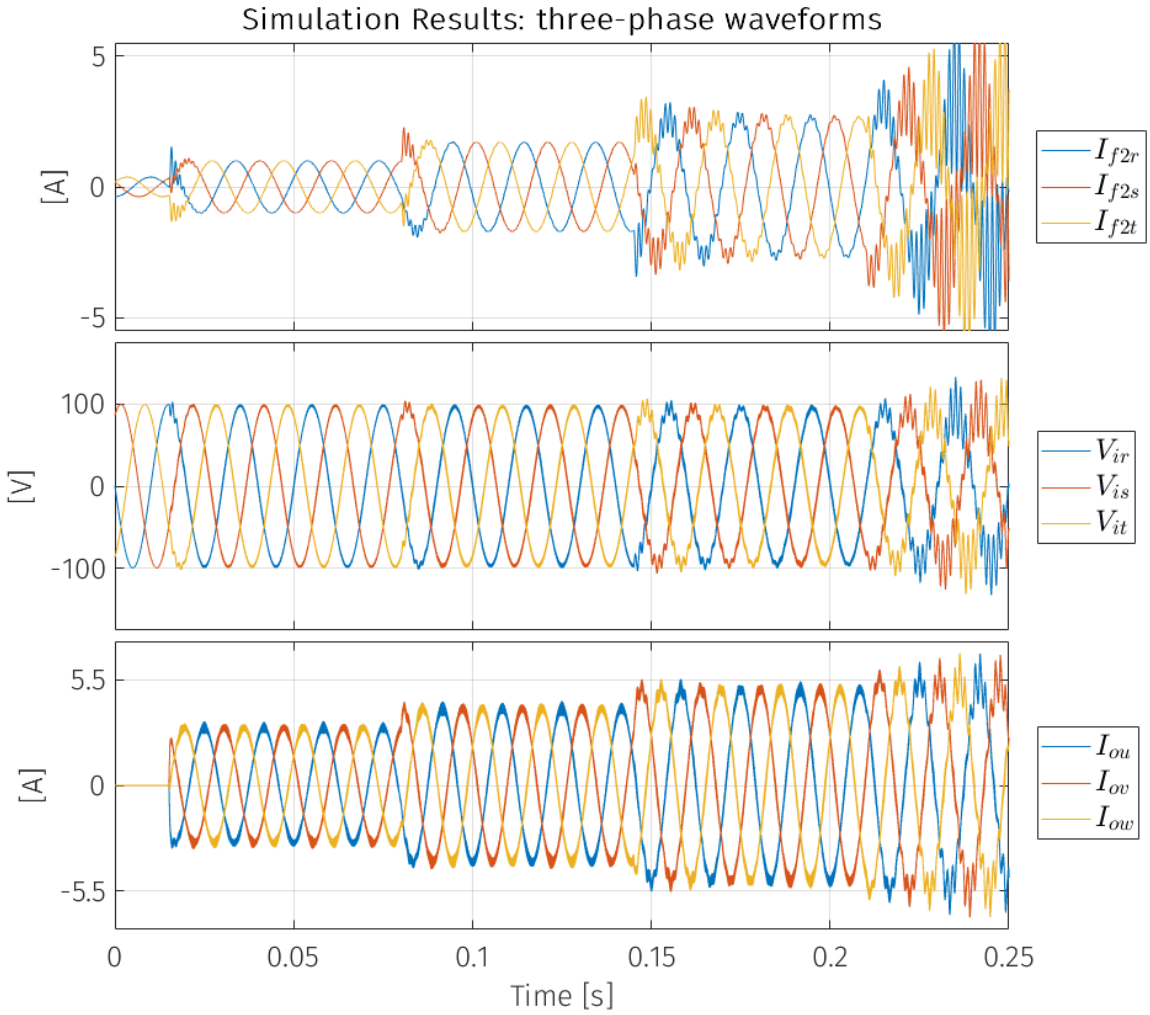

Figure 3.9: Three-Phase waveforms as I_{od_r} increases, sample time $T_s/10$

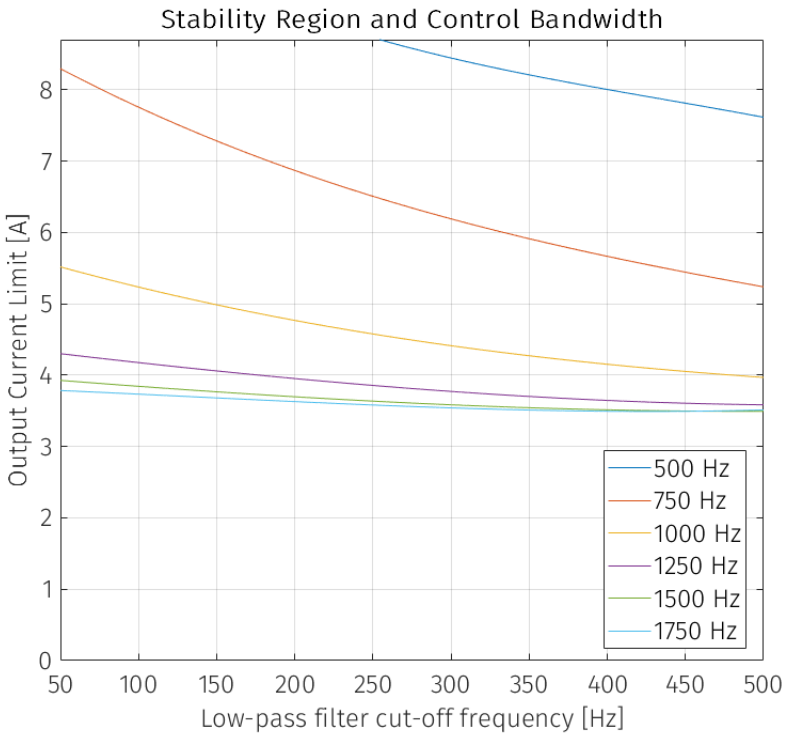

Figure 3.10: Stabilization Method Analysis as a function of cut-off frequency and control bandwidth

3.4 Stability Analysis: Bidirectional Power Flow

In the following, the stability of the system in the case of bidirectional load is analysed. The bidirectional load, as illustrated in the previous chapter, consists of an SM-PMSM motor, controlled through a FOC algorithm and supplied by the matrix converter, whose speed is set by another SM-PMSM directly connected to its shaft. The motor supplied by the matrix converter imposes a torque, either positive or negative, on the second motor, whose control algorithm allows to maintain a constant speed by compensating it. From the point of view of the matrix converter, the control algorithm, which consists of two PI controllers, simply imposes current references on it. The d-axis current reference I_{od_r} is kept at zero, while the q-axis reference I_{od_r} is free to vary , thus varying the torque delivered by the motor. It is thus possible to direct the power flow from the grid to the motor and vice versa. This load will be the one that will be used to test the stabilization strategy that will be presented in the next chapter, and will thus be the one that will be implemented experimentally.

3.4.1 Closed-Loop Stability Analysis with Bidirectional Power Flow

Starting from the nonlinear system given in (2.102) for the system with the SM-PMSM, the steps outlined earlier in this chapter, the linearized and discretized open-loop state-space model is obtained:

$$\boldsymbol{x}\left(k+1\right)=\overline{\boldsymbol{\Phi}}_{op}\,\boldsymbol{x}\left(k\right)+\overline{\boldsymbol{\Gamma}}_{op}\,\boldsymbol{u}\left(k\right)+\overline{\boldsymbol{\Psi}}_{op}\,\boldsymbol{d}\left(k\right) \tag{3.56}$$

Where:

$$\begin{aligned}\boldsymbol{x}&=\begin{bmatrix} I_{f2d} & I_{f2q} & V_{id} & V_{iq} & I_{od} & I_{oq}\end{bmatrix}^{T}\\ \boldsymbol{u}&=\begin{bmatrix} V_{od\_r} & V_{oq\_r}\end{bmatrix}^{T}\\ \boldsymbol{d}&=\begin{bmatrix} V_{gd} & V_{gq}\end{bmatrix}^{T}\end{aligned} \tag{3.57}$$

The systems model with the RL load and the SM-PMSM are actually very similar mathematically. The only difference being the contribution of the back EMF, located on the

equation describing the behaviour of the output current I_{oq}, and of course the system parameters. This time the quantity that is varied iteratively to evaluate the stability region is the current I_{oq}. Exactly as in the case of the RL load, the relationships describing the discrete PI controllers are introduced to obtain the closed-loop state-space model. In the case of the SM-PMSM the current controllers would provide a feedback for back EMF compensation. Given the small contribution of this feedback to the control dynamic, it is neglected in order to simplify the calculations. The vector of state variables, that of inputs and that of disturbances for the discrete closed-loop system are reported below:

$$\boldsymbol{x}_{cl}(k) = \begin{bmatrix} \left[\, \boldsymbol{x}(k) \,\right]_{6\times 2} \\ X_{id}(k) \\ X_{iq}(k) \\ V^{d}_{od\_r}(k) \\ V^{d}_{od\_r}(k) \end{bmatrix}; \quad \boldsymbol{u}_{cl}(k) = \begin{bmatrix} I_{od\_r}(k) \\ I_{od\_r}(k) \end{bmatrix}; \quad \boldsymbol{d}_{cl}(k) = \begin{bmatrix} V_{gd}(k) \\ V_{gq}(k) \end{bmatrix} \tag{3.58}$$

The controller relationships with respect to $\boldsymbol{x}_{cl}(k)$ and $\boldsymbol{u}_{cl}(k)$ as already shown can be represented as:

$$\begin{bmatrix} X_{id}(k+1) \\ X_{iq}(k+1) \\ V^{d}_{od\_r}(k+1) \\ V^{d}_{od\_r}(k+1) \end{bmatrix} = \boldsymbol{A}_c\, \boldsymbol{x}_{cl}(k) + \boldsymbol{B}_c\, \boldsymbol{u}_{cl}(k) \tag{3.59}$$

Where:

$$\boldsymbol{A}_c = \begin{bmatrix} 0 & 0 & 0 & 0 & -T_s & 0 & 1 & 0 & 0 & 0 \\ 0 & 0 & 0 & 0 & 0 & -T_s & 0 & 1 & 0 & 0 \\ 0 & 0 & 0 & 0 & -K_p & 0 & K_i & 0 & 0 & 0 \\ 0 & 0 & 0 & 0 & 0 & -K_p & 0 & K_i & 0 & 0 \end{bmatrix}; \qquad \boldsymbol{B}_c = \begin{bmatrix} T_s & 0 \\ 0 & T_s \end{bmatrix} \tag{3.60}$$

The closed-loop state-space model is is derived as follows:

$$\boldsymbol{x}_{cl}\left(k+1\right)=\overline{\boldsymbol{A}}_{cl}\,\boldsymbol{x}_{cl}\left(k\right)+\overline{\boldsymbol{B}}_{cl}\,\boldsymbol{u}_{cl}\left(k\right)+\overline{\boldsymbol{G}}_{cl}\,\boldsymbol{d}_{cl}\left(k\right) \tag{3.61}$$

With:

$$\overline{\boldsymbol{A}}_{cl}=\begin{bmatrix}\left[\overline{\boldsymbol{\Phi}}_{op}\right]_{6\times6} & \left[\boldsymbol{0}\right]_{6\times2} & \left[\overline{\boldsymbol{\Gamma}}_{op}\right]_{6\times2}\\ \left[\qquad\qquad\boldsymbol{A}_{c}\qquad\qquad\right]_{4\times10}\end{bmatrix};\qquad\begin{matrix}\overline{\boldsymbol{B}}_{cl}=\boldsymbol{B}_{c};\\ \\ \overline{\boldsymbol{G}}_{cl}=\overline{\boldsymbol{\Psi}}_{op}\end{matrix} \tag{3.62}$$

Now recalculating the matrices of the linearized and discretized system in (3.56) by varying I_{oq}, it is possible to study the stability region of the system by analysing the eigenvalues of the matrix $\overline{\boldsymbol{A}}_{cl}$. The parameter used for this study are reported in Tab. 3.5 and 3.6.

Table 3.5: System Variables and Parameters

System Variables			System Parameters		
V_{gd}	100	V	L_f	2.4	mH
V_{gq}	0	V	C_f	12	μF
I_{oq_r}	0	A	R_{pf}	200	Ω
			R_{sf}	1.5	Ω
			R_o	0.1	Ω
			L_o	0.3	mH
			Φ_{PM}	0.1	Wb
			ω_i	$2\,\pi\,50$	$\frac{rad}{s}$
			ω_o	$2\,\pi\,60$	$\frac{rad}{s}$
			ϕ_r	0	rad

Table 3.6: Control Parameters

Control Parameters		
ω_c	$2\,\pi\,1000$	$\frac{rad}{s}$
ξ	1	
K_p	3.6699	
K_i	11844	

In the following, motor mode will be used to talk about positive power flow, and

generator mode to talk about negative power flow. The study of eigenvalues shows that instability motor mode occurs for I_{oq} values is higher than $3.7\,A$, while in generator mode when I_{oq} is lower then $-4\,A$. These results are tested through simulations, whose schematic is reported in Fig. 3.11 and the results obtained are shown in the following figures. Fig. 3.12 shows the result in the input and output side dq reference frames. The quantities are sampled at the switching frequency T_s. It turns out that the system already at $I_{oq\_r} = 3\,A\,(171\,W)$ becomes unstable. The reason can be found in Fig. 3.13 where the three-phase waveforms sampled at Ts/10 are shown. The low resistance and inductance generate high current ripple that trigger instabilities. For the generator mode the situation is the opposite, result are reported in Fig. 3.14 and 3.15, instability occurs when $I_{oq\_r} = -5\,A\,(-278\,W)$. The simulator is therefore more stable than the prediction. This can always be caused by the current ripple which has, in the case of generator mode, a stabilizing effect.

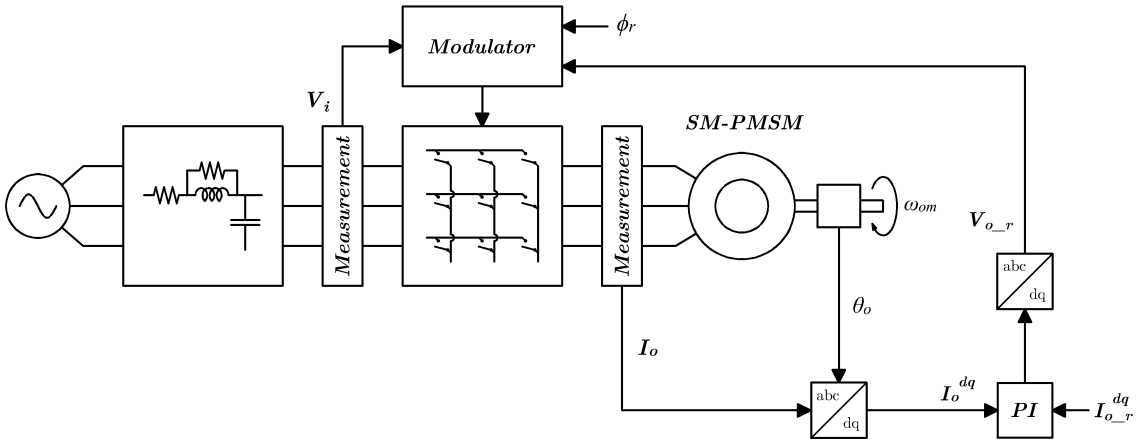

Figure 3.11: Closed-loop schematic with SM-PMSM

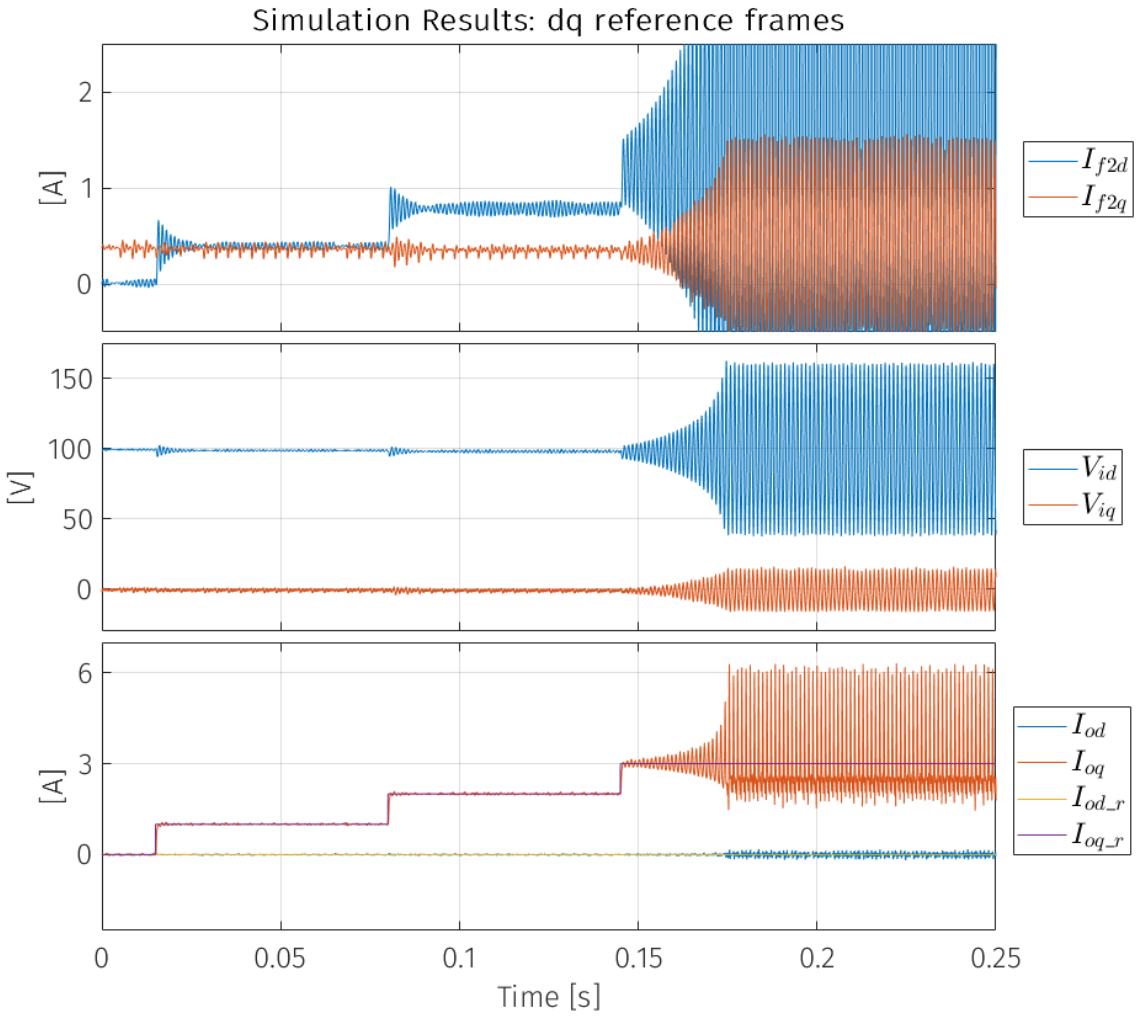

Figure 3.12: Simulations result in the input and output dq reference frame as I_{oq_r} increases, sample time T_s

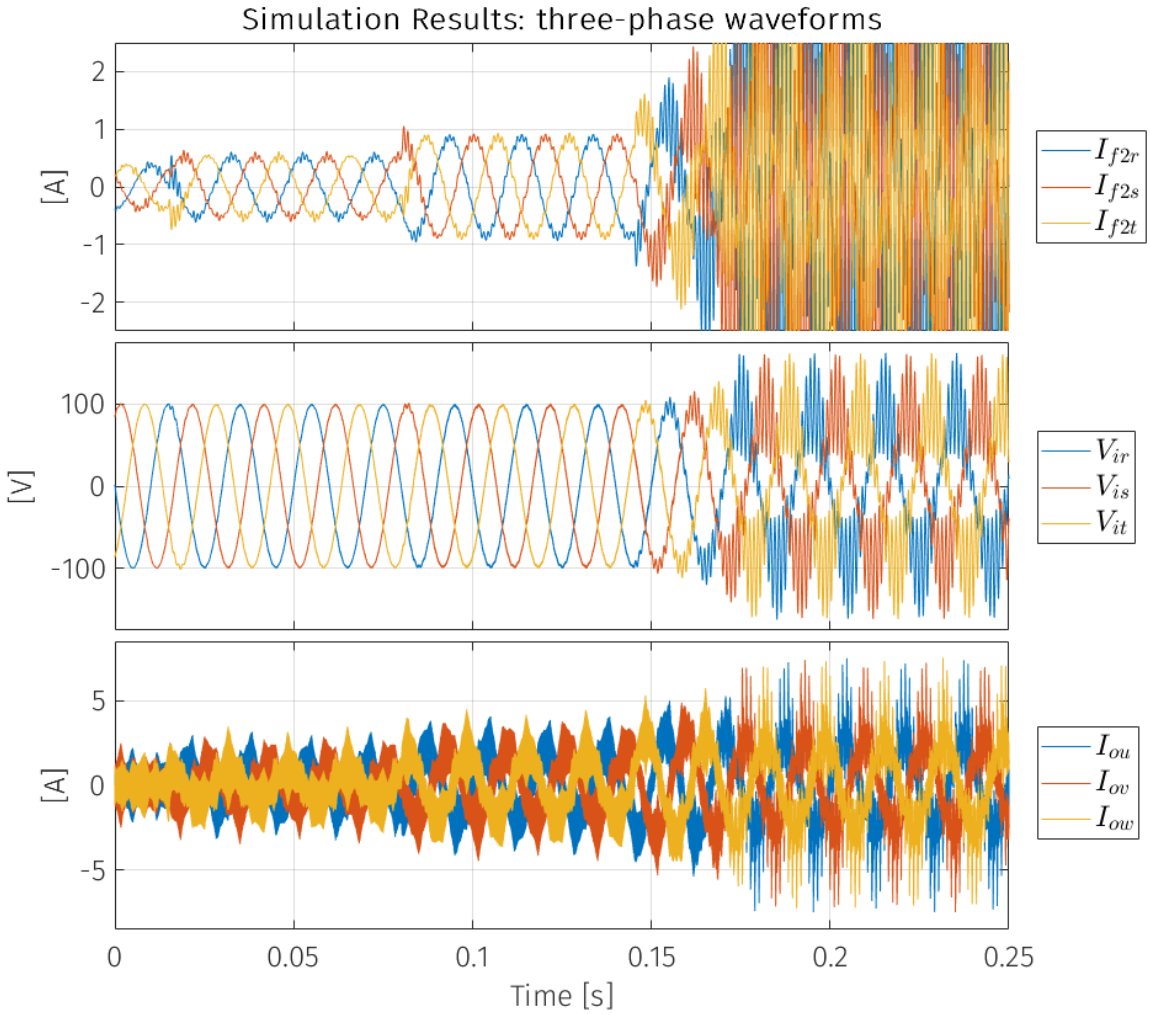

Figure 3.13: Three-Phase waveforms as I_{od_r} increases, sample time $T_s/10$

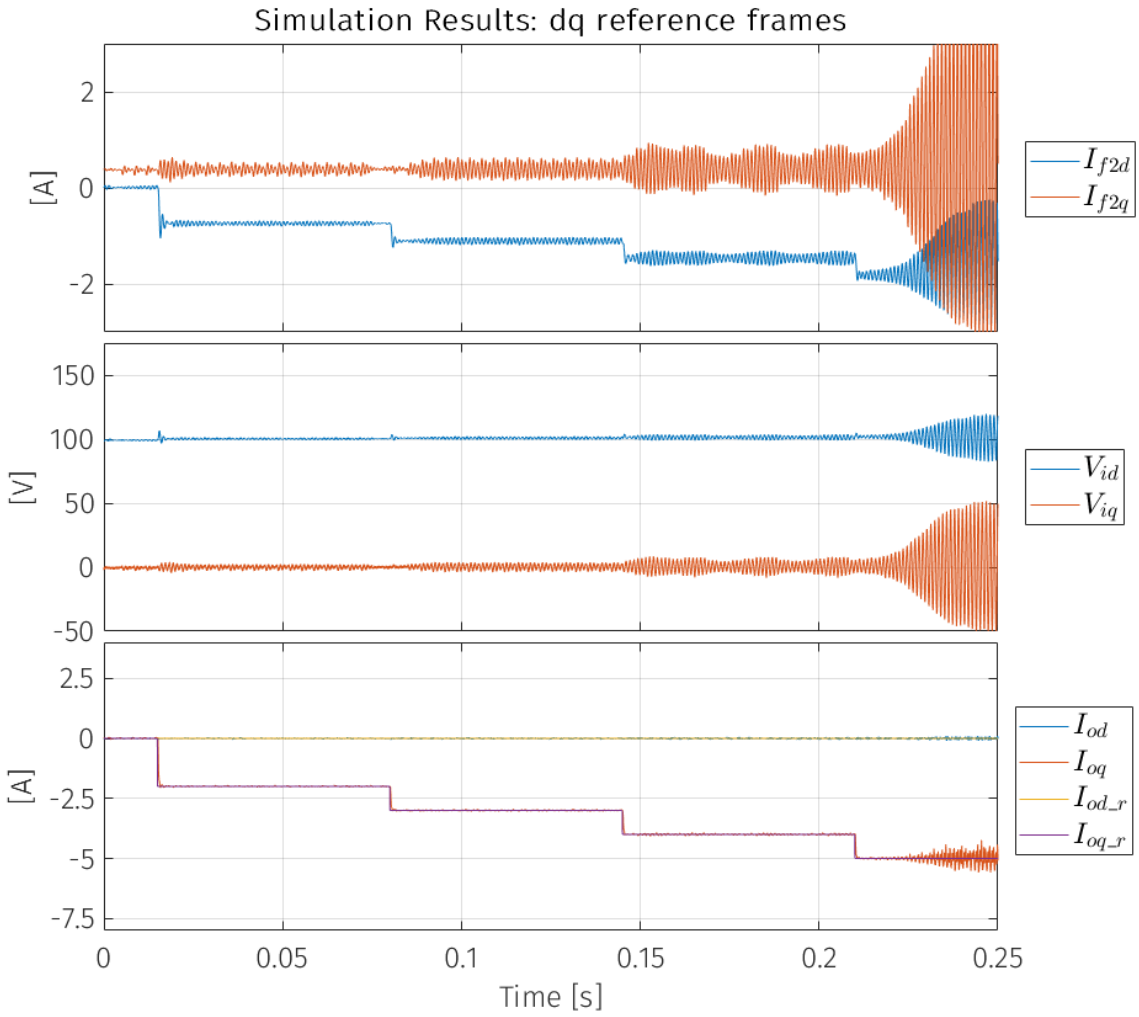

Figure 3.14: Simulations result in the input and output dq reference frame as I_{oq_r} decreases, sample time T_s

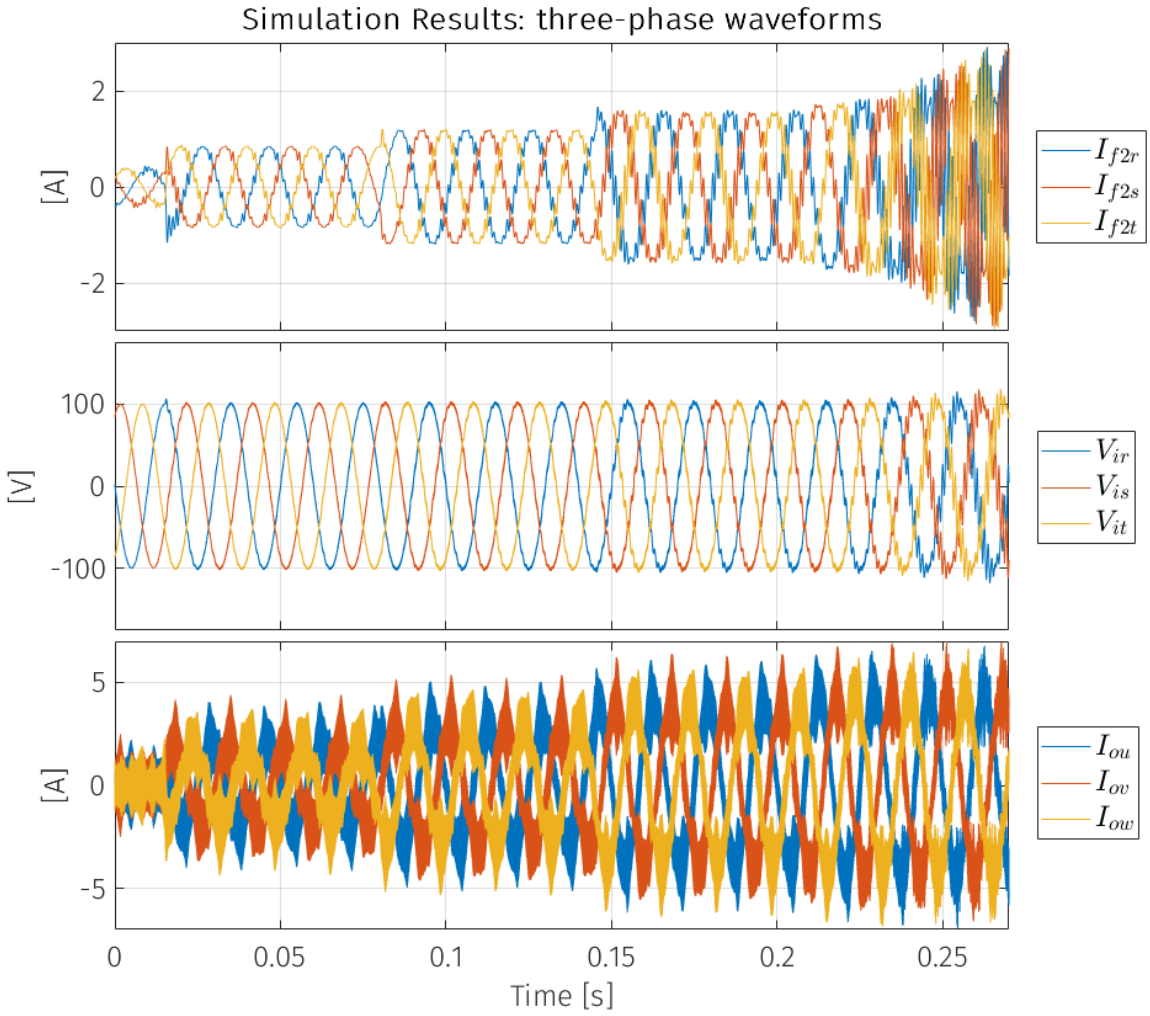

Figure 3.15: Three-Phase waveforms as I_{od_r} increases, sample time $T_s/10$

3.5 HPF Stabilization Method: Bidirectional Power Flow

A stabilization method for bidirectional power flow was presented in [4]. The authors investigate the stability of the converter by analyzing its equivalent impedance. They attribute the origin of instabilities to the fact that beyond a certain power threshold, the input impedance becomes negative. They proposed then a method to increase the input impedance. The method consists of two separate strategies, one for motor mode and one for generator mode. For motor mode, the stabilizing action consists of the addition of a correction term on one of the components of the reference output voltage vector $V_{o\_r}^{dq}$. In generator mode, the correction term is applied to the angle of the input voltage measurement V_i that are provided to the modulator. The two strategies are analysed in detail below. Both methods employ High-Pass Filters (HPF) to calculate the correction components, which is why the stabilisation method in the following discussion will be referred to as HPF.

3.5.1 Motor Mode Stabilization Method and Analysis

The motor mode method in [4] is proposed as a more flexible equivalent of the method proposed in [3]. It consists of adding to one of components of the reference output voltage vector $\boldsymbol{V}_{o\_r}^{dq}$ a compensation term calculated from the d-axis component of the input voltage $\boldsymbol{V}_{i}^{dq}$, filtered by an HPF and then multiplied by a gain k. The input side dq reference frame is synchronous and oriented with the grid voltage $\boldsymbol{V}_g$, while the output dq reference frame is oriented with the rotor position. The axis to which the correction is applied is selected by evaluating which of the two components of the $\boldsymbol{I}_{o}^{dq}$ vector is greater. Flexibility is provided by the gain k, which can be chosen depending on the application. In the case of the SM-PMSM load, since the output current vector is aligned with the q-axis, the correction term is applied to the q-axis component of the vector $\boldsymbol{V}_{o\_r}^{dq}$ and is defined as follows:

$$c = k \left(\frac{\tau\, s}{\tau\, s + 1} \right) V_{id} \tag{3.63}$$

Where: $\tau = \dfrac{1}{2\,\pi\, f_{cut\_HPF}}$

With the application of the correction term, a reference voltage vector $\tilde{\boldsymbol{V}}_{o\_r}^{dq}$ is obtained, the components of which are shown below.

$$\begin{aligned} \tilde{V}_{od\_r} &= V_{od\_r} \\ \tilde{V}_{oq\_r} &= V_{oq\_r} + c \end{aligned} \tag{3.64}$$

It is necessary to study the dynamics of the system in closed loop as in the previous cases. Thus as seen above, V_{od_r} and V_{oq_r} are the output of PI controllers, these have been discretized in order to be implemented in the DSP. The correction term must therefore also be discretized in order to add it to the current references coming out of the discrete PI controllers and study its effect on stability. The HPF filter in (3.63) can be decomposed as the difference between the signal V_{id} and the same signal filtered through a LPF.

$$c = k \left(V_{id} - \frac{1}{\tau\, s + 1} V_{id} \right) \tag{3.65}$$

The LPF can therefore be discretized using the Forward Euler method, resulting in the following difference equation:

$$z\left(k+1\right) = \left(1-\mu\right) z\left(k\right) + \mu V_{id}\left(k\right) \tag{3.66}$$

With: $\mu = \dfrac{T_s}{T_s + \tau}$

The discretized compensation term is thus:

$$c\left(k\right) = k\, \left(V_{id}\left(k\right) - z\left(k\right) \right) \tag{3.67}$$

The reference voltages vector with the correction term applied $\tilde{\boldsymbol{V}}_{o\_r}^{dq}$ can be written in discrete form as follows:

$$\begin{aligned} \tilde{V}_{od\_r}\left(k\right) &= V_{od\_r}\left(k\right) \\ \tilde{V}_{oq\_r}\left(k\right) &= V_{oq\_r}\left(k\right) + c\left(k\right) = V_{oq\_r}\left(k\right) + k\, \left(V_{id}\left(k\right) - z\left(k\right) \right) \end{aligned} \tag{3.68}$$

At this point, the relations of the discretized PI presented above are recalled:

$$\begin{aligned} X_{id}\left(k+1\right) &= X_{id}\left(k\right) + T_s\left(I_{od\_r} - I_{od}\right) \\ X_{iq}\left(k+1\right) &= X_{iq}\left(k\right) + T_s\left(I_{oq\_r} - I_{oq}\right) \\ V_{od\_r}\left(k\right) &= -K_p\, I_{od}\left(k\right) + K_i\, X_{id}\left(k\right) \\ V_{oq\_r}\left(k\right) &= -K_p\, I_{oq}\left(k\right) + K_i\, X_{iq}\left(k\right) \end{aligned} \tag{3.69}$$

The correction term is then added to the voltage reference and the filter difference equation included, which leads to the system of equations that describe the whole control dynamic:

$$\begin{aligned} z\left(k+1\right) &= \left(1-\mu\right) z\left(k\right) + \mu V_{id}\left(k\right) \\ X_{id}\left(k+1\right) &= X_{id}\left(k\right) + T_s\left(I_{od\_r} - I_{od}\right) \\ X_{iq}\left(k+1\right) &= X_{iq}\left(k\right) + T_s\left(I_{oq\_r} - I_{oq}\right) \\ \tilde{V}_{od\_r}\left(k\right) &= -K_p\, I_{od}\left(k\right) + K_i\, X_{id}\left(k\right) \\ \tilde{V}_{oq\_r}\left(k\right) &= -K_p\, I_{oq}\left(k\right) + K_i\, X_{iq}\left(k\right) + k\,\left(V_{id}\left(k\right) - z\left(k\right)\right) \end{aligned} \tag{3.70}$$

It is time to calculate the complete closed-loop model of the system. The linearized and discretized state-space model is given by the following relation:

$$\boldsymbol{x}\left(k+1\right) = \overline{\boldsymbol{\Phi}}_{op}\,\boldsymbol{x}\left(k\right) + \overline{\boldsymbol{\Gamma}}_{op}\,\boldsymbol{u}\left(k\right) + \overline{\boldsymbol{\Psi}}_{op}\,\boldsymbol{d}\left(k\right) \tag{3.71}$$

Where:

$$\begin{aligned} \boldsymbol{x} &= \begin{bmatrix} I_{f2d} & I_{f2q} & V_{id} & V_{iq} & I_{od} & I_{oq} \end{bmatrix}^T \\ \boldsymbol{u} &= \begin{bmatrix} V_{od\_r} & V_{oq\_r} \end{bmatrix}^T \\ \boldsymbol{d} &= \begin{bmatrix} V_{gd} & V_{gq} \end{bmatrix}^T \end{aligned} \tag{3.72}$$

The closed-loop state variables vector, input vector and disturbance vector are defined

as follows;

$$\boldsymbol{x}_{cl\_c}(k) = \begin{bmatrix} \left[\, \boldsymbol{x}(k) \,\right]_{6\times 2} \\ z(k) \\ X_{id}(k) \\ X_{iq}(k) \\ V^{d}_{od\_r}(k) \\ V^{d}_{od\_r}(k) \end{bmatrix}; \quad \boldsymbol{u}_{cl\_c}(k) = \begin{bmatrix} I_{od\_r}(k) \\ I_{od\_r}(k) \end{bmatrix}; \quad \boldsymbol{d}_{cl\_c}(k) = \begin{bmatrix} V_{gd}(k) \\ V_{gq}(k) \end{bmatrix} \tag{3.73}$$

The controller relationships with respect to $\boldsymbol{x}_{cl\_c}(k)$ and $\boldsymbol{u}_{cl\_c}(k)$ as already shown can be represented as:

$$\begin{bmatrix} z(k+1) \\ X_{id}(k+1) \\ X_{iq}(k+1) \\ V^{d}_{od\_r}(k+1) \\ V^{d}_{od\_r}(k+1) \end{bmatrix} = \boldsymbol{A}_{c\_c}\,\boldsymbol{x}_{cl\_c}(k) + \boldsymbol{B}_{c\_c}\,\boldsymbol{u}_{cl\_c}(k) \tag{3.74}$$

Where:

$$\boldsymbol{A}_{c\_c} = \begin{bmatrix} 0 & 0 & \mu & 0 & 0 & 0 & (1-\mu) & 0 & 0 & 0 & 0 \\ 0 & 0 & 0 & 0 & -T_s & 0 & 0 & 1 & 0 & 0 & 0 \\ 0 & 0 & 0 & 0 & 0 & -T_s & 0 & 0 & 1 & 0 & 0 \\ 0 & 0 & 0 & 0 & -K_p & 0 & 0 & K_i & 0 & 0 & 0 \\ 0 & 0 & k & 0 & 0 & -K_p & -k & K_i & 0 & 0 & \end{bmatrix}; \qquad \boldsymbol{B}_{c\_c} = \begin{bmatrix} T_s & 0 \\ 0 & T_s \end{bmatrix} \tag{3.75}$$

The closed-loop state-space model is is derived as follows:

$$\boldsymbol{x}_{cl\_c}(k+1) = \overline{\boldsymbol{A}}_{cl\_c}\,\boldsymbol{x}_{cl\_c}(k) + \overline{\boldsymbol{B}}_{cl\_c}\,\boldsymbol{u}_{cl\_c}(k) + \overline{\boldsymbol{G}}_{cl\_c}\,\boldsymbol{d}_{cl\_c}(k) \tag{3.76}$$

With:

$$\overline{\boldsymbol{A}}_{cl\_c} = \begin{bmatrix} \left[\overline{\boldsymbol{\Phi}}_{op}\right]_{6\times6} & \left[\boldsymbol{0}\right]_{6\times3} & \left[\overline{\boldsymbol{\Gamma}}_{op}\right]_{6\times2} \\ \left[\right. & \boldsymbol{A}_{c\_c} & \left.\right]_{5\times10} \end{bmatrix}; \qquad \begin{aligned} \boldsymbol{B}_{cl\_c} &= \boldsymbol{B}_{c\_c}; \\ \boldsymbol{G}_{cl\_c} &= \overline{\boldsymbol{\Psi}}_{op} \end{aligned} \tag{3.77}$$

By studying the eigenvalues of the matrix $\overline{\boldsymbol{A}}_{cl\_c} \in \mathbb{R}^{11\times11}$, it is therefore possible to evaluate the effectiveness of the method proposed in [4] for the motor mode. Several variables are involved in this study. There is the parameter k, the filter cut-off frequency, the I_{oq} current and finally the control bandwidth. Below three graphs are shown, each graph is made with a different control bandwidth. The system parameters are reported in Tab. 3.5. On the x-axis is the parameter k, and on the y-axis the HPF filter cut-off frequency. Concentric areas with different colours are shown on the graphs. Each colour corresponds to a different current value. The larger areas relate to lower currents, the smaller areas to larger currents. The area of the plane identified by the parameters k and cut-off frequency indicates the range of these values for which the current value relative to that area does not generate instability. Note that the larger areas include the smaller areas within them. Fig. 3.16 refers to the study of stability regions at the $500\,Hz$ control bandwidth. As can be seen there is a value of k beyond which the system is not stable for any control bandwidth and current, it is the one coloured white. Taking the current value $I_{oq} = 7\,A$ as an example, it can be seen that it is stable within the yellow region, which in turn include the purple and green regions. For $I_{oq} = 10\,A$ the system is stable in the violet region, which also includes the green region. The higher the value of the current, the more the stability region tightens around precise values of k and filter cut-off frequency. In Fig. 3.17 the same analysis is carried out with a control bandwidth of $1000\,Hz$. As can be seen, the stability region relative to $I_{oq} = 13\,A$ has disappeared, the remaining ones are shrunken. Finally, Fig. 3.18 shows the analysis for the $1200\,Hz$ control bandwidth. Where the maximum current appears to be $I_{oq} = 7\,A$. So the higher the control bandwidth, the lower the stabilizing effect. In addition, a control bandwidth limit has been found, in fact above $1200\,Hz$ the system is always unstable.

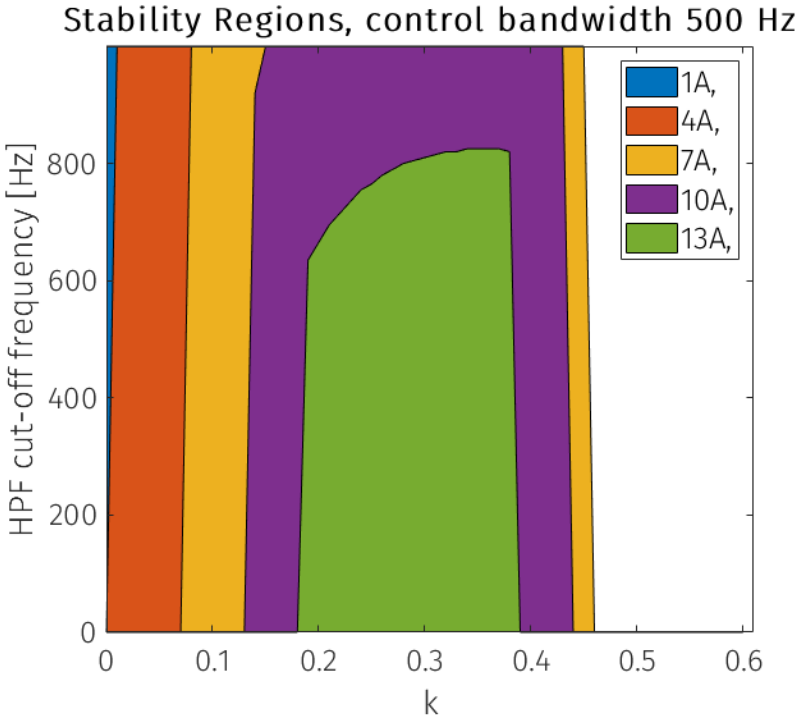

Figure 3.16: Stability Analysis as a function of k, f_{cut_HPF} and I_{oq}, $\omega_c = 500\,Hz$

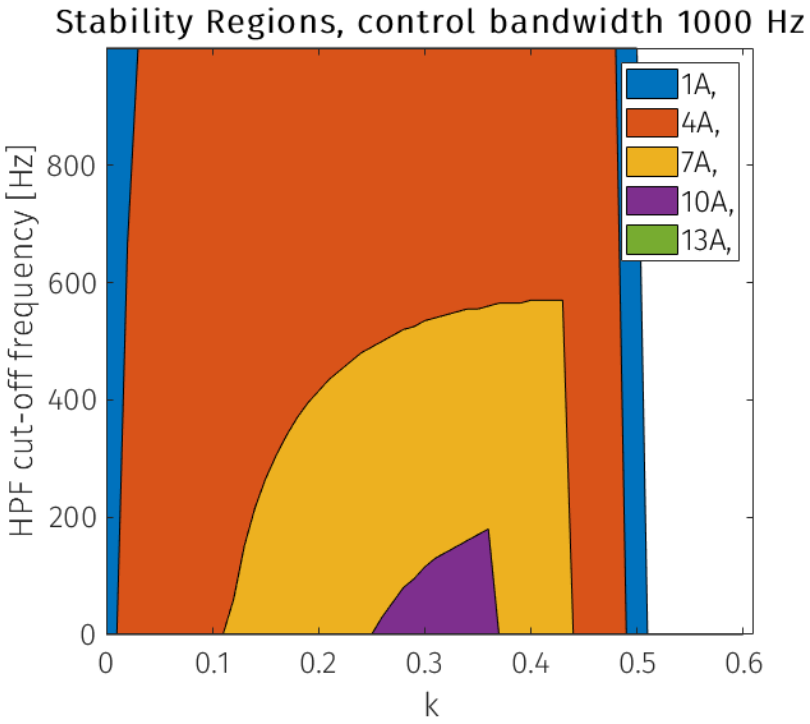

Figure 3.17: Stability Analysis as a function of k, f_{cut_HPF} and I_{oq}, $\omega_c = 1000\,Hz$

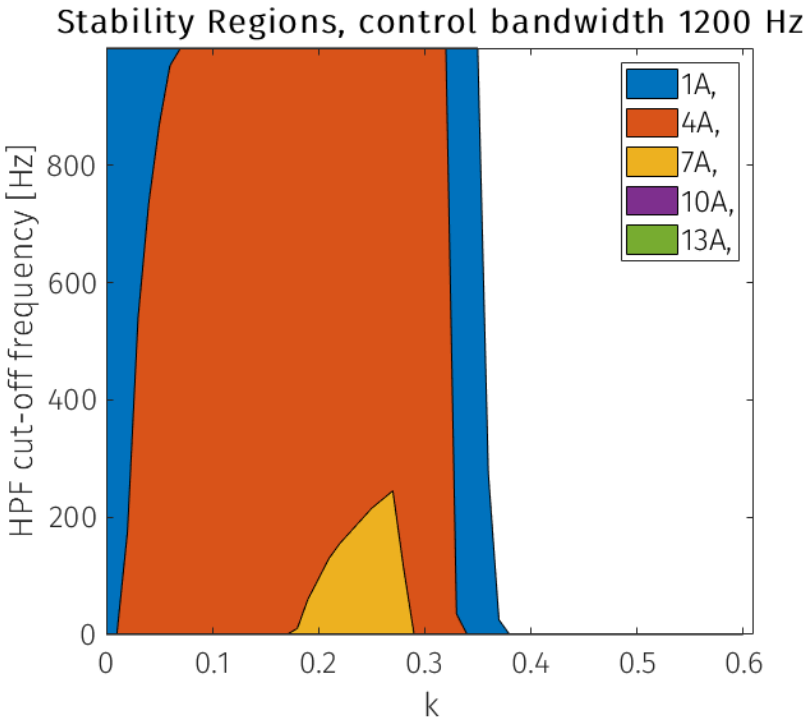

Figure 3.18: Stability Analysis as a function of k, f_{cut_HPF} and I_{oq}, $\omega_c = 1200\,Hz$

3.5.2 Motor Mode Stabilization Method Simulation

The results of the simulation of the stabilisation method in motor mode are presented below. A schematic of the simulation is presented in Fig. 3.19. In Fig. 3.20 the input and output variables are reported in their corresponding dq reference frame, with a sampling time equal to T_s, while in Fig. 3.21 the three-phase waveforms are reported with a sampling time of $T_s/10$. The simulations are carried out with the system parameters reported in Tab. 3.5 and the control parameters reported in 3.6. The gain k has been set equal to 0.3 and the cut-off frequency has been selected equal to $100\,Hz$, according with the results in Fig. 3.17. As the simulations show, the system is unstable at $I_{oq\_r} = 10\,A$. But as observed in the case of the closed-loop SM-PMSM system without any stabilisation, the system is slightly more unstable than predicted. For the same control bandwidth $1000\,Hz$, the system without control was already unstable at $3\,A$ $(171\,W)$, whereas by applying stabilisation, the system was unstable at $10\,A$ $(580\,W)$. The power capacity of the converter was more then tripled. This will be the benchmark in motor mode for the new stabilization method proposed in the following chapter.

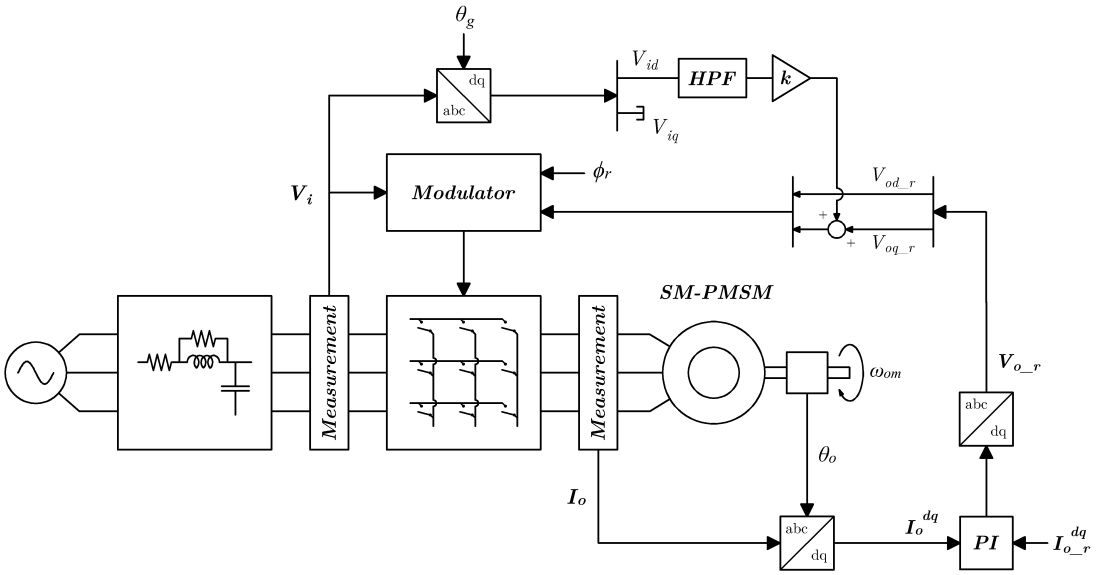

Figure 3.19: Closed-loop schematic with HPF motor mode stabilization method

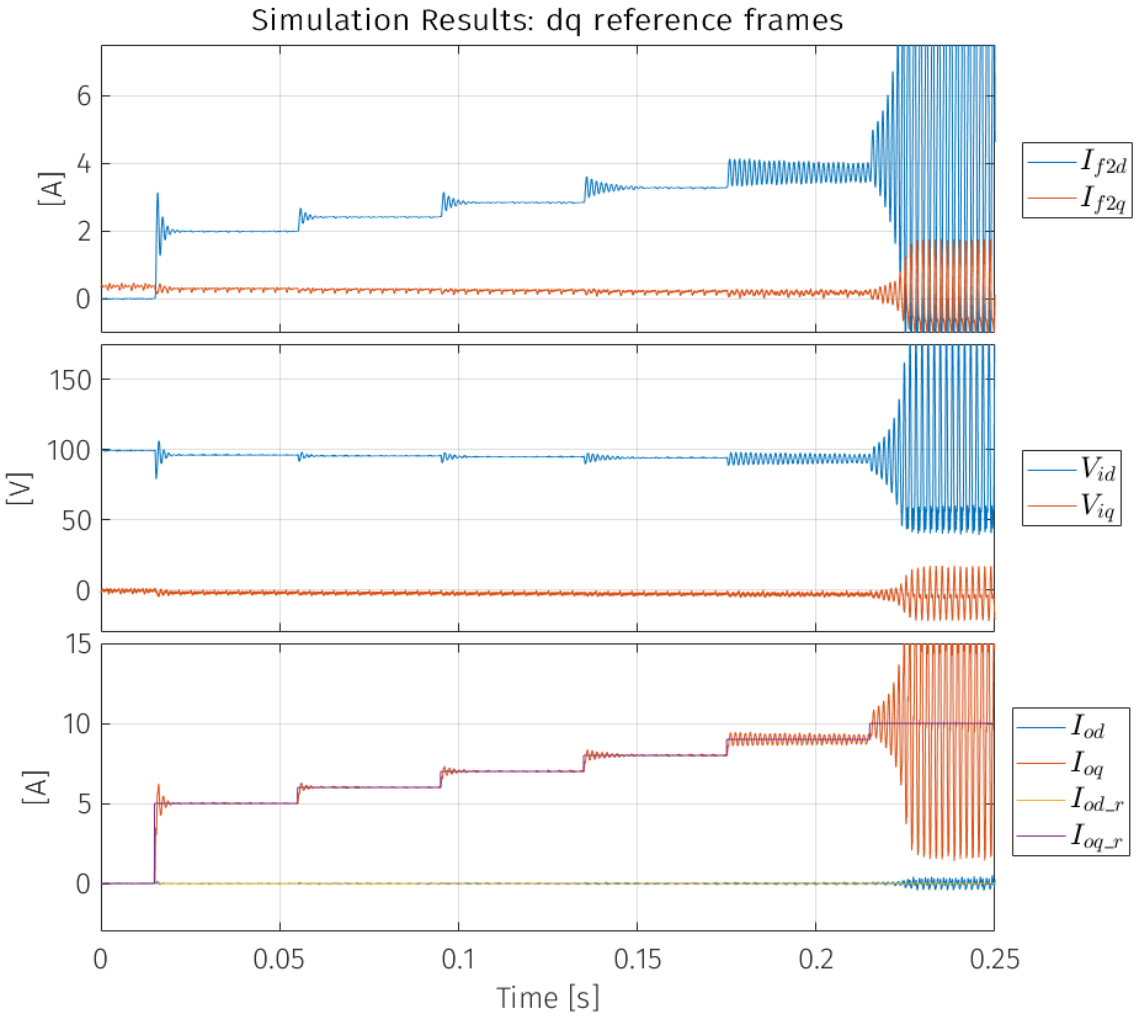

Figure 3.20: Simulations result in the input and output dq reference frame as I_{oq_r} increases, sample time T_s

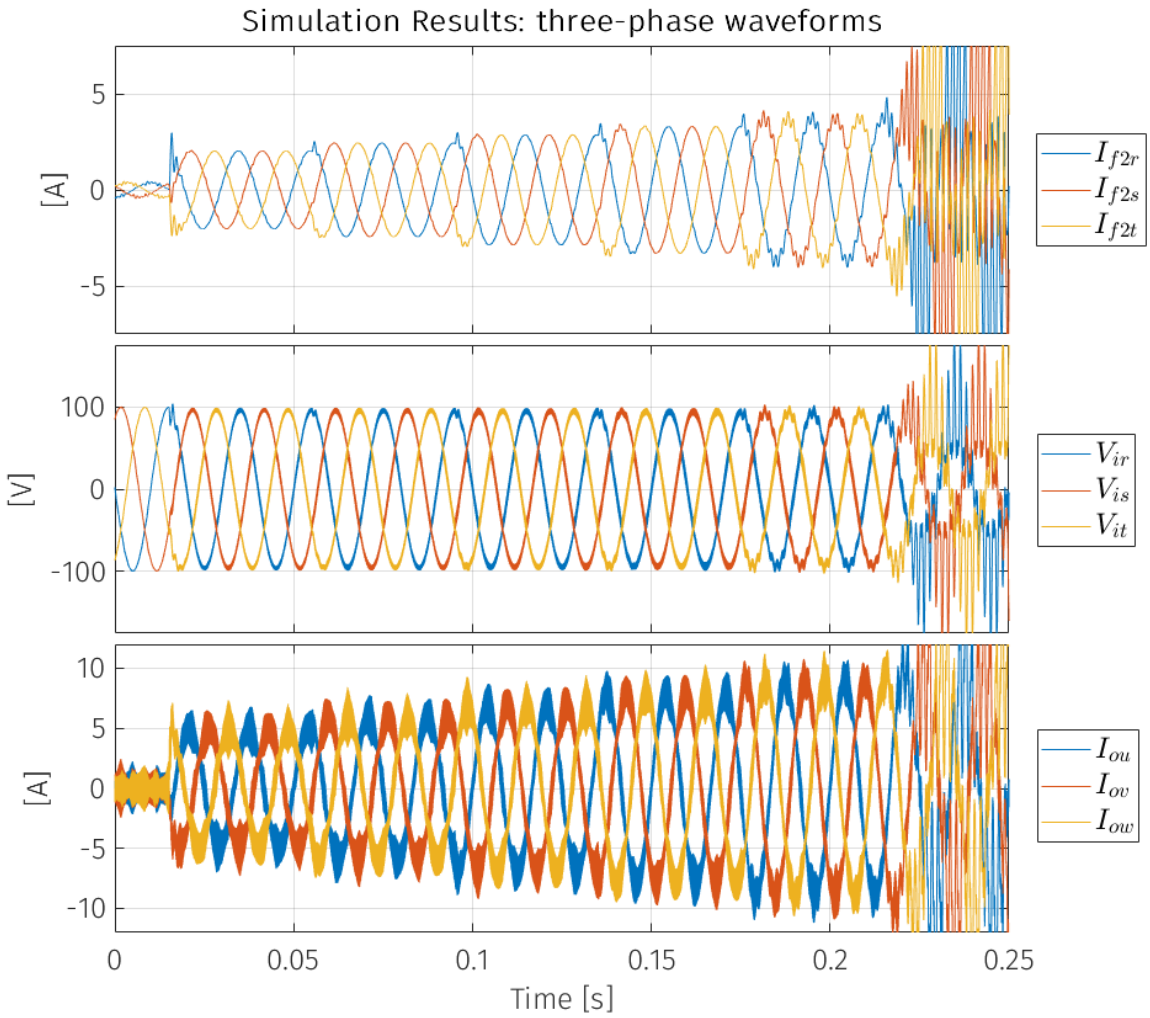

Figure 3.21: Three-Phase waveforms as I_{od_r} increases, sample time $T_s/10$

3.5.3 Generator Mode Stabilization Method

In generator mode, the correction term is no longer applied to the voltage reference, but the stabilising action is applied by modifying the voltage measurement $\boldsymbol{V}_i$ supplied to the modulator. This time, however, the measurements are not simply filtered, but the angle of $\boldsymbol{V}_i$ modified. The angle θ_v as shown in the previous chapter can be calculated as follows, transforming the three-phase vector $\boldsymbol{V}_i$ in the $\alpha\beta$ domain.

$$\theta_v = arctan\left(\frac{V_{i\beta}}{V_{i\alpha}}\right) \tag{3.78}$$

This angle is used to transform the vector $\boldsymbol{V}_i$ in to the dq reference frame oriented with itself, obtaining $\boldsymbol{V}_i^{dq}$. The correction term is obtained filtering the angle θ_v trough an HPF and multiplied by the gain k_θ.

$$c_\theta = k_\theta \left(\frac{\tau_\theta\, s}{\tau_\theta\, s + 1}\right) \theta_v \tag{3.79}$$

With: $\tau_\theta = \dfrac{1}{2\,\pi\, f_{cut\_HPF\_\theta}}$

The correction term is then add to $theta_v$:

$$\tilde{\theta}_v = \theta_v + c_\theta = \theta_v + k_\theta \left(\frac{\tau_\theta\, s}{\tau_\theta\, s + 1}\right) \theta_v \tag{3.80}$$

The angle thus obtained is used to anti-transform the vector $\boldsymbol{V}_i^{dq}$ thus obtaining the vector $\tilde{\boldsymbol{V}}_i$. This is then supplied to the modulator. No studies have been carried out on the closed-loop stability of this stabilisation method. Unfortunately, no mathematical procedure has been found to analyse the effect of changing the angle of the voltage used for modulation. However, the method was tested in simulation and the tuning of the k_θ and $f_{cut\_HPF\_\theta}$ parameters was carried out as indicated in [4] by simulations, to find the values that maximise the improvement. The best results have been carried out with $k_\theta = -0.63$ and $f_{cut\_HPF\_\theta} = 100\,Hz$

3.5.4 Generator Mode Stabilization Method Simulation

The simulator schematic is reported in Fig. 3.22. Fig. 3.23 shows the simulation results, sampled at the switching frequency T_s, in the usual dq synchronous reference frame, while Fig. 3.24 shows the waveform trends, sampled at $T_s/10$. The simulations are obtained using the system parameters given in Tab. 3.5 and the control parameters reported in Tab. 3.6. Instability occurs for $I_{oq\_r} = -14\,A\,(-762\,W)$. Compared to the case without the stabilisation method, whose instability occurred at $I_{oq\_r} = -5\,A\,(-278\,W)$, the power in this case is almost three times higher. Note, however, the progressive worsening of the oscillations and ripple of the output current and input voltage in the figure. The result of this method for the generator mode will be the benchmark for the generator mode stabilization method presented in the following chapter.

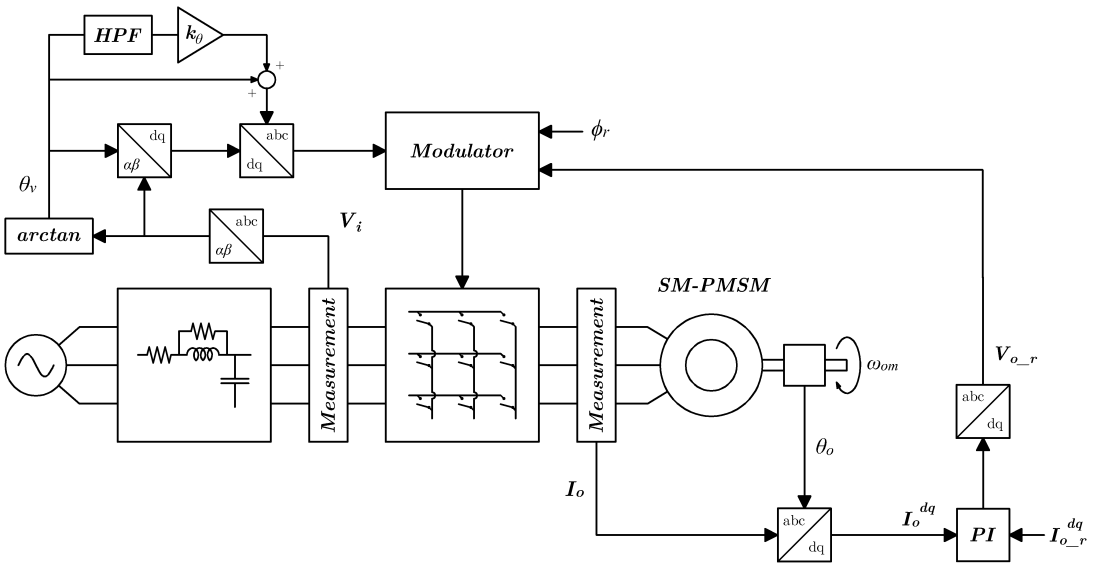

Figure 3.22: Closed-loop schematic with HPF generator mode stabilization method

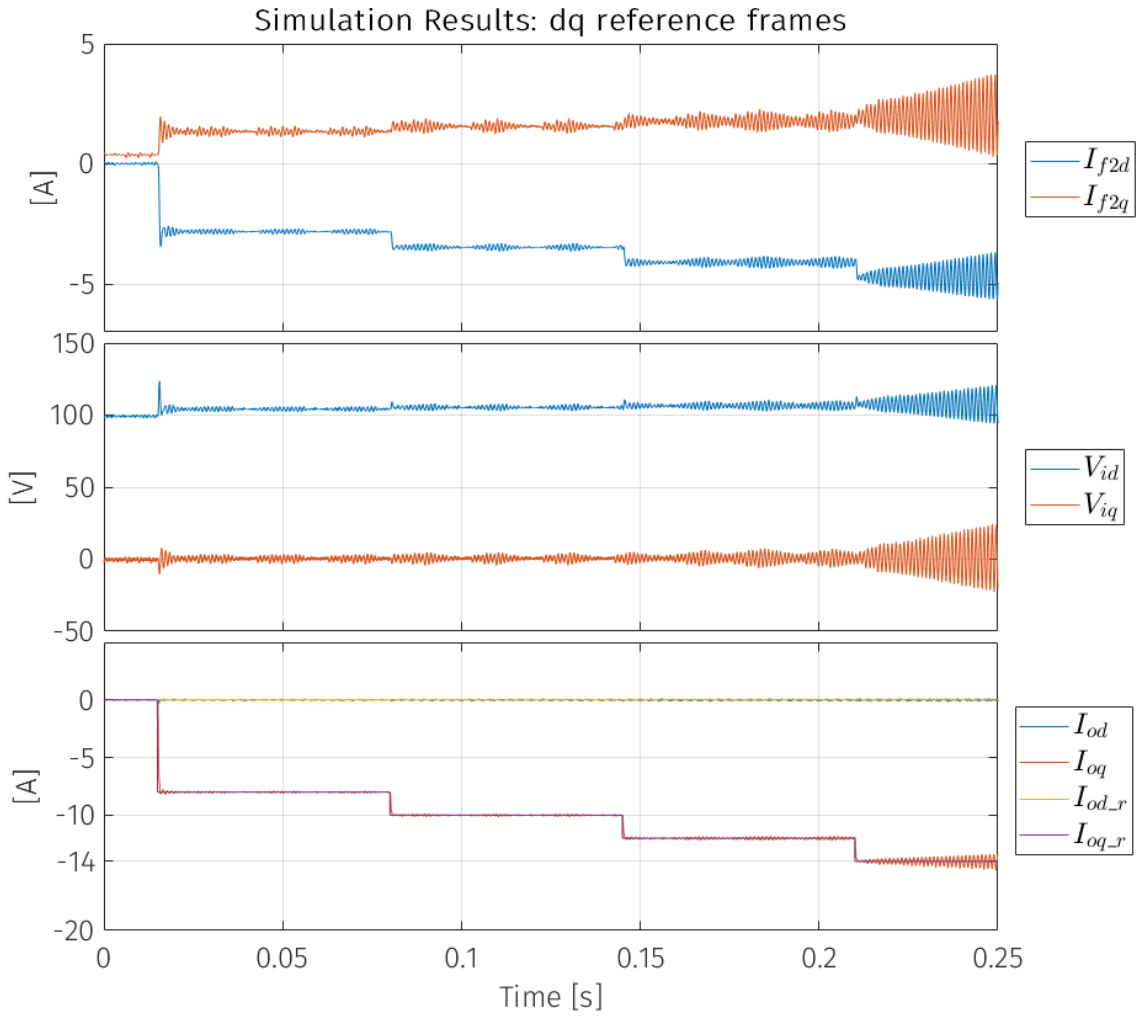

Figure 3.23: Simulations result in the input and output dq reference frame as I_{oq_r} increases, sample time T_s

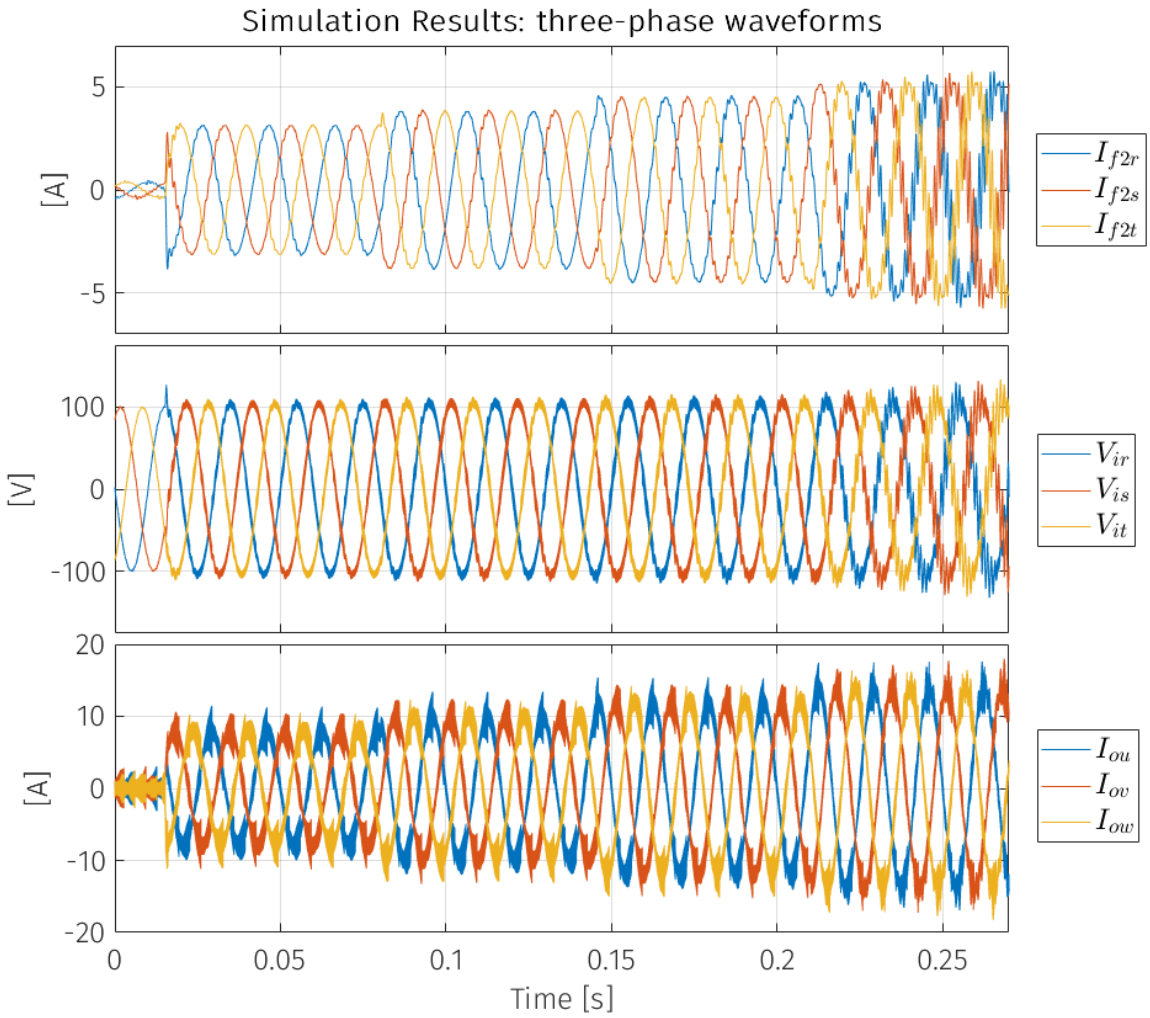

Figure 3.24: Three-Phase waveforms as I_{od_r} increases, sample time $T_s/10$

3.6 Chapter Summary

In this chapter, the methodology used to study the closed-loop stability of the system in the case of both RL and bidirectional load was presented. The stabilization methods have also been studied and their performance in terms of stability has been analysed through modelling and simulation. It is concluded that the main limitation of the proposed stabilisation methods is the control bandwidth, which limits their effectiveness.

References 3

[1] G. F. Franklin, J. D. Powell, and M. L. Workman, Digital control of dynamic systems, vol. 3. Addison-wesley Menlo Park, CA, 1998.

[2] L. Zarri, Control of matrix converters. PhD thesis, alma, Maggio 2007.

[3] D. Casadei, G. Serra, A. Tani, and L. Zarri, "Effects of input voltage measurement on stability of matrix converter drive system," IEE Proceedings - Electric Power Applications, vol. 151, pp. 487–497, July 2004.

[4] Y. Sun, M. Su, X. Li, H. Wang, and W. Gui, "A general constructive approach to matrix converter stabilization," IEEE Transactions on Power Electronics, vol. 28, no. 1, pp. 418–431, 2013.

Chapter 4:

New Stabilization Strategy based on Full State Feedback

The stabilization method proposed in this dissertation is based on full state feedback also known as pole placement. The methods proposed up to now were designed to work together with classical control methods such as PI controllers, which use the output current measurement as feedback to its control. Full state feedback, on the other hand, uses all system variables as feedback to control the output current, as will be seen, and allows control of the position of the poles of the closed-loop system through the feedback gains ensuring high robustness and control bandwidth. The only limitation to this method is that it is necessary to know all the state variables of the system. In the previously proposed algorithms, the only measurements required for their operation were the input voltages for modulation and the output current for control. In the case of full state feedback, it is also necessary to know the current flowing in the filter inductor. This problem can be solved by the use of an observer, which allows an estimate of the current value so that no additional measurements need to be added. Also in the full state feedback case, two separate controls are defined for motor mode and generator mode. In motor mode the control input are the output current reference, while in generator mode also the input phase shift is considered as control input. This chapter will introduce the concept of full state feedback and its operating principle. Next, the system used for the design of control algorithms in motor mode and generator mode will be introduced together with the input current observer. Subsequently, the control algorithms in motor mode and generator mode will be introduced and described. The algorithm for calculating feedback gains is then presented. Finally, stability analysis and simulated results are presented.

4.1 Discrete Full State Feedback

Consider the discrete dynamic system defined by the following equations:

$$\begin{aligned} \boldsymbol{x}(k+1) &= \boldsymbol{\Phi}\,\boldsymbol{x}(k) + \boldsymbol{\Gamma}\,\boldsymbol{u}(k) \\ \boldsymbol{y}(k) &= \boldsymbol{H}\boldsymbol{x}(k) + \boldsymbol{J}\boldsymbol{u}(k) \end{aligned} \tag{4.1}$$

Where $\boldsymbol{x} \in \mathbb{R}^{m\times 1}$, $\boldsymbol{u} \in \mathbb{R}^{n\times 1}$ and $\boldsymbol{y} \in \mathbb{R}^{h\times 1}$. The dynamics of the system and information on its stability are encapsulated within the $\boldsymbol{\Phi}$ matrix. Now, assuming access to all state variables of system $\boldsymbol{x}(k)$, consider the system shown in the figure, where full state feedback is added.

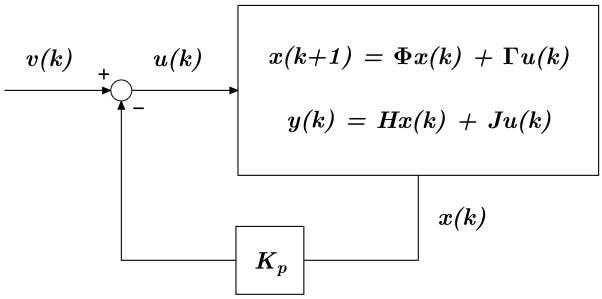

Figure 4.1: Full State Feedback Schematic

Where $\boldsymbol{v} \in \mathbb{R}^{n\times 1}$. The feedback is given by a linear combination of all the state variables:

$$\boldsymbol{u}(k) = \boldsymbol{v}(k) - \boldsymbol{K}_p\,\boldsymbol{x}(k) = \boldsymbol{v}(k) - \begin{bmatrix} K_{p\_11} & K_{p\_12} & \dots & K_{p\_1m} \\ K_{p\_21} & K_{p\_22} & \dots & K_{p\_2m} \\ \vdots & \vdots & \ddots & \vdots \\ K_{p\_n1} & K_{p\_n2} & \dots & K_{p\_nm} \end{bmatrix} \begin{bmatrix} x_1(k) \\ x_2(k) \\ \vdots \\ x_m(k) \end{bmatrix} \tag{4.2}$$

The input vector thus obtained is substituted in the first equation of (4.1).

$$\boldsymbol{x}(k+1) = \boldsymbol{\Phi}\,\boldsymbol{x}(k) + \boldsymbol{\Gamma}\left[\boldsymbol{v}(k) - \boldsymbol{K}_p\,\boldsymbol{x}(k)\right] \tag{4.3}$$

It is now possible to collect everything that depends on $\boldsymbol{x}$ in the (4.3), obtaining:

$$\boldsymbol{x}\left(k+1\right)=\left[\boldsymbol{\Phi}-\boldsymbol{\Gamma}\boldsymbol{K}_{p}\right]\boldsymbol{x}\left(k\right)+\boldsymbol{\Gamma}\boldsymbol{v}\left(k\right) \tag{4.4}$$

The dynamics of the obtained system is therefore different from that of the starting system. In particular it depends on the eigenvalues of the following matrix:

$$\left[\boldsymbol{\Phi}-\boldsymbol{\Gamma}\boldsymbol{K}_{p}\right] \tag{4.5}$$

Through the appropriate choice of the $\boldsymbol{K}_{p}\in\mathbb{R}^{n\times m}$ matrix, it is possible to select the position of the poles of the system, that is why the method is also named pole placement. The choice of poles and consequently of the $\boldsymbol{K}_{p}$ is a complex problem to solve in the case of Multiple-Input and Multiple-Output (MIMO) systems. They must in fact be chosen in such a way as to guarantee stability and robustness. The method applied for the calculation of the K-matrix will be introduced later in a dedicated section. The assumption that all the system variables are available is typically not met in real application, as it is neither convenient nor possible to measure all system variables. To this end, observers of state variables are introduced, which overcome this inconvenience.

4.1.1 Integral Control Introduction by State Augmentation

What was presented above related to the poles placement of the open loop system. In the reality of the application, it is necessary to control one or more of the system state variables or an output variables. It is therefore necessary to include a controller. An integrator is added to evaluate the integral of the error between the reference vector $\boldsymbol{r}$ and the variables to be controlled, defined as $\boldsymbol{x}_{i},\boldsymbol{r}\in\mathbb{R}^{w\times 1}$ The error is then multiplied by the gain matrix $\boldsymbol{K}_{i}\in\mathbb{R}^{n\times w}$. Consider the schematic reported in Fig. 4.2. To simplify the calculation, the output equation of the open-loop state-space system is reduced as follows:

$$\begin{aligned}\boldsymbol{x}\left(k+1\right)&=\boldsymbol{\Phi}\,\boldsymbol{x}\left(k\right)+\boldsymbol{\Gamma}\,\boldsymbol{u}\left(k\right)\\ \boldsymbol{y}\left(k\right)&=\boldsymbol{H}\boldsymbol{x}\left(k\right)\end{aligned} \tag{4.6}$$

The integrator is discretized with Forward Euler method with respect to the switching frequency. The introduction of this component introduces additional state variables,

defined by the following equations:

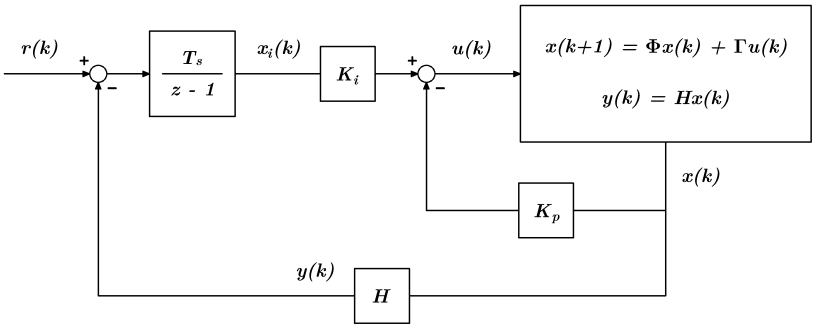

Figure 4.2: Full State Feedback with Integrator Schematic

$$\boldsymbol{x}_i\left(k+1\right)=\boldsymbol{x}_i\left(k\right)+T_s\ \left(\boldsymbol{r}\left(k\right)-\boldsymbol{H}\boldsymbol{x}\left(k\right)\right) \tag{4.7}$$

The input voltage vector $\boldsymbol{u}$ is now defined as:

$$\boldsymbol{u}\left(k\right)=\boldsymbol{K}_i\,\boldsymbol{x}_i\left(k\right)-\boldsymbol{K}_p\,\boldsymbol{x}\left(k\right) \tag{4.8}$$

Which can be replaced in (4.6) resulting in.

$$\boldsymbol{x}\left(k+1\right)=\boldsymbol{\Phi}\,\boldsymbol{x}\left(k\right)+\boldsymbol{\Gamma}\left[\boldsymbol{K}_i\,\boldsymbol{x}_i\left(k\right)-\boldsymbol{K}_p\,\boldsymbol{x}\left(k\right)\right]. \tag{4.9}$$

It is possible to obtain the augmented system representing the behaviour of the closed-loop state-space by combining (4.7) and (4.9).

$$\begin{bmatrix}\boldsymbol{x}\left(k+1\right)\\ \boldsymbol{x}_i\left(k+1\right)\end{bmatrix}=\begin{bmatrix}\boldsymbol{\Phi}-\boldsymbol{\Gamma}\boldsymbol{K}_p & \boldsymbol{\Gamma}\boldsymbol{K}_i\\ -T_s\boldsymbol{H} & \boldsymbol{I}\end{bmatrix}\begin{bmatrix}\boldsymbol{x}\left(k\right)\\ \boldsymbol{x}_i\left(k\right)\end{bmatrix}+\begin{bmatrix}\boldsymbol{0}\\ T_s\boldsymbol{I}\end{bmatrix}\boldsymbol{r}\left(k\right) \tag{4.10}$$

The input vector can therefore be represented as follows:

$$\boldsymbol{u}\left(k\right)=\begin{bmatrix}-\boldsymbol{K}_p & \boldsymbol{K}_i\end{bmatrix}\begin{bmatrix}\boldsymbol{x}\left(k\right)\\ \boldsymbol{x}_i\left(k\right)\end{bmatrix} \tag{4.11}$$

It is evident that the integrator gain matrix $\boldsymbol{K}_i$ and $\boldsymbol{K}_p$ state feedback matrix generate an augmented state feedback matrix that can be calculated to ensure stability and high control bandwidth. But in order to be able to integrate the control within a DSP, a further step must be taken.

4.1.2 Delay Step Application

As introduced for PI controllers, the DSP at each switching period applies the control output that has been calculated in the previous switching period. In terms of the control algorithm, this means that the input vector of the state-space system is affected by a delay. This can be written as:

$$\boldsymbol{u}_d\left(k+1\right) = \boldsymbol{u}\left(k\right) \tag{4.12}$$

New state variables are then introduced into the system, and a new feedback gain matrix $\boldsymbol{K}_d \in \mathbb{R}^{n\times n}$ for these state variables must be added. Please refer to Fig. 4.3

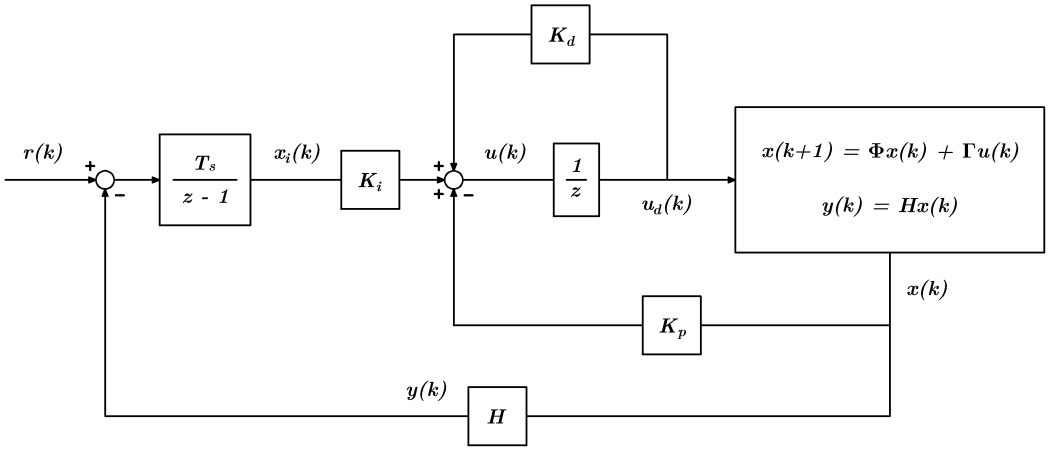

Figure 4.3: Full State Feedback with Integrator and Delay Step Schematic

The equations of state variables of the resulting closed loop system are given below:

$$\begin{aligned}
\boldsymbol{x}\left(k+1\right) &= \boldsymbol{\Phi}\,\boldsymbol{x}\left(k\right) + \boldsymbol{\Gamma}\,\boldsymbol{u}_d\left(k\right) \\
\boldsymbol{x}_i\left(k+1\right) &= \boldsymbol{x}_i\left(k\right) + T_s\,\left(\boldsymbol{r}\left(k\right) - \boldsymbol{H}\boldsymbol{x}\left(k\right)\right) \\
\boldsymbol{u}_d\left(k+1\right) &= \boldsymbol{K}_i\,\boldsymbol{x}_i\left(k\right) + \boldsymbol{K}_d\,\boldsymbol{u}\left(k\right) - \boldsymbol{K}_p\,\boldsymbol{x}\left(k\right)
\end{aligned} \tag{4.13}$$

The system can be rewritten by combining the state variables into a single vector and constructing the augmented matrix of the closed-loop system.

$$\begin{bmatrix} \boldsymbol{x}(k+1) \\ \boldsymbol{x}_i(k+1) \\ \boldsymbol{u}_d(k+1) \end{bmatrix} = \begin{bmatrix} \boldsymbol{\Phi} & \mathbf{0} & \boldsymbol{\Gamma} \\ -T_s\boldsymbol{H} & \boldsymbol{I} & \mathbf{0} \\ -\boldsymbol{K}_p & \boldsymbol{K}_i & \boldsymbol{K}_d \end{bmatrix} \begin{bmatrix} \boldsymbol{x}(k) \\ \boldsymbol{x}_i(k) \\ \boldsymbol{u}_d(k) \end{bmatrix} + \begin{bmatrix} \mathbf{0} \\ T_s\boldsymbol{I} \\ \mathbf{0} \end{bmatrix} \boldsymbol{r}(k) \tag{4.14}$$

The input vector of the state-space model is then defined as follows, with respect to the augmented state vector.

$$\boldsymbol{u}(k) = \begin{bmatrix} -\boldsymbol{K}_p & \boldsymbol{K}_i & \boldsymbol{K}_d \end{bmatrix} \begin{bmatrix} \boldsymbol{x}(k) \\ \boldsymbol{x}_i(k) \\ \boldsymbol{u}_d(k) \end{bmatrix} = \boldsymbol{K}\,\boldsymbol{x}_{cl}(k) \tag{4.15}$$

Where $\boldsymbol{K}_d \in \mathbb{R}^{n\times(m+w+n)}$. The closed-loop model to be used and implemented on the DSP was then defined. Through the appropriate choice of $\boldsymbol{K}_p$, $\boldsymbol{K}_i$ and $\boldsymbol{K}_d$ matrices, it is possible to obtain in simulation and experimentally a control capable of guaranteeing high performance in terms of control bandwidth and robustness.

4.2 H_2-LMI control tuning

To proceed to the calculation of the $\boldsymbol{K}$, consider (4.15) rewritten in the following form:

$$\boldsymbol{x}_{cl}(k+1) = \boldsymbol{A}\,\boldsymbol{x}_{cl}(k) + \boldsymbol{B}\,\boldsymbol{u}_d(k) + \boldsymbol{F}\,\boldsymbol{r}(k) \tag{4.16}$$

An elegant way to calculate the feedback gain $\boldsymbol{K}$ is to solve an H_2 control problem. The system can be rewritten as

$$\begin{cases} \boldsymbol{x}(k+1) = \boldsymbol{A}\boldsymbol{x}(k) + \boldsymbol{B}\boldsymbol{u}_d(k) + \boldsymbol{B}_1\boldsymbol{\xi}(k) \\ \boldsymbol{y}(k) = \boldsymbol{C}_2 x + \boldsymbol{D}_2 u_d(k) \\ \boldsymbol{u}_d(k) = \boldsymbol{K}\boldsymbol{x}(k) \end{cases} \tag{4.17}$$

where the reference $\boldsymbol{r}$ has been dropped, $\boldsymbol{\xi} \in \mathbb{R}^{12\times1}$ is the system disturbance, $\boldsymbol{y} \in \mathbb{R}^{15\times1}$ is the performance output and $\boldsymbol{B}_1$, $\boldsymbol{C}_2$ and $\boldsymbol{D}_2$ are matrices of appropriate dimentions.

It can be demonstrated [1, 2] the optimal feedback gain $\boldsymbol{K}$ that minimizes the H_2 norm from $\boldsymbol{\xi}$ to $\boldsymbol{y}$ can be found solving the following Linear Matrix Inequality (LMI) problem

$$\begin{aligned}
&\min_{\boldsymbol{L},\boldsymbol{P}} \quad \text{trace}(\boldsymbol{Z}) \\
&s.t. \\
&\begin{bmatrix} -\boldsymbol{P} & \boldsymbol{P}\boldsymbol{A}^T + \boldsymbol{L}^T\boldsymbol{B}^T \\ \boldsymbol{A}\boldsymbol{P} + \boldsymbol{B}\boldsymbol{L} & -\boldsymbol{P} + \boldsymbol{B}_1\boldsymbol{B}_1^T \end{bmatrix} \leq 0 \\
&\begin{bmatrix} -\boldsymbol{Z} & \boldsymbol{C}_2\boldsymbol{P} + \boldsymbol{D}_2\boldsymbol{L} \\ \boldsymbol{P}\boldsymbol{C}_2^T + \boldsymbol{L}^T\boldsymbol{D}_2 & -\boldsymbol{P} \end{bmatrix} \leq 0
\end{aligned} \tag{4.18}$$

where $\boldsymbol{K} = \boldsymbol{L}\boldsymbol{P}^{-1}$. The advantage of solving the H_2 control problem as an LMI problem is the possibility to keep in consideration system parameters change. If n affine parameters $p_1, \ldots, p_n$ are uncertain and can vary in the intervals $[p_1^{min}, p_1^{max}] \ldots [p_n^{min}, p_n^{max}]$, it is possible to represent the uncertain system as a polytopic system with 2^n vertices obtained by all the possible combinations of interval extremes. The first equation in (4.17) is modified as

$$\boldsymbol{x}(k+1) = \boldsymbol{A}_i\boldsymbol{x}(k) + \boldsymbol{B}_i\boldsymbol{u}_d(k) + \boldsymbol{B}_1\boldsymbol{\xi}(k) \tag{4.19}$$

with $i \in [1, \ldots, 2^n]$. Problem (4.18) can be adapted by adding an LMI constraint for each vertices

$$\begin{bmatrix} -\boldsymbol{P} & \boldsymbol{P}\boldsymbol{A}_i^T + \boldsymbol{L}^T\boldsymbol{B}_i^T \\ \boldsymbol{A}_i\boldsymbol{P} + \boldsymbol{B}_i\boldsymbol{L} & -\boldsymbol{P} + \boldsymbol{B}_1\boldsymbol{B}_1^T \end{bmatrix} \leq 0, \quad i \in [1, \ldots, 2^n] \tag{4.20}$$

This ensures system stability for any parameters value inside the convex polytope [1]. This property can be also exploited to improve the stabilization property of the full state feedback control when applied to nonlinear systems. In fact, matrix $\boldsymbol{\Phi}$ and $\boldsymbol{\Gamma}$ (and in turn $\boldsymbol{A}$ and $\boldsymbol{B}$) in the matrix converter applications have some terms that depend from system states, due to the linearization, that can be treated as varying parameters. The polytopic representation previously described can be utilized to handle their variation and improve the overall system stability.

4.2.1 H_2-LQR Relation

It can be demonstrated [2] problem (4.18) is equivalent to the Linear Quadratic Regulator (LQR) problem, i.e. finding the control action that minimizes the performance index

$$\boldsymbol{J} = \sum_{k=1}^{\infty} \boldsymbol{x}(k)^T \boldsymbol{Q} \boldsymbol{x}(k) + \boldsymbol{u}(k)^T \boldsymbol{R} \boldsymbol{u}(k) \tag{4.21}$$

if the following relations hold

$$\boldsymbol{C}_2 = \begin{bmatrix} \sqrt{\boldsymbol{Q}} \\ 0 \end{bmatrix}, \quad \boldsymbol{D}_2 = \begin{bmatrix} 0 \\ \sqrt{\boldsymbol{R}} \end{bmatrix}, \quad \boldsymbol{B}_2 = \boldsymbol{I} \tag{4.22}$$

Where $\boldsymbol{Q}$ is the weighting matrix for the system states and $\boldsymbol{R}$ is the weighting matrix for the control input. This equivalence between the two problems result is useful to simplify the controller tuning, as described previously.

4.3 Simplified Open-Loop State-Space Model for H_2-LMI

The mathematical open-loop state-space model of the system that is used for tuning of the matrix $\boldsymbol{K}$ is similar to that presented in (2.102) in Chapter 2. In this case, however, a modification is made to the input filter model. The parallel resistor R_{pf} inserted to reduce the gain at the filter resonance frequency and make it more similar to the experimental apparatus is removed, as shown in Fig. 4.4.

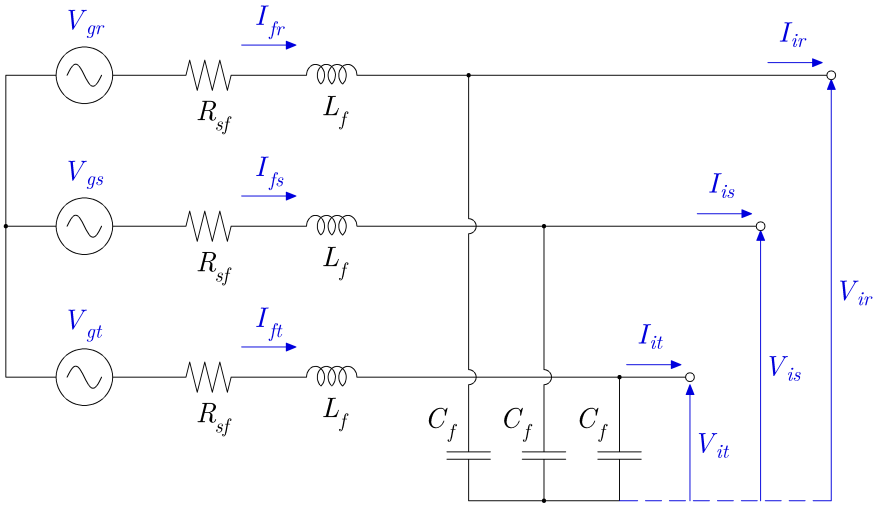

Figure 4.4: Input Filter Design

This implies a higher degree of instability in the model. However, this condition is beneficial, as stabilizing the model without this resistance ensures an even greater stability in the presence of the resistance, and, consequently, in the real system. The input-side equations in the abc domain are reported in the following:

$$\begin{aligned} \frac{d}{dt}\boldsymbol{I}_f &= \frac{1}{L_f}\left(\boldsymbol{V}_g - R_{sf}\,\boldsymbol{I}_f - \boldsymbol{V}_i\right) \\ \frac{d}{dt}\boldsymbol{V}_i &= \frac{1}{C_f}\left(\boldsymbol{I}_f - \boldsymbol{I}_{id}\right) \end{aligned} \tag{4.23}$$

That can be transformed in the dq reference frame

$$\begin{aligned} \frac{d}{dt}I_{fd} &= \frac{1}{L_f}\left(V_{gd} - R_{sf}\,I_{fd} - V_{id}\right) + \omega_i\,I_{f2q} \\ \frac{d}{dt}I_{fq} &= \frac{1}{L_f}\left(V_{gq} - R_{sf}\,I_{fq} - V_{iq}\right) - \omega_i\,I_{f2d} \\ \frac{d}{dt}V_{id} &= \frac{1}{C_f}\left(I_{fd} - I_{id}\right) + \omega_i\,V_{iq} \\ \frac{d}{dt}V_{iq} &= \frac{1}{C_f}\left(I_{f2q} - I_{iq}\right) - \omega_i\,V_{id} \end{aligned} \tag{4.24}$$

At the output-side it is connected the SM-PMSM with imposed speed, the relations remains unchanged and are the following:

$$\begin{aligned} \frac{d}{dt}\,I_{od} &= \frac{1}{L_o}\left(V_{od} - R_o\,I_{od}\right) + \omega_o\,I_{oq} \\ \frac{d}{dt}\,I_{oq} &= \frac{1}{L_o}\left(V_{oq} - R_o\,I_{oq} - \omega_o\,\Phi_{PM}\right) - \omega_o\,I_{od} \end{aligned} \tag{4.25}$$

As seen in previous chapters, the equations are linked by the relationships of the average model of the matrix converter.

$$\begin{aligned} I_{id} &= \left(V_{od\_r}I_{od} + V_{oq\_r}I_{oq}\right)\,\frac{V_{id}\,cos\left(\phi_r\right) - V_{iq}\,sin\left(\phi_r\right)}{\left|\boldsymbol{V}_i^{\,dq}\right|^2\,cos\left(\phi_r\right)}; \\ I_{iq} &= \left(V_{od\_r}I_{od} + V_{oq\_r}I_{oq}\right)\,\frac{V_{iq}\,cos\left(\phi_r\right) + V_{id}\,sin\left(\phi_r\right)}{\left|\boldsymbol{V}_i^{\,dq}\right|^2\,cos\left(\phi_r\right)} \\ V_{od} &= V_{od\_r} \qquad V_{oq} = V_{oq\_r} \end{aligned} \tag{4.26}$$

In the following page the complete system model is reported. As before the resulting system of equations identifies a nonlinear model.

$$
\underbrace{
\begin{aligned}
\frac{d}{dt} I_{fd} &= \frac{1}{L_f}\left(V_{gd} - R_{sf}\, I_{fd} - V_{id}\right) + \omega_i\, I_{f2q} \\
\frac{d}{dt} I_{fq} &= \frac{1}{L_f}\left(V_{gq} - R_{sf}\, I_{f2q} - V_{iq}\right) - \omega_i\, I_{f2d} \\
\frac{d}{dt} V_{id} &= \frac{1}{C_f}\left(I_{fd} - \left(V_{od\_r} I_{od} + V_{oq\_r} I_{oq}\right)\frac{V_{id}\, cos\left(\phi_r\right) - V_{iq}\, sin\left(\phi_r\right)}{\left|\boldsymbol{V}_i^{dq}\right|^2\, cos\left(\phi_r\right)}\right) + \omega_i\, V_{iq} \\
\frac{d}{dt} V_{iq} &= \frac{1}{C_f}\left(I_{fq} - \left(V_{od\_r} I_{od} + V_{oq\_r} I_{oq}\right)\frac{V_{iq}\, cos\left(\phi_r\right) + V_{id}\, sin\left(\phi_r\right)}{\left|\boldsymbol{V}_i^{dq}\right|^2\, cos\left(\phi_r\right)}\right) - \omega_i\, V_{id} \\
\frac{d}{dt} I_{od} &= \frac{V_{od\_r} - R_o\, I_{od}}{L_o} + \omega_o\, I_{oq} \\
\frac{d}{dt} I_{oq} &= \frac{V_{oq\_r} - R_o\, I_{oq} - \omega_o\, \Phi_{PM}}{L_o} - \omega_o\, I_{od}
\end{aligned}
} \tag{4.27}
$$

4.4 Input Current Observer

The model defined in Section 4.3 will be used for tuning the $\boldsymbol{K}$ for the stabilization methods that will be presented later. However, it is also useful for defining a fundamental component of this control algorithm, the observer of the input currents $\boldsymbol{I}_f$. The other control strategies rely only on the measurement of input voltages $\boldsymbol{V}_i$ and on the output current $\boldsymbol{I}_o$. $\boldsymbol{V}_i$ is necessary for the modulation, while $\boldsymbol{I}_o$ is the controlled quantity and has to be measured to be compared with its reference. The full state feedback algorithm, on the other hand, requires the measurement of all state variables, and in the model presented in Section 4.3. The only state variable that is not available is the input current $\boldsymbol{I}_f$. In order to compare the proposed method with those in the literature and analyzed in Chapter 3, an observer is introduced. The observer design starts by applying the Clarke transform to (4.23). This transform involves no changes to the structure of the equations since the matrices of the transform are constant matrices.

$$\begin{aligned}\frac{d}{dt}\boldsymbol{I}_f^{\alpha\beta} &= \frac{1}{L_f}\left(\boldsymbol{V}_g^{\alpha\beta} - R_{sf}\,\boldsymbol{I}_f^{\alpha\beta} - \boldsymbol{V}_i^{\alpha\beta}\right)\\ \frac{d}{dt}\boldsymbol{V}_i^{\alpha\beta} &= \frac{1}{C_f}\left(\boldsymbol{I}_f^{\alpha\beta} - \boldsymbol{I}_{id}^{\alpha\beta}\right)\end{aligned} \tag{4.28}$$

The following state-space model can be derived:

$$\begin{aligned}\begin{bmatrix}\dot{I}_{f\alpha}\\ \dot{I}_{f\beta}\\ \dot{V}_{i\alpha}\\ \dot{V}_{i\beta}\end{bmatrix} &= \underbrace{\begin{bmatrix}-\frac{R_{sf}}{L_f} & 0 & -\frac{1}{L_f} & 0\\ 0 & -\frac{R_{sf}}{L_f} & 0 & -\frac{1}{L_f}\\ \frac{1}{C_f} & 0 & 0 & 0\\ 0 & \frac{1}{C_f} & 0 & 0\end{bmatrix}}_{\boldsymbol{\Phi}_1}\begin{bmatrix}I_{f\alpha}\\ I_{f\beta}\\ V_{i\alpha}\\ V_{i\beta}\end{bmatrix} + \dots\\ &\dots + \underbrace{\begin{bmatrix}0 & 0\\ 0 & 0\\ -\frac{1}{C_f} & 0\\ 0 & -\frac{1}{C_f}\end{bmatrix}}_{\boldsymbol{\Gamma}_1}\underbrace{\begin{bmatrix}I_{i\alpha}\\ I_{i\alpha}\end{bmatrix}}_{\boldsymbol{v}} + \underbrace{\begin{bmatrix}\frac{1}{L_f} & 0\\ 0 & \frac{1}{L_f}\end{bmatrix}}_{\boldsymbol{\Sigma}}\begin{bmatrix}V_{g\alpha}\\ V_{g\beta}\end{bmatrix}\end{aligned} \tag{4.29}$$

The input current $\boldsymbol{I}_i^{\alpha\beta}$ can be estimated from the equations that relate matrix converter input power to the output power. Its module can be computed as

$$|\boldsymbol{I}_i^{\alpha\beta}| = \frac{2}{3}\frac{(V_{od}I_{od} + V_{oq}I_{oq})}{|V_i^{\alpha\beta}|cos\phi} \tag{4.30}$$

while its phase is $\theta_v + \phi$ where θ_v is the input voltage angle. Input currents in the stationary reference frame can then be derived as

$$I_{i\alpha} = |\boldsymbol{I}_i^{\alpha\beta}|cos(\theta_v + \phi), \quad I_{i\beta} = |\boldsymbol{I}_i^{\alpha\beta}|sin(\theta_v + \phi) \tag{4.31}$$

The input grid voltage $\boldsymbol{V}_g$ is not measurable and must be estimated along with the system states. It can be modeled as a sinusoidal disturbance composed of two sinusoids phase shifted 90 degrees to each other.

$$\begin{bmatrix} \dot{V}_{g\alpha} \\ V_{g\beta} \end{bmatrix} = \underbrace{\begin{bmatrix} 0 & -\omega_i \\ \omega_i & 0 \end{bmatrix}}_{\boldsymbol{\Sigma}} \begin{bmatrix} V_{g\alpha} \\ V_{g\beta} \end{bmatrix} \tag{4.32}$$

(4.29) can be extended with (4.32) resulting in

$$\begin{cases} \dot{\boldsymbol{w}} = \Phi\boldsymbol{w} + \Gamma\boldsymbol{v} + \boldsymbol{\eta} \\ \boldsymbol{z} = H\boldsymbol{w} + \boldsymbol{\zeta} \end{cases} \tag{4.33}$$

with:

$$\begin{gathered} \boldsymbol{w} = \begin{bmatrix} \tilde{I}_{f\alpha} & \tilde{I}_{f\beta} & \tilde{V}_{i\alpha} & \tilde{V}_{i\beta} & \tilde{V}_{g\alpha} & \tilde{V}_{g\beta} \end{bmatrix}^T; \\ \boldsymbol{\Phi} = \begin{bmatrix} \boldsymbol{\Phi}_1 & \boldsymbol{\Sigma} \\ 0 & \boldsymbol{\Phi}_2 \end{bmatrix}; \boldsymbol{\Gamma} = \begin{bmatrix} \boldsymbol{\Gamma}_1 \\ 0 \end{bmatrix}; \boldsymbol{H} = \begin{bmatrix} 0 & \boldsymbol{I} & 0 \end{bmatrix} \end{gathered} \tag{4.34}$$

where $\boldsymbol{\eta} \in \mathbb{R}^{6\times1}$ is the state noise with covariance matrix $\boldsymbol{\Omega}_1$, $\boldsymbol{\zeta} \in \mathbb{R}^{2\times1}$ is the output noise with covariance matrix $\boldsymbol{\Omega}_2$. It is possible to implement a discrete Kalman filter for system (4.33) in order to estimate both system states ($\boldsymbol{V}_i$ and $\boldsymbol{I}_f$) and the grid voltage

$\boldsymbol{V}_g$ [3]. The grid angle can be calculated from the observed grid voltage as follows

$$\tilde{\theta}_g = tan^{-1}\left(\frac{\tilde{V}_{g\beta}}{\tilde{V}_{g\alpha}}\right) \tag{4.35}$$

As the model described in Section 4.3 is represented in the dq reference frame, $\tilde{\theta}_g$ is used to compute all transformations of the input side quantities, so all the quantities result oriented with the grid voltage $\tilde{\boldsymbol{V}}_g$. Fig. 4.5 shows how the observer is used to obtain what will be the feedback of the control algorithms.

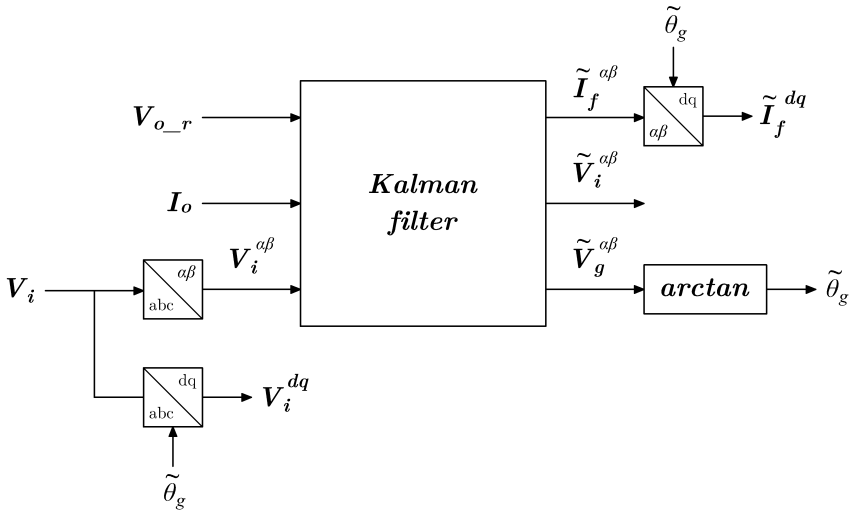

Figure 4.5: Feedback calculation from the Kalman Filter

The dynamics of a closed-loop system that employs an observer for the estimation of control variables is given by the combination of the system, the control algorithm and the observer. However, it can be shown that if the observer is designed to have higher dynamics than the control, the latter is irrelevant, and therefore the dynamics of the closed-loop system can be studied by considering only the system and the control algorithm. [3].

4.5 Motor Mode Full State Feedback Control

At this point, everything is ready to implement full state feedback control for the matrix converter. Remember that the modulator inputs are the input voltage $\boldsymbol{V}_i$, the reference voltage to be applied at the output side $\boldsymbol{V}_{o\_r}$, and the phase shift between

the input voltage and current ϕ. In motor mode the active controller outputs are V_{od_r} and V_{oq_r}, while ϕ is kept equal to its reference ϕ_r. From the equations given in (4.27) it is possible to calculate the linearized system around a steady-state operation point, considering the following state variable, input and disturbance vector.

$$\boldsymbol{x} = \begin{bmatrix} I_{fd} \\ I_{fq} \\ V_{id} \\ V_{iq} \\ I_{od} \\ I_{oq} \end{bmatrix}; \qquad \boldsymbol{u}_m = \begin{bmatrix} V_{od\_r} \\ V_{oq\_r} \end{bmatrix}; \qquad \boldsymbol{d} = \begin{bmatrix} V_{gd} \\ V_{gq} \end{bmatrix} \tag{4.36}$$

The linearized state-space model can be represented as follows:

$$\dot{\boldsymbol{x}} = \overline{\boldsymbol{A}}_{op\_m}\, \boldsymbol{x} + \overline{\boldsymbol{B}}_{op\_m}\, \boldsymbol{u}_m + \overline{\boldsymbol{G}}_{op}\, \boldsymbol{d} \tag{4.37}$$

Where:

$$\boldsymbol{A}_{op\_m} = \begin{bmatrix} -\frac{R_{sf}}{L_f} & \omega_i & -\frac{1}{L_f} & 0 & 0 & 0 \\ -\omega_i & -\frac{R_{sf}}{L_f} & 0 & -\frac{1}{L_f} & 0 & 0 \\ \frac{1}{C_f} & 0 & -\sigma_1 & \sigma_2 & -\overline{V}_{od\_r}\,\sigma_6 & -\overline{V}_{oq\_r}\,\sigma_6 \\ 0 & \frac{1}{C_f} & \sigma_3 & \sigma_1 & -\overline{V}_{od\_r}\,\sigma_7 & -\overline{V}_{oq\_r}\,\sigma_7 \\ 0 & 0 & 0 & 0 & -\frac{R_o}{L_o} & \omega_o \\ 0 & 0 & 0 & 0 & -\omega_o & -\frac{R_o}{L_o} \end{bmatrix} \tag{4.38}$$

$$\boldsymbol{B}_{op\_m} = \begin{bmatrix} 0 & 0 \\ 0 & 0 \\ -\overline{I}_{od}\,\sigma_6 & -\overline{I}_{oq}\,\sigma_6 \\ -\overline{I}_{od}\,\sigma_7 & -\overline{I}_{oq}\,\sigma_7 \\ \frac{1}{L_o} & 0 \\ 0 & \frac{1}{L_o} \end{bmatrix}; \qquad \boldsymbol{G}_{op} = \begin{bmatrix} \frac{1}{L_f} & 0 \\ 0 & \frac{1}{L_f} \\ 0 & 0 \\ 0 & 0 \\ 0 & 0 \\ 0 & 0 \end{bmatrix} \tag{4.39}$$

with:

$$
\begin{aligned}
&\sigma_1 = \sigma_4\,\sigma_8; \quad \sigma_2 = \sigma_5\,\sigma_8 + \omega_g; \quad \sigma_3 = \sigma_5\,\sigma_8 - \omega_g;\\
&\sigma_4 = \frac{[\,\overline{V}_{iq}\,cos\,(\phi_r) + \overline{V}_{id}\,sin\,(\phi_r)\,]^2 - {\overline{V}_{id}}^2}{C_f\;cos^2\,(\phi_r)\,\left({\overline{V}_{id}}^2 + {\overline{V}_{iq}}^2\right)^2};\\
&\sigma_5 = \frac{[\,\overline{V}_{id}\,sin\,(\phi_r) + \overline{V}_{iq}\,cos\,(\phi_r)\,]^2 - {\overline{V}_{iq}}^2}{C_f\,sin\,(\phi_r)\;cos\,(\phi_r)\,\left({\overline{V}_{id}}^2 + {\overline{V}_{iq}}^2\right)^2};\\
&\sigma_6 = \frac{\overline{V}_{id}\,cos\,(\phi_r) - \overline{V}_{iq}\,sin\,(\phi_r)}{C_f\,cos\,(\phi_r)\,\left({\overline{V}_{id}}^2 + {\overline{V}_{iq}}^2\right)};\\
&\sigma_7 = \frac{\overline{V}_{iq}\,cos\,(\phi_r) + \overline{V}_{id}\,sin\,(\phi_r)}{C_f\,cos\,(\phi_r)\,\left({\overline{V}_{id}}^2 + {\overline{V}_{iq}}^2\right)};\\
&\sigma_8 = \overline{I}_{od}\,\overline{V}_{od\_r} + \overline{I}_{oq}\,\overline{V}_{oq\_r};
\end{aligned}
\tag{4.40}
$$

Where the overline represent the steady-state variables. The system can be discretized with the Zero-Order Hold apporach resulting in:

$$
\boldsymbol{x}\,(k+1) = \overline{\boldsymbol{\Phi}}_{op\_m}\,\boldsymbol{x}\,(k) + \overline{\boldsymbol{\Gamma}}_{op\_m}\,\boldsymbol{u}_m\,(k) + \overline{\boldsymbol{\Psi}}_{op}\,\boldsymbol{d}\,(k) \tag{4.41}
$$

Full state feedback is then implemented, an integral controller has been added to control the output current $\boldsymbol{I}_o^{dq}$ and eliminate the steady-state error with respect to its reference $\boldsymbol{r}_c$. The integrator is represented by the following state equations:

$$
\boldsymbol{x}_{ic}(k+1) = \boldsymbol{x}_{ic}(k) + T_s\,\left[\boldsymbol{r}_c(k) - \boldsymbol{I}_o^{dq}(k)\right] \tag{4.42}
$$

where $\boldsymbol{x}_{ic} \in \mathbb{R}^{2\times 1}$ are the integral states of the control loop, T_s is the switching period and $\boldsymbol{r}_c \in \mathbb{R}^{2\times 1}$ are the motor current reference vector. In addition, as discussed in the Full State Feedback section and Chapter 3, it is necessary to consider the controller output delay by including another state equation:

$$
\boldsymbol{u}_m(k+1) = \boldsymbol{u}_{dm}(k) \tag{4.43}
$$

where $\boldsymbol{u}_{dm} \in \mathbb{R}^{2\times 1}$ represents the open-loop system input and $\boldsymbol{u}_m \in \mathbb{R}^{2\times 1}$ represents the controller output. At this point, to obtain the augmented closed-loop dynamic model for

the H_2-LMI tuning, it is sufficient to combine equations (4.41), (4.42) and (4.43) as follows:

$$\boldsymbol{x}_{cl\_m}(k+1) = \boldsymbol{A}_{cl\_m}\,\boldsymbol{x}_{cl\_m}(k) + \boldsymbol{B}_{cl\_m}\,\boldsymbol{u}_{dm}(k) + \boldsymbol{F}_{cl\_m}\,\boldsymbol{r}_c(k) \tag{4.44}$$

with:

$$\boldsymbol{A}_{cl\_m} = \begin{bmatrix} \boldsymbol{\Phi}_{op\_m} & \boldsymbol{0} & \boldsymbol{\Gamma}_{op\_m} \\ -\boldsymbol{H}\,T_s & \boldsymbol{I} & \boldsymbol{0} \\ \boldsymbol{0} & \boldsymbol{0} & \boldsymbol{0} \end{bmatrix}; \quad \boldsymbol{B}_{cl\_m} = \begin{bmatrix} \boldsymbol{0} \\ \boldsymbol{0} \\ \boldsymbol{I} \end{bmatrix}; \quad \boldsymbol{F}_{cl\_m} = \begin{bmatrix} \boldsymbol{0} \\ \boldsymbol{I}T_s \\ \boldsymbol{0} \end{bmatrix}$$
$$\boldsymbol{x}_{cl\_m}(k) = \begin{bmatrix} \boldsymbol{x}(k) & \boldsymbol{x}_{ic}(k) & \boldsymbol{u}_{dm}(k) \end{bmatrix}^T; \quad \boldsymbol{H} = \begin{bmatrix} 0 & 0 & \boldsymbol{I} \end{bmatrix} \tag{4.45}$$

where, $\boldsymbol{A}_{cl\_m} \in \mathbb{R}^{10\times10}$, $\boldsymbol{B}_{cl\_m} \in \mathbb{R}^{10\times2}$, $\boldsymbol{F}_{cl\_m} \in \mathbb{R}^{10\times2}$, $\boldsymbol{H} \in \mathbb{R}^{2\times6}$; $\boldsymbol{0}$ represents a zero matrix and $\boldsymbol{I}$ represents an identity matrix, both of appropriate dimensions. $\boldsymbol{H}$ is the matrix that is defined to separate I_{od} and I_{oq} from the state variable vector. Note that the grid contribution, represented by the vector d in is neglected. This because it does not involve any changes to the system dynamics and is therefore not necessary for tuning. It is now possible to design a full state feedback controller in the form

$$\boldsymbol{u}_m(k) = \boldsymbol{K}_m\boldsymbol{x}(k) = \begin{bmatrix} \boldsymbol{K}_{pm} & \boldsymbol{K}_{im} & \boldsymbol{K}_{dm} \end{bmatrix} \boldsymbol{x}(k) \tag{4.46}$$

where $\boldsymbol{K}_{pm} \in \mathbb{R}^{2\times6}$, $\boldsymbol{K}_{im} \in \mathbb{R}^{2\times2}$ and $\boldsymbol{K}_{dm} \in \mathbb{R}^{2\times2}$ are the motor mode gain matrices. The filter current is observed starting from the available measurements thanks to the Kalman Filter. The resulting control scheme is reported in Fig. 4.6 The tuning of the $\boldsymbol{K}_m$ is carried out via the H_2-LMI algorithm with the weighting matrix $\boldsymbol{Q}_m \in \mathbb{R}^{10\times10}$ and $\boldsymbol{R}_m \in \mathbb{R}^{2\times2}$. It has been said that this method allows for parameter variations within the model of the system to be controlled. In the case of the system obtained by discretizing (4.48), it is clear that for each steady-state point, the matrix varies due to variations of the steady-state variables. In order to exploit this potential, a range of positive current I_{oq} and angular frequency ω_o is defined where stability is to be ensured, shown in Fig. 4.7. I_{oq} has to be positive because the motor mode scenario is considered. Through the linearization and discretization process, all the matrices corresponding to each vertex of the defined area are calculated. The complex of the matrices calculated at each vertex

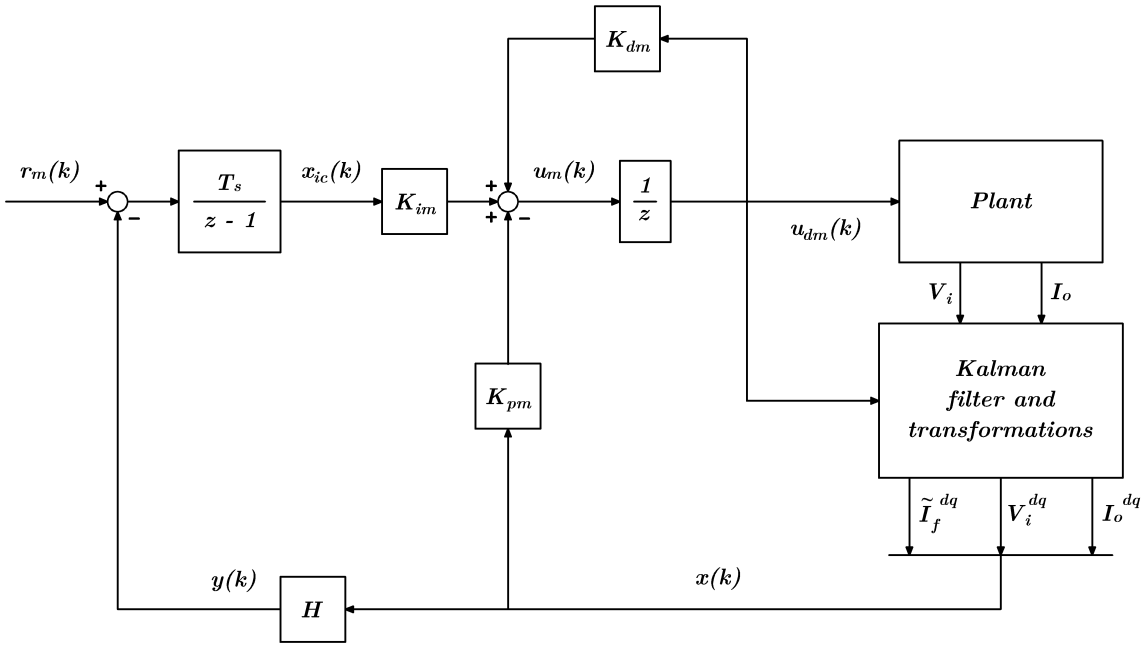

Figure 4.6: Motor Mode Full State Feedback Control Schematic

forms the so-called polytope. At this point, by providing the appropriate matrices Q and R, the algorithm will provide a matrix $\boldsymbol{K}_m$ such that stability in the defined range is guaranteed.

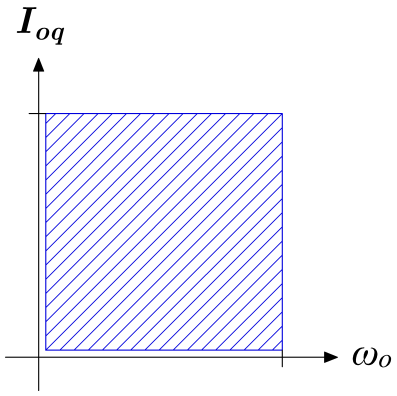

Figure 4.7: Stability area definition

4.6 Generator Mode Full State Feedback Control

In generator mode the input phase shift ϕ is also used as active controller output together with V_{od_r} and V_{oq_r}. It is then necessary to redefine the linearized system ma-

trices obtained from (4.27). The state variables, input and disturbance vector are defined in the following:

$$\boldsymbol{x} = \begin{bmatrix} I_{fd} \\ I_{fq} \\ V_{id} \\ V_{iq} \\ I_{od} \\ I_{oq} \end{bmatrix}; \qquad \boldsymbol{u}_g = \begin{bmatrix} V_{od\_r} \\ V_{oq\_r} \\ \phi \end{bmatrix}; \qquad \boldsymbol{d} = \begin{bmatrix} V_{gd} \\ V_{gq} \end{bmatrix} \tag{4.47}$$

The open-loop state-space model is defined as follows

$$\dot{\boldsymbol{x}} = \overline{\boldsymbol{A}}_{op\_g}\, \boldsymbol{x} + \overline{\boldsymbol{B}}_{op\_g}\, \boldsymbol{u}_g + \overline{\boldsymbol{G}}_{op}\, \boldsymbol{d} \tag{4.48}$$

Where:

$$\boldsymbol{A}_{op\_g} = \begin{bmatrix} -\frac{R_{sf}}{L_f} & \omega_i & -\frac{1}{L_f} & 0 & 0 & 0 \\ -\omega_i & -\frac{R_{sf}}{L_f} & 0 & -\frac{1}{L_f} & 0 & 0 \\ \frac{1}{C_f} & 0 & -\sigma_1 & \sigma_2 & -\overline{V}_{od\_r}\,\sigma_6 & -\overline{V}_{oq\_r}\,\sigma_6 \\ 0 & \frac{1}{C_f} & \sigma_3 & \sigma_1 & -\overline{V}_{od\_r}\,\sigma_7 & -\overline{V}_{oq\_r}\,\sigma_7 \\ 0 & 0 & 0 & 0 & -\frac{R_o}{L_o} & \omega_o \\ 0 & 0 & 0 & 0 & -\omega_o & -\frac{R_o}{L_o} \end{bmatrix} \tag{4.49}$$

$$\boldsymbol{B}_{op\_g} = \begin{bmatrix} 0 & 0 & 0 \\ 0 & 0 & 0 \\ -\overline{I}_{od}\,\sigma_6 & -\overline{I}_{oq}\,\sigma_6 & -\frac{\overline{V}^*_{iq}\,\sigma_8}{\sigma_9} \\ -\overline{I}_{od}\,\sigma_7 & -\overline{I}_{oq}\,\sigma_7 & \frac{\overline{V}^*_{id}\,\sigma_8}{\sigma_9} \\ \frac{1}{L_o} & 0 & 0 \\ 0 & \frac{1}{L_o} & 0 \end{bmatrix}; \quad \boldsymbol{G}_{op} = \begin{bmatrix} \frac{1}{L_f} & 0 \\ 0 & \frac{1}{L_f} \\ 0 & 0 \\ 0 & 0 \\ 0 & 0 \\ 0 & 0 \end{bmatrix} \tag{4.50}$$

With:

$$
\begin{aligned}
&\sigma_1 = \sigma_4\,\sigma_8; \quad \sigma_2 = \sigma_5\,\sigma_8 + \omega_g; \quad \sigma_3 = \sigma_5\,\sigma_8 - \omega_g;\\
&\sigma_4 = \frac{[\,\overline{V}_{iq}\,cos\left(\overline{\phi}\right) + \overline{V}_{id}\,sin\left(\overline{\phi}\right)\,]^2 - \overline{V}_{id}{}^2}{C_f\;cos^2\left(\overline{\phi}\right)\;\left(\overline{V}_{id}{}^2 + \overline{V}_{iq}{}^2\right)^2};\\
&\sigma_5 = \frac{[\,\overline{V}_{id}\,sin\left(\overline{\phi}\right) + \overline{V}_{iq}\,cos\left(\overline{\phi}\right)\,]^2 - \overline{V}_{iq}{}^2}{C_f\,sin\left(\overline{\phi}\right)\;cos\left(\overline{\phi}\right)\;\left(\overline{V}_{id}{}^2 + \overline{V}_{iq}{}^2\right)^2};\\
&\sigma_6 = \frac{\overline{V}_{id}\,cos\left(\overline{\phi}\right) - \overline{V}_{iq}\,sin\left(\overline{\phi}\right)}{C_f\,cos\left(\overline{\phi}\right)\;\left(\overline{V}_{id}{}^2 + \overline{V}_{iq}{}^2\right)};\\
&\sigma_7 = \frac{\overline{V}_{iq}\,cos\left(\overline{\phi}\right) + \overline{V}_{id}\,sin\left(\overline{\phi}\right)}{C_f\,cos\left(\overline{\phi}\right)\;\left(\overline{V}_{id}{}^2 + \overline{V}_{iq}{}^2\right)};\\
&\sigma_8 = \overline{I}_{od}\,\overline{V}_{od\_r} + \overline{I}_{oq}\,\overline{V}_{oq\_r};\\
&\sigma_9 = C_f\left(sin\left(\overline{\phi}\right)^2 - 1\right)\left(\overline{V}_{id}{}^2 + \overline{V}_{iq}{}^2\right).
\end{aligned}
\tag{4.51}
$$

Where the oveline represent the steady-state variables. Again, the system has to discretized resulting in:

$$
\boldsymbol{x}\,(k+1) = \overline{\boldsymbol{\Phi}}_{op\_g}\,\boldsymbol{x}\,(k) + \overline{\boldsymbol{\Gamma}}_{op\_g}\,\boldsymbol{u}_g\,(k) + \overline{\boldsymbol{\Psi}}_{op}\,\boldsymbol{d}\,(k) \tag{4.52}
$$

As in the previous case a integral controller is added to ensure the controlled variables to follow the reference. This time an integrator for the control of ϕ is also added, this to ensure that at steady state it follow its reference r_ϕ. The integrator state space equation are then:

$$
\begin{aligned}
\boldsymbol{x}_{ic}(k+1) &= \boldsymbol{x}_{ic}(k) + T_s\,\left[\boldsymbol{r}_c(k) - \boldsymbol{I}_o^{dq}(k)\right]\\
x_{i\phi}(k+1) &= x_{i\phi}(k) + T_s\,\left[r_\phi(k) - \phi(k)\right]
\end{aligned}
\tag{4.53}
$$

The reference vector in generator mode can be expressed as follows:

$$
\boldsymbol{r}_g = \begin{bmatrix} \boldsymbol{r}_c \\ r_\phi \end{bmatrix} \tag{4.54}
$$

This means that in generator mode is $\boldsymbol{r}_g \in \mathbb{R}^{3\times 1}$. Now, as in the previous case, the one-step delay is introduced:

$$\boldsymbol{u}_g(k+1) = \boldsymbol{u}_{dg}(k) \tag{4.55}$$

where $\boldsymbol{u}_{dg} \in \mathbb{R}^{3\times 1}$ represents the plant input in generator mode and $\boldsymbol{u}_g \in \mathbb{R}^{3\times 1}$ represents the controller output. At this point, it is possible to derive the closed-loop model of the system for the H_2-LMI tuning as follows, again neglecting the contribution of the grid, which makes no change to the system's dynamics.

$$\boldsymbol{x}_{cl\_g}(k+1) = \boldsymbol{A}_{cl\_g}\,\boldsymbol{x}_{cl\_g}(k) + \boldsymbol{B}_{cl\_g}\,\boldsymbol{u}_{dg}(k) + \boldsymbol{F}_{cl\_g}\,\boldsymbol{r}_g(k) \tag{4.56}$$

with:

$$\boldsymbol{A}_{cl\_g} = \begin{bmatrix} \boldsymbol{\Phi}_{op\_g} & \mathbf{0} & \boldsymbol{\Gamma}_{op\_g} \\ -\boldsymbol{H}\,T_s & \boldsymbol{I} & \mathbf{0} \\ 0 & 1 & -T_s\,\boldsymbol{D} \\ \mathbf{0} & \mathbf{0} & \mathbf{0} \end{bmatrix}; \quad \boldsymbol{B}_{cl\_g} = \begin{bmatrix} \mathbf{0} \\ \mathbf{0} \\ \boldsymbol{I} \end{bmatrix}; \quad \boldsymbol{F}_{cl\_g} = \begin{bmatrix} \mathbf{0} \\ \boldsymbol{I}T_s \\ \mathbf{0} \end{bmatrix}$$
$$\boldsymbol{x}_{cl\_g}(k) = \begin{bmatrix} \boldsymbol{x}(k) & \boldsymbol{x}_{ic}(k) & x_{i\phi} & \boldsymbol{u}_{dg}(k) \end{bmatrix}^T; \quad \boldsymbol{D} = \begin{bmatrix} 0 & 0 & 1 \end{bmatrix} \tag{4.57}$$

where, $\boldsymbol{A}_{cl\_g} \in \mathbb{R}^{12\times 12}$, $\boldsymbol{B}_{cl\_m} \in \mathbb{R}^{11\times 2}$, $\boldsymbol{F}_{cl\_m} \in \mathbb{R}^{12\times 2}$. $\boldsymbol{D}$ is a matrix that has been defined to extract $\phi(k)$ from $\boldsymbol{u}_{dg}(k)$. Finally it is possible to design a full state feedback controller in the form:

$$\boldsymbol{u}_g(k) = \boldsymbol{K}_g\boldsymbol{x}(k) = \begin{bmatrix} \boldsymbol{K}_{pg} & \boldsymbol{K}_{ig} & \boldsymbol{K}_{dg} \end{bmatrix} \boldsymbol{x}(k) \tag{4.58}$$

where $\boldsymbol{K}_{pg} \in \mathbb{R}^{3\times 6}$, $\boldsymbol{K}_{ig} \in \mathbb{R}^{3\times 2}$ and $\boldsymbol{K}_{dg} \in \mathbb{R}^{3\times 2}$ are the generator mode gain matrices. The control schematic is reported in Fig. 4.8. The weighting matrix are $\boldsymbol{Q}_g \in \mathbb{R}^{12\times 12}$ and $\boldsymbol{R}_g \in \mathbb{R}^{3\times 3}$. The tuning procedure is the same as that presented for the motor mode case, the only difference is clearly the sign of the current, in fact the area used for the definition of the polytope this time is identified by negative current values, as visible in the Fig. 4.9.

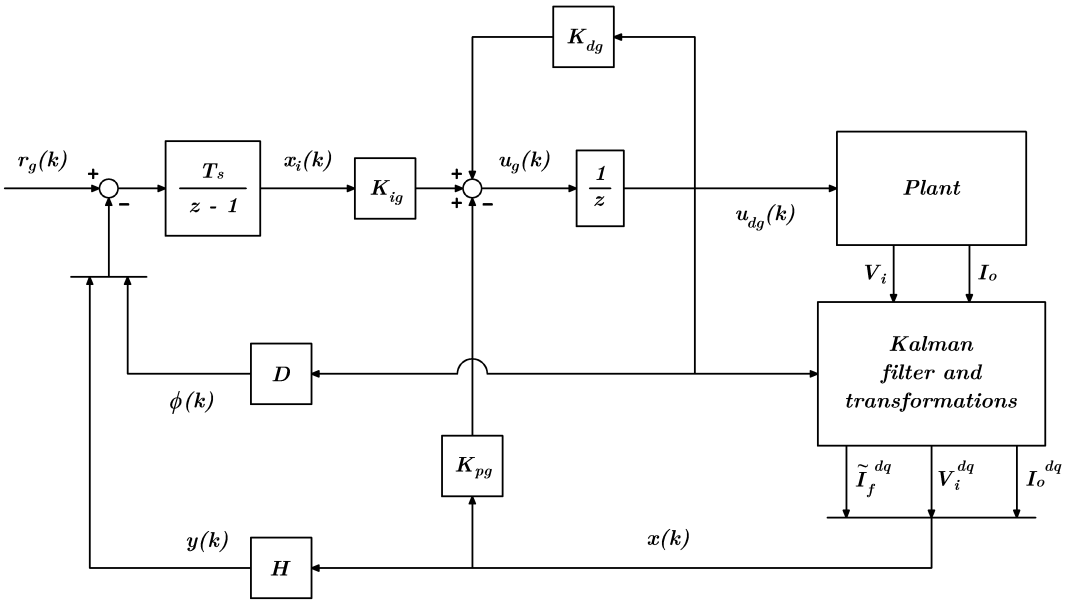

Figure 4.8: Generator Mode Full State Feedback Control Schematic

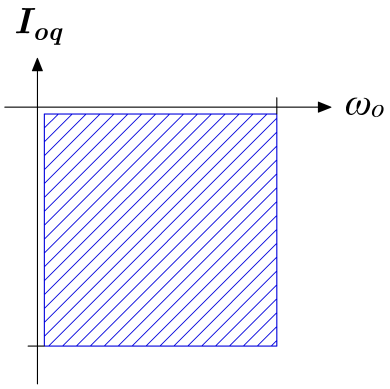

Figure 4.9: Stability area definition

4.7 Simulation Results

The system consisting of input filter, matrix converter and SM-PMSM is simulated as already done in Chapter 3, this time using the full state feedback control algorithm based on H_2-LMI tuning. From this point the acronym H_2-LMI will simply be used to refer to the algorithm. The motor speed ω_{om} is imposed, so there are no speed dynamics. Within the simulator, the filter is simulated taking into account the presence of the R_{pf} resistor, in order to obtain a behaviour closer to the experimental setup. The system parameters are reported in Chapter 3 Tab. 3.5. The simulations in motor mode and generator mode are discussed below.

4.7.1 Motor Mode H_2-LMI

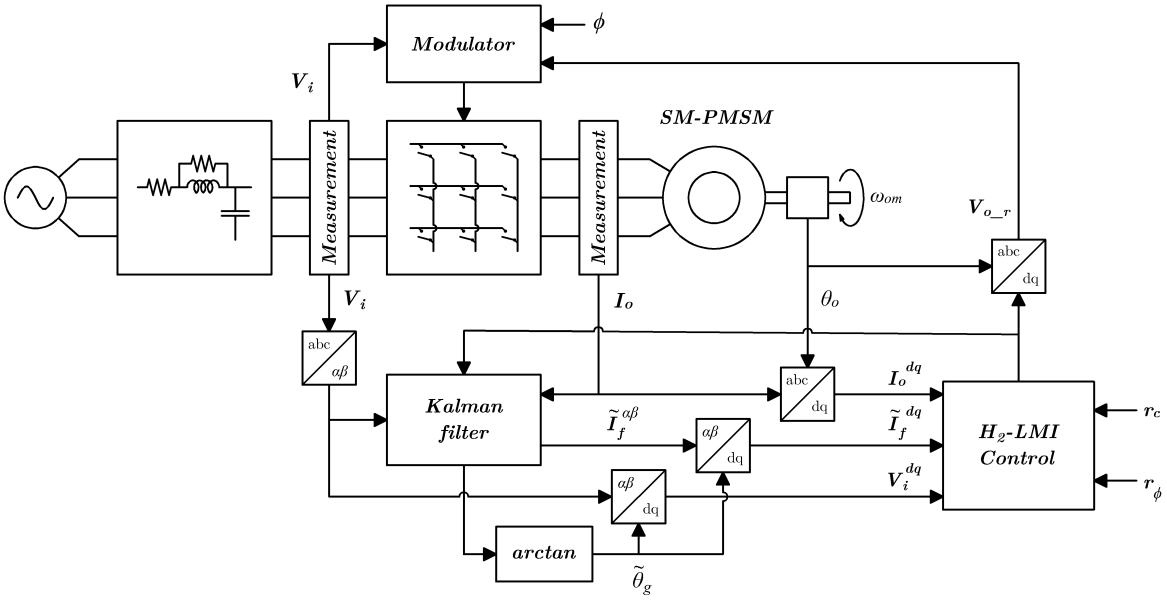

Figure 4.10: H_2-LMI motor mode Simulator Schematic

Fig.4.10 illustrates a schematic of the simulator in motor mode. The feedback gain matrix $\boldsymbol{K}_m$ has been tuned using the following weighting matrix:

$$\begin{aligned} \boldsymbol{R}_m &= diag(1,1); \\ \boldsymbol{Q}_m &= 2.5 \cdot 10^8 \cdot diag(0,0,0,0,0,0,1,1,0,0); \end{aligned} \tag{4.59}$$

These values turned out to be those that allowed the highest possible bandwidth with the lowest possible harmonic contribution. The polytopic system has been created assuming $\omega_o \in [0, 2\,\pi\,60] rad/s$ and $I_{oq} \in [0, 15] A$. The Kalman filter has been tuned using the following noise covariance matrices to achieve a good compromise between noise immunity and dynamic response.

$$\begin{aligned} \boldsymbol{\Omega}_1 &= 10^5 \cdot diag(1,1,1,1,1,1); \\ \boldsymbol{\Omega}_2 &= 10^{-3} \cdot diag(1,1) \end{aligned} \tag{4.60}$$

A comparison of voltage $\boldsymbol{V}_g^{\alpha\beta}$ and its estimated value $\tilde{\boldsymbol{V}}_g^{\alpha\beta}$ in the $\alpha\beta$ domain is presented in Fig. (4.11). It can be seen from the figure that the two quantities are practically equal given the almost complete overlap.

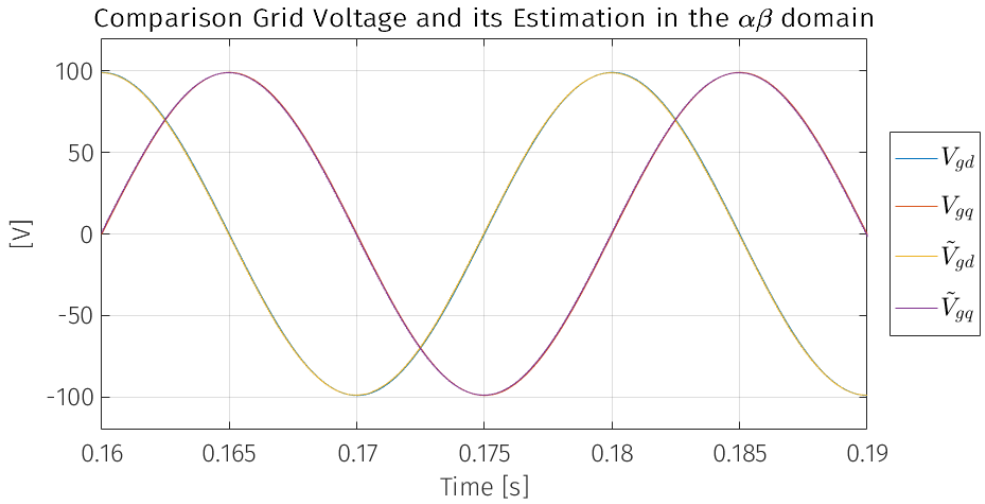

Figure 4.11: Comparison between grid voltage and its estimation in the $\alpha\beta$ domain

Given the correct estimation of the grid voltage, the correct orientation of the dq transform is guaranteed. The results in the input and output dq reference systems are shown below in Fig. (4.12). For the measured input quantities, the original grid angle θ_g of the simulated grid was used. Whereas for the estimated filter current, the estimated angle $\tilde{\theta}_g$ is used. This is to test the effectiveness of the observer in estimating both the grid angle and the amplitude of the filter current. The output dq reference frame is oriented with the rotor position. The quantities are sampled at the switching frequency T_s. It is evident from the perfect overlap that the observer correctly estimates the filter current. From the graph results that the stability is guaranteed even beyond the region defined by the polytope. In fact the system is stable also with $I_{oq\_r} = 20A$. However, it can be seen that the settling time is significantly increased. In Fig. 4.13 the three-phase waveforms are reported with sampling time $T_s/10$. As the current supplied to the output increases, the ripple on the input voltage increases significantly. It is much more evident than before because a much higher current is being supplied to the output than in the HPF motor mode case. In that case, instability occurs when the output current exceeds $10\,A\,(580\,W)$. H_2-LMI motor mode algorithm allows to provide to the output $15\,A\,(880\,W)$ stably.

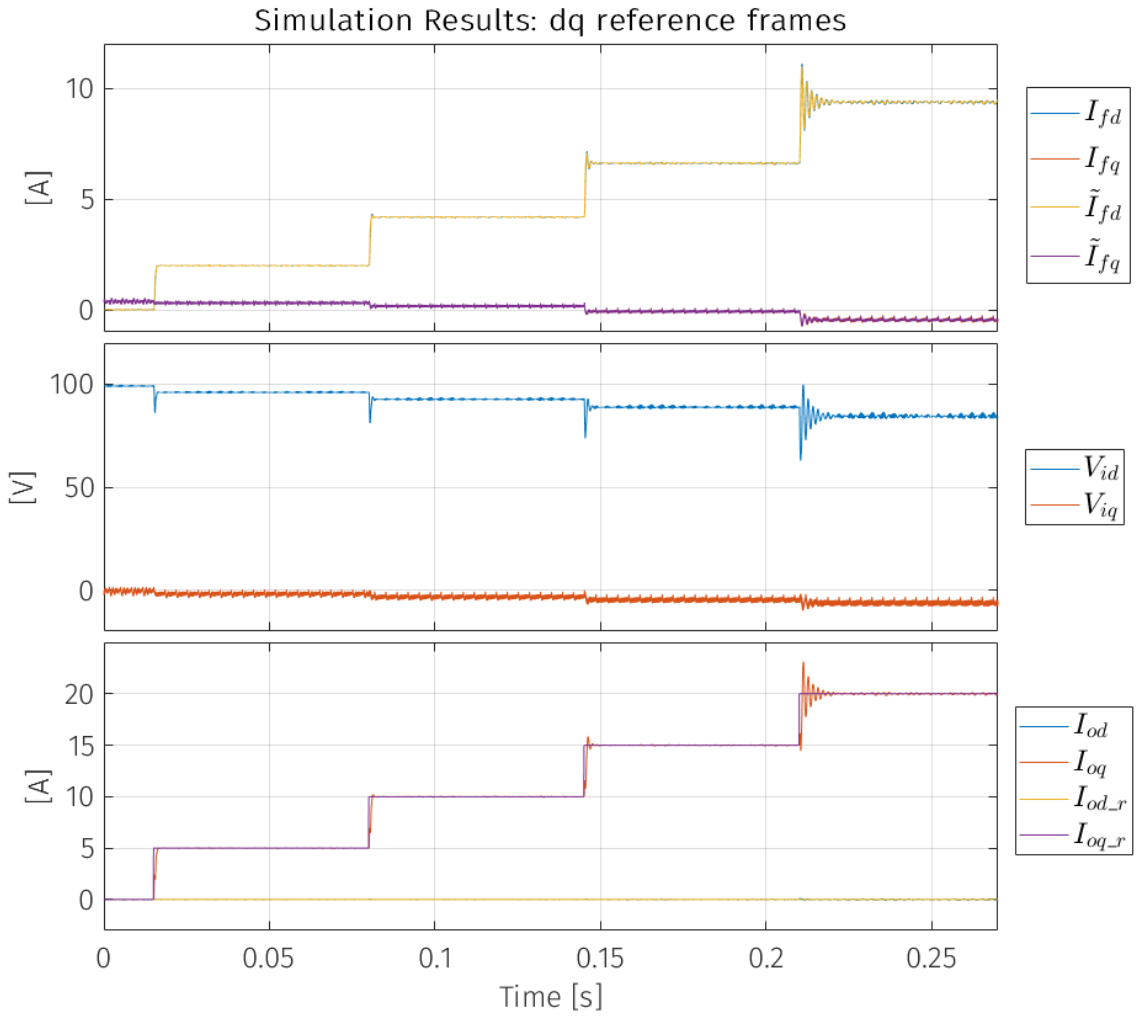

Figure 4.12: Simulation results in the input and output dq reference frames as I_{oq_r} increases, sample time T_s

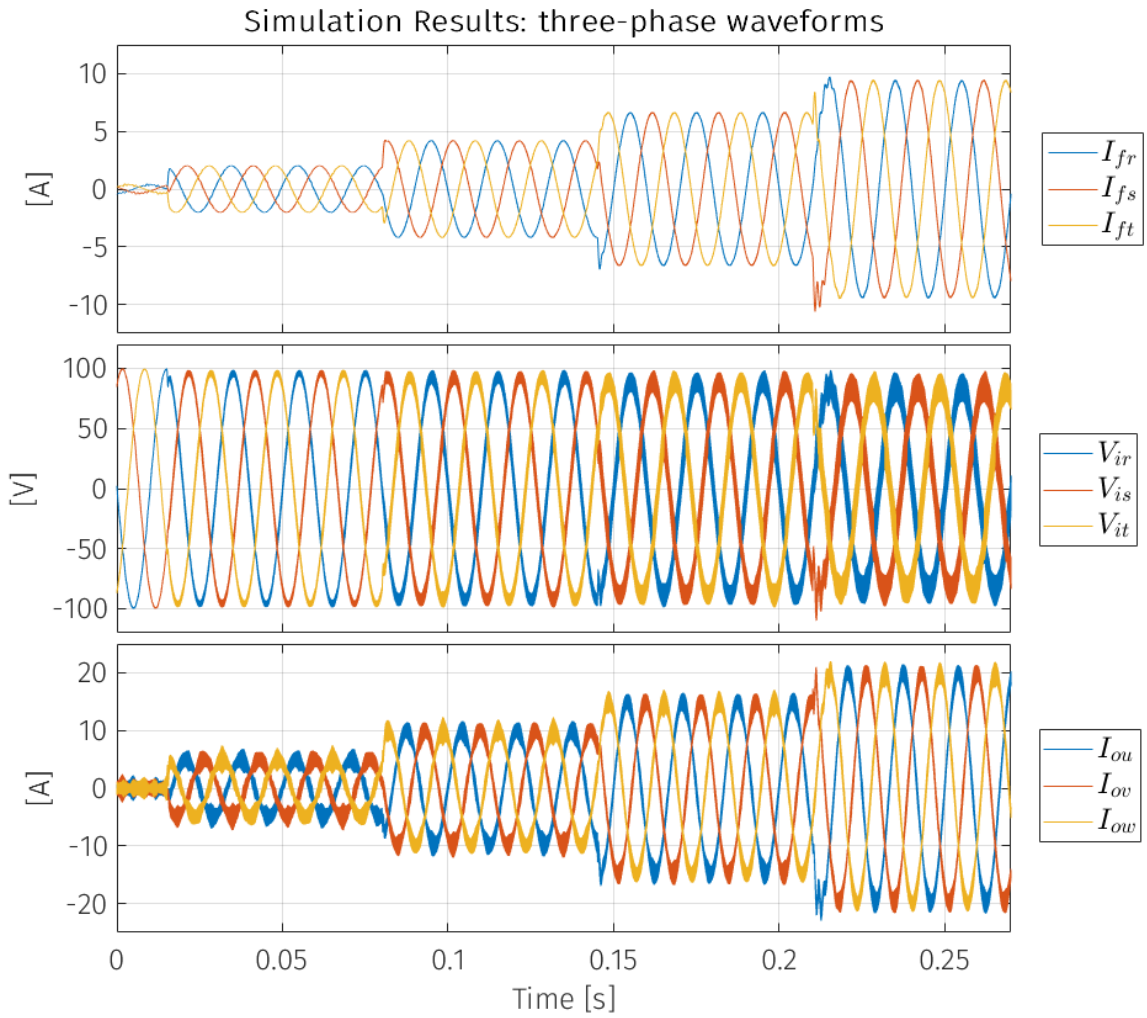

Figure 4.13: Three-Phase waveforms as I_{oq_r} increases, sample time $T_s/10$

For the analysis of the control bandwidth, as this is not imposed through the tuning of PI controllers, it is necessary to evaluate it by comparison with known dynamic systems. A second-order system is used, the transfer function of which was shown in Chapter 2 in (2.79). The step response of the H_2-LMI control algorithm and of the one of the second order system are compared keeping the damping factor ξ constant and equal to zero, and varying the bandwidth ω_c. When the step responses are comparable, an evaluation of the H_2-LMI control bandwidth is obtained. In Fig. 4.14 this comparison is presented.

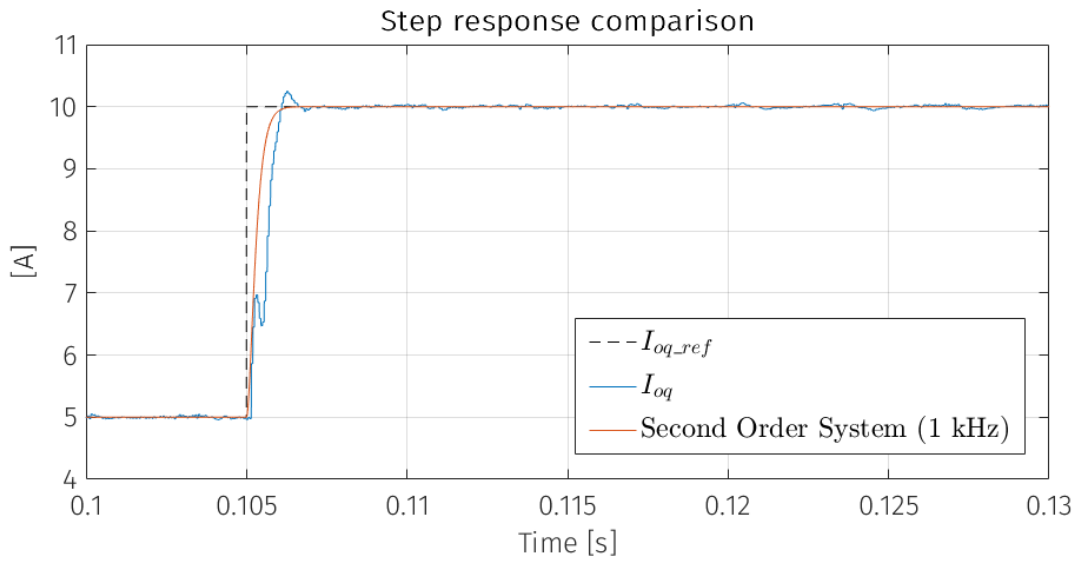

Figure 4.14: Comparison step response H_2-LMI and Second Order System with 1 kHz control bandwidth

The above analysis shows that the control bandwidth of the H_2-LMI algorithm in motor mode is approximately 1 kHz. It therefore appears from the simulations that for the same control bandwidth, the H_2-LMI algorithm compared to the HPF algorithm is able to provide more output power stably.

4.7.2 Generator Mode H_2-LMI

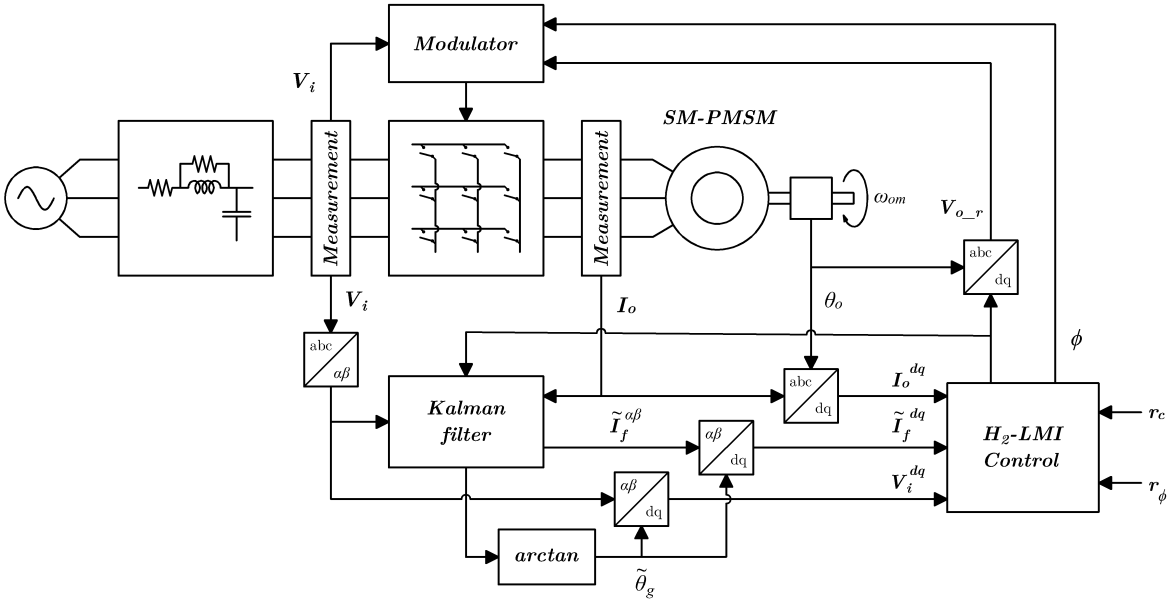

Figure 4.15: H_2-LMI generator mode Simulator Schematic

Fig.4.10 shows simulator schematic in generator mode. For the generator mode the weighting matrix are:

$$\begin{aligned} \boldsymbol{R}_g &= diag(1,1,1); \\ \boldsymbol{Q}_g &= 2.5 \cdot 10^8 \cdot diag(0,0,0,0,0,0,1,1,1,0,0,0); \end{aligned} \tag{4.61}$$

This time the polytopic system has been created assuming $\omega_o \in [0, 2\,\pi\,60] rad/s$ and $I_{oq} \in [-15, 0] A$. The Kalman filter design is the same that has been presented for the motor mode algorithm. In the following, Fig. 4.16 reports the results in the input-side and output-side dq frames. The input measured quantities are oriented with the actual grid voltage angle θ_g, while those estimated with estimated angle $\tilde{\theta}_g$. The output-side is oriented with the rotor position. In generator mode, the phase shift ϕ is also considered an active output of the controller. It must therefore be ensured that at steady-state it is close to its reference r_ϕ, Fig.4.17 is introduced for this purpose. In Fig. 4.18 the three-phase waveforms are reported.

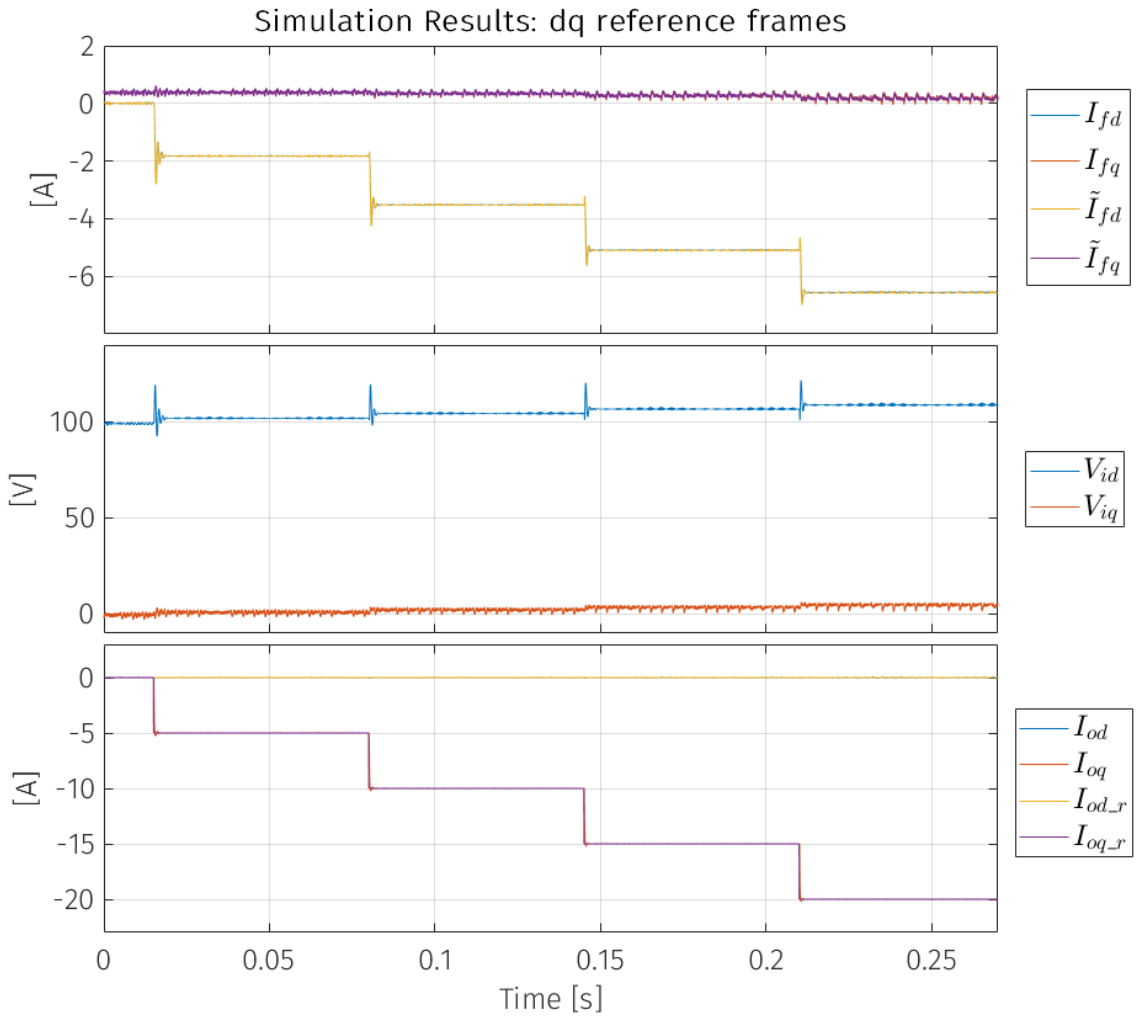

Figure 4.16: Simulation results in the input and output dq reference frames as I_{oq_r} decreases, sample time T_s

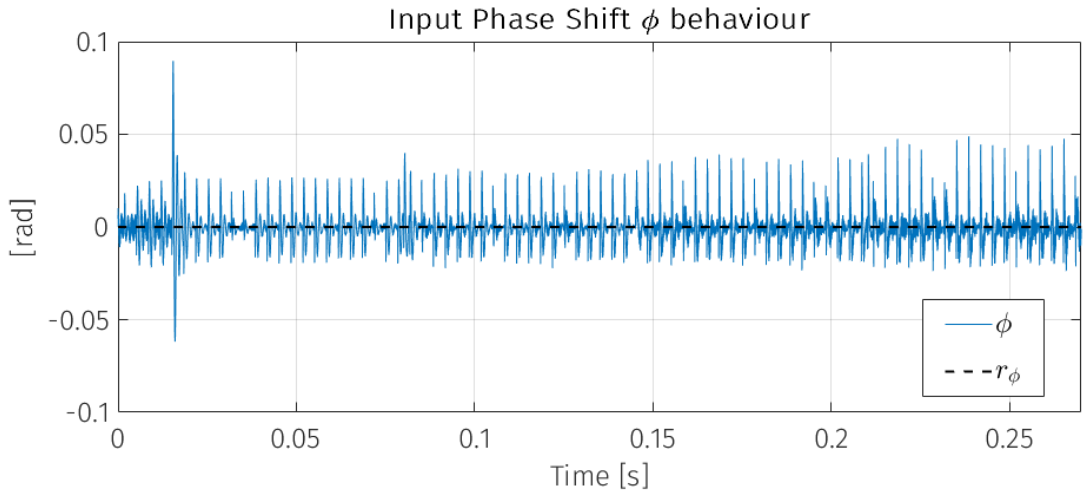

Figure 4.17: Input phase shift ϕ as I_{oq_r} decreases, sample time T_s

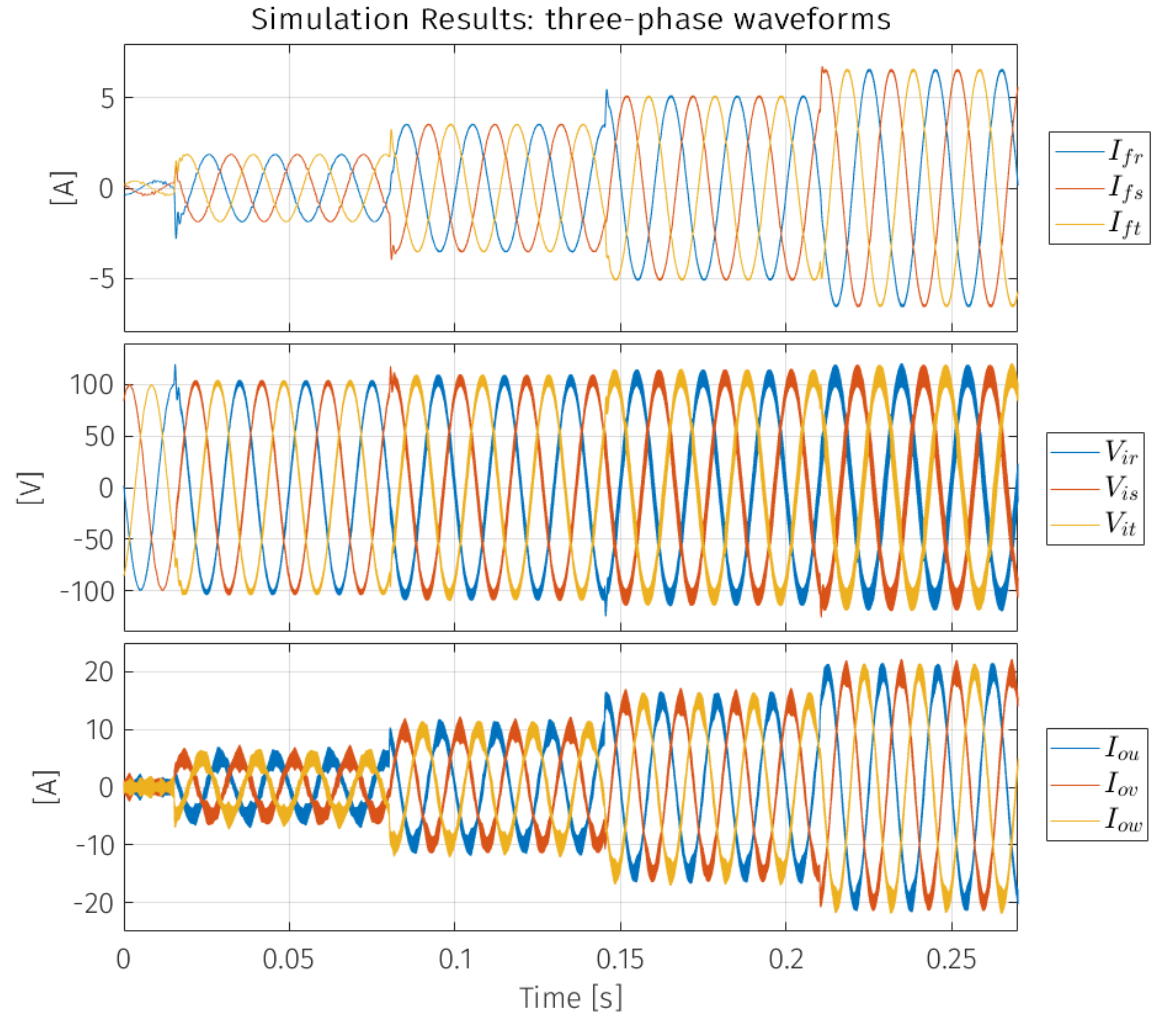

Figure 4.18: Three-Phase waveforms as I_{oq_r} decreases, sample time $T_s/10$

To evaluate the control bandwidth, the comparison with the second order system is proposed also in this case in Fig. 4.19. This time the step is obviously negative.

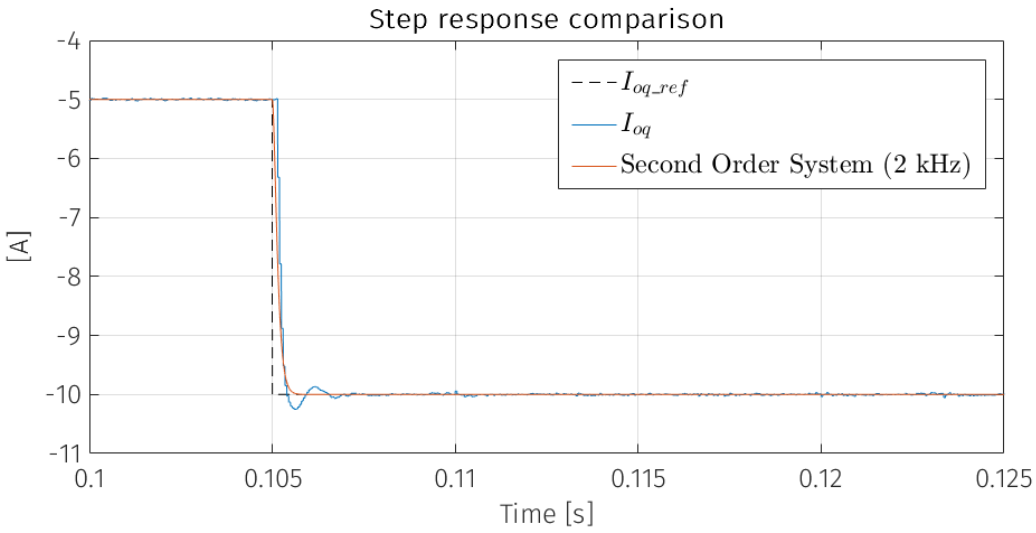

Figure 4.19: Comparison step response H_2-LMI and Second Order System with 2 kHz control bandwidth

It turns out that the control bandwidth in generator mode is about 2 kHz. Thus, not only can the H_2-LMI algorithm handle a higher negative power than the HPF algorithm ($-762\,W$ the HPF and $-814\,W$ the H_2-LMI) but it also has a control bandwidth that turns out to be twice as high.

4.8 Chapter Summary

In this chapter, the theory of full state feedback control was discussed and the H_2-LMI tuning methodology was presented. This strategy has the potential to be used to realize robust controllers for nonlinear dynamic systems within a defined operating range. This was then applied to the case of the matrix converter and two control algorithms were developed, one for the motor mode and one for the generator mode. An observer was also defined for estimating the variables necessary for full state feedback but for which there was no measurement. Simulations have been carried out to prove the effectiveness of the proposed methods.

References 4

[1] M. C. De Oliveira, J. C. Geromel, and J. Bernussou, "Extended h_2 and h_∞ characterizations and controller parametrizations for discrete-time systems," International journal of control, vol. 75, no. 9, pp. 666–679, 2002.

[2] G.-R. Duan and H.-H. Yu, LMIs in control systems: analysis, design and applications. CRC press, 2013.

[3] G. F. Franklin, J. D. Powell, and M. L. Workman, Digital control of dynamic systems, vol. 3. Addison-wesley Menlo Park, CA, 1998.

Chapter 5:

Experimental Results

In this chapter, the performance of the control algorithms for bidirectional power flow HPF and H_2-LMI will be compared through experimental tests. Initially, the experimental setup used will be illustrated, analysing its various components. The aim of the experimentation is to assess which of the two algorithms can handle the higher positive and negative power flow with the same control bandwidth. In addition, the coefficients of Total Harmonic Distortion (THD) for the input and output quantities will be compared as well as the computational burden of the two algorithms.

5.1 Experimental Setup

The experimental setup used is, of course, the one in which SM-PMSM motors are used to generate a bidirectional load for the matrix converter. The operating principle has been presented in Chapter 2. Ideally, the setup can be divided into two parts, the matrix converter side and the dynamic load side. The matrix converter side, through the control algorithm impose a current I_{oq} oriented with the rotor angle to the SM-PMSM1, thus generating a torque at the motor shaft. In the dynamic load side, thanks to its control algorithm, the SM-PMSM2, supplied by a two-level inverter, opposes the torque generated by the SM-PMSM1 and keeps the speed constant. The control algorithms are implemented within a single control board called uCube. In the following, the control board will be described initially and then the two sections of the setup will be described in detail.

5.1.1 Control Board uCube

The uCube, presented in [1], is a development control platform composed by an evaluation board and different multipurpose expansion boards. The evaluation board is

based on a System on Chip (SoC), which integrates in a single device a dual-core ARM and a Field Programmable Gate Array (FPGA). The control strategies described are implemented in the ARM while FPGA is used to implement the low-level modulation part, the four-steps algorithm, the ADCs reading and all system protections. The modulation strategy employed was the Optimum Alesina-Venturini modulation presented in [2]. In Fig. 5.1 a the uCube control board is shown.

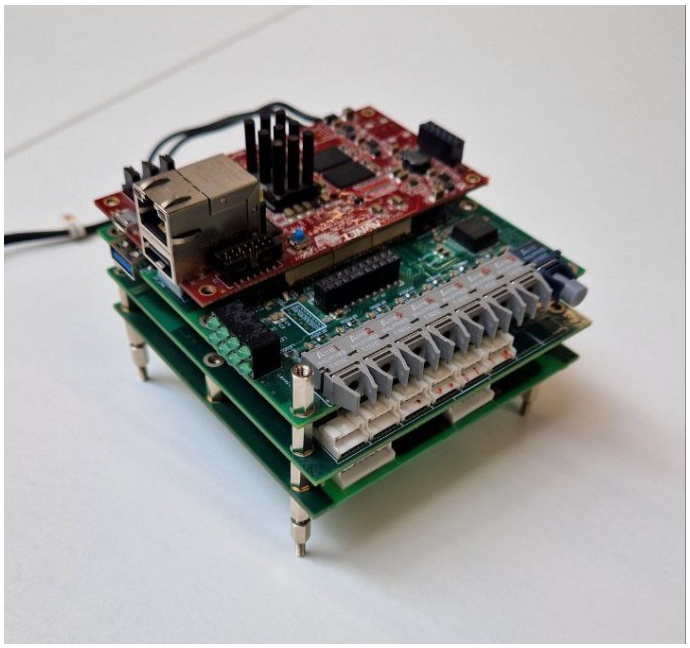

Figure 5.1: uCube Control Board

The uCube consists of a set of boards that are connected to each other through a connector whose layout allows the various boards to be stacked, each with a specific function. There is a fibre-optic board for controlling the two-level inverter, a board for acquiring analogue measurements, one for reading encoders and resolvers, and finally a board dedicated to drive the gate signal of the 18 IGBT of the matrix converter. The board also allows serial communication with the PC so that data acquired from measurements on the system and used for control can be monitored.

5.1.2 Matrix Converter Side

The matrix converter side is composed by a variac, also known as autotransformer, to reduce the filter input voltage, the LC filter, the matrix converter and finally the SM-PMSM1. A schematic of the matrix converter side setup is presented in Fig. 5.2

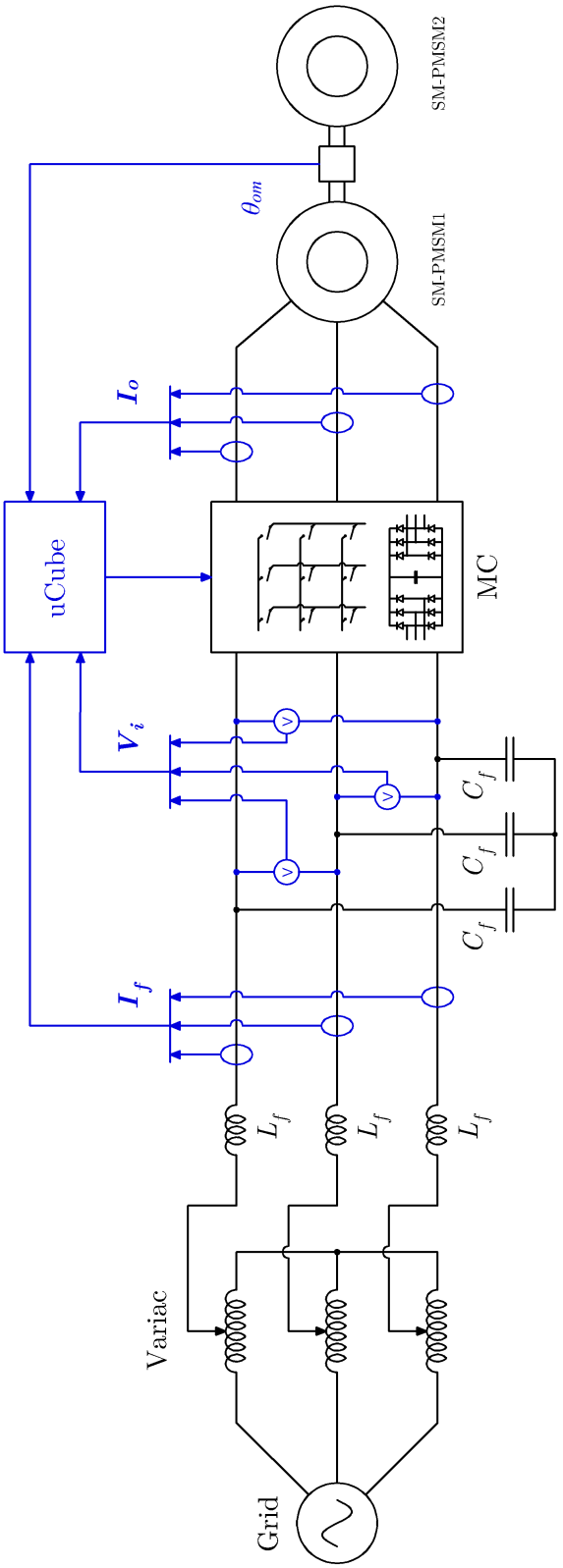

Figure 5.2: Matrix Converter Side Schematic

As mentioned in Chapter 3, voltage is a parameter that has a big impact on system stability. The lower the voltage, the lower the power that the system is able to provide or withdraw from the output. To evaluate the performance of the control algorithms, it is necessary to place the system under the most unfavourable conditions. Thus a variac is used to lower the grid phase-to-phase voltage from 380 V to 120 V. This value is a lower limit as the autotransformer distorts the grid waveform too much. After the variac is the filter inductor followed by the measurement of the filter currents. These measurements are not used to control the system but just to have a comparison with the estimated filter current. The filter capacitors are mounted on the matrix converter board as well as the input voltage measurement, the clamp circuit and the output current measurement. Finally the SM-PMSM1 is connected to the matrix converter output. The rotor angle is measured using a single resolver for both motors, as their shafts are directly connected. From the rotor angle it is possible to obtain the rotor speed that is the feedback of the speed control loop of the SM-PMSM2. In Fig. 5.3 the matrix converter is shown, while the Matrix Side Parameters are reported in Tab 5.1.

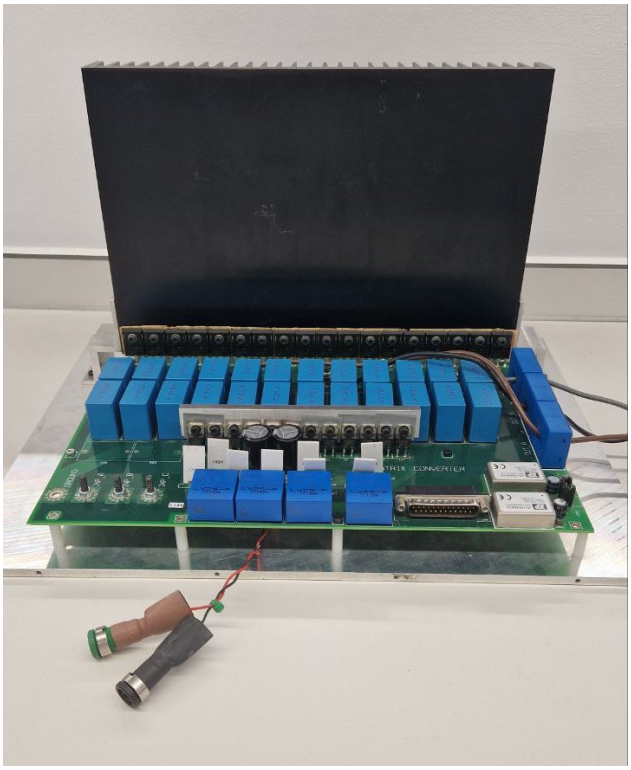

Figure 5.3: Matrix Converter

Table 5.1: Matrix Converter Side Experimental Setup Parameters

Supply and LC filter	V_{g_pp}	120	V
	R_f	1.5	Ω
	L_f	2.4	mH
	C_f	1.2	μF
Matrix Converter	P^n	25	kW
	V^n	380	V
	f_s	10	kHz

SM-PMSM1	P^n	3.8	kW
	V^n	172	V
	w_m^n	314	rad/s
	R_o	0.1	Ω
	L_o	0.3	mH
	ϕ_{PM}	0.134	Wb
	p	4	

5.1.3 Dynamic Load Side

The dynamic load side consists of the SM-PMSM2, which is driven by a two-level inverter, whose DC link is fed by a DC power supply. Parallel to the DC link capacitor is the breaking chopper. A breaking chopper is composed of a switch and a breaking resistor. This component is fundamental when the SM-PMSM1, supplied by the matrix converter, is providing torque and the SM-PMSM2 has to break to keep constant the speed. In this scenario the power flows from the motor to the DC link rising its voltage. The voltage is kept constant driving correctly the switch and dissipating the energy in the resistor. This is necessary because the DC power supply used is not able to supply power to the grid. The dynamic load parameters are reported, while in Fig. 5.4 the schematic of the dynamic load is reported.

Table 5.2: Dynamic Load Side Experimental Setup Parameters

Two-level Inverter	P^n	15	kW
	V^n	380	V
	f_s	10	kHz

SM-PMSM2	P^n	1	kW
	V^n	401	V
	w_m^n	125	rad/s
	R_o	1	Ω
	L_o	1	mH
	ϕ_{PM}	0.8	Wb
	p	4	

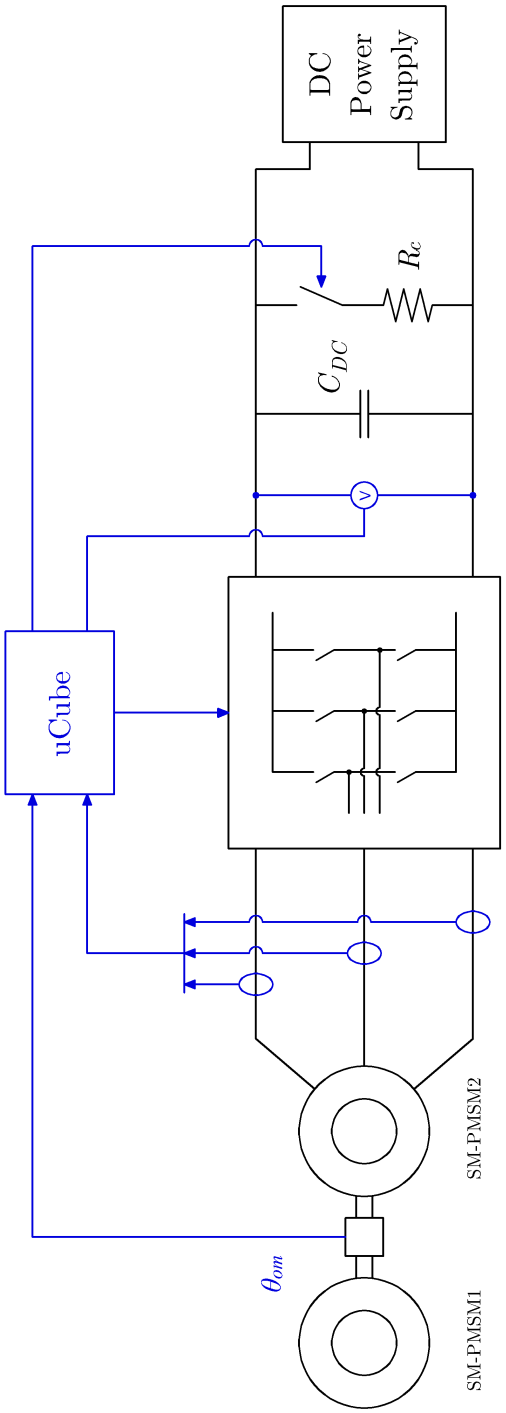

Figure 5.4: Dynamic Load Schematic

In the following some pictures of the experimental setup are reported. Fig. 5.5 reports the filter and the converters, Fig. 5.6 shows the SM-PMSM motors and a picture of the variac is presented in Fig. 5.7

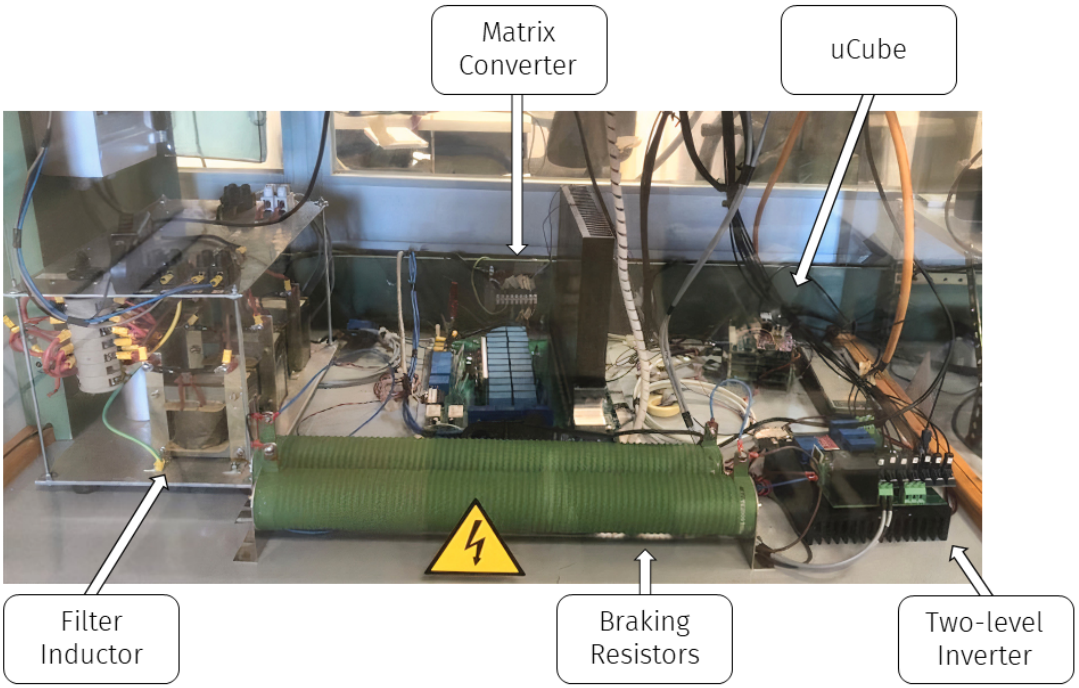

Figure 5.5: Experimental setup, filter and converters

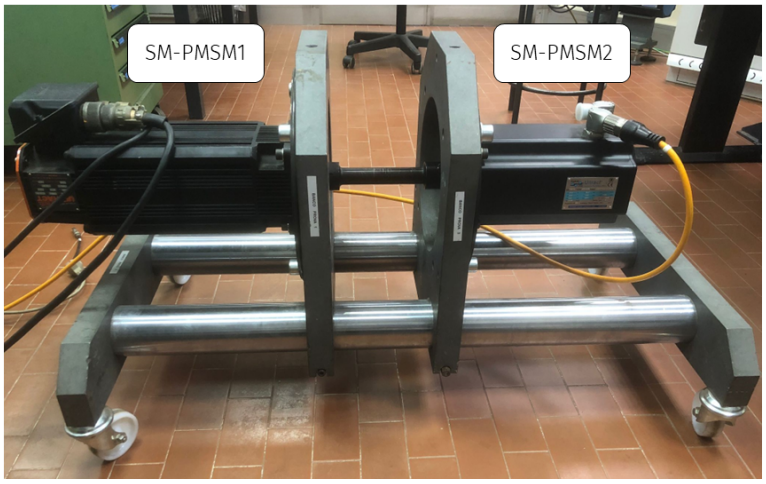

Figure 5.6: Experimental setup, SM-PMSM motors

Figure 5.7: Experimental setup, variac

5.2 Control Algorithms Tuning

The aim of these experiments is to verify which of the two methods provides the best performance in terms of power and harmonic content with the same control bandwidth. The real system proved to be more stable than the mathematical model and the simulated system. In fact, it has been possible to tune control algorithm at higher bandwidth than those proposed in simulation, approximately 2 kHz. The control bandwidth of the HPF method depends on the K_p and K_i gains that are chosen for the PI current controllers. The gain tuning procedure presented in Chapter 2 has been used to define starting values from which gains were then empirically derived to provide the desired control band with the best possible damping ratio. Regarding the gains and cut-off frequency of the stabilization method, in motor mode the cut-off frequency f_{cut_HPF} and gain k have been tuned primarily through the mathematical method proposed in Chapter 3 and then the tuning has been refined by varying the k until the maximum possible power was achieved with the lowest possible harmonic content. In generator mode the cut-off frequency $f_{cut\_HPF\theta}$ and the gain k_θ have been tuned following the guidelines presented in [3]. In Tab. 5.3 the HPF gains and cut-off frequencies are reported: The H_2-LMI algorithms, motor mode and generator mode, have been tuned using the same

Table 5.3: HPF gains and cut-off frequencies

PI	K_p	4	
	K_i	15000	
HPF Motor Mode	k	1.1	
	f_{cut_HPF}	100	Hz
HPF Generator Mode	k_θ	-0.6	
	$f_{cut\_HPF\_\theta}$	100	Hz

weighting matrices and polytope that were presented in the simulation case. In the experimental apparatus, these matrices resulted in a control band of approximately 2 kHz in both motor mode and generator mode. The matrices are re-presented below:

$$\begin{aligned} \boldsymbol{R}_m &= diag(1,1); \\ \boldsymbol{Q}_m &= 2.5 \cdot 10^8 \cdot diag(0,0,0,0,0,0,1,1,0,0); \\ \boldsymbol{R}_g &= diag(1,1,1); \\ \boldsymbol{Q}_g &= 2.5 \cdot 10^8 \cdot diag(0,0,0,0,0,0,1,1,1,0,0,0); \end{aligned} \tag{5.1}$$

In motor mode the polytope is generated with $\omega_o \in [0, 2\,\pi\,60]\,rad/s$ and $I_{oq} \in [0, 15]\,A$, while in generator mode considering $\omega_o \in [0, 2\,\pi\,60]\,rad/s$ and $I_{oq} \in [-15, 0]\,A$. The observer is also implemented using the same covariance matrices used in the simulator, reported in the following:

$$\boldsymbol{\Omega}_1 = 10^5 \cdot diag(1,1,1,1,1,1); \qquad \boldsymbol{\Omega}_2 = 10^{-3} \cdot diag(1,1) \tag{5.2}$$

The system in this way exhibited behaviour almost entirely similar to that simulated, except for the control bandwidth in motor mode, which was higher in the experimental setup. At this point, it is necessary to compare the control bandwidth the two algorithm to ensure that they are comparable. For this purpose, in simulation the response of the system to a I_{oq_r} step was analyzed comparing it with the response of a second order system. In the experimental setup, this test has been carried out with a I_{od_r} step with the motors at standstill because, unlike the simulation in which the speed of the SM-PMSM fed by the matrix converter was mathematically imposed, in the real case the slower

speed dynamics would have compromised the analysis. The reason for using the d-axis is simply to avoid generating torque. In Fig. 5.8 the step response of the HPF and H_2-LMI algorithms is presented.

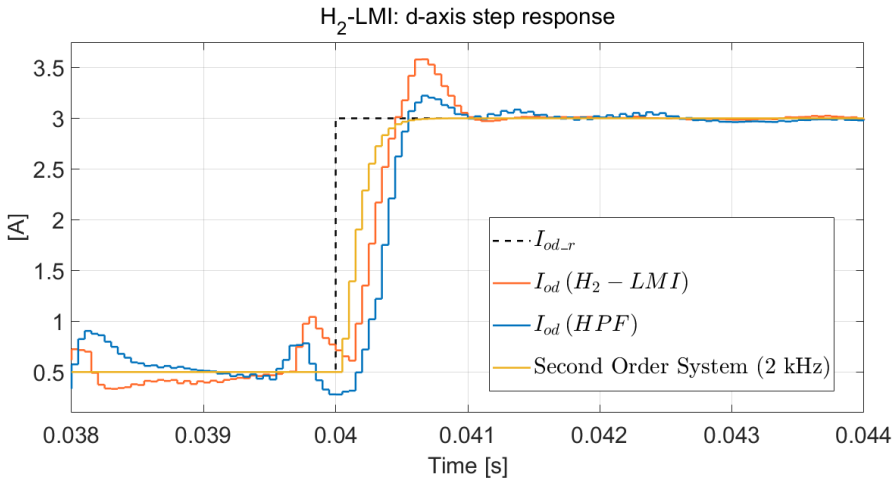

Figure 5.8: H_2-LMI and HPF d-axis step response comparison.

The data presented were obtained through the serial communication of the uCube. The step response of the two systems was compared with that of a second-order model with a control band of $2\,kHz$. As can be seen, the responses of the systems are comparable and approximately around $2\,kHz$. The systems thus tuned are ready for the final comparison.

5.3 Results

5.3.1 HPF method

The analysis of the results begins with an evaluation of the performance of the HPF system in motor mode and generator mode. The system is found to be stable in motor mode up to a maximum output current $I_{oq} = 10\,A$ with unity power factor. In generator mode, with unity power factor, when I_{oq} is lower then $-10\,A$ the system is still stable but it is heavily affected by harmonic distortion. Therefore, $I_{oq} = -10\,A$ will be considered as the lowest useful stable value from an application point of view. Please note that the power factor is imposed by the phase shift between input voltages and currents ϕ provided to the modulator, that in this case is zero. The steady-state waveforms at $I_{oq} = 10\,A$ are presented in Fig. 5.9, while those at $I_{oq} = -10\,A$ in Fig. 5.10.

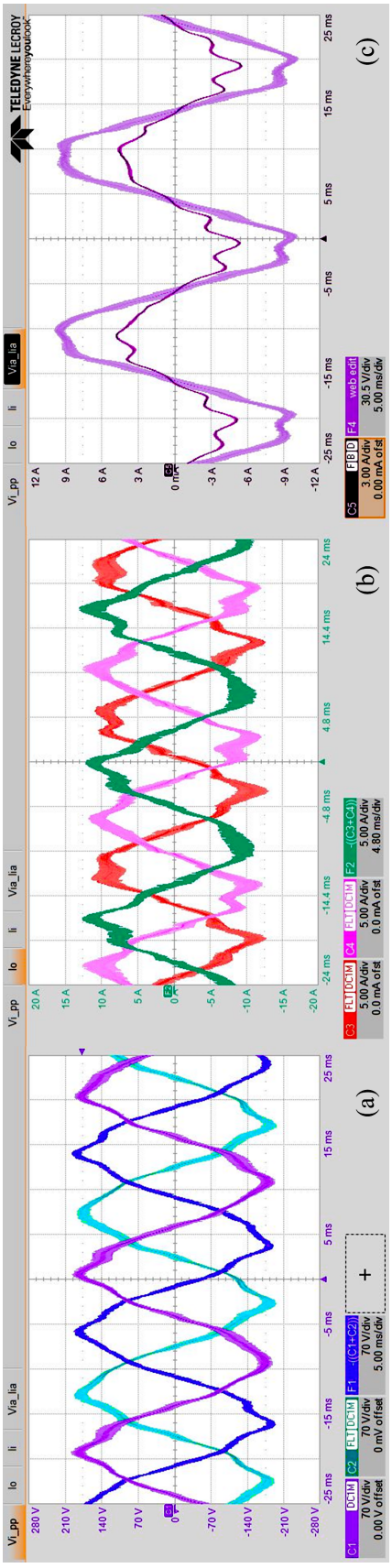

Figure 5.9: HPF, $I_{q\_ref} = 10$ A (544 W): input phase to phase Voltage (a), Output Current (b), Input single phase voltage and current (c).

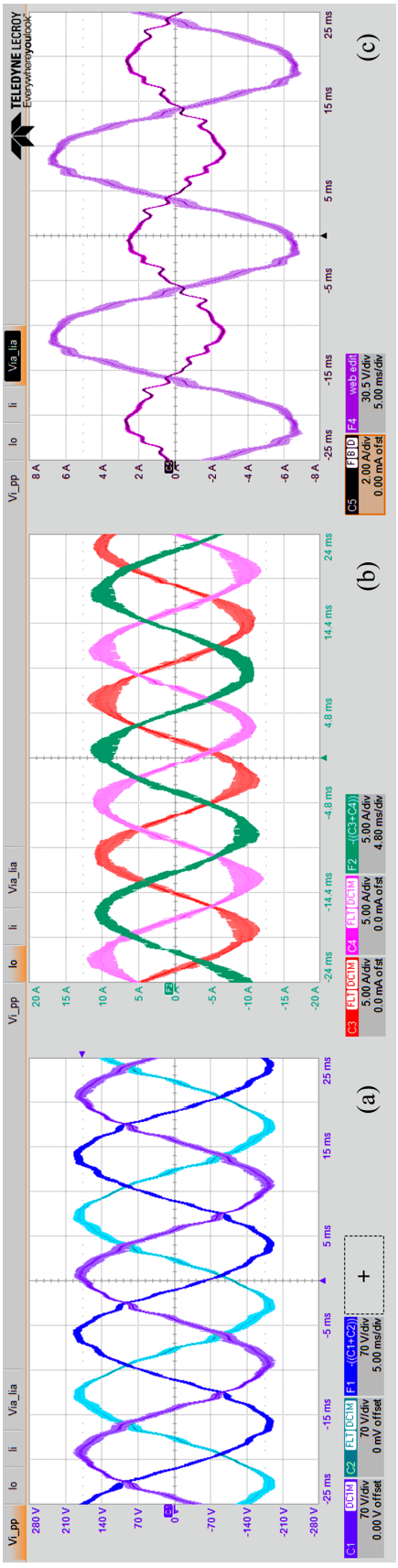

Figure 5.10: HPF, $I_{q\_ref} = -10$ A (544 W): input phase to phase Voltage (a), Output Current (b), Input single phase voltage and current (c).

In the figures 5.9 and 5.10 graphs (a) and (b) depict the input phase-to-phase voltage and the output current while (c) reports a comparison between one phase input voltage and current. As can be seen in Fig. 5.9 (c) the voltage of the single phase is in phase with filter current of the corresponding phase, resulting in unity power factor. In contrast, in Fig. 5.10 (c) the current is out of phase respect to the voltage, this is because the power flow is negative. In motor mode, as soon as the reference I_{oq_r} is changed from 10 to $10.5\,A$, the system becomes unstable, causing the protections to trip. In Fig. 5.11 a single input phase voltage is reported in (a) and the filter current of the corresponding phase is reported in (b).

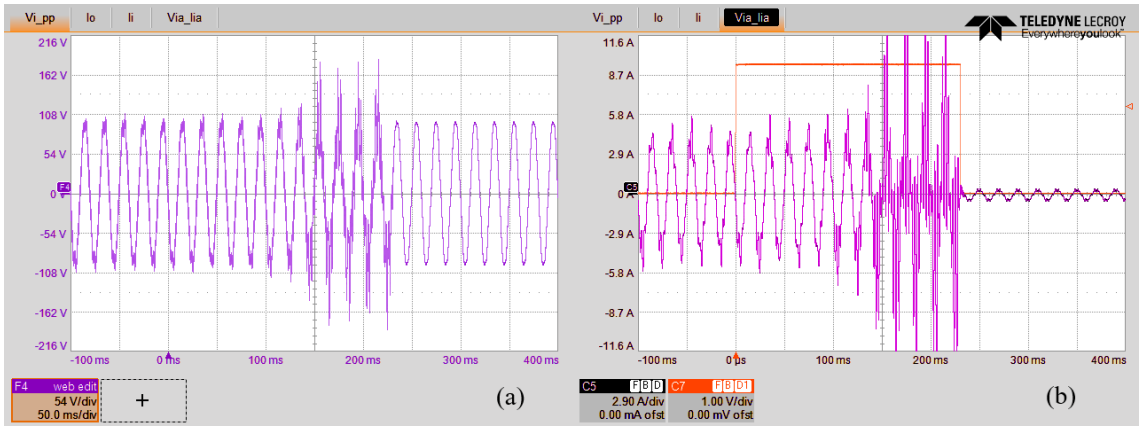

Figure 5.11: HPF instability: single phase input voltage and filter current, detail of instability due to the power request exceeding the stability range.

In Fig. 5.11 (b) a step signal is also shown; this was provided by the control board in order to trigger the oscilloscope in the exact moment when the reference was changed from $10\,A$ to $10.5\,A$. An enlargement showing the development of the instability on the filter current is shown in Fig. 5.12.

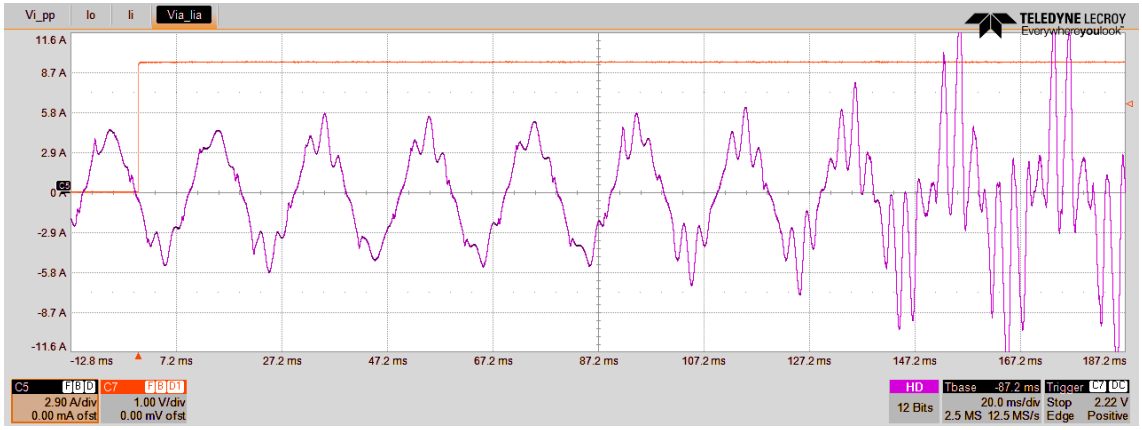

Figure 5.12: HPF instability: development of the instability on the filter current.

The output currents behaviour during the instability is shown in the Fig. 5.13

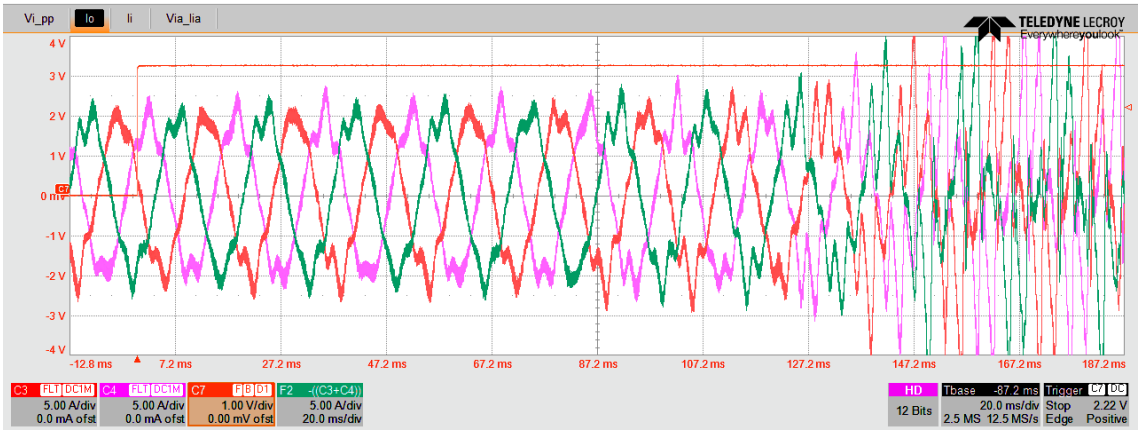

Figure 5.13: HPF instability: output currents during instability.

5.3.2 H_2-LMI method

At this point, experimental results are introduced in the case of the H_2-LMI control algorithms. The system is stable within the defined ranges. In motor mode the system is stable at $I_{oq} = 15\,A$, just as the system is stable in generator mode with $I_{oq} = -15\,A$. In motor mode the unity input power factor was imposed by imposing $\phi = 0\,rad$, while in generator mode imposing the reference $r_\theta = 0\,rad$. Fig. 5.14 shows the steady-state waveforms with $I_{oq} = 15\,A$, while Fig. 5.15 shows the waveforms with $I_{oq} = -15\,A$. As in the case of the HPF results, the figures graphs (a) and (b) report the input phase-to-phase voltage and the output current while (c) shows a comparison between one phase input voltage and current. The system was also tested with I_{oq} values beyond the values within which the polytope was defined, but no instabilities occurred. In order not to damage the motor, the tests were not extended beyond $20\,A$.

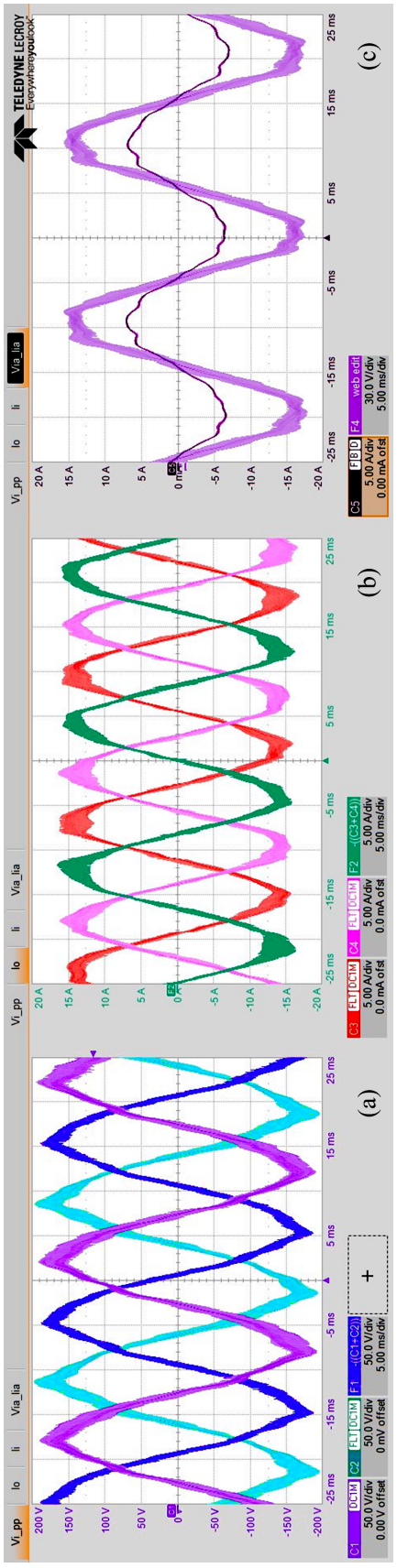

Figure 5.14: H_2-LMI, $I_{q\_ref} = 15$ A (880 W): input phase to phase Voltage (a), Output Current (b), Input single phase voltage and current (c).

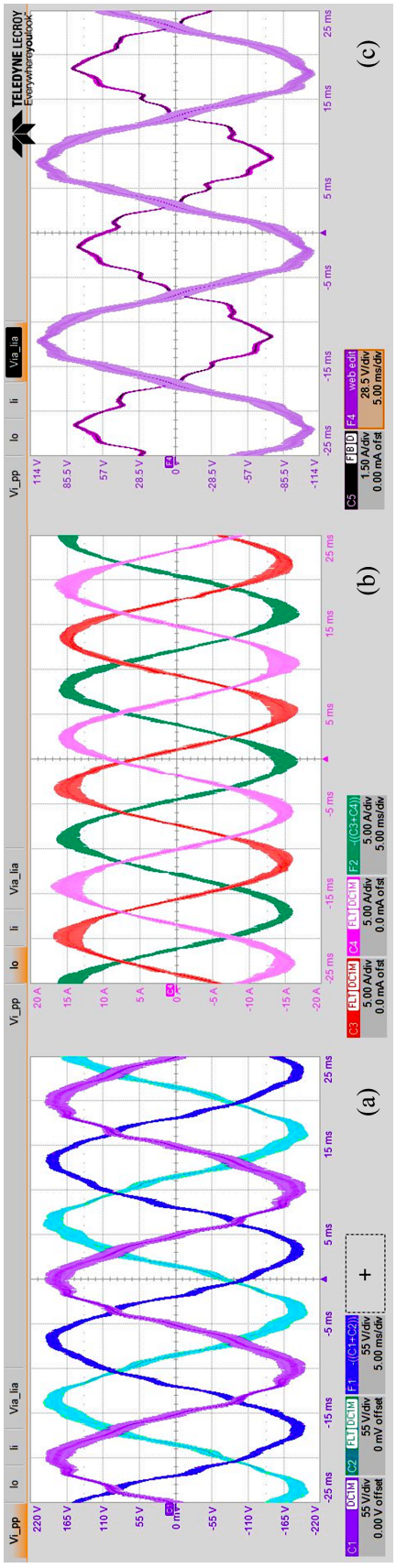

Figure 5.15: H_2-LMI, $I_{q\_ref} = -15$ A (-810 W): input phase to phase Voltage (a), Output Current (b), Input single phase voltage and current (c)

A I_{oq_r} step reference from positive to negative is presented. The two controllers in motor mode and generator mode are in fact different as seen, and to perform a switch between the two controllers, the outputs of the two controllers must be the same at the time of the switch. The generator mode controller also has an additional output, the input phase shift ϕ, that is kept close to zero. In the case of switching between motor mode and generator mode the switch occurs when, as a result of the change in the sign of the reference I_{oq_r}, the current I_{oq} becomes negative. In the case of switching from generator mode to motor mode, the opposite occurs. In order to keep the outputs constant at the moment of the switch, it is necessary to calculate at the exact instant of the switch the value of the state variables x_{ic} and $x_{i\phi}$ to be applied to initialise the integrators, of the method being switched, to such that the same V_{od_r}, V_{oq_r} and ϕ are guaranteed.Fig. 5.16 reports the comparison between the output phase current (blue) and the q-axis output current step (orange) when an I_{oq_r} reference step from $-10\,A$ to $+10\,A$ is applied, while Fig. 5.17 shows the three-phase waveforms, in the following page.

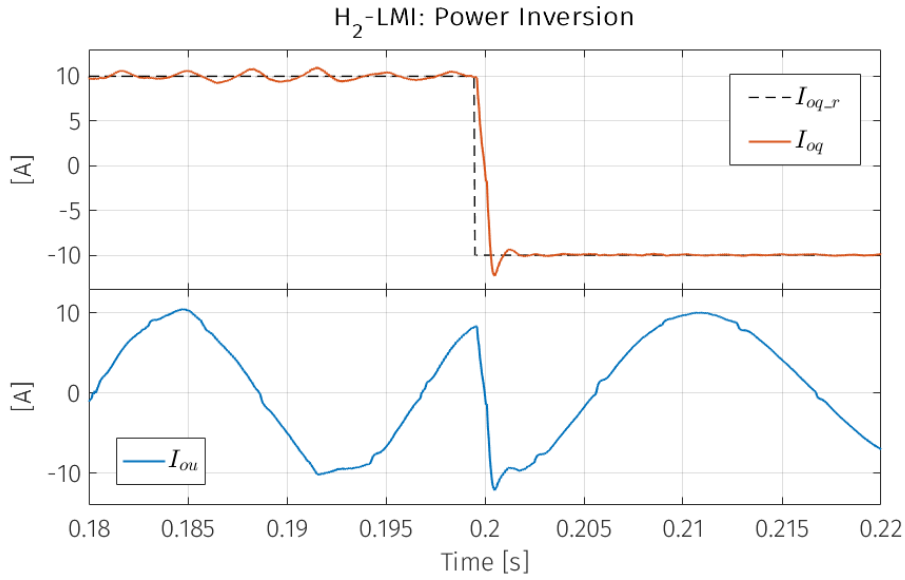

Figure 5.16: H_2-LMI: q-axis reference step, $I_{q\_ref} = 10$ A $\rightarrow -10$ A.

In Fig. 5.17 (c) and in Fig. 5.16 it is possible to notice the phase change of the input current. The switch showed stable and smooth behavior proving the effectiveness of the adopted gain scheduling solution.

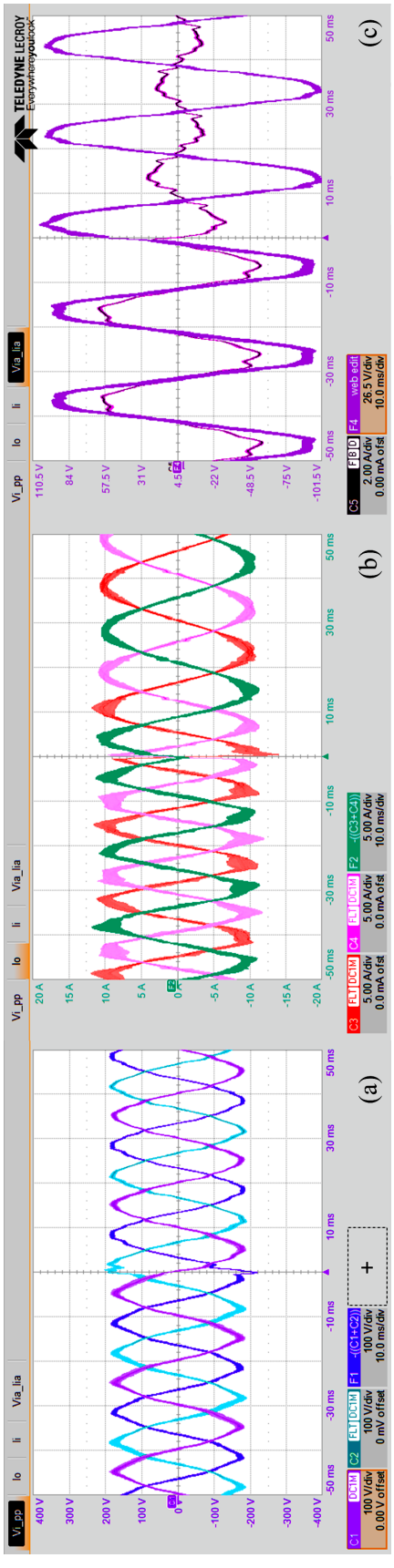

Figure 5.17: H_2-LMI, $I_{q\_ref} = 10\ A \rightarrow -10\ A$.: input phase to phase Voltage (a), Output Current (b), Input single phase voltage and current (c).

5.3.3 Methods Comparison

At this point, the comparison between the two stabilisation methods can be made. First of all, as already noted, the H_2-LMI method allows a 60% increase in transmissible power in both motor mode and generator mode. Secondly, it is possible to perform a harmonic distortion analysis of the waveforms. Tab. 5.4 shows the THD values of the filter and output currents for each of the two methods at different current values.

Table 5.4: THD Analysis Results

		$P\ [W]$	$\lvert\boldsymbol{I}_o\rvert\ [A]$	$THD\ \boldsymbol{I}_o$ [%]	$THD\ \boldsymbol{I}_f$ [%]
H_2-LMI	M	262	5	11.0	14.3
		544	10	7.5	8.3
		880	15	6.5	7.2
	G	-255	-5	6.7	15.7
		-495	-10	5.4	12.2
		-810	-15	4.8	12.1
HPF	M	262	5	21.2	29.8
		544	10	14.2	22.6
	G	-255	-5	13.9	14.1
		-495	-10	7.3	11.8

The table shows that The H_2-LMI methods reduces the harmonic content by 50% compared to the HPF methods for the same current value. The THD of the filter input currents is also reduced in all cases except one. In fact, the HPF method in generator mode at a current of $I_{oq} = -10\,A$ turns out to have a slightly lower THD than the H_2-LMI method. The last comparison that can be made between the two control algorithms is the computational burden. the computational time has been measured for both the algorithms: the H2-LMI requires 14.5 us for the motor mode and 15.5 us for the regenerating mode, while HPF requires 8.2 us for the motor mode and 8.8 us for the regenerating mode. These times account for the execution of the whole interrupt functions, including input readings, output writing and some other auxiliary tasks. Considering that the switching period is 100 us, the slight execution time increment of H2-LMI can be reasonably considered acceptable.

5.3.4 Chapter Summary

In this chapter, the experimental setup employed to test the HPF and H_2-LMI stabilization algorithms has been introduced. The performance of these algorithms was compared under equal control bandwidth conditions. An increase in transmissible power of approximately 60% and a reduction of 50% in the THD of the output currents have been observed. The computational burden is increased by 50%, but compared to the switching period and given the results obtained, this increase is reasonable. It is therefore concluded that the H_2-LMI algorithm is a good solution for stabilizing the matrix converter application requiring a low computational burden.

References 5

[1] A. Galassini, G. Lo Calzo, A. Formentini, C. Gerada, P. Zanchetta, and A. Costabeber, "ucube: Control platform for power electronics," in 2017 IEEE Workshop on Electrical Machines Design, Control and Diagnosis (WEMDCD), pp. 216–221, 2017.

[2] A. Alesina and M. G. Venturini, "Analysis and design of optimum-amplitude nine-switch direct ac-ac converters," IEEE Transactions on Power Electronics, vol. 4, no. 1, pp. 101–112, 1989.

[3] Y. Sun, M. Su, X. Li, H. Wang, and W. Gui, "A general constructive approach to matrix converter stabilization," IEEE Transactions on Power Electronics, vol. 28, no. 1, pp. 418–431, 2013.

Conclusion

In this thesis, the problem of matrix converter stability and control was addressed. The absence of a DC stage, often seen as the main advantage of the matrix converter, poses stability problems. In particular, the absence of a DC link, combined with the presence of the input filter, triggers resonance phenomena that increase with power increasing, leading to instability. In the course of the thesis, the instabilities were analysed from a mathematical and simulative point of view. Stabilisation methods proposed in the literature have been analysed mathematically in order to study their limits in terms of power and control bandwidth. Subsequently, a stabilization strategy based on full state feedback was introduced, a control strategy that allows the poles of the system to be re-placed in such a way as to model the dynamics of the system. The method used for positioning the poles and thus tuning the full state feedback algorithm is H_2-LMI. This method has the particularity of being able to realise stable controllers even in the case of systems with variable parameters or non-linear systems. The proposed method was finally tested experimentally and compared with an existing method, resulting in an improvement in transmissible power around 60% and a reduction of the output current THD around 50%, with an acceptable increase in computational burden.

Future Development

The experimental and simulative results were all obtained considering the unit power factor. A future development could be to study the effect of power factor variation on stability. Furthermore, the effect on stability of the presented algorithm in the case of different applications scenario could be investigated. For example, it could be analyzed how this behaves when introduced into a microgrid, such as an aircraft electrical plant. Finally, it could be investigated how to tune the presented algorithm to mitigate the effect of distortion on the converter output as a function of input disturbance. This in fact turns out to be another matrix converter problem that can be solved by the H_2-LMI algorithm